UNIVERSITÄT ZU LÜBECK
INSTITUTE FOR SIGNAL PROCESSING

From the Institute for Signal Processing
of the University of Lübeck

Acting Director: Prof. Dr. rer. nat. habil. Heinz Handels

A Fourier-Analytical Approach for Field-Free-Point Magnetic Particle Imaging

Dissertation
for Fulfillment of
Requirements
for the Doctoral Degree
of the University of Lübeck

from the Department of Computer Sciences and Technical Engineering

Submitted by

Marco Maaß
from Pinneberg

Lübeck, 2024

First referee:	Prof. Dr.-Ing. Alfred Mertins
Second referee:	Prof. Dr. rer. nat. Jürgen Prestin
Date of oral examination:	December 17th, 2024

Approved for printing. Lübeck, April 3rd, 2025

Abstract

Magnetic particle imaging is a tracer-based medical imaging technique that measures the spatial distribution of superparamagnetic nanoparticles. Alternating magnetic fields with different excitation sequences are used to measure the nanoparticle distribution in a scanner. Usually, the simplified Langevin model of paramagnetism is used as a first approximation for the complicated nonlinear magnetization behavior of nanoparticles. Although the modified Langevin model of paramagnetism can provide suitable image reconstructions for one-dimensional excitation, the situation is more complicated for higher-dimensional excitation, as several aspects cannot be fully explained by the Langevin model. A well-known example is the spatial similarity of the frequency components of the system function with tensor products of Chebyshev polynomials. This was observed for a higher-dimensional excitation of the Lissajous trajectory type and was unproven for almost ten years. With the aim of explaining such observations mathematically, this thesis makes an important contribution to the mathematical foundations of magnetic particle imaging. To this end, the spatio-temporal system function based on the Langevin model is transformed into the frequency domain using various concepts of Fourier analysis. The scientific contribution of the newly developed mathematical framework is manifold. Firstly, the developed model is able to separate the scanner-dependent excitation from the particle magnetization model, allowing better utilization of the imaging operator so that faster reconstruction methods could be developed. Secondly, it is now easier to investigate both the effect of the magnetization model and that of the excitation sequence in the imaging model separately. Thus, an extended equilibrium magnetization model is introduced in this thesis and a series representation is developed for it. Furthermore, the exact relationship between the frequency components of the system function and the tensor products of Chebyshev polynomials is shown for excitations of the Lissajous trajectory type. Finally, using the developed mathematical framework, the frequency representations of various excitation sequences known from the literature are calculated, which further increases the applicability of the model for magnetic particle imaging.

Zusammenfassung

Die Magnetpartikelbildgebung ist ein auf Tracern basierendes medizinisches Bildgebungsverfahren, das die räumliche Verteilung von superparamagnetischen Nanopartikeln misst. In der Magnetpartikelbildgebung werden wechselnde Magnetfelder mit unterschiedlichen Anregungssequenzen zur Messung der Nanopartikelverteilung in einem Scanner verwendet. In einer ersten Annäherung wird normalerweise das vereinfachte Langevin-Modell des Paramagnetismus als Approximation für das komplizierte nichtlineare Magnetisierungsverhalten von Nanopartikeln genutzt. Obwohl das modifizierte Langevin-Modell des Paramagnetismus bei eindimensionaler Anregung geeignete Bildrekonstruktionen liefern kann, ist die Situation bei höherdimensionaler Anregung komplizierter, da mehrere Aspekte nicht vollständig durch das Modell erklärt werden können. Ein bekanntes Beispiel ist die räumliche Ähnlichkeit der Frequenzkomponenten der Systemfunktion mit Tensorprodukten von Tschebyscheff-Polynomen. Dies wurde für eine höherdimensionale Anregung vom Lissajous-Trajektorie-Typ beobachtet und war fast zehn Jahre lang unbewiesen. Mit dem Ziel, solche Beobachtungen mathematisch erklären zu können, leistet diese Arbeit einen wichtigen Beitrag zu den mathematischen Grundlagen der Magnetpartikelbildgebung. Zu diesem Zweck wird die auf dem Langevin-Modell basierende raum-zeitliche Systemfunktion mit Hilfe verschiedener Konzepte der Fourier-Analyse in den Frequenzbereich transformiert. Die wissenschaftlichen Beiträge der neu entwickelten mathematischen Beschreibung ist vielfältig. Unter anderen ist das entwickelte Modell in der Lage, die scannerabhängige Anregung vom Partikelmagnetisierungsmodell zu trennen, was eine bessere Nutzung des Bildgebungsoperators ermöglicht, so dass schnellere Rekonstruktionsmethoden entwickelt werden können. Außerdem ist es nun einfacher, sowohl den Effekt des Magnetisierungsmodells als auch den der Anregungssequenz im Abbildungsmodell separat zu untersuchen. Daher wird in dieser Arbeit ein erweitertes Gleichgewichtsmagnetisierungsmodell eingeführt und eine Reihendarstellung dafür entwickelt. Darüber hinaus wird die exakte Beziehung zwischen den Frequenzkomponenten der Systemfunktion und den Tensorprodukten von Tschebyscheff-Polynomen für Anregungen vom Lissajous-Trajektorien-Typ gezeigt.

Schließlich werden mit Hilfe der entwickelten mathematischen Methoden die Frequenzdarstellungen verschiedener aus der Literatur bekannter Anregungssequenzen berechnet, was die Anwendbarkeit des Modells für die Magnetpartikelbildgebung weiter erhöht.

Contents

1 Introduction

Magnetic particle imaging (MPI) is a medical imaging technique in preclinical development stage that was developed in 2001 by researchers at Philips Research in Hamburg and first published in 2005 [30]. As the name suggests, the aim of MPI is to measure certain particles, so-called tracers, with the help of magnetic fields. These tracers are superparamagnetic iron oxide nanoparticles (SPIOs). The special feature of SPIOs is their non-linear magnetization characteristic and superparamagnetic behavior. This means that the magnetic particles align their magnetic moment in the direction of the applied magnetic field, but when the external magnetic field is switched off, the particles lose the alignment of their magnetic moment again. It is precisely this nonlinear magnetization of the SPIOs that makes it possible to simultaneously measure the spatial distribution and concentration of the SPIOs. MPI can therefore be classified as a tracer-based imaging modality, just like positron emission tomography. In contrast to positron emission tomography, however, the tracer material of MPI is non-ionizing. Although MPI is still in a preclinical phase, there are a number of potential applications such as vascular imaging [42, 46, 101, 106], cancer imaging [44, 117], and interventional imaging [41, 82, 87, 110]. In MPI, various static and time-varying magnetic fields are applied to measure the spatial SPIO distribution. One magnetic field is the selection field, which is a spatially inhomogeneous magnetic field that enables a spatial encoding. The selection field has a different dominant magnetization direction and field strength in the entire area of interest except for the field-free region. The field-free region is an area in which no magnetic field can be measured, which can be achieved, for example, by superimposing different magnetic fields. In the context of this thesis, the field-free region is a field-free point (FFP). The idea behind this is to saturate the SPIOs differently across the entire field of view (FOV), which thus represents spatial encoding. In order to move the FFP through the FOV, the selection field must also be superimposed with a time-varying magnetic field, the so-called drive field.

SPIOs that are far away from the FFP are magnetically saturated because their magnetic moments are almost all aligned in the direction of the applied magnetic field, i.e., if the field strength of the applied magnetic field is increased without changing its direction, the magnetization of the SPIO distribution will not increase further. In contrast, the magnetic moments of the particles in the vicinity of the FFP are not strongly aligned with the direction of the applied magnetic field, so that the magnetization of an SPIO distribution in the vicinity of the FFP can change significantly when the FFP is moved. According to the law of induction, a change in magnetization induces a voltage signal in the receive path of the MPI scanner, which can be measured. A relationship between the spatial distribution of the SPIOs and the measured voltage signal can be established, which allows for the reconstruction of SPIO distributions.

In recent years, various steps have been taken in the direction of the scanner design [30, 33, 35, 39, 72, 88, 102, 103, 107, 113]. There are currently two commercially available preclinical scanners, the FFP scanner from Bruker and the one from Magnetic Insight, a field-free line (FFL) scanner, which uses an FFL instead of an FFP to measure spatial particle distributions. However, many scanners are just large enough to measure small rat-sized animals. More recently, initial concepts for a human-sized scanner have led to scanners that can measure a human head [35, 71, 103]. In the first multimodal medical imaging combinations, MPI was combined with magnetic resonance imaging [27, 104] or with computed tomography [105].

One of the major problems in MPI is the lack of good mathematical models to describe the magnetization behavior of SPIOs. In general, the Langevin model of paramagnetism is often used for first theoretical considerations and numerical simulations in MPI. But this model neglects the particle anisotropy, particle-particle interactions, and any form of relaxation behavior of the particles. Even for such a simplified model, it has not yet been possible to uncover all the relationships of the MPI system function. Since the fundamental work of Rahmer et al. [81], which was able to derive an exact relationship for the one-dimensional periodic excitation case in MPI and also hypothesized that there should be a relationship to tensor products of Chebyshev polynomials of the second kind for two-dimensional periodic excitations, the exact relationship was unknown. In [80], the tensor-product structure of Chebyshev polynomials was also observed for three-dimensional periodic excitations in MPI. This crucial aspect is shown in this thesis and was firstly mathematical proven in [F1]. Although these models have been widely

used to explain the spatial structure of the system function components and to deduce various strategies for compressing them as well as for the compressed sensing based calibration, there was no mathematical justification of these strategies and the use was rather based on the empirical success of this assumption [F2, F3, 56, 60, 91, 109]. In this thesis, the exact relationship of the Chebyshev polynomials to the system function components for different drive-field excitations is derived. For this purpose, a proof via the spatio-temporal Fourier domain is chosen. In a first step, it is shown that the spatio-temporal Fourier transform of the system function is related to a multiplication between the Fourier-transformed magnetization curve of the SPIOs and a series of tensor products of Bessel functions. In a second step, it can then be shown that the system function component in the spatial domain is related to a convolution between the spatial derivatives of the magnetization curve of the SPIOs and a series of tensor products of Chebyshev polynomials.

Regardless of the results, which were theoretically substantiated for the first time by the work [F1], a number of other publications have emerged for MPI. First of all, the direct and system-matrix-free multidimensional reconstruction method for MPI based on Chebyshev polynomials [C1], which was previously only possible for one-dimensional excitation [40, 81], should be mentioned. Closely related to the direct reconstruction based on Chebyshev polynomials is the direct reconstruction based on Bessel functions, which was first presented for the one-dimensional case in [F4]. Furthermore, with the help of the theoretical understanding, the compression of the system matrix could be further increased [C2]. Also, it served as a theoretical justification for the fact that the so-called overscanned FOV, the area outside the drive-field FOV, in the system function components is only an analytical continuation of the drive-field FOV to the overscanned FOV [89].

Since the techniques developed in this work allow to replace the magnetization curve, i.e., the Langevin function in the Langevin model of paramagnetism, this model was extended in a subsequent steps with an anisotropic equilibrium magnetization model resulting in [F5, C3] and recently experimentally validated in [F6]. Nevertheless, this thesis will focus on the Langevin model of paramagnetism, but the anisotropic model will be outlined too.

The work is divided into the following chapters:

- Chapter 2 introduces the basic theory and fundamental principles of MPI.

- Chapter 3 presents the more complex relaxation and magnetization models for SPIOs and shows how the simplified Langevin model of paramagnetism is related to these more advanced models. The models presented in this chapter form the foundation of [F7]. Furthermore, the calculation of the anisotropic equilibrium model is discussed in more detail, which is the basis of [F5, F6, C3].

- Chapter 4 provides some basic knowledge regarding the Fourier analysis used in this work, briefly discussing the Fourier series at the beginning and then the Fourier transform on $\mathbb{R}^n$ in more detail.

- Chapter 5 introduces orthogonal polynomials and in particular Chebyshev polynomials of the first and second kind, followed by a section on Bessel functions. The last section explains how Bessel functions and weighted Chebyshev polynomials are related to each other via a Fourier transform on $\mathbb{R}$.

- Chapter 6 has two sections. The first section derives the spatio-temporal Fourier representation of the MPI system equation. The second section deals with the Fourier transform of the Langevin function and its properties. Parts of this chapter are published in [F1].

- Chapter 7 deals with various FFP-trajectories for MPI from the literature. The first three sections deal with the Lissajous trajectory for the FFP. These results were first published in [F1]. The following section contains unpublished work and deals with arbitrary periodic FFP-trajectories. A general concept for deriving the mapping function and thus the system function components is proposed. Subsequently, the corresponding mapping function is calculated for different FFP-trajectories from the literature.

The thesis is concluded with the chapter Conclusions & Outlook.

2 Principles of Magnetic Particle Imaging

This chapter is divided into two parts. In the first section, the principles of signal generation in MPI are explained mathematically, but without explaining the actual structure of an MPI scanner. The chapter is mainly based on the mathematical models of MPI in [33, 53, 70, 92]. Subsequently, the proof from [81] for MPI system function components with one-dimensional FFP excitation is discussed and the problem of extending the proof to higher-dimensional FFP excitation is briefly explained, which motivates the proof strategies used in this thesis.

2.1 Signal Generation

The central signal equation in MPI can be explained by the Faraday induction law which is a part of the Maxwell equations. The voltage signal $u_\nu^{\mathrm{P}} : \mathbb{R} \to \mathbb{R}$ induced from the SPIOs in the ν-th receive coil is given by

$$\begin{aligned} u_\nu^{\mathrm{P}}(t) &= -\mu_0 \frac{\mathrm{d}}{\mathrm{d}t} \int_\Omega \boldsymbol{p}_\nu^{\mathsf{T}}(\boldsymbol{x})\, \boldsymbol{M}(\boldsymbol{x}, t)\, \mathrm{d}\boldsymbol{x} \\ &= -\mu_0 \int_\Omega \boldsymbol{p}_\nu^{\mathsf{T}}(\boldsymbol{x})\, \frac{\partial \boldsymbol{M}(\boldsymbol{x}, t)}{\partial t}\, \mathrm{d}\boldsymbol{x}, \end{aligned} \tag{2.1}$$

where $\boldsymbol{p}_\nu : \mathbb{R}^N \to \mathbb{R}^{N'}$ denotes the receiver coil sensitivity profiles, which can be determined by reciprocity principle [43, 53, 94], $\Omega \subset \mathbb{R}^N$ denotes the FOV, and $\boldsymbol{M} : \mathbb{R}^N \times \mathbb{R} \to \mathbb{R}^N$ the magnetization of the SPIO distribution. Besides, μ_0 denotes the vacuum permeability. It should be noted that physically motivated, MPI has three spatial dimensions and one time dimension, so N must be three. In MPI, however,

the spatial dimensions are ranging from one-dimensional ($N = 1$) to two-dimensional ($N = 2$) to three-dimensional ($N = 3$), so that $N \in \mathbb{N}$ is generally considered first. The coil sensitivity profile $\boldsymbol{p}_\nu(\boldsymbol{x})$ is a magnetic field $\boldsymbol{H}_\nu^{\mathrm{R}} : \mathbb{R}^N \to \mathbb{R}^{N'}$ that would be generated by a unit current I^{R} at the coil:

$$\boldsymbol{p}_\nu(\boldsymbol{x}) = \frac{\boldsymbol{H}_\nu^{\mathrm{R}}(\boldsymbol{x})}{I^{\mathrm{R}}}. \tag{2.2}$$

A spatially inhomogeneous and time-varying magnetic field $\boldsymbol{H} : \mathbb{R}^N \times \mathbb{R} \to \mathbb{R}^N$ is used to change the magnetization $\boldsymbol{M}(\boldsymbol{x}, t)$ of the SPIOs. Since the applied magnetic field $\boldsymbol{H}(\boldsymbol{x}, t)$ is by itself a dynamic, time-varying magnetic field, it also contributes to the overall MPI voltage signal in the scanner, which is denoted by

$$u_\nu^{\mathrm{E}}(t) = -\mu_0 \frac{\mathrm{d}}{\mathrm{d}t} \oint_{S_\nu} \boldsymbol{H}(\boldsymbol{x}, t) \cdot \mathrm{d}\boldsymbol{A}, \tag{2.3}$$

where S_ν describes the surface area spanned by the receive coil and $\mathrm{d}\boldsymbol{A}$ denotes the infinitesimally oriented surface element of S_ν.

The total induced voltage signal in an MPI scanner results from the superposition of the particle voltage signal $u_\nu^{\mathrm{P}}(t)$ and the excitation voltage signal $u_\nu^{\mathrm{E}}(t)$:

$$u_\nu(t) = u_\nu^{\mathrm{P}}(t) + u_\nu^{\mathrm{E}}(t). \tag{2.4}$$

Unfortunately, the excitation signal $u_\nu^{\mathrm{E}}(t)$ is about 120 dB higher than the particle-induced signal $u^{\mathrm{P}}(t)$ [36, 53], which makes it necessary to remove the excitation signal before discretizing and quantizing the signal in an analog-to-digital (A/D) converter. Modern A/D converters are not capable of resolving such a wide range of energy differences between two signals, and after quantization only the excitation signal would remain. A common method is to use an analog filter $a(t)$ with $a : \mathbb{R} \to \mathbb{R}$, which is designed to remove the fundamentals of the excitation signal so that

$$\tilde{u}_\nu^{\mathrm{P}}(t) = (a * u_\nu)(t) \approx (a * u_\nu^{\mathrm{P}})(t). \tag{2.5}$$

In addition, $a(t)$ can be used to describe the receive path of the MPI scanner and is therefore also referred to as the transfer function. An alternative, but technically more

complex option is to couple an additional third signal into the receive chain with the aim of canceling out the excitation signal [32, 36, 53]. Since the SPIO voltage signal $u_\nu^{\mathrm{P}}(t)$ is of interest for estimating the SPIO distribution in MPI, only $u_\nu^{\mathrm{P}}(t)$ will be considered for the moment.

The magnetization $\boldsymbol{M}(\boldsymbol{x},t)$ of an SPIO distribution $c_t : \Omega \times \mathbb{R} \to \mathbb{R}_+$ can be described by

$$\boldsymbol{M}(\boldsymbol{x},t) = \overline{\boldsymbol{m}}(\boldsymbol{x},t)c_t(\boldsymbol{x},t), \tag{2.6}$$

in which $\overline{\boldsymbol{m}} : \Omega \times \mathbb{R} :\to \mathbb{R}^N$ denotes the mean magnetic moment of one particle. Note that the SPIO distribution $c_t(\boldsymbol{x},t)$ could be time-dependent, but since a static SPIO distribution $c : \Omega \to \mathbb{R}_+$ is easier to consider for modeling the system function, the particle distribution $c(\boldsymbol{x}) = c_t(\boldsymbol{x},t)$ is now assumed to be time-independent in (2.6). Concepts for considering the time dependence of the SPIO distribution can be found in [11, 12, 28, 29, 90].

In a first approximation it is assumed that the SPIOs show no relaxation effects, no particle-particle interactions, and no significant anisotropies. Under these assumptions, the magnetization can be written as

$$\begin{aligned} \boldsymbol{M}(\boldsymbol{x},t) &= c(\boldsymbol{x})\overline{\boldsymbol{m}}(\boldsymbol{x},t), \\ \overline{\boldsymbol{m}}(\boldsymbol{x},t) &= \overline{m}(H)\boldsymbol{e}_{\boldsymbol{H}}, \\ \boldsymbol{e}_{\boldsymbol{H}} &= \frac{\boldsymbol{H}(\boldsymbol{x},t)}{H}, \\ H &= \|\boldsymbol{H}(\boldsymbol{x},t)\|, \end{aligned} \tag{2.7}$$

where $\overline{m} : \mathbb{R}_+ \to \mathbb{R}_+$ denotes the magnitude of the mean magnetic moment of a particle as a function of the magnitude $H : \mathbb{R}^N \times \mathbb{R} \to \mathbb{R}_+$ of the applied magnetic field $\boldsymbol{H}(\boldsymbol{x},t)$. The expression in (2.7) describes that the magnetization $\boldsymbol{M}(\boldsymbol{x},t)$ of the SPIO distribution is instantly aligned in the direction of the applied magnetic field $\boldsymbol{H}(\boldsymbol{x},t)$.

To describe the magnetization behavior of nanoparticles in MPI, the Langevin theory of paramagnetism has usually been used in a first step since the beginnings of MPI [30]. This highly simplified model demonstrates for MPI with one-dimensional excitation its ability to reconstruct particle distributions from the SPIO voltage signal $u^{\mathrm{P}}(t)$ when combined with a Debey relaxation model [32, 40, 55, 81].

In the Langevin model, the nonlinear magnetization behavior of the SPIOs is described using the Langevin function $\mathscr{L} : \mathbb{R} \to \mathbb{R}$, which is given by

$$\mathscr{L}(\xi) = \begin{cases} \coth(\xi) - \frac{1}{\xi} & \text{if } \xi \neq 0 \\ 0 & \text{if } \xi = 0. \end{cases} \tag{2.8}$$

Therefore, the magnitude of the mean magnetic moment for one nanoparticle can be described as function of the magnetic field strength H through

$$\overline{m}(H) = m_0 \, \mathscr{L}(\beta H), \qquad \beta = \frac{\mu_0 m_0}{k_\mathrm{B} T_\mathrm{P}}, \tag{2.9}$$

where $m_0 = V_\mathrm{C} M_\mathrm{S}$ describes the mean magnetic moment of a spherically symmetric particle in saturation with the volume $V_\mathrm{C} = \frac{\pi D^3}{6}$, the diameter D, and the Boltzmann constant k_B. The constant M_S denotes the saturation magnetization of the material of the particle and T_P the temperature of the SPIOs.

A key role for the magnitude of $u^\mathrm{P}(t)$ (see (2.1) and (2.7)) is played by the derivative of the mean magnetic moment, which is connected via

$$\frac{\mathrm{d}\overline{m}(H)}{\mathrm{d}H} = m_0 \beta \, \mathscr{L}'(\beta H) \tag{2.10}$$

to the derivative of the Langevin function

$$\mathscr{L}'(\xi) = \frac{\mathrm{d}\,\mathscr{L}(\xi)}{\mathrm{d}\xi} = \begin{cases} \dfrac{1}{\xi^2} - \dfrac{1}{\sinh^2(\xi)} & \text{if } \xi \neq 0 \\ \frac{1}{3} & \text{if } \xi = 0. \end{cases} \tag{2.11}$$

In addition, a “normalized” version of the Langevin function $\mathscr{L}_\mathrm{n} : \mathbb{R} \to \mathbb{R}_+$ is used in this work, which was introduced in [F8] and allows for a simplified notation in the further parts of the thesis:

$$\mathscr{L}_\mathrm{n}(\xi) = \frac{\mathscr{L}(\xi)}{\xi} = \frac{\mathscr{L}(|\xi|)}{|\xi|} = \begin{cases} \frac{\coth(\xi) - \frac{1}{\xi}}{\xi} & \text{if } \xi \neq 0 \\ \frac{1}{3} & \text{if } \xi = 0. \end{cases} \tag{2.12}$$

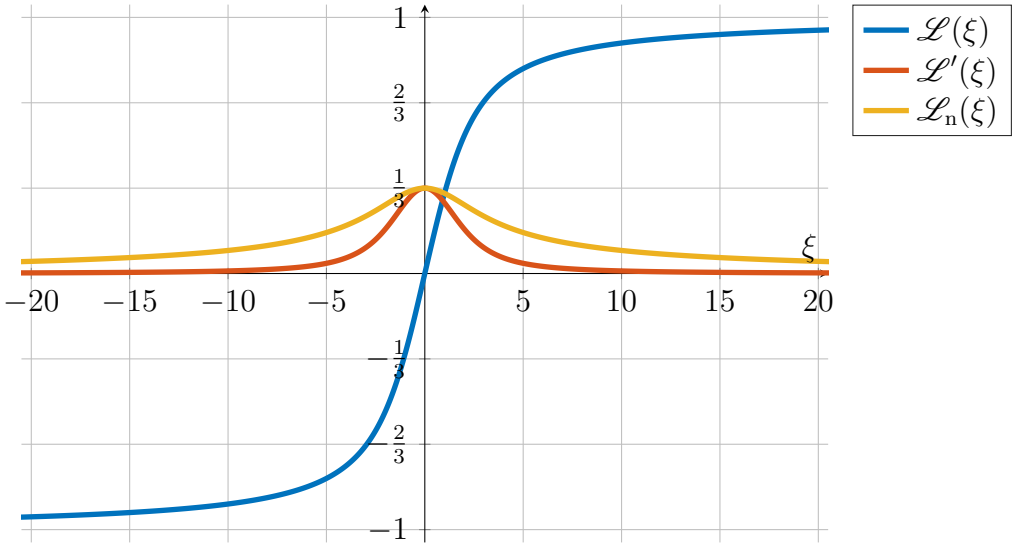

Figure 2.1: The Langevin function $\mathscr{L}(\xi)$, its derivative $\mathscr{L}'(\xi)$ and the "normalized" Langevin function $\mathscr{L}_{\mathrm{n}}(\xi)$.

The Langevin function $\mathscr{L}(\xi)$, its derivative $\mathscr{L}'(\xi)$, and the "normalized" version $\mathscr{L}_{\mathrm{n}}(\xi)$ are shown in Figure 2.1. It can be observed that the Langevin function $\mathscr{L}(\xi)$ is an odd-symmetric monotonically increasing function which maps the values $\xi \in \mathbb{R}$ to the open interval $(-1, 1)$. Consequently, $\mathscr{L}'(\xi)$ and $\mathscr{L}_{\mathrm{n}}(\xi)$ are even-symmetrical functions that are always positive and larger than zero.

With the help of the Langevin model of paramagnetism for the magnetization, it is now possible to investigate $\frac{\partial \boldsymbol{M}(\boldsymbol{x},t)}{\partial t}$ in (2.1). Thus, the SPIO-dependent term $\frac{\partial \boldsymbol{M}(\boldsymbol{x},t)}{\partial t}$ can now be rewritten with (2.7) and (2.9) as

$$\begin{aligned} \frac{\partial \boldsymbol{M}(\boldsymbol{x},t)}{\partial t} &= c(\boldsymbol{x}) \frac{\partial \overline{\boldsymbol{m}}(H)}{\partial t} = c(\boldsymbol{x}) \frac{\partial (\overline{m}(H) \boldsymbol{e}_{\boldsymbol{H}})}{\partial t} \\ &= c(\boldsymbol{x}) \boldsymbol{\kappa}(\boldsymbol{H}) \frac{\partial \boldsymbol{H}}{\partial t} \end{aligned} \tag{2.13}$$

with $\boldsymbol{\kappa} : \mathbb{R}^N \to \mathbb{R}^{N \times N}$

$$\begin{aligned} \boldsymbol{\kappa}(\boldsymbol{H}) &= \frac{\mathrm{d}\overline{m}(H)}{\mathrm{d}H} \boldsymbol{e}_{\boldsymbol{H}} \boldsymbol{e}_{\boldsymbol{H}}^{\mathsf{T}} + \frac{\overline{m}(H)}{H} \left(\boldsymbol{I}_N - \boldsymbol{e}_{\boldsymbol{H}} \boldsymbol{e}_{\boldsymbol{H}}^{\mathsf{T}} \right) \\ &= m_0 \beta \Big(\mathscr{L}'(\beta H) \boldsymbol{e}_{\boldsymbol{H}} \boldsymbol{e}_{\boldsymbol{H}}^{\mathsf{T}} + \mathscr{L}_{\mathrm{n}}(\beta H) \left(\boldsymbol{I}_N - \boldsymbol{e}_{\boldsymbol{H}} \boldsymbol{e}_{\boldsymbol{H}}^{\mathsf{T}} \right) \Big). \end{aligned} \tag{2.14}$$

The expressions in (2.13) and (2.14) are proven briefly.

Proof of Eq. (2.13). The partial derivatives of $H = \|\boldsymbol{H}\|$ are initially given by

$$\frac{\partial H}{\partial t} = \frac{\partial \|\boldsymbol{H}\|}{\partial t} = \frac{\boldsymbol{H}^{\mathsf{T}} \frac{\partial \boldsymbol{H}}{\partial t}}{\|\boldsymbol{H}\|} = \boldsymbol{e}_{\boldsymbol{H}}^{\mathsf{T}} \frac{\partial \boldsymbol{H}}{\partial t}. \tag{2.15}$$

Now a partial derivative can be calculated for $\boldsymbol{e}_{\boldsymbol{H}} = \frac{\boldsymbol{H}}{H}$ using the quotient rule, which is

$$\frac{\partial \frac{\boldsymbol{H}}{H}}{\partial t} = \frac{\frac{\partial \boldsymbol{H}}{\partial t} H - \boldsymbol{H} \frac{\partial H}{\partial t}}{H^2} \overset{(2.15)}{=} \frac{\frac{\partial \boldsymbol{H}}{\partial t} H - \boldsymbol{H} \boldsymbol{e}_{\boldsymbol{H}}^{\mathsf{T}} \frac{\partial \boldsymbol{H}}{\partial t}}{H^2} = \frac{\left(\boldsymbol{I}_N - \boldsymbol{e}_{\boldsymbol{H}} \boldsymbol{e}_{\boldsymbol{H}}^{\mathsf{T}}\right)}{H} \frac{\partial \boldsymbol{H}}{\partial t}. \tag{2.16}$$

Using (2.15) and (2.16) and applying the chain rule, the partial derivative of $\boldsymbol{M}(\boldsymbol{x}, t)$ is

$$\begin{aligned}
\frac{\partial \boldsymbol{M}(\boldsymbol{x}, t)}{\partial t} &= c(\boldsymbol{x}) \frac{\partial (\overline{m}(H) \boldsymbol{e}_{\boldsymbol{H}})}{\partial t} \\
&= c(\boldsymbol{x}) \left(\frac{\mathrm{d}\overline{m}(H)}{\mathrm{d}H} \frac{\partial H}{\partial t} \boldsymbol{e}_{\boldsymbol{H}} + \overline{m}(H) \frac{\partial \boldsymbol{e}_{\boldsymbol{H}}}{\partial t} \right) \\
&= c(\boldsymbol{x}) \left(\frac{\mathrm{d}\overline{m}(H)}{\mathrm{d}H} \left(\boldsymbol{e}_{\boldsymbol{H}}^{\mathsf{T}} \frac{\partial \boldsymbol{H}}{\partial t} \right) \boldsymbol{e}_{\boldsymbol{H}} + \overline{m}(H) \frac{\left(\boldsymbol{I}_N - \boldsymbol{e}_{\boldsymbol{H}} \boldsymbol{e}_{\boldsymbol{H}}^{\mathsf{T}}\right)}{H} \frac{\partial \boldsymbol{H}}{\partial t} \right) \\
&= c(\boldsymbol{x}) \underbrace{\left(\frac{\mathrm{d}\overline{m}(H)}{\mathrm{d}H} \boldsymbol{e}_{\boldsymbol{H}} \boldsymbol{e}_{\boldsymbol{H}}^{\mathsf{T}} + \overline{m}(H) \frac{\left(\boldsymbol{I}_N - \boldsymbol{e}_{\boldsymbol{H}} \boldsymbol{e}_{\boldsymbol{H}}^{\mathsf{T}}\right)}{H} \right)}_{= \boldsymbol{\kappa}(\boldsymbol{H})} \frac{\partial \boldsymbol{H}}{\partial t}.
\end{aligned} \tag{2.17}$$

By comparing the last equation in (2.17) with the final result in (2.13) and identifying $\boldsymbol{\kappa}(\boldsymbol{H})$, it can be seen that they are identical after rearranging the terms in (2.17). □

Inserting (2.7) and (2.9) and then using the Langevin function or its "normalized" version in (2.1) results in the simplified version of the system equation:

$$\begin{aligned}
u_\nu^{\mathrm{P}}(t) &= -\mu_0 \frac{\mathrm{d}}{\mathrm{d}t} \int_\Omega c(\boldsymbol{x}) \overline{m}(\|\boldsymbol{H}(\boldsymbol{x}, t)\|) \frac{\boldsymbol{p}_\nu^{\mathsf{T}}(\boldsymbol{x}) \boldsymbol{H}(\boldsymbol{x}, t)}{\|\boldsymbol{H}(\boldsymbol{x}, t)\|} \, \mathrm{d}\boldsymbol{x}, \\
&= -\mu_0 m_0 \frac{\mathrm{d}}{\mathrm{d}t} \int_\Omega c(\boldsymbol{x}) \, \mathscr{L}(\beta \|\boldsymbol{H}(\boldsymbol{x}, t)\|) \frac{\boldsymbol{p}_\nu^{\mathsf{T}}(\boldsymbol{x}) \boldsymbol{H}(\boldsymbol{x}, t)}{\|\boldsymbol{H}(\boldsymbol{x}, t)\|} \, \mathrm{d}\boldsymbol{x}, \\
&= -\mu_0 m_0 \beta \frac{\mathrm{d}}{\mathrm{d}t} \int_\Omega c(\boldsymbol{x}) \, \mathscr{L}_{\mathrm{n}}(\beta \|\boldsymbol{H}(\boldsymbol{x}, t)\|) \boldsymbol{p}_\nu^{\mathsf{T}}(\boldsymbol{x}) \boldsymbol{H}(\boldsymbol{x}, t) \, \mathrm{d}\boldsymbol{x}.
\end{aligned} \tag{2.18}$$

Alternatively, using the second equation in (2.1) and the temporal partial derivative of the magnetization in (2.13), the system equation can be written as

$$u_\nu^{\mathrm{P}}(t) = -\mu_0 \int_\Omega c(\boldsymbol{x}) \boldsymbol{p}_\nu^{\mathsf{T}}(\boldsymbol{x}) \boldsymbol{\kappa}(\boldsymbol{H}(\boldsymbol{x}, t)) \frac{\partial \boldsymbol{H}(\boldsymbol{x}, t)}{\partial t} \, \mathrm{d}\boldsymbol{x}. \tag{2.19}$$

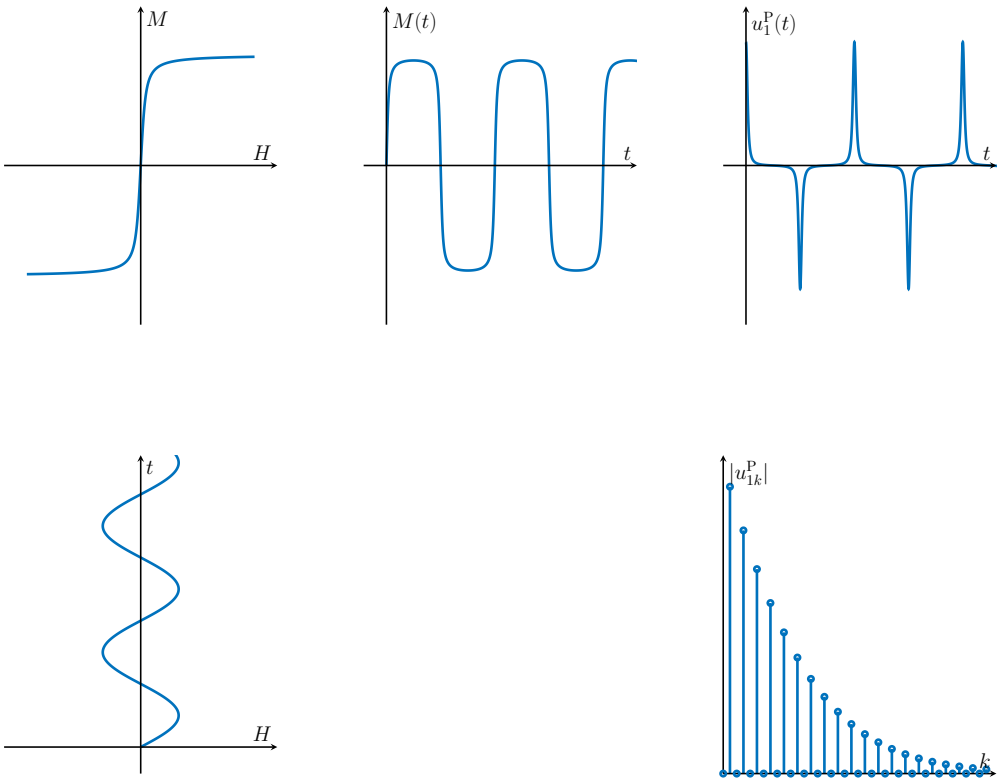

Figure 2.2: The signal generation in the MPI if the excitation signal oscillates around $H = 0$. A sinusoidal excitation field excites the magnetic moments of the SPIOs, which leads to a periodic rectangular shaped magnetization curve $M(t)$ for the SPIO distribution due to the nonlinear magnetization behavior of the SPIOs. The temporal change in the magnetization of the SPIO distribution induces a particle voltage signal $u_1^{\mathrm{P}}(t)$ in the receive path of the scanner. The magnitude values of the Fourier coefficients of $u_1^{\mathrm{P}}(t)$ are denoted by $|u_{1k}^{\mathrm{P}}|$ and the corresponding spectrum of $u_1^{\mathrm{P}}(t)$ is shown in the lower right diagram.

In (2.19) it can be seen that for a certain SPIO distribution $c(\boldsymbol{x})$, the induced voltage has a large magnitude, if $\boldsymbol{p}_\nu^{\mathsf{T}}(\boldsymbol{x})\boldsymbol{\kappa}(\boldsymbol{H}(\boldsymbol{x},t))\,\frac{\partial \boldsymbol{H}(\boldsymbol{x},t)}{\partial t}$ has a large contribution in terms of magnitude. The function that is related to the magentic moment of the particle distribution is $\boldsymbol{\kappa}(\boldsymbol{H})$. The matrix entries in $\boldsymbol{\kappa}(\boldsymbol{H})$ are large if $\mathscr{L}'(\beta H)$ and $\mathscr{L}_{\mathrm{n}}(\beta H)$ have large values (see (2.14)). However, the values are only large in the vicinity of $H = 0$, the field-free region, as can be seen in Figure 2.1 with $\xi = \beta H$. The physical reason is that SPIOs in the field-free region are not saturated and can therefore be significantly remagnetized, which contributes to the induced voltage signal. It is precisely this nonlinear magnetization behavior of SPIOs that is used in MPI for imaging [30, 53]. The principle of signal generation in MPI is shown in Figure 2.2 for the case that SPIOs

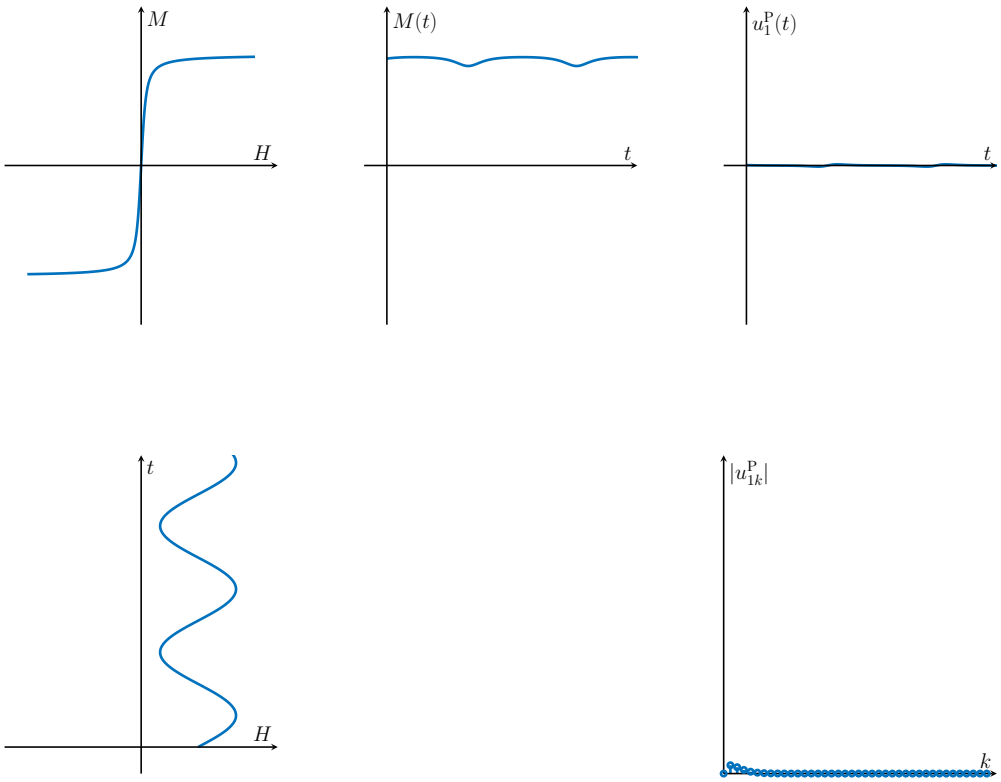

Figure 2.3: The signal generation in MPI if a large offset $H \gg 0$ is present. Due to the large offset, the SPIOs are already saturated, therefore the sinusoidal excitation only weakly influences the moments of the SPIOs, which leads to an almost constant magnetization curve $M(t)$ for the SPIO distribution. Since the magnetization change of the SPIO distribution is weak, the induced voltage signal $u_1^{\mathrm{P}}(t)$ in the receive path of the scanner is weak and almost no signal is induced. The magnitude values of the Fourier coefficients of $u_1^{\mathrm{P}}(t)$ are denoted by $|u_{1k}^{\mathrm{P}}|$ and the corresponding spectrum of $u_1^{\mathrm{P}}(t)$ is shown in the lower right diagram.

near the field-free region, i.e., $H = 0$, are excited by a sinusoidal excitation field. They experience a high magnetization change $M(t)$ and thus make a large contribution to the voltage signal $u_1^{\mathrm{P}}(t)$. In contrast, Figure 2.3 shows the signal generation of SPIOs that are saturated, i.e. $H \gg 0$, so that the magnetization change $M(t)$ is small and thus the induced voltage signal $u_1^{\mathrm{P}}(t)$ is low.

For the imaging process in MPI, the applied field $\boldsymbol{H}(\boldsymbol{x}, t)$ is normally a superposition of the dynamic drive field $\boldsymbol{H}^{\mathrm{D}} : \mathbb{R}^N \times \mathbb{R} \to \mathbb{R}^N$ and the static selection field $\boldsymbol{H}^{\mathrm{S}} : \mathbb{R}^N \to \mathbb{R}^N$:

$$\boldsymbol{H}(\boldsymbol{x}, t) = \boldsymbol{H}^{\mathrm{S}}(\boldsymbol{x}) + \boldsymbol{H}^{\mathrm{D}}(\boldsymbol{x}, t). \tag{2.20}$$

In most models, it is assumed that the sensitivities of the drive-field coils are spatially homogeneous, i.e., $\boldsymbol{H}^{\mathrm{D}}(\boldsymbol{x}, t) = \boldsymbol{H}^{\mathrm{D}}(t)$ with $\boldsymbol{H}^{\mathrm{D}} : \mathbb{R} \to \mathbb{R}^3$. The static selection field $\boldsymbol{H}^{\mathrm{S}}(\boldsymbol{x})$ is a spatially inhomogeneous magnetic field that creates a field-free region and saturates SPIOs outside the field-free region, thus laying the foundation for the spatial encoding of MPI. The additional dynamic drive field $\boldsymbol{H}^{\mathrm{D}}(t)$ then moves the field-free region on a specific trajectory through the drive-field FOV, the area covered by the trajectory, to change the magnetic moments in the SPIOs at different locations in the FOV, resulting in a temporal voltage signal in the MPI scanner, which in turn provides information on the distribution and concentration of the SPIOs.

In this thesis, an FFP is used as a field-free region. The FFP is defined as the spatial point in time $\boldsymbol{x}_{\mathrm{FFP}} : \mathbb{R} \to \mathbb{R}^N$ where the applied magnetic field vanishes:

$$\boldsymbol{H}(\boldsymbol{x}_{\mathrm{FFP}}(t), t) = \boldsymbol{0}. \tag{2.21}$$

This always applies to the drive field if

$$\boldsymbol{H}^{\mathrm{D}}(t) = -\boldsymbol{H}^{\mathrm{S}}(\boldsymbol{x}_{\mathrm{FFP}}(t)). \tag{2.22}$$

With the new expression for the drive field in (2.22), the applied magnetic field can be described by only using the spatial position of the FFP $\boldsymbol{x}_{\mathrm{FFP}}(t)$ and the selection field $\boldsymbol{H}^{\mathrm{S}}(\boldsymbol{x})$:

$$\boldsymbol{H}(\boldsymbol{x}, t) = \boldsymbol{H}^{\mathrm{S}}(\boldsymbol{x}) - \boldsymbol{H}^{\mathrm{S}}(\boldsymbol{x}_{\mathrm{FFP}}(t)). \tag{2.23}$$

A typical selection field $\boldsymbol{H}^{\mathrm{S}}(\boldsymbol{x})$ is generated with the help of two permanent magnets or a Maxwell coil pair, so that an almost linear gradient field is created, which is described by

$$\boldsymbol{H}^{\mathrm{S}}(\boldsymbol{x}) = \boldsymbol{G}\boldsymbol{x}, \tag{2.24}$$

where $\boldsymbol{G} \in \mathbb{R}^{N \times N}$ is a gradient matrix and due to the Gaussian law of magnetism for $N = 3$ it must be fulfilled that $\mathrm{tr}(\boldsymbol{G}) = 0$, since the magnetic field is divergence-free. Assuming that $\boldsymbol{G}$ is invertible, whereby it should be noted that otherwise one would generally speak of an FFL, the position of the FFP is given by

$$\boldsymbol{x}_{\mathrm{FFP}}(t) = -\boldsymbol{G}^{-1}\boldsymbol{H}^{\mathrm{D}}(t). \tag{2.25}$$

The compact expression for the applied magnetic field is

$$\boldsymbol{H}(\boldsymbol{x},t) = \boldsymbol{G}\left(\boldsymbol{x} - \boldsymbol{x}_{\mathrm{FFP}}(t)\right). \tag{2.26}$$

Using the expression (2.26), further simplifications of the system equation can be made by substituting (2.26) into (2.18), resulting in the following

$$\begin{aligned} u_\nu^{\mathrm{P}}(t) &= -\mu_0 m_0 \boldsymbol{\rho}_\nu^{\mathsf{T}} \frac{\mathrm{d}}{\mathrm{d}t} \int_\Omega c(\boldsymbol{x})\, \mathscr{L}_{\mathrm{n}}(\beta \| \boldsymbol{G}\left(\boldsymbol{x} - \boldsymbol{x}_{\mathrm{FFP}}(t)\right) \|) \beta \boldsymbol{G}\left(\boldsymbol{x} - \boldsymbol{x}_{\mathrm{FFP}}(t)\right) \mathrm{d}\boldsymbol{x} \\ &= \mu_0 m_0 \boldsymbol{\rho}_\nu^{\mathsf{T}} \frac{\mathrm{d}}{\mathrm{d}t} \int_\Omega c(\boldsymbol{x})\, \mathscr{L}_{\mathrm{n}}(\beta \| \boldsymbol{G}\left(\boldsymbol{x}_{\mathrm{FFP}}(t) - \boldsymbol{x}\right) \|)\, \beta \boldsymbol{G}\left(\boldsymbol{x}_{\mathrm{FFP}}(t) - \boldsymbol{x}\right)\, \mathrm{d}\boldsymbol{x} \\ &= \mu_0 m_0 \boldsymbol{\rho}_\nu^{\mathsf{T}} \frac{\mathrm{d}}{\mathrm{d}t} \int_\Omega c(\boldsymbol{x})\, \boldsymbol{\mathscr{L}}(\beta \boldsymbol{G}\left(\boldsymbol{x}_{\mathrm{FFP}}(t) - \boldsymbol{x}\right)) \mathrm{d}\boldsymbol{x}, \end{aligned} \tag{2.27}$$

where it is assumed that the receive coils also have homogeneous sensitivity, i.e., $\boldsymbol{p}_\nu(\boldsymbol{x}) = \boldsymbol{\rho}_\nu$ with $\boldsymbol{\rho}_\nu \in \mathbb{R}^N$, and the multidimensional version of the Langevin function $\boldsymbol{\mathscr{L}} : \mathbb{R}^N \to \mathbb{R}^N$ is defined by

$$\boldsymbol{\mathscr{L}}(\boldsymbol{\xi}) = \mathscr{L}(\|\boldsymbol{\xi}\|) \frac{\boldsymbol{\xi}}{\|\boldsymbol{\xi}\|} = \mathscr{L}_{\mathrm{n}}(\|\boldsymbol{\xi}\|)\boldsymbol{\xi}. \tag{2.28}$$

In (2.27) it can be observed that the equation is almost described by a convolution between the particle distribution $c(\boldsymbol{x})$ and the multidimensional Langevin function $\boldsymbol{\mathscr{L}}(\beta \boldsymbol{G}\boldsymbol{x})$. This fact becomes clear when the convolution part is split into an auxiliary function $\boldsymbol{\Phi} : \mathbb{R}^N \to \mathbb{R}^N$ by

$$\boldsymbol{\Phi}(\boldsymbol{z}) = \int_\Omega c(\boldsymbol{x})\, \boldsymbol{\mathscr{L}}(\beta \boldsymbol{G}\left(\boldsymbol{z} - \boldsymbol{x}\right)) \mathrm{d}\boldsymbol{x}. \tag{2.29}$$

If $\boldsymbol{x}_{\mathrm{FFP}}(t)$ is now inserted into (2.29), the voltage signal in (2.27) can be described by

$$u_\nu^{\mathrm{P}}(t) = \mu_0 m_0 \boldsymbol{\rho}_\nu^{\mathsf{T}} \frac{\mathrm{d}}{\mathrm{d}t} \big(\boldsymbol{\Phi}(\boldsymbol{x}_{\mathrm{FFP}}(t))\big). \tag{2.30}$$

Equivalently, (2.19) can be rewritten with (2.26) by

$$\begin{aligned} u_\nu^{\mathrm{P}}(t) &= \mu_0 \boldsymbol{\rho}_\nu^{\mathsf{T}} \int_\Omega c(\boldsymbol{x}) \boldsymbol{\kappa}\big(\boldsymbol{G}\left(\boldsymbol{x}_{\mathrm{FFP}}(t) - \boldsymbol{x}\right)\big) \boldsymbol{G} \frac{\mathrm{d}\boldsymbol{x}_{\mathrm{FFP}}(t)}{\mathrm{d}t}\, \mathrm{d}\boldsymbol{x} \\ &= \mu_0 \boldsymbol{\rho}_\nu^{\mathsf{T}} \int_\Omega c(\boldsymbol{x}) \boldsymbol{\kappa}\big(\boldsymbol{G}\left(\boldsymbol{x}_{\mathrm{FFP}}(t) - \boldsymbol{x}\right)\big)\, \mathrm{d}\boldsymbol{x} \cdot \boldsymbol{G} \frac{\mathrm{d}\boldsymbol{x}_{\mathrm{FFP}}(t)}{\mathrm{d}t} \\ &= -\mu_0 \boldsymbol{\rho}_\nu^{\mathsf{T}} \int_\Omega c(\boldsymbol{x}) \boldsymbol{\kappa}\big(\boldsymbol{G}\left(\boldsymbol{x}_{\mathrm{FFP}}(t) - \boldsymbol{x}\right)\big)\, \mathrm{d}\boldsymbol{x} \cdot \frac{\mathrm{d}\boldsymbol{H}^{\mathrm{D}}(t)}{\mathrm{d}t}, \end{aligned} \tag{2.31}$$

using that $\frac{\partial \boldsymbol{H}(\boldsymbol{x},t)}{\partial t} = -\boldsymbol{G}\frac{\mathrm{d}\boldsymbol{x}_{\mathrm{FFP}}(t)}{\mathrm{d}t}$ and $\boldsymbol{\kappa}(\boldsymbol{H}) = \boldsymbol{\kappa}(-\boldsymbol{H})$. The last formulation is generally used in multidimensional x-space MPI, where the SPIO distribution is reconstructed in time domain [33]. It can be seen that the imaging process for the simplified model is described by a convolution between the particle distribution $c(\boldsymbol{x})$ and a matrix-valued kernel $\boldsymbol{\kappa}(\boldsymbol{G}\boldsymbol{x})$. To illustrate this fact, the MPI auxiliary function $\boldsymbol{C}_{\mathrm{ore}} : \mathbb{R}^N \to \mathbb{R}^{N\times N}$ is defined as

$$\boldsymbol{C}_{\mathrm{ore}}(\boldsymbol{z}) = \int_{\Omega} c(\boldsymbol{x})\boldsymbol{\kappa}\big(\boldsymbol{G}\left(\boldsymbol{z}-\boldsymbol{x}\right)\big)\,\mathrm{d}\boldsymbol{x},$$

which is a component-wise convolution between $c(\boldsymbol{x})$ and $\boldsymbol{\kappa}\left(\boldsymbol{G}\boldsymbol{x}\right)$. If this convolution kernel is inserted into (2.31) and $\boldsymbol{x}_{\mathrm{FFP}}(t)$ is used as an argument of $\boldsymbol{C}_{\mathrm{ore}}(\boldsymbol{z})$, the result is

$$\begin{aligned} u_\nu^{\mathrm{P}}(t) &= \mu_0\boldsymbol{\rho}_\nu^{\mathsf{T}}\boldsymbol{C}_{\mathrm{ore}}(\boldsymbol{x}_{\mathrm{FFP}}(t))\cdot\boldsymbol{G}\frac{\partial\boldsymbol{x}_{\mathrm{FFP}}(t)}{\partial t} \\ &= -\mu_0\boldsymbol{\rho}_\nu^{\mathsf{T}}\boldsymbol{C}_{\mathrm{ore}}(\boldsymbol{x}_{\mathrm{FFP}}(t))\frac{\partial\boldsymbol{H}^{\mathrm{D}}(t)}{\partial t}. \end{aligned} \tag{2.32}$$

The relationship in (2.27) and (2.31) is often written as the inner product between the SPIO distribution $c(\boldsymbol{x})$ and the coil-depend system function $s_\nu : \mathbb{R}^N \times \mathbb{R} \to \mathbb{R}$, which contains all terms that are independent of $c(\boldsymbol{x})$, by

$$u_\nu^{\mathrm{P}}(t) = \int_{\mathbb{R}^N} s_\nu(\boldsymbol{x},t)c(\boldsymbol{x})\,\mathrm{d}\boldsymbol{x}. \tag{2.33}$$

In (2.33) it is implicitly assumed that the SPIO distribution $c : \Omega \subset \mathbb{R}^N \to \mathbb{R}_+$ has a bounded support, and (2.33) is commonly referred to as the system equation in the time domain. A comparison with (2.27) and (2.31) shows that the system function is implicitly given by

$$\begin{aligned} s_\nu(\boldsymbol{x},t) &= \mu_0 m_0\boldsymbol{\rho}_\nu^{\mathsf{T}}\frac{\partial}{\partial t}\left[\mathscr{L}(\beta\,\|\boldsymbol{G}(\boldsymbol{x}_{\mathrm{FFP}}(t)-\boldsymbol{x})\|)\frac{\beta\boldsymbol{G}\left(\boldsymbol{x}_{\mathrm{FFP}}(t)-\boldsymbol{x}\right)}{\|\beta\boldsymbol{G}(\boldsymbol{x}_{\mathrm{FFP}}(t)-\boldsymbol{x})\|}\right] \\ &= \mu_0 m_0\boldsymbol{\rho}_\nu^{\mathsf{T}}\frac{\partial}{\partial t}[\boldsymbol{\mathscr{L}}(\beta\boldsymbol{G}(\boldsymbol{x}_{\mathrm{FFP}}(t)-\boldsymbol{x}))] \\ &= \mu_0\boldsymbol{\rho}_\nu^{\mathsf{T}}\boldsymbol{\kappa}\big(\boldsymbol{G}\left(\boldsymbol{x}_{\mathrm{FFP}}(t)-\boldsymbol{x}\right)\big)\boldsymbol{G}\frac{\partial\boldsymbol{x}_{\mathrm{FFP}}(t)}{\partial t}. \end{aligned} \tag{2.34}$$

Another common approach in the Lissajous FFP-trajectory MPI community is to define the MPI system function based on the Fourier series representation of the T_{D}-periodic voltage signal $u_\nu^{\mathrm{P}}(t)$ [80, 81]. It is easy to show that the voltage signal $u_\nu^{\mathrm{P}}(t)$ is T_{D}-periodic whenever the drive field $\boldsymbol{H}^{\mathrm{D}}(t)$ is T_{D}-periodic, which is the usual choice

for the drive-field excitation in MPI. The k-th Fourier series component of the system function $s_\nu(\boldsymbol{x}, t)$ can be calculated by

$$s_{\nu k}(\boldsymbol{x}) = \frac{1}{T_\mathrm{D}} \int_{-\frac{T_\mathrm{D}}{2}}^{\frac{T_\mathrm{D}}{2}} s_\nu(\boldsymbol{x}, t) \mathrm{e}^{-\mathrm{i}\omega_k t} \,\mathrm{d}t, \tag{2.35}$$

where $\omega_k = \frac{2\pi k}{T_\mathrm{D}} = 2\pi k f_\mathrm{D}, k \in \mathbb{Z}$ and thus the temporal frequency domain version of the system equation (2.33) is

$$\begin{aligned} u_{\nu k}^\mathrm{P} &= \frac{1}{T_\mathrm{D}} \int_{-\frac{T_\mathrm{D}}{2}}^{\frac{T_\mathrm{D}}{2}} u_\nu^\mathrm{P}(t) \mathrm{e}^{-\mathrm{i}\omega_k t} \,\mathrm{d}t \\ &= \int_{\mathbb{R}^N} s_{\nu k}(\boldsymbol{x}) c(\boldsymbol{x}) \,\mathrm{d}\boldsymbol{x}. \end{aligned} \tag{2.36}$$

It should be noted that $s_{\nu k} : \mathbb{R}^N \to \mathbb{C}$ is usually only referred to as the k-th system function component and the components of the Fourier series $\left(u_{\nu k}^\mathrm{P}\right)_{k \in \mathbb{Z}}$ are usually referred to as the frequency components of the voltage signal in MPI. Therefore, in this model of MPI, it is implicitly assumed that the T_D-periodic voltage signal $u_\nu^\mathrm{P}(t)$ can be expressed by

$$u_\nu^\mathrm{P}(t) = \sum_{k \in \mathbb{Z}} u_{\nu k}^\mathrm{P} \mathrm{e}^{\mathrm{i}\omega_k t}, \tag{2.37}$$

i.e., by a series of complex sinusoidal signals.

The choice of the Fourier series expression has, among others, its motivation in (2.5), since the k-th Fourier series component of $\tilde{u}_\nu^\mathrm{P}(t)$ can be written by

$$\tilde{u}_{\nu k}^\mathrm{P} \approx a_k u_{\nu k}^\mathrm{P}, \qquad \text{where} \qquad a_k = \hat{a}(\omega_k) \tag{2.38}$$

with the one-dimensional Fourier-transformed transfer function

$$\hat{a}(\omega) = \int_{\mathbb{R}} a(t) \mathrm{e}^{-\mathrm{i}\omega t} \,\mathrm{d}t$$

and it is assumed that the transfer function $a(t)$ can be modeled as the impulse response of a linear time-invariant system.

In practice, only some frequency components $\tilde{u}_{\nu k}^\mathrm{P}$ are of interest and even if the transfer function is not known, an estimate for a_k can be obtained by a comparison of the

model-based choice for $s_{\nu k}(\boldsymbol{x})$ with a certain number of calibration scans from an MPI scanner [51, 55]. Furthermore, for Lissajous-like FFP-trajectories, it is common to use (2.36) as a basis to model the system equation by spatial discretization of the integral equation (2.36) for different values of k, resulting in a system of linear equations. The resulting inverse problem can then be solved by various image reconstruction methods on basis of a system matrix [F9, F10, C4, 54, 62, 97].

2.1.1 One-Dimensional Drive-Field Excitation

Since the work of [81] is the starting point and the basis for this work, the proof of [81] is repeated and the problems of extending the proof to multidimensional excitation MPI are outlined in the next section. The authors in [81] were the first to be able to find a closed-form solution for the one-dimensional case, i.e., $N = 1$, for the system function component $s_{1k}(x)$, if the excitation signal has the form

$$H^{\mathrm{D}}_{\cos}(t) = -A_1 \cos(2\pi f_{\mathrm{D}} t) = A_1 \sin\Big(2\pi f_{\mathrm{D}} t - \frac{\pi}{2}\Big)$$

or

$$H^{\mathrm{D}}_{\mathrm{tri}}(t) = -A_1 \left(2\,\mathrm{tri}\left(\frac{2t}{T_{\mathrm{D}}}\right) - 1\right) \quad \text{for} \quad t \in \left[-\frac{T_{\mathrm{D}}}{2}, \frac{T_{\mathrm{D}}}{2}\right]$$

and $H^{\mathrm{D}}_{\mathrm{tri}}(t) = H^{\mathrm{D}}_{\mathrm{tri}}(t - \ell T_{\mathrm{D}})$ $(\ell \in \mathbb{Z})$ is periodic with T_{D}. The excitation signals $H^{\mathrm{D}}_{\cdot}(t)$ are shown in Figure 2.4. Note that the triangular excitation is slightly different from the definition in [81], but this does not change the idea of the proof used by the authors.

In this setting, the selection field reads $H^{\mathrm{S}}(x) = G_1 x$ and only one receive coil with the constant coil sensitivity $\rho_1 \in \mathbb{R}$ is taken into account. Note that the approach of [81] can also be extended to the spatially multidimensional case, provided that the drive-field excitation is still one-dimensional, which means that the FFP-trajectory $\boldsymbol{x}_{\mathrm{FFP}}(t)$ is a line (FFP) or plane (FFL) in space. For the sake of clarity, however, only one spatial

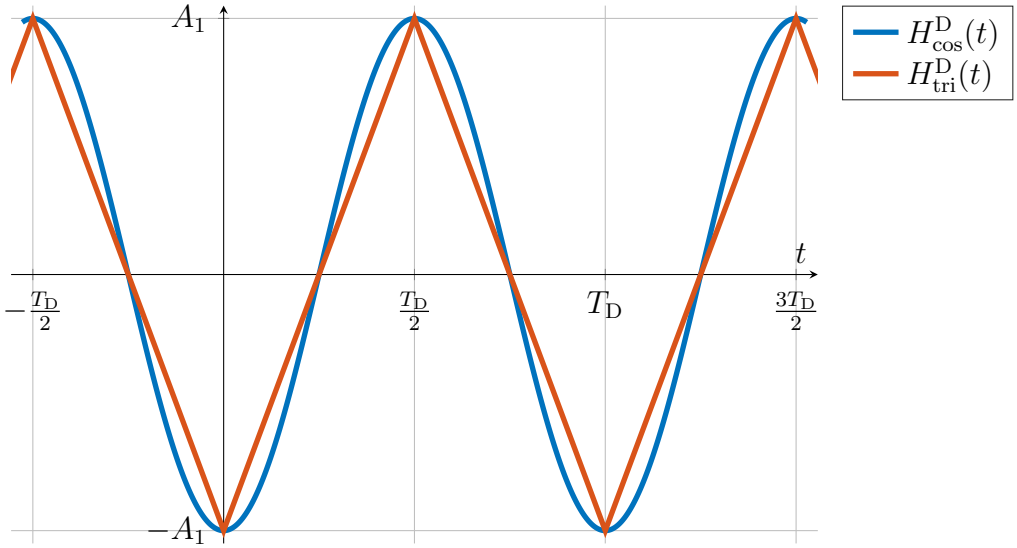

Figure 2.4: A sinusoidal drive-field excitation $H^{\mathrm{D}}_{\cos}(t)$ and a triangular drive-field excitation $H^{\mathrm{D}}_{\mathrm{tri}}(t)$. Both excitation signals have the period length T_{D} and the amplitude A_1.

dimension is considered here. Let $\frac{A_1}{G_1} > 0$. The system equation in (2.27) and (2.31) simplifies to

$$\begin{aligned} u_1^{\mathrm{P}}(t) &= \mu_0\rho_1 \int_\Omega c(x)\kappa(G_1\left(x_{\mathrm{FFP}}(t) - x\right))\, G_1 \frac{\mathrm{d}x_{\mathrm{FFP}}(t)}{\mathrm{d}t}\,\mathrm{d}x \\ &= \mu_0\rho_1 \int_\Omega c(x)\beta m_0\, \mathscr{L}'(\beta G_1\left(x_{\mathrm{FFP}}(t) - x\right)) G_1 \frac{\mathrm{d}x_{\mathrm{FFP}}(t)}{\mathrm{d}t}\,\mathrm{d}x \end{aligned}$$

and the system function $s_1(x,t)$ finally reads

$$s_1(x,t) = \mu_0\rho_1 m_0 \beta G_1\, \mathscr{L}'(\beta G_1\left(x_{\mathrm{FFP}}(t) - x\right)) \frac{\mathrm{d}x_{\mathrm{FFP}}(t)}{\mathrm{d}t}.$$

First, a sinusoidal excitation for the drive field $H^{\mathrm{D}}_{\cos}(t)$ is considered:

$$x_{\mathrm{FFP}}(t) = \frac{A_1}{G_1}\cos(2\pi f_{\mathrm{D}} t) \qquad \frac{\mathrm{d}x_{\mathrm{FFP}}(t)}{\mathrm{d}t} = -2\pi f_{\mathrm{D}} \frac{A_1}{G_1}\sin(2\pi f_{\mathrm{D}} t). \tag{2.39}$$

The authors in [81] prove the following relationship, which is formulated as a theorem in this work.

Theorem 2.1

The system function components $s_{1k} : \mathbb{R} \to \mathbb{C}$ for a one-dimensional sinusoidal excitation signal that leads to an FFP-trajectory

$$x_{\mathrm{FFP}}(t) = \frac{A_1}{G_1} \cos(2\pi f_{\mathrm{D}} t)$$

with $A_1/G_1 > 0$ and $k \in \mathbb{Z}$ can be written as

$$s_{1k}(x) = \begin{cases} \frac{2\mathrm{i}\mu_0\rho_1 m_0 \beta G_1}{T_{\mathrm{D}}} \int_{\mathbb{R}} \mathscr{L}'(\beta G_1 (x - z)) \tilde{V}_k \left(\frac{G_1}{A_1} z \right) \mathrm{d}z & \text{if } k \geq 1 \\ 0 & \text{if } k = 0 \\ \left(s_{1|k|}(x) \right)^* & \text{if } k \leq -1, \end{cases} \tag{2.40}$$

where

$$\tilde{V}_n(\xi) = \mathrm{rect}\left(\frac{\xi}{2} \right) \sqrt{1 - \xi^2} U_{n-1}(\xi)$$

and $U_\ell : \mathbb{R} \to \mathbb{R}$ denotes the Chebyshev polynomial of the second kind with order $\ell \in \mathbb{N}_0$.

Note that the notation in [81] is slightly different, so that a change of sign can be observed. The proof strategy from [81] will now be carried out with the notation used in this work.

Proof of Theorem 2.1. Following the idea in [81], an expression for $s_{1k} : \mathbb{R} \to \mathbb{C}$ and $k \in \mathbb{N}$ can be found with integration by substitution:

$$\begin{aligned} s_{1k}(x) &= \frac{1}{T_{\mathrm{D}}} \int_{\Omega_{T_{\mathrm{D}}}} s_1(x,t) \mathrm{e}^{-\mathrm{i}\omega_k t} \, \mathrm{d}t \\ &= \frac{\mu_0\rho_1 m_0}{T_{\mathrm{D}}} \int_{\Omega_{T_{\mathrm{D}}}} \beta G_1 \, \mathscr{L}'(\beta G_1 (x_{\mathrm{FFP}}(t) - x)) \frac{\mathrm{d}x_{\mathrm{FFP}}(t)}{\mathrm{d}t} \mathrm{e}^{-\mathrm{i}\omega_k t} \, \mathrm{d}t \\ &= \frac{\mu_0\rho_1 m_0}{T_{\mathrm{D}}} \int_{\Omega^+_{T_{\mathrm{D}}}} \beta G_1 \, \mathscr{L}'(\beta G_1 (x_{\mathrm{FFP}}(t) - x)) \frac{\mathrm{d}x_{\mathrm{FFP}}(t)}{\mathrm{d}t} \mathrm{e}^{-\mathrm{i}\omega_k t} \, \mathrm{d}t \\ &\quad + \frac{\mu_0\rho_1 m_0}{T_{\mathrm{D}}} \int_{\Omega^-_{T_{\mathrm{D}}}} \beta G_1 \, \mathscr{L}'(\beta G_1 (x_{\mathrm{FFP}}(t) - x)) \frac{\mathrm{d}x_{\mathrm{FFP}}(t)}{\mathrm{d}t} \mathrm{e}^{-\mathrm{i}\omega_k t} \, \mathrm{d}t \\ &= \frac{\mu_0\rho_1 m_0}{T_{\mathrm{D}}} \int_{x_{\mathrm{FFP}}\left[\Omega^+_{T_{\mathrm{D}}}\right]} \beta G_1 \, \mathscr{L}'(\beta G_1 (z - x)) \mathrm{e}^{-\mathrm{i}\omega_k x^{-1}_{\mathrm{FFP}}(z)} \, \mathrm{d}z \\ &\quad + \frac{\mu_0\rho_1 m_0}{T_{\mathrm{D}}} \int_{x_{\mathrm{FFP}}\left[\Omega^-_{T_{\mathrm{D}}}\right]} \beta G_1 \, \mathscr{L}'(\beta G_1 (z - x)) \mathrm{e}^{-\mathrm{i}\omega_k x^{-1}_{\mathrm{FFP}}(z)} \, \mathrm{d}z, \end{aligned} \tag{2.41}$$

where $\Omega_{T_\mathrm{D}} = \left[-\frac{T_\mathrm{D}}{2}, \frac{T_\mathrm{D}}{2}\right]$, $\Omega^+_{T_\mathrm{D}} = \left[0, \frac{T_\mathrm{D}}{2}\right]$, $\Omega^-_{T_\mathrm{D}} = \left[-\frac{T_\mathrm{D}}{2}, 0\right)$, and $X' = x_\mathrm{FFP}[X] = \{x_\mathrm{FFP}(t) \mid t \in X\}$ is the image of $X \subseteq \Omega_{T_\mathrm{D}}$ for the function $x_\mathrm{FFP}(t)$ and the preimage is defined by $x^{-1}_\mathrm{FFP}[X'] = \{t \in \Omega_{T_\mathrm{D}} \mid x_\mathrm{FFP}(t) \in X'\}$. It is now necessary to determine the inverse function of (2.39). For the inverse function, a case analysis is required for $t \in \left[-\frac{T}{2}, 0\right)$ and $t \in \left[0, \frac{T}{2}\right]$. The inverse mapping for t in the interval $\left[0, \frac{T}{2}\right]$ is

$$x^{-1}_\mathrm{FFP}(z) = \frac{1}{2\pi f_\mathrm{D}} \arccos\left(\frac{G_1}{A_1} z\right)$$

and for t in the interval $\left[-\frac{T_\mathrm{D}}{2}, 0\right)$ the inverse mapping is

$$x^{-1}_\mathrm{FFP}(z) = -\frac{1}{2\pi f_\mathrm{D}} \arccos\left(\frac{G_1}{A_1} z\right).$$

Using the inverse mapping, (2.41) can be represented as

$$\begin{aligned}
s_{1k}(x) &= \frac{\mu_0 \rho_1 m_0}{T_\mathrm{D}} \left(\int_{\frac{A_1}{G_1}}^{-\frac{A_1}{G_1}} \beta G_1 \mathscr{L}'(\beta G_1 (z - x)) \mathrm{e}^{-\mathrm{i}k \arccos\left(\frac{G_1}{A_1} z\right)} \,\mathrm{d}z \right. \\
&\quad \left. + \int_{-\frac{A_1}{G_1}}^{\frac{A_1}{G_1}} \beta G_1 \mathscr{L}'(\beta G_1 (z - x)) \mathrm{e}^{\mathrm{i}k \arccos\left(\frac{G_1}{A_1} z\right)} \,\mathrm{d}z \right) \\
&= \frac{\mu_0 \rho_1 m_0}{T_\mathrm{D}} \int_{-\frac{A_1}{G_1}}^{\frac{A_1}{G_1}} \beta G_1 \mathscr{L}'(\beta G_1 (z - x)) \left(\mathrm{e}^{\mathrm{i}k \arccos\left(\frac{G_1}{A_1} z\right)} - \mathrm{e}^{-\mathrm{i}k \arccos\left(\frac{G_1}{A_1} z\right)} \right) \,\mathrm{d}z \\
&= \frac{2\mathrm{i}\mu_0 \rho_1 m_0}{T_\mathrm{D}} \int_{-\frac{A_1}{G_1}}^{\frac{A_1}{G_1}} \beta G_1 \mathscr{L}'(\beta G_1 (z - x)) \sin\left(k \arccos\left(\frac{G_1}{A_1} z\right)\right) \,\mathrm{d}z. \qquad (2.42)
\end{aligned}$$

The term $\sin(n \arccos(\xi))$ can also be expressed for $n \in \mathbb{Z} \backslash \{0\}$ as a weighted Chebyshev polynomial of the second kind of the form

$$\sin(n \arccos(\xi)) = \operatorname{sgn}(n) \sqrt{1 - \xi^2} U_{|n|-1}(\xi),$$

where $U_\ell(\xi)$ denotes the Chebyshev polynomial of the second kind with order $\ell \in \mathbb{N}_0$. More details on this type of polynomial will be given in Chapter 5.

Using $\mathscr{L}'(\xi) = \mathscr{L}'(-\xi)$ and

$$\tilde{V}_n(\xi) = \operatorname{rect}\left(\frac{\xi}{2}\right) \sqrt{1 - \xi^2} U_{|n|-1}(\xi)$$

(2.42) can be rewritten as the following convolution:

$$s_{1k}(x) = \frac{2\mathrm{i}\mu_0\rho_1 m_0 \beta G_1 \operatorname{sgn}(k)}{T_\mathrm{D}} \int_{-\infty}^{\infty} \mathscr{L}'(\beta G_1 (x-z)) \tilde{V}_k\left(\frac{G_1}{A_1} z\right) \mathrm{d}z.$$

Note that $\operatorname{sgn}(k)$ gives the relation $s_{1,-k} = (s_{1,k})^*$ for all $k \in \mathbb{Z}$, which is to be expected since the excitation signal is an even symmetrical and real-valued periodic signal. □

In a second step, the system function components for a triangular excitation $H^\mathrm{D}_\mathrm{tri}(t)$ with the FFP position

$$\begin{aligned} x_\mathrm{FFP}(t) &= \frac{A_1}{G_1} \left(2 \operatorname{tri}(2 f_\mathrm{D} t) - 1\right), \\ \frac{\mathrm{d}x_\mathrm{FFP}(t)}{\mathrm{d}t} &= -\frac{4A_1}{G_1} f_\mathrm{D} \operatorname{sgn}(2 f_\mathrm{D} t) \end{aligned}$$

in the interval $t \in [-\frac{T_\mathrm{D}}{2}, \frac{T_\mathrm{D}}{2}]$ are calculated.

Theorem 2.2

The system function components $s_{1k} : \mathbb{R} \to \mathbb{C}$ for a one-dimensional T_D-periodic triangular excitation signal for the drive field with the FFP-trajectory

$$x_\mathrm{FFP}(t) = \frac{A_1}{G_1} \left(2 \operatorname{tri}(2 f_\mathrm{D} t) - 1\right), \qquad t \in \left[-\frac{T_\mathrm{D}}{2}, \frac{T_\mathrm{D}}{2}\right] \tag{2.43}$$

with $A_1/G_1 > 0$ and $k \in \mathbb{Z}$ is

$$\begin{aligned} s_{1k}(x) =& \frac{(-1)^{\lfloor (k-1)/2 \rfloor} 2\mathrm{i}\mu_0\rho_1 m_0 \beta G_1}{T_\mathrm{D}} \\ &\times \begin{cases} \int_{-\frac{A_1}{G_1}}^{\frac{A_1}{G_1}} \mathscr{L}'(\beta G_1 (x-z)) \cos\left(\frac{\pi}{2} \frac{k G_1}{A_1} z\right) \mathrm{d}z, & \text{if } k \text{ is odd} \\ \int_{-\frac{A_1}{G_1}}^{\frac{A_1}{G_1}} \mathscr{L}'(\beta G_1 (x-z)) \sin\left(\frac{\pi}{2} \frac{k G_1}{A_1} z\right) \mathrm{d}z, & \text{if } k \text{ is even.} \end{cases} \end{aligned} \tag{2.44}$$

Proof of Theorem 2.2. Starting from the integration by substitution

$$\begin{aligned} s_{1k}(x) = & \frac{\mu_0\rho_1 m_0}{T_\mathrm{D}} \int_{x_\mathrm{FFP}\left[\Omega^+_{T_\mathrm{D}}\right]} \beta G_1 \mathscr{L}'(\beta G_1 (z-x)) \mathrm{e}^{-\mathrm{i}\omega_k x^{-1}_\mathrm{FFP}(z)} \mathrm{d}z \\ & + \frac{\mu_0\rho_1 m_0}{T_\mathrm{D}} \int_{x_\mathrm{FFP}\left[\Omega^-_{T_\mathrm{D}}\right]} \beta G_1 \mathscr{L}'(\beta G_1 (z-x)) \mathrm{e}^{-\mathrm{i}\omega_k x^{-1}_\mathrm{FFP}(z)} \mathrm{d}z \end{aligned}$$

and the decomposition of Ω_{T_D} into its positive-valued $\Omega^+_{T_\mathrm{D}}$ and negative-valued $\Omega^-_{T_\mathrm{D}}$ subintervals and using the inverse mapping

$$x^{-1}_{\mathrm{FFP}}(z) = \frac{1 - \frac{G_1}{A_1} z}{4 f_\mathrm{D}}$$

for the case $\Omega^+_{T_\mathrm{D}} = \left[0, \frac{T_\mathrm{D}}{2}\right]$ and the inverse mapping

$$x^{-1}_{\mathrm{FFP}}(z) = \frac{\frac{G_1}{A_1} z - 1}{4 f_\mathrm{D}}$$

for the case $\Omega^-_{T_\mathrm{D}} = \left[-\frac{T_\mathrm{D}}{2}, 0\right)$, the system function component is

$$\begin{aligned}
s_{1k}(x) =& \frac{\mu_0 \rho_1 m_0}{T_\mathrm{D}} \left(\int_{\frac{A_1}{G_1}}^{-\frac{A_1}{G_1}} \beta G_1 \mathscr{L}'(\beta G_1 (z - x)) \mathrm{e}^{-\mathrm{i}\omega_k \frac{1 - \frac{G_1}{A_1} z}{4 f_\mathrm{D}}} \,\mathrm{d}z \right. \\
&\left. + \int_{-\frac{A_1}{G_1}}^{\frac{A_1}{G_1}} \beta G_1 \mathscr{L}'(\beta G_1 (z - x)) \mathrm{e}^{\mathrm{i}\omega_k \frac{1 - \frac{G_1}{A_1} z}{4 f_\mathrm{D}}} \,\mathrm{d}z \right) \\
=& \frac{\mu_0 \rho_1 m_0}{T_\mathrm{D}} \int_{-\frac{A_1}{G_1}}^{\frac{A_1}{G_1}} \beta G_1 \mathscr{L}'(\beta G_1 (z - x)) \left(\mathrm{e}^{\mathrm{i}\omega_k \frac{1 - \frac{G_1}{A_1} z}{4 f_\mathrm{D}}} - \mathrm{e}^{-\mathrm{i}\omega_k \frac{1 - \frac{G_1}{A_1} z}{4 f_\mathrm{D}}} \right) \,\mathrm{d}z \\
=& \frac{2\mathrm{i}\mu_0 \rho_1 m_0}{T_\mathrm{D}} \int_{-\frac{A_1}{G_1}}^{\frac{A_1}{G_1}} \beta G_1 \mathscr{L}'(\beta G_1 (z - x)) \sin\left(\omega_k \frac{1 - \frac{G_1}{A_1} z}{4 f_\mathrm{D}} \right) \,\mathrm{d}z.
\end{aligned}$$

Since $\sin\left(\omega_k \frac{1 - \frac{G_1}{A_1} z}{4 f_\mathrm{D}}\right)$ can be reformulated to

$$\sin\left(\omega_k \frac{1 - \frac{G_1}{A_1} z}{4 f_\mathrm{D}} \right) = \sin\left(\pi k \frac{1 - \frac{G_1}{A_1} z}{2} \right) = \sin\left(\frac{\pi k}{2} - \frac{\pi}{2} \frac{k G_1}{A_1} z \right),$$

the result is

$$\sin\left(\omega_k \frac{1 - \frac{G_1}{A_1} z}{4 f_\mathrm{D}} \right) = (-1)^{\lfloor (k-1)/2 \rfloor} \begin{cases} \cos\left(\frac{\pi}{2} \frac{k G_1}{A_1} z \right) & \text{if } k \text{ is odd,} \\ \sin\left(\frac{\pi}{2} \frac{k G_1}{A_1} z \right) & \text{if } k \text{ is even.} \end{cases}$$

This gives the result to be proven from (2.44). □

2.1.2 Higher-Dimensional Excitation

This section provides a basic introduction to MPI with higher-dimensional excitation of the Lissajous FFP-trajectory type. In Chapter 7, FFP-trajectories other than those presented here are also investigated. As part of this introduction, the problem of adapting the proof from [81] to higher-dimensional excitation is discussed and reasons for the proof in Chapter 7 are examined. If higher-dimensional excitations of the Lissajous trajectory type are used for the drive fields in MPI, they have the form

$$\boldsymbol{H}_{2\mathrm{D}}^{\mathrm{D}}(t) = -\begin{pmatrix} A_1 \sin(2\pi f_1 t + \varphi_1) \\ A_2 \sin(2\pi f_2 t + \varphi_2) \\ 0 \end{pmatrix}$$

in the case of two-dimensional excitation and the form

$$\boldsymbol{H}_{3\mathrm{D}}^{\mathrm{D}}(t) = -\begin{pmatrix} A_1 \sin(2\pi f_1 t + \varphi_1) \\ A_2 \sin(2\pi f_2 t + \varphi_2) \\ A_3 \sin(2\pi f_3 t + \varphi_3) \end{pmatrix}$$

in the case of three-dimensional excitation, where the frequencies $f_i \in \mathbb{R}$ are selected so that a periodic trajectory results, $\varphi_i \in \mathbb{R}$ denotes the phase shifts, and $A_i \in \mathbb{R}$ denotes the amplitudes. This can be obtained in the two-dimensional case with the choice

$$K_2 f_1 = K_1 f_2 = f_{\mathrm{B}}$$

and in the three-dimensional case with

$$K_3 K_2 f_1 = K_3 K_1 f_2 = K_1 K_2 f_3 = f_{\mathrm{B}},$$

where $K_1, K_2, K_3 \in \mathbb{Z}\backslash\{0\}$ and f_{B} denotes some arbitrary basis frequency. This means that the frequencies have a common multiplier and the drive fields $\boldsymbol{H}_{2\mathrm{D}}^{\mathrm{D}}(t)$ and $\boldsymbol{H}_{3\mathrm{D}}^{\mathrm{D}}(t)$ are therefore periodic. The period length T_{D} is depending on the specific choice of K_1, K_2, K_3, and the basis frequency f_{B} of the MPI scanner. Figure 2.5 shows different two-dimensional Lissajous trajectories for different values of K_1 and K_2.

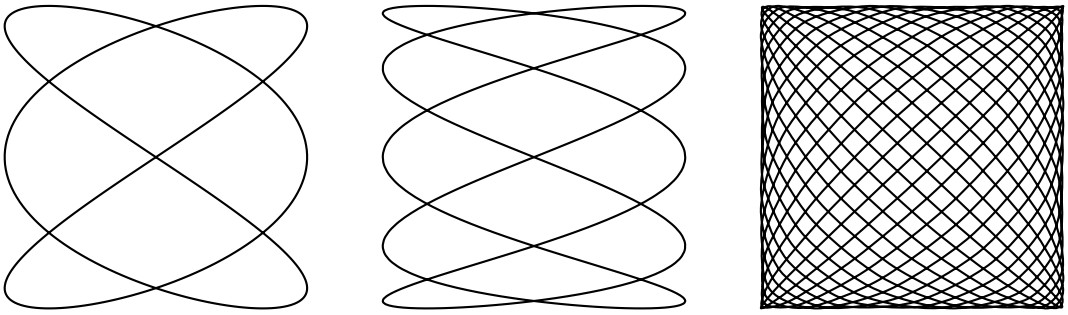

(a) (b) (c)

Figure 2.5: Different two-dimensional Lissajous trajectory type like curves for different values of K_1 and K_2. (a) $K_1 = 2$ and $K_2 = 3$, (b) $K_1 = 2$ and $K_2 = 5$, (c) $K_1 = 16$ and $K_2 = 17$.

To clarify the problem with the adaptation of the proof in [81], the Fourier series representation of the system function $s_\nu(\boldsymbol{x}, t)$ for higher-dimensional excitation in MPI using (2.34) in (2.35) will be examined in more detail:

$$s_{\nu k}(\boldsymbol{x}) = \frac{\mu_0 \boldsymbol{\rho}_\nu^{\mathsf{T}}}{T_{\mathrm{D}}} \int_{-\frac{T_{\mathrm{D}}}{2}}^{\frac{T_{\mathrm{D}}}{2}} \boldsymbol{\kappa}\left(\boldsymbol{G}\left(\boldsymbol{x}_{\mathrm{FFP}}(t) - \boldsymbol{x}\right)\right) \boldsymbol{G} \frac{\partial \boldsymbol{x}_{\mathrm{FFP}}(t)}{\partial t} \mathrm{e}^{-\mathrm{i}\omega_k t} \,\mathrm{d}t. \tag{2.45}$$

It does not seem to be as easy to apply the substitution trick for such an integral as it was done in the one-dimensional case in (2.41). The main reason for this lies in the complexity of describing the preimage of the function $\boldsymbol{x}_{\mathrm{FFP}}(t)$.

However, one would like to be able to specify a kind of volumetric convolution integral of the form

$$s_{\nu k}(\boldsymbol{x}) = \int_{\mathbb{R}^3} L_\nu(\boldsymbol{x} - \boldsymbol{z}) P_k(\boldsymbol{z}) \,\mathrm{d}\boldsymbol{z}, \tag{2.46}$$

where one part depends on the SPIOs distribution $L_\nu : \mathbb{R}^3 \to \mathbb{C}$ and another part depends only on the FFP-trajectory $P_k : \mathbb{R}^3 \to \mathbb{C}$. The reason for the desire for a function like (2.46) is not accidental, because in [81] for two-dimensional and in [80] for three-dimensional MPI a relationship of numerically calculated system function components to tensor products of Chebyshev polynomials of the second kind was observed and also frequency components in measured system functions show such a related structure in the center. The assumed relationship was frequently used in the MPI research community for interpolation [45], system matrix compression [60], denoising [63] and reconstruction [91]. However, until the work in [F1], this relationship was unproven for

ten years and not even in the ideal case the exact relationship to the observation could be uncovered, except for the one-dimensional case presented earlier.

Finally, the following relationship defined by

$$\begin{aligned} s_{\nu k}(\boldsymbol{x}) &= \frac{\mu_0 m_0 \boldsymbol{\rho}_\nu^{\mathsf{T}}}{T_\mathrm{D}} \int_{-\frac{T_\mathrm{D}}{2}}^{\frac{T_\mathrm{D}}{2}} \frac{\partial}{\partial t} [\boldsymbol{\mathscr{L}}(\beta \boldsymbol{G}(\boldsymbol{x}_\mathrm{FFP}(t) - \boldsymbol{x}))] \, \mathrm{e}^{-\mathrm{i}\omega_k t} \, \mathrm{d}t \\ &= \frac{\mu_0 m_0 \mathrm{i}\omega_k \boldsymbol{\rho}_\nu^{\mathsf{T}}}{T_\mathrm{D}} \int_{-\frac{T_\mathrm{D}}{2}}^{\frac{T_\mathrm{D}}{2}} \boldsymbol{\mathscr{L}}(\beta \boldsymbol{G}(\boldsymbol{x}_\mathrm{FFP}(t) - \boldsymbol{x})) \, \mathrm{e}^{-\mathrm{i}\omega_k t} \, \mathrm{d}t \end{aligned} \tag{2.47}$$

is to be checked, assuming that the Fourier series coefficients of $\boldsymbol{\mathscr{L}}(\beta \boldsymbol{G}(\boldsymbol{x}_\mathrm{FFP}(t) - \boldsymbol{x}))$ exist and $\boldsymbol{\mathscr{L}}(\beta \boldsymbol{G}(\boldsymbol{x}_\mathrm{FFP}(t) - \boldsymbol{x}))$ is continuously partially differentiable at least once and periodic with respect to time t. This relationship helps to express the system function components as the desired convolution in the further parts of the thesis.

Proof of Eq. (2.47). Let $\mathscr{L}_\nu(\boldsymbol{\xi})$ be defined by $\mathscr{L}_\nu(\boldsymbol{\xi}) = \boldsymbol{\rho}_\nu^{\mathsf{T}} \boldsymbol{\mathscr{L}}(\boldsymbol{\xi})$, then

$$s_{\nu k}(\boldsymbol{x}) = \frac{\mu_0 m_0}{T_\mathrm{D}} \int_{-\frac{T_\mathrm{D}}{2}}^{\frac{T_\mathrm{D}}{2}} \frac{\partial}{\partial t} [\mathscr{L}_\nu(\beta \boldsymbol{G}(\boldsymbol{x}_\mathrm{FFP}(t) - \boldsymbol{x}))] \, \mathrm{e}^{-\mathrm{i}\omega_k t} \, \mathrm{d}t. \tag{2.48}$$

Integration by parts shows that

$$\begin{aligned} s_{\nu k}(\boldsymbol{x}) =& \frac{\mu_0 m_0}{T_\mathrm{D}} \underbrace{\mathscr{L}_\nu(\beta \boldsymbol{G}(\boldsymbol{x}_\mathrm{FFP}(t) - \boldsymbol{x})) \, \mathrm{e}^{-\mathrm{i}\omega_k t} \Big|_{-\frac{T_\mathrm{D}}{2}}^{\frac{T_\mathrm{D}}{2}}}_{=0} \\ &- \frac{\mu_0 m_0}{T_\mathrm{D}} \int_{-\frac{T_\mathrm{D}}{2}}^{\frac{T_\mathrm{D}}{2}} \mathscr{L}_\nu(\beta \boldsymbol{G}(\boldsymbol{x}_\mathrm{FFP}(t) - \boldsymbol{x})) \frac{\partial}{\partial t} \left[\mathrm{e}^{-\mathrm{i}\omega_k t}\right] \, \mathrm{d}t \\ =& \frac{\mu_0 m_0 \mathrm{i}\omega_k}{T_\mathrm{D}} \int_{-\frac{T_\mathrm{D}}{2}}^{\frac{T_\mathrm{D}}{2}} \mathscr{L}_\nu(\beta \boldsymbol{G}(\boldsymbol{x}_\mathrm{FFP}(t) - \boldsymbol{x})) \, \mathrm{e}^{-\mathrm{i}\omega_k t} \, \mathrm{d}t, \end{aligned} \tag{2.49}$$

where the second equation is valid because the FFP $\boldsymbol{x}_\mathrm{FFP}(t)$ is T_D-periodic. □

3 Relaxation and Magnetization of SPIOs

Relaxation effects and magnetic anisotropy play a key role in real measurements. Even though these effects are not covered by the Langevin model used in this work, it is helpful to discuss relaxation models as they allow for the introduction of an anisotropic equilibrium model [18, 19, 83, 86]. Recently, an extended anisotropic equilibrium model seems to be very promising for model-based MPI. Therefore, its contribution to model-based MPI will be briefly outlined below, as it is beyond the scope of this thesis, but is, nevertheless, important for the field of MPI in general and the anisotropic equilibrium model presented in Section 3.1 in particular. The conference article [F7] proposed to replace the Langevin model with the anisotropic equilibrium model by using the spatial SPIO anisotropy model for fluid tracers from [49]. In [49] this model is used in connection with the Néel rotation Fokker-Planck equation. At the same conference, [3] proposed the same anisotropic equilibrium model for the case of an oriented and immobilized SPIO tracer. For typical MPI tracers, in [F7] it is shown that the anisotropic equilibrium model can compete with the more complex Néel rotation model, but can be evaluated several orders of magnitude faster with the series expression presented in Section 3.1.3. In [F5] the "fluid" anisotropic equilibrium model was applied to the system function component model, which was firstly presented in [F1]. The essence is that the anisotropic equilibrium model can be used instead of the Langevin model [F5, F7, F11, C3], although the Langevin model is mostly used in this thesis. Initial numerical experiments carried out in [F5, F7] show a high degree of agreement between the Néel rotation Fokker-Planck model and the anisotropic equilibrium model for typical MPI scanners and SPIO tracers. Using the model in [F5], the direct Chebyshev polynomial MPI reconstruction was extended to the anisotropic MPI model in [C3]. In addition, the model in [F7] was used to show that in the case of immobilized and non-oriented SPIOs the Langevin model of paramagnetism is sufficient, since the anisotropic

equilibrium model is reduced to the Langevin model of paramagnetism in this particular case [F11]. Due to the potential of [F7] and its importance for the field of MPI, three research groups joined forces to further evaluate the models potential. The mutual efforts resulted in a journal article [F6]. The article [F6] shows that for typical SPIO tracers the Néel rotation model can be substituted by the anisotropic equilibrium model in Proposition 3.3. For this purpose, numerous numerical and experimental tests were performed. Furthermore, the speed advantage of the implementation of the anisotropic equilibrium model over the numerical solution of the Néel rotation Fokker-Planck equation is demonstrated and the proof for Theorem 3.1 omitted in [F7] is included in the submitted article for the first time. With this overview in mind, the transition from the more complex relaxation models based on differential equations to the equilibrium models will now be discussed.

3.1 Relaxation and Equilibrium Models

Two different types of remagnetization effects play an important role in nanoparticles. They are also responsible for relaxation. Firstly, Brownian rotation [14], which describes the spatial rotation of a nanoparticle in the direction of the applied magnetic field $\boldsymbol{H} \in \mathbb{R}^3$. Secondly, the Néel rotation [14, 74], which instead describes the rotation of the magnetic moment $\boldsymbol{m} \in \mathbb{R}^3$ of a particle in the direction of the applied magnetic field $\boldsymbol{H} \in \mathbb{R}^3$. The Néel rotation model also includes magnetic anisotropies of the particles, which are modeled, for example, as easy axes for the magnetic moment. The two rotation mechanism are shown in Figure 3.1 from left to right as the temporal development of the rotation with respect to the magnetic moment $\boldsymbol{m} \in \mathbb{R}^3$, a easy axis $\boldsymbol{n} \in \mathbb{R}^3$, and a constant applied field $\boldsymbol{H} \in \mathbb{R}^3$. In practice, with different SPIO tracers and excitation sequences, one, the other or even both dominate the relaxation behavior and the overall behavior may be difficult to describe [34, 67, 68, 116].

The most general model for the distribution behavior of SPIOs is to model each particle individually in the presence of a time-varying field $\boldsymbol{H} : \mathbb{R} \to \mathbb{R}^3$, which leads to a system of stochastic ordinary differential equations, also known as Langevin equations [34, 86, 112]. Once a large number of particles have been modeled, they can be used to estimate the mean magnetic moment within a volume as a function of

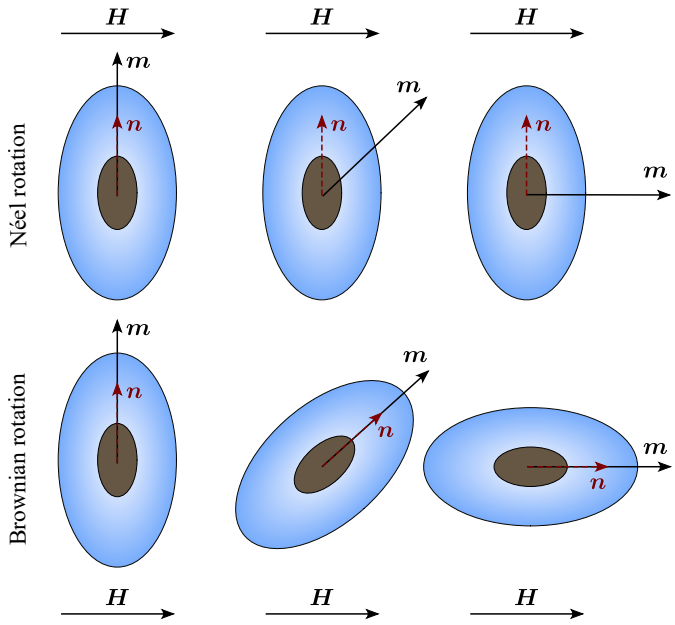

Figure 3.1: The both dominant remagnetization mechanisms for SPIOs are shown. The development over time for a constant field $\boldsymbol{H}$ is shown from left to right, whereby the mean magnetic moment $\boldsymbol{m}$ and the easy axis $\boldsymbol{n}$ are initially aligned and oriented orthogonally to $\boldsymbol{H}$. In the pure Néel rotation case, the magnetic moment $\boldsymbol{m}$ of the SPIO changes in the direction $\boldsymbol{H}$, while the SPIO itself does not rotate in space, i.e., the easy axis does not change. In contrast, pure Brownian rotation describes the spatial rotation of the SPIO in the direction of the applied field $\boldsymbol{H}$, as the SPIO rotates in the direction of its magnetic shape anisotropy, i.e., it is assumed here that the mean magnetic moment $\boldsymbol{m}$ and the easy axis $\boldsymbol{n}$ are aligned with each other.

time. Unfortunately, even for a small volume, several hundreds to thousands of simulated particles are needed to estimate the mean magnetic moment of the SPIO distribution accurately enough [47, 75, 112]. A second approach is to calculated the probability density function (PDF) for the magnetic moments $\boldsymbol{m} \in \mathbb{S}^2$ of the stochastic process as a limit value for a large number of particles, instead of modeling each particle individually as a function of time $t \in \mathbb{R}$. The transition of the Langevin equations results in so-called Fokker-Planck equations, which result in case of SPIOs in a partial parabolic differential equation on the surface of the unit sphere $\mathbb{S}^2 \subset \mathbb{R}^3$ [48, 111]. In general, however, there is no closed-form solution for the Fokker-Planck equations and numerical solutions must be calculated. The Fokker-Planck equations for coupled Brownian and Néelian rotation are described in [111] or [93]. In contrast, this work only describes the pure Brownian [115] or the pure Néel rotation, which are special cases of the coupled version. This thesis follows the presentation and notation presented in [48, 49]. In MPI, the

Fokker-Planck equation for the Brownian rotation of spherical particles to obtain the PDF of the magnetic moment $p_{\mathrm{B}} : \mathbb{S}^2 \times \mathbb{R} \times C(\mathbb{R}, \mathbb{R}^3) \to \mathbb{R}_+$ is usually described by

$$2\tau_{\mathrm{B}} \frac{\partial p_{\mathrm{B}}(\boldsymbol{m}, t; \boldsymbol{H})}{\partial t} = -\operatorname{div}_{\mathbb{S}^2}\Big(\beta\big((\boldsymbol{m} \times \boldsymbol{H}) \times \boldsymbol{m}\big) p_{\mathrm{B}} - \nabla_{\mathbb{S}^2} p_{\mathrm{B}}\Big), \tag{3.1}$$

where $\nabla_{\mathbb{S}^2}$ and $\operatorname{div}_{\mathbb{S}^2}(\cdot)$ denote the gradient and divergence operator with respect to the surface of the unit sphere $\mathbb{S}^2$, respectively. For the sake of clarity the dependency of $\boldsymbol{H}(\boldsymbol{x}, \cdot)$ from the spatial position $\boldsymbol{x}$ is omitted and the notation $\boldsymbol{H}(\boldsymbol{x}, \cdot) \in C(\mathbb{R}, \mathbb{R}^3)$ means that the function $\boldsymbol{H}$ is parametrized in the first argument and remains a function with respect to the time argument and is also continuous at least with respect to time. The constant $\tau_{\mathrm{B}} = \frac{3V_{\mathrm{H}}\eta}{k_{\mathrm{B}}T_{\mathrm{P}}}$ denotes the Brownian relaxation time, which depends on the hydrodynamic volume V_{H}, the dynamic viscosity η, and $\beta = \frac{m_0\mu_0}{k_{\mathrm{B}}T_{\mathrm{P}}}$ is defined as in the previous chapter. The hydrodynamic volume V_{H} depends also on the particle diameter D, therefore it is often used that $V_{\mathrm{H}} = V_{\mathrm{C}}$. The second Fokker-Planck equation for the Néel-rotation PDF of the magnetic moment $p_{\mathrm{N}} : \mathbb{S}^2 \times \mathbb{R} \times C(\mathbb{R}, \mathbb{R}^3) \times \mathbb{S}^2 \to \mathbb{R}_+$ is defined by

$$\begin{aligned} 2\tau_{\mathrm{N}} \frac{\partial p_{\mathrm{N}}(\boldsymbol{m}, t; \boldsymbol{H}, \boldsymbol{n})}{\partial t} &= -\operatorname{div}_{\mathbb{S}^2}\left(\frac{\beta}{\alpha}\big(\boldsymbol{H}_{\text{eff}} \times \boldsymbol{m} + \alpha\,(\boldsymbol{m} \times \boldsymbol{H}_{\text{eff}}) \times \boldsymbol{m}\big) p_{\mathrm{N}} - \nabla_{\mathbb{S}^2} p_{\mathrm{N}}\right), \\ \boldsymbol{H}_{\text{eff}}(\boldsymbol{m}, t; \boldsymbol{H}, \boldsymbol{n}) &= \boldsymbol{H}(\boldsymbol{x}, \cdot) + \boldsymbol{H}_{\text{anis}}(\boldsymbol{m}, \boldsymbol{n}), \\ \boldsymbol{H}_{\text{anis}}(\boldsymbol{m}, \boldsymbol{n}) &= 2\frac{K_{\text{anis}} V_{\mathrm{C}}}{m_0\mu_0} \boldsymbol{n}\boldsymbol{m}^{\mathsf{T}}\boldsymbol{n}, \end{aligned} \tag{3.2}$$

where $\boldsymbol{H}_{\text{anis}} : \mathbb{S}^2 \times \mathbb{S}^2 \to \mathbb{R}^3$ models a uniaxial particle anisotropy for an easy axis $\boldsymbol{n} \in \mathbb{S}^2$ and $\tau_{\mathrm{N}} = \frac{\beta}{2\alpha\tilde{\gamma}\mu_0}$ denotes the Néel relaxation constant. The model of uniaxial particle anisotropy is also known as the Stoner-Wohlfarth model [96]. Besides, $\alpha > 0$ is a damping parameter, $\tilde{\gamma} = \frac{\gamma}{1+\alpha^2}$ with γ the material-dependent gyromagnetic ratio, and $K_{\text{anis}} \in \mathbb{R}$ is the anisotropy parameter. The mean magnetic moment of the SPIOs distribution in (2.6) can be calculated for both remagnitization models as the following expected value

$$\overline{\boldsymbol{m}}(\boldsymbol{x}, t) = \tilde{\boldsymbol{m}}_{\cdot}(\boldsymbol{H}(\boldsymbol{x}, \cdot), t) = m_0 \int_{\mathbb{S}^2} \boldsymbol{m} p_{\cdot}\big(\boldsymbol{m}, t; \boldsymbol{H}(\boldsymbol{x}, \cdot)\big)\, \mathrm{d}\boldsymbol{m},$$

where m_0 is the modal value of the magnetic moment of one nanoparticle and is material and diameter specific. The solution of the Fokker-Planck equations in MPI is based for the multidimensional MPI case on a spherical harmonic expansion [49, 111] or simplified

in the one-dimensional case on an expansion with Legendre polynomials [16, 23, 48]. After the expansion one needs to solve a coupled ordinary differential equation system to estimate the PDF or just the mean magnetic moment. An MNPDynamics toolbox for solving the Fokker-Planck equation for pure Neél and Brownian rotation was published in [4].

The Langevin function $\mathscr{L}(\xi)$, which is used as the central part of the simplified magnetization model for the SPIO distribution, can be derived from the solution of the Brownian Fokker-Planck equation (3.1) when the SPIO distribution is in equilibrium. At equilibrium, the temporal derivative of $\frac{\partial p_{\mathrm{B}}}{\partial t} = 0$ disappears, since no more temporal changes take place or, mathematically equivalent, $\tau_{\mathrm{B}} = 0$. In other words, one can say that the temporal relaxation effects in the SPIO distribution are neglected in the Langevin model of paramagnetism. For the Néel rotation, the equilibrium solution with assumed uniaxial anisotropy for the SPIOs will not necessarily yield the Langevin function. This fact is often ignored in the MPI literature, although there are a few references that take this fact into account [83, 86]. The main reason for this is that in a scenario where the particle is in a fluid, Brownian rotation will always rotate the particle in its energetically optimal direction, i.e., towards the uniaxial easy axis in the Stoner-Wolfarth model, and therefore the simplified magnetization model will always be observed in equilibrium. However, there are scenarios in which the particles are immobilized and oriented to a certain degree and the anisotropy becomes important for the equilibrium solution [3, 5, 73]. However, it was shown for MPI based on Lissajous FFP-trajectories that the anisotropic equilibrium model falls back to the Langevin model, if the particles were immobilized unoriented [F11]. In the next sections, the two equilibrium solutions for the Brownian rotation and for the Néel rotation are formulated in propositions and are subsequently proven, whereby it should not go unmentioned that the equilibrium models can be found in the literature [48, 83, 93].

3.1.1 Equilibrium: Brownian Rotation Model

The equilibrium model for the Brownian rotation is formulated below in a proposition and subsequently proven. This model leads to the Langevin model of paramagnetism, which was introduced in Section 2.1 and is later further investigated for different drive-field sequences in the spatio-temporal Fourier space.

Proposition 3.1. *The Brownian Fokker-Planck equation in an equilibrium state reads*

$$0 = -\operatorname{div}_{\mathbb{S}^2}\Big(\beta\big((\boldsymbol{m}\times\boldsymbol{H})\times\boldsymbol{m}\big)p_{\mathrm{B}}^{\mathrm{EQ}} - \nabla_{\mathbb{S}^2}p_{\mathrm{B}}^{\mathrm{EQ}}\Big)$$

and has the Boltzmann distribution $p_{\mathrm{B}}^{\mathrm{EQ}} : \mathbb{S}^2 \times \mathbb{R}^3 \to \mathbb{R}_+$ *as its solution, where the Boltzmann distribution is given by*

$$p_{\mathrm{B}}^{\mathrm{EQ}}(\boldsymbol{m};\boldsymbol{H}) = \frac{1}{\mathcal{Z}(\boldsymbol{H})}\mathrm{e}^{-\frac{\beta}{\mu_0 m_0}E(m_0\boldsymbol{m};\,\boldsymbol{H})}$$

with the partition function ($\mathcal{Z} : \mathbb{R}^3 \to \mathbb{R}_+$*)*

$$\mathcal{Z}(\boldsymbol{H}) = \frac{2\pi}{\beta\|\boldsymbol{H}\|}\left(\mathrm{e}^{\beta\|\boldsymbol{H}\|} - \mathrm{e}^{-\beta\|\boldsymbol{H}\|}\right)$$

and the free energy ($E : \mathbb{R}^3 \times \mathbb{R}^3 \to \mathbb{R}$*)*

$$E(\boldsymbol{\xi};\boldsymbol{H}) = -\mu_0\boldsymbol{H}^{\mathsf{T}}\boldsymbol{\xi}.$$

The mean magnetic moment $\tilde{\boldsymbol{m}}_0 : \mathbb{R}^3 \to \mathbb{R}^3$ *for* $p_{\mathrm{B}}^{\mathrm{EQ}}(\boldsymbol{m};\boldsymbol{H})$ *and a given magnetic field* $\boldsymbol{H} \in \mathbb{R}^3$ *is therefore given by*

$$\tilde{\boldsymbol{m}}_0(\boldsymbol{H}) = m_0\,\mathscr{L}(\beta\|\boldsymbol{H}\|)\,\boldsymbol{e}_{\boldsymbol{H}},$$

where $\mathscr{L}(\xi)$ *denotes the Langevin function. Note that the equilibrium model in* (2.7) *is obtained by* $\overline{\boldsymbol{m}}(\boldsymbol{x},t) = \tilde{\boldsymbol{m}}_0(\boldsymbol{H}(\boldsymbol{x},t))$ *for an applied magnetic field* $\boldsymbol{H} : \mathbb{R}^3 \times \mathbb{R} \to \mathbb{R}^3$*.*

Proof of Proposition 3.1. It should first be considered that the solution follows a Boltzmann distribution $f_0 : \mathbb{S}^2 \to \mathbb{R}_+$, assuming that $f_0(\boldsymbol{m}) \approx p_{\mathrm{B}}(\boldsymbol{m}, t_0; \boldsymbol{H}_0)$ denotes the distribution at time t_0 at which the distribution tends to equilibrium and $\boldsymbol{H}_0(\boldsymbol{x}) = \boldsymbol{H}(\boldsymbol{x}, t_0)$ is the temporally constant applied field. Specifically, the Boltzmann distribution is [48]

$$f_0(\boldsymbol{m}) = \frac{1}{\mathcal{Z}}\mathrm{e}^{-\frac{\beta}{\mu_0 m_0}E(m_0\boldsymbol{m};\,\boldsymbol{H}_0)} \tag{3.3}$$

with $\mathcal{Z}$ a normalization constant, which in the context of statistical physics is also known as the partition function, so that $f_0(\boldsymbol{m})$ is a PDF and the free energy is given by

$$E(\boldsymbol{\xi}; \boldsymbol{H}_0) = -\mu_0 \boldsymbol{H}_0^{\mathsf{T}} \boldsymbol{\xi}. \tag{3.4}$$

First of all, a helpful formula shall be introduced, which is

$$(\boldsymbol{m} \times \boldsymbol{H}_0) \times \boldsymbol{m} = \underbrace{(\boldsymbol{m}^{\mathsf{T}}\boldsymbol{m})}_{=1} \boldsymbol{H}_0 - (\boldsymbol{m}^{\mathsf{T}}\boldsymbol{H}_0)\boldsymbol{m} = \boldsymbol{H}_0 - \boldsymbol{m}(\boldsymbol{m}^{\mathsf{T}}\boldsymbol{H}_0). \tag{3.5}$$

The surface gradient $\nabla_{\mathbb{S}^2} f_0$ is related to the Cartesian gradient $\nabla_{\boldsymbol{m}} f_0$ [48, 69] as follows

$$\nabla_{\mathbb{S}^2} f_0(\boldsymbol{m}) = \nabla_{\boldsymbol{m}} f_0(\boldsymbol{m}) - \boldsymbol{n} \left(\boldsymbol{n}^{\mathsf{T}} \nabla_{\boldsymbol{m}} f_0(\boldsymbol{m}) \right),$$

where $\boldsymbol{n} \in \mathbb{S}^2$ denotes a normal vector on the surface of the sphere. Since $\boldsymbol{n}$ for the surface function $f_0 : \mathbb{S}^2 \to \mathbb{R}_+$ corresponds to the argument $\boldsymbol{m}$, the following is obtained

$$\nabla_{\mathbb{S}^2} f_0(\boldsymbol{m}) = \nabla_{\boldsymbol{m}} f_0(\boldsymbol{m}) - \boldsymbol{m} \left(\boldsymbol{m}^{\mathsf{T}} \nabla_{\boldsymbol{m}} f_0(\boldsymbol{m}) \right). \tag{3.6}$$

This can be checked by calculating that $\nabla_{\mathbb{S}^2} f_0(\boldsymbol{m}) = \nabla_{\boldsymbol{m}} f_0 \left(\frac{\boldsymbol{m}}{\|\boldsymbol{m}\|_2} \right)$ and finally using that the norm $\|\boldsymbol{m}\| = 1$. The surface gradient is orthogonal to the normal vector $\boldsymbol{m}$, as can be verified by

$$\begin{aligned} \boldsymbol{m}^{\mathsf{T}} \nabla_{\mathbb{S}^2} f_0(\boldsymbol{m}) &= \boldsymbol{m}^{\mathsf{T}} \left(\nabla_{\boldsymbol{m}} f_0(\boldsymbol{m}) - \boldsymbol{m} \left(\boldsymbol{m}^{\mathsf{T}} \nabla_{\boldsymbol{m}} f_0(\boldsymbol{m}) \right) \right) \\ &= \boldsymbol{m}^{\mathsf{T}} \nabla_{\boldsymbol{m}} f_0(\boldsymbol{m}) - \underbrace{\boldsymbol{m}^{\mathsf{T}}\boldsymbol{m}}_{=1} \left(\boldsymbol{m}^{\mathsf{T}} \nabla_{\boldsymbol{m}} f_0(\boldsymbol{m}) \right) = 0. \end{aligned}$$

Hence it follows that $\nabla_{\mathbb{S}^2} f_0$ and $\boldsymbol{m}$ result in an orthogonal system and it holds that

$$(\boldsymbol{m} \times \nabla_{\mathbb{S}^2} f_0) \times \boldsymbol{m} = \nabla_{\mathbb{S}^2} f_0.$$

If $f_0(\boldsymbol{m})$ is inserted into the differential equation

$$0 = -\operatorname{div}_{\mathbb{S}^2} \Big(\beta \big((\boldsymbol{m} \times \boldsymbol{H}_0) \times \boldsymbol{m} \big) f_0 - \nabla_{\mathbb{S}^2} f_0 \Big), \tag{3.7}$$

this helps to prove that the Boltzmann distribution (3.3) with the free energy (3.4) is actually the solution of the differential equation (3.1) in the equilibrium case. Since the Cartesian gradient of $f_0(\boldsymbol{m})$ is

$$\nabla_{\boldsymbol{m}} f_0(\boldsymbol{m}) = f_0(\boldsymbol{m}) \left(-\frac{\beta}{\mu_0 m_0} \nabla_{\boldsymbol{m}} E(m_0 \boldsymbol{m}, \boldsymbol{H}_0) \right) = \beta f_0(\boldsymbol{m}) \boldsymbol{H}_0$$

the surface gradient of $f_0(\boldsymbol{m})$ is

$$\nabla_{\mathbb{S}^2} f_0(\boldsymbol{m}) = \beta f_0(\boldsymbol{m})(\boldsymbol{H}_0 - \boldsymbol{m}(\boldsymbol{m}^\mathsf{T} \boldsymbol{H}_0)) \overset{(3.5)}{=} \beta f_0(\boldsymbol{m}) \left((\boldsymbol{m} \times \boldsymbol{H}_0) \times \boldsymbol{m} \right) \tag{3.8}$$

with the help of (3.6). By inserting (3.8) into (3.7), it becomes clear that the Boltzmann distribution in (3.3) solves the differential equation. In [84] it is stated that the Fokker-Planck equation in equilibrium corresponds to a Boltzmann distribution and that the Boltzmann distribution is the only solution if the partition function $\mathcal{Z}$ has a finite value.

Finally, it is now shown that the equilibrium solution of Brownian rotation for the mean magnetic moment is the Langevin function. The partition function can be calculated by

$$\mathcal{Z} = \int_{\mathbb{S}^2} \mathrm{e}^{-\frac{\beta}{\mu_0 m_0} E(m_0 \boldsymbol{m}, \boldsymbol{H}_0)} \, \mathrm{d}\boldsymbol{m} = \int_{\mathbb{S}^2} \mathrm{e}^{\beta \boldsymbol{H}_0^\mathsf{T} \boldsymbol{m}} \, \mathrm{d}\boldsymbol{m}.$$

Now let $\boldsymbol{R} \in \mathbb{R}^{3\times 3}$ be such a rotation matrix that $\boldsymbol{R}^\mathsf{T} \boldsymbol{H}_0 = H_0 \boldsymbol{e}_3$ with $H_0 = \|\boldsymbol{H}_0\|$, where $\boldsymbol{e}_3 = (0, 0, 1)^\mathsf{T}$ denotes the third Euclidean basis vector, and using the fact that a rotation is an orthogonal transform $\boldsymbol{R}\boldsymbol{R}^\mathsf{T} = \boldsymbol{R}^\mathsf{T}\boldsymbol{R} = \boldsymbol{I}$, one can write

$$\mathcal{Z} = \int_{\mathbb{S}^2} \mathrm{e}^{\beta \boldsymbol{H}_0^\mathsf{T} \boldsymbol{R}\boldsymbol{R}^\mathsf{T} \boldsymbol{m}} \, \mathrm{d}\boldsymbol{m} = \int_{\mathbb{S}^2} \mathrm{e}^{\beta H_0 \boldsymbol{e}_3^\mathsf{T} \boldsymbol{R}^\mathsf{T} \boldsymbol{m}} \, \mathrm{d}\boldsymbol{m} = \int_{\mathbb{S}^2} \mathrm{e}^{\beta H_0 \boldsymbol{e}_3^\mathsf{T} \boldsymbol{r}} \, \mathrm{d}\boldsymbol{r}.$$

In the last equals sign, it is used that the surface of the sphere $\mathbb{S}^2$ is invariant under rotation, $\mathrm{e}^{\beta H_0 \boldsymbol{e}_3^\mathsf{T} \boldsymbol{R}^\mathsf{T} \boldsymbol{m}} > 0$ for all $\boldsymbol{m} \in \mathbb{S}^2$, and for the substitution $\boldsymbol{r} = \boldsymbol{R}^\mathsf{T} \boldsymbol{m}$ the following applies $\mathrm{d}\boldsymbol{m} = |\det(\boldsymbol{R})| \, \mathrm{d}\boldsymbol{r} = \mathrm{d}\boldsymbol{r}$ and $\boldsymbol{m} = \boldsymbol{R}\boldsymbol{r}$. If the surface of the sphere is represented using spherical coordinates

$$\boldsymbol{r} = \begin{pmatrix} \sin(\theta)\cos(\varphi) \\ \sin(\theta)\sin(\varphi) \\ \cos(\theta) \end{pmatrix} \qquad \text{with } \varphi \in [0, 2\pi) \text{ and } \theta \in [0, \pi],$$

the result is

$$\begin{aligned}\mathcal{Z} &= \int_{\mathbb{S}^2} \mathrm{e}^{\beta H_0 r_3}\,\mathrm{d}\boldsymbol{r} = \int_0^{\pi}\int_0^{2\pi} \mathrm{e}^{\beta H_0\cos(\theta)}\sin(\theta)\,\mathrm{d}\varphi\,\mathrm{d}\theta \\ &= 2\pi\int_0^{\pi} \mathrm{e}^{\beta H_0\cos(\theta)}\sin(\theta)\,\mathrm{d}\theta.\end{aligned}$$

With the substitution $x = \cos(\theta)$ and $\mathrm{d}\theta = -\frac{\mathrm{d}x}{\sin(\theta)}$ this finally results in

$$\mathcal{Z} = 2\pi\int_{-1}^{1} \mathrm{e}^{\beta H_0 x}\,\mathrm{d}x = \frac{2\pi}{\beta H_0}\mathrm{e}^{\beta H_0 x}\Big|_{-1}^{1} = \frac{2\pi}{\beta H_0}\left(\mathrm{e}^{\beta H_0} - \mathrm{e}^{-\beta H_0}\right). \tag{3.9}$$

The partition function is finite if one assumes that the magnetic field strength H_0 is finite. Everything is now ready to calculate the mean magnetic moment of the equilibrium distribution

$$\tilde{\boldsymbol{m}}(\boldsymbol{H}_0, t_0) = m_0\int_{\mathbb{S}^2} \boldsymbol{m} f_0(\boldsymbol{m})\,\mathrm{d}\boldsymbol{m}. \tag{3.10}$$

As a shorthand notation, $\tilde{\boldsymbol{m}}_0(\boldsymbol{H}_0) = \tilde{\boldsymbol{m}}(\boldsymbol{H}_0, t_0)$ is introduced. In general, the way to solve (3.10) is similar to the way to derive the partition function, so the intermediate steps are not explained further:

$$\begin{aligned}\tilde{\boldsymbol{m}}_0(\boldsymbol{H}_0) &= \frac{m_0}{\mathcal{Z}}\int_{\mathbb{S}^2} \boldsymbol{m}\mathrm{e}^{\beta\boldsymbol{H}_0^{\mathsf{T}}\boldsymbol{m}}\,\mathrm{d}\boldsymbol{m} = \frac{m_0}{\mathcal{Z}}\int_{\mathbb{S}^2} \boldsymbol{m}\mathrm{e}^{\beta\boldsymbol{H}_0^{\mathsf{T}}\boldsymbol{R}\boldsymbol{R}^{\mathsf{T}}\boldsymbol{m}}\,\mathrm{d}\boldsymbol{m} \\ &= \frac{m_0}{\mathcal{Z}}\int_{\mathbb{S}^2} \boldsymbol{R}\boldsymbol{r}\mathrm{e}^{\beta H_0\boldsymbol{e}_3^{\mathsf{T}}\boldsymbol{r}}\,\mathrm{d}\boldsymbol{r} \\ &= \frac{m_0}{\mathcal{Z}}\boldsymbol{R}\int_0^{\pi}\int_0^{2\pi}\begin{pmatrix}\sin(\theta)\cos(\varphi)\\ \sin(\theta)\sin(\varphi)\\ \cos(\theta)\end{pmatrix}\mathrm{e}^{\beta H_0\cos(\theta)}\sin(\theta)\,\mathrm{d}\varphi\,\mathrm{d}\theta \\ &= \frac{m_0}{\mathcal{Z}}\boldsymbol{R}\int_0^{\pi} 2\pi\cos(\theta)\boldsymbol{e}_3\mathrm{e}^{\beta H_0\cos(\theta)}\sin(\theta)\,\mathrm{d}\theta \\ &= \frac{2\pi m_0}{\mathcal{Z}}\underbrace{\boldsymbol{R}\boldsymbol{e}_3}_{=\frac{\boldsymbol{H}_0}{\|H_0\|}=\boldsymbol{e}_{\boldsymbol{H}_0}}\int_0^{\pi}\cos(\theta)\mathrm{e}^{\beta H_0\cos(\theta)}\sin(\theta)\,\mathrm{d}\theta \\ &= \frac{2\pi m_0}{\mathcal{Z}}\boldsymbol{e}_{\boldsymbol{H}_0}\int_{-1}^{1} x\mathrm{e}^{\beta H_0 x}\,\mathrm{d}x.\end{aligned}$$

With the help of integration by parts, the mean magnetic moment results in

$$\begin{aligned}
\tilde{\boldsymbol{m}}_0(\boldsymbol{H}_0) &= \frac{2\pi m_0}{\mathcal{Z}} \boldsymbol{e}_{\boldsymbol{H}_0} \left(\frac{1}{\beta H_0} x \mathrm{e}^{\beta H_0 x} \Big|_{-1}^{1} - \frac{1}{\beta H_0} \underbrace{\int_{-1}^{1} e^{\beta H_0 x} \, \mathrm{d}x}_{=\frac{\mathcal{Z}}{2\pi}} \right) \\
&= \frac{2\pi m_0}{\mathcal{Z}} \boldsymbol{e}_{\boldsymbol{H}_0} \left(\frac{1}{\beta H_0} \mathrm{e}^{\beta H_0} + \frac{1}{\beta H_0} \mathrm{e}^{-\beta H_0} - \frac{\mathcal{Z}}{2\pi \beta H_0} \right) \\
&\overset{(3.9)}{=} m_0 \boldsymbol{e}_{\boldsymbol{H}_0} \left(\frac{\mathrm{e}^{\beta H_0} + \mathrm{e}^{-\beta H_0}}{\mathrm{e}^{\beta H_0} - \mathrm{e}^{-\beta H_0}} - \frac{1}{\beta H_0} \right) \\
&= m_0 \left(\coth(\beta H_0) - \frac{1}{\beta H_0} \right) \boldsymbol{e}_{\boldsymbol{H}_0} = m_0 \, \mathscr{L}(\beta H_0) \, \boldsymbol{e}_{\boldsymbol{H}_0}.
\end{aligned} \tag{3.11}$$

By comparing the result in (3.11) with the equations in Proposition 3.1, the proof is complete. □

3.1.2 Equilibrium: Néel Rotation Model

The Langevin model of paramagnetism is a special case of this more general anisotropic equilibrium model, for the case where there is no SPIO anisotropy. Therefore, it can be used to generalize the Langevin model in the MPI system equation function in (2.34). In the following, the PDF for the Néel rotation Fokker-Planck equation is formulated in a proposition assuming equilibrium. The proposition is then proved, reusing parts of the proof for the Brownian rotation Fokker-Planck equation without recalculating it.

Proposition 3.2. *The Néel rotation Fokker-Planck equation of the equilibrium reads*

$$0 = -\operatorname{div}_{\mathbb{S}^2} \left(\frac{\beta}{\alpha} \big(\boldsymbol{H}_{\text{eff}} \times \boldsymbol{m} + \alpha \, (\boldsymbol{m} \times \boldsymbol{H}_{\text{eff}}) \times \boldsymbol{m} \big) p_{\text{N}}^{\text{EQ}} - \nabla_{\mathbb{S}^2} p_{\text{N}}^{\text{EQ}} \right),$$

where the magnetic fields $\boldsymbol{H}_{\text{eff}} : \mathbb{S}^2 \times \mathbb{R}^3 \times \mathbb{S}^2 \to \mathbb{R}^3$ *and* $\boldsymbol{H} \in \mathbb{R}^3$ *are related to each other by*

$$\boldsymbol{H}_{\text{eff}}(\boldsymbol{m}; \boldsymbol{H}, \boldsymbol{n}) = \boldsymbol{H} + 2 \frac{K_{\text{anis}} V_{\text{C}}}{m_0 \mu_0} \boldsymbol{n} \boldsymbol{n}^{\mathsf{T}} \boldsymbol{m}.$$

The differential equation has the Boltzmann distribution $p_{\mathrm{N}}^{\mathrm{EQ}} : \mathbb{S}^2 \times \mathbb{R}^3 \times \mathbb{S}^2 \to \mathbb{R}_+$ *as a solution, where the Boltzmann distribution is given by*

$$p_{\mathrm{N}}^{\mathrm{EQ}}(\boldsymbol{m}; \boldsymbol{H}, \boldsymbol{n}) = \frac{1}{\mathcal{Z}} \mathrm{e}^{-\frac{\beta}{\mu_0 m_0} E(m_0 \boldsymbol{m};\, \boldsymbol{H}, \boldsymbol{n})} \tag{3.12}$$

with the free energy ($E : \mathbb{R}^3 \times \mathbb{R}^3 \times \mathbb{S}^2 \to \mathbb{R}$*)*

$$E(\boldsymbol{\xi}; \boldsymbol{H}, \boldsymbol{n}) = -\mu_0 \left(\boldsymbol{H} + \frac{K_{\mathrm{anis}} V_{\mathrm{C}}}{m_0^2 \mu_0} \boldsymbol{n}\boldsymbol{n}^{\mathsf{T}} \boldsymbol{\xi} \right)^{\mathsf{T}} \boldsymbol{\xi}$$

and the partition function ($\mathcal{Z} : \mathbb{R}^3 \times \mathbb{S}^2 \to \mathbb{R}_+$*)*

$$\mathcal{Z}(\boldsymbol{H}, \boldsymbol{n}) = \int_{\mathbb{S}^2} \mathrm{e}^{\beta \boldsymbol{H}^{\mathsf{T}} \boldsymbol{m} + \alpha_{\mathrm{K}} (\boldsymbol{n}^{\mathsf{T}} \boldsymbol{m})^2} \, \mathrm{d}\boldsymbol{m}$$

with $\alpha_{\mathrm{K}} = \frac{\beta K_{\mathrm{anis}} V_{\mathrm{C}}}{m_0 \mu_0} = \frac{K_{\mathrm{anis}} V_{\mathrm{C}}}{k_{\mathrm{B}} T_{\mathrm{P}}}$.

Proof of Proposition 3.2. It should first be considered that the solution follows a Boltzmann distribution $f_0 : \mathbb{S}^2 \to \mathbb{R}_+$, assuming that $f_0(\boldsymbol{m}) \approx p_{\mathrm{N}}(\boldsymbol{m}, t_0; \boldsymbol{H}_0, \boldsymbol{n})$ denotes the distribution at time t_0 at which the distribution tends to equilibrium and $\boldsymbol{H}_0(\boldsymbol{x}) = \boldsymbol{H}(\boldsymbol{x}, t_0)$ is the temporally constant applied field.

The Boltzmann distribution for the equilibrium solution of the Néel model in (3.2) is as follows

$$f_0(\boldsymbol{m}) = \frac{1}{\mathcal{Z}} \mathrm{e}^{-\frac{\beta}{m_0 \mu_0} E(m_0 \boldsymbol{m};\, \boldsymbol{H}_0, \boldsymbol{n})}$$

with the free energy

$$E(\boldsymbol{\xi}; \boldsymbol{H}_0, \boldsymbol{n}) = -\mu_0 \left(\boldsymbol{H}_0 + \frac{K_{\mathrm{anis}} V_{\mathrm{C}}}{m_0^2 \mu_0} \boldsymbol{n}\boldsymbol{n}^{\mathsf{T}} \boldsymbol{\xi} \right)^{\mathsf{T}} \boldsymbol{\xi},$$

and then the gradient of the free energy is

$$\nabla_{\boldsymbol{m}} E(m_0 \boldsymbol{m}; \boldsymbol{H}_0, \boldsymbol{n}) = -\mu_0 m_0 \left(\boldsymbol{H}_0 + \frac{2 K_{\mathrm{anis}} V_{\mathrm{C}}}{m_0 \mu_0} \boldsymbol{n}\boldsymbol{n}^{\mathsf{T}} \boldsymbol{m} \right) = -\mu_0 m_0 \boldsymbol{H}_{\mathrm{eff}}(\boldsymbol{m}; \boldsymbol{H}_0, \boldsymbol{n}).$$

Therefore, the gradient of the Boltzmann distribution with respect to $\boldsymbol{m}$ is

$$\nabla_{\boldsymbol{m}} f_0(\boldsymbol{m}) = \beta f_0(\boldsymbol{m}) \boldsymbol{H}_{\mathrm{eff}}(\boldsymbol{m}; \boldsymbol{H}_0, \boldsymbol{n}) \tag{3.13}$$

and consequently the gradient with respect to the surface of the sphere $\mathbb{S}^2$ is

$$\begin{aligned}\nabla_{\mathbb{S}^2} f_0(\boldsymbol{m}) &= \beta f_0(\boldsymbol{m}) \left(\boldsymbol{H}_{\text{eff}}(\boldsymbol{m}; \boldsymbol{H}_0, \boldsymbol{n}) - \boldsymbol{m}\boldsymbol{m}^{\mathsf{T}} \boldsymbol{H}_{\text{eff}}(\boldsymbol{m}; \boldsymbol{H}_0, \boldsymbol{n})\right) \\ &= \beta f_0(\boldsymbol{m}) \big((\boldsymbol{m} \times \boldsymbol{H}_{\text{eff}}) \times \boldsymbol{m}\big).\end{aligned} \tag{3.14}$$

The PDF for the equilibrium state of the Néel rotation can be derived from the following differential equation:

$$0 = -\operatorname{div}_{\mathbb{S}^2} \left(\frac{\beta}{\alpha} \big(\boldsymbol{H}_{\text{eff}} \times \boldsymbol{m} + \alpha \left(\boldsymbol{m} \times \boldsymbol{H}_{\text{eff}}\right) \times \boldsymbol{m}\big) f_0(\boldsymbol{m}) - \nabla_{\mathbb{S}^2} f_0(\boldsymbol{m}) \right). \tag{3.15}$$

Since the divergence operator is linear and the form of the Fokker-Planck differential equation for the Néel roation is quite similar to the Brownian rotation case in equilibrium, most parts can be proved similarly to the Brownian case. It therefore remains to show that

$$\begin{aligned}\frac{\beta}{\alpha} \operatorname{div}_{\mathbb{S}^2} \Big(\big(\boldsymbol{H}_{\text{eff}}(\boldsymbol{m}) \times \boldsymbol{m}\big) f_0(\boldsymbol{m}) \Big) &= \frac{\beta}{\alpha} \operatorname{div}_{\mathbb{S}^2} \Big(\big(\boldsymbol{H}_{\text{eff}}(\boldsymbol{m}) f_0(\boldsymbol{m}) \times \boldsymbol{m}\big) \Big) \\ &\overset{(3.13)}{=} \alpha \operatorname{div}_{\mathbb{S}^2} \Big(\big(\nabla_{\boldsymbol{m}} f_0(\boldsymbol{m}) \times \boldsymbol{m}\big) \Big) = 0\end{aligned}$$

holds. The surface divergence operator for a vector field $\boldsymbol{F} : \mathbb{S}^2 \to \mathbb{R}^3$ is defined for the surface of the unit sphere $\mathbb{S}^2$ by [69]

$$\operatorname{div}_{\mathbb{S}^2}\big(\boldsymbol{F}(\boldsymbol{m})\big) = \operatorname{tr}\Big(\boldsymbol{J}_{\boldsymbol{F}}^{\mathbb{S}^2}(\boldsymbol{m})\Big) = \operatorname{tr}\big(\boldsymbol{J}_{\boldsymbol{F}}(\boldsymbol{m}) \boldsymbol{P}_{\mathbb{S}^2}(\boldsymbol{m})\big),$$

where $\boldsymbol{J}_{\boldsymbol{F}}^{\mathbb{S}^2} : \mathbb{S}^2 \to \mathbb{R}^{3\times 3}$ denotes the Jacobian matrix of $\boldsymbol{F}$ with respect to the surface $\mathbb{S}^2$ and $\boldsymbol{J}_{\boldsymbol{F}} : \mathbb{S}^2 \to \mathbb{R}^{3\times 3}$ denotes the classical Euclidean space Jacobian matrix of $\boldsymbol{F}$. They are associated by the projection matrix $\boldsymbol{P}_{\mathbb{S}^2} : \mathbb{S}^2 \to \mathbb{R}^{3\times 3}$. This projector can be identified for a vector $\boldsymbol{m} \in \mathbb{S}^2$ by

$$\boldsymbol{P}_{\mathbb{S}^2}(\boldsymbol{m}) = \boldsymbol{I}_3 - \boldsymbol{m}\boldsymbol{m}^{\mathsf{T}}.$$

Implicitly, the projector $\boldsymbol{P}_{\mathbb{S}^2}$ can be identified by taking the surface gradient definition from [48, 69] and convincing oneself that

$$\nabla_{\mathbb{S}^2} f_0(\boldsymbol{m}) = \big(\boldsymbol{P}_{\mathbb{S}^2}(\boldsymbol{m})\big)^{\mathsf{T}} \nabla_{\boldsymbol{m}} f_0(\boldsymbol{m}) = \big(\boldsymbol{I}_3 - \boldsymbol{m}\boldsymbol{m}^{\mathsf{T}}\big) \nabla_{\boldsymbol{m}} f_0(\boldsymbol{m})$$

corresponds to the surface gradient in (3.6). Therefore, it follows for the surface divergence on $\mathbb{S}^2$ that

$$\begin{aligned}\operatorname{div}_{\mathbb{S}^2}\big(\boldsymbol{F}(\boldsymbol{m})\big) &= \operatorname{tr}\big(\boldsymbol{J}_{\boldsymbol{F}}(\boldsymbol{m}) - \boldsymbol{J}_{\boldsymbol{F}}(\boldsymbol{m})\boldsymbol{m}\boldsymbol{m}^{\mathsf{T}}\big)\\ &= \operatorname{tr}\big(\boldsymbol{J}_{\boldsymbol{F}}(\boldsymbol{m})\big) - \operatorname{tr}\big(\boldsymbol{J}_{\boldsymbol{F}}(\boldsymbol{m})\boldsymbol{m}\boldsymbol{m}^{\mathsf{T}}\big)\\ &= \operatorname{div}_{\boldsymbol{m}}\big(\boldsymbol{F}(\boldsymbol{m})\big) - \boldsymbol{m}^{\mathsf{T}}\boldsymbol{J}_{\boldsymbol{F}}(\boldsymbol{m})\boldsymbol{m},\end{aligned}$$

since the trace operator is linear and the following applies to the trace operator $\operatorname{tr}(\boldsymbol{A}\boldsymbol{B}) = \operatorname{tr}(\boldsymbol{B}\boldsymbol{A})$ and $\operatorname{tr}(\xi) = \xi$ with $\boldsymbol{A} \in \mathbb{R}^{M\times N}$, $\boldsymbol{B} \in \mathbb{R}^{N\times M}$, and $\xi \in \mathbb{R}$. After clarifying the divergence operator with respect to $\mathbb{S}^2$, the original problem can be solved as follows

$$\operatorname{div}_{\mathbb{S}^2}(\nabla_{\boldsymbol{m}} f_0(\boldsymbol{m}) \times \boldsymbol{m}) = \underbrace{\operatorname{div}_{\boldsymbol{m}}(\nabla_{\boldsymbol{m}} f_0 \times \boldsymbol{m})}_{=0} + \underbrace{\boldsymbol{m}^{\mathsf{T}}\boldsymbol{J}_{\nabla_{\boldsymbol{m}} f_0 \times \boldsymbol{m}}\boldsymbol{m}}_{\ddagger}. \tag{3.16}$$

The term $\operatorname{div}_{\boldsymbol{m}}(\nabla_{\boldsymbol{m}} f_0(\boldsymbol{m}) \times \boldsymbol{m})$ is zero, since for $\boldsymbol{m}$ and $\nabla_{\boldsymbol{m}} f_0(\boldsymbol{m})$ two potential functions $\phi_{\boldsymbol{m}}(\boldsymbol{m}) = \frac{1}{2}\boldsymbol{m}^{\mathsf{T}}\boldsymbol{m}$ and $f_0(\boldsymbol{m})$ can be found. As a result, the Euclidean divergence of the cross product is zero, since for any two functions $g : \Omega \to \mathbb{R}$ and $h : \Omega \to \mathbb{R}$ with $\Omega \subseteq \mathbb{R}^3$ which have a well-defined continuous Jacobian matrix on Ω, it will always hold that

$$\operatorname{div}_{\boldsymbol{m}}(\nabla_{\boldsymbol{m}} g(\boldsymbol{m}) \times \nabla_{\boldsymbol{m}} h(\boldsymbol{m})) = 0.$$

To analyze the second term marked with ‡ in (3.16), the Jacobian matrix of a cross product must be solved. For this purpose, the cross product can be rewritten as a matrix-vector product. The cross product between two vectors $\boldsymbol{a} \in \mathbb{R}^3$ and $\boldsymbol{b} \in \mathbb{R}^3$ can also be expressed by a matrix-vector product

$$\boldsymbol{a} \times \boldsymbol{b} = [\boldsymbol{a}]^{\times}\boldsymbol{b} = -[\boldsymbol{b}]^{\times}\boldsymbol{a},$$

where the cross product matrix for a vector $\boldsymbol{\xi} \in \mathbb{R}^3$ is defined by

$$[\boldsymbol{\xi}]^{\times} = \begin{pmatrix} 0 & -\xi_3 & \xi_2 \\ \xi_3 & 0 & -\xi_1 \\ -\xi_2 & \xi_1 & 0 \end{pmatrix}.$$

With this definition, the Jacobian matrix of the cross product between to vectors $\boldsymbol{a}$ and $\boldsymbol{b}$ can be written using the product rule as

$$\boldsymbol{J}_{\boldsymbol{a}\times\boldsymbol{b}}(\boldsymbol{m}) = [\boldsymbol{a}]^{\times}\, \boldsymbol{J}_{\boldsymbol{b}}(\boldsymbol{m}) - [\boldsymbol{b}]^{\times}\, \boldsymbol{J}_{\boldsymbol{a}}(\boldsymbol{m}).$$

Using $\boldsymbol{a}(\boldsymbol{m}) = \nabla_{\boldsymbol{m}} f_0(\boldsymbol{m})$ and $\boldsymbol{b}(\boldsymbol{m}) = \boldsymbol{m}$, it is true that

$$\begin{aligned}\boldsymbol{m}^{\mathsf{T}} \boldsymbol{J}_{\nabla_{\boldsymbol{m}} f_0 \times \boldsymbol{m}}(\boldsymbol{m})\boldsymbol{m} &= \boldsymbol{m}^{\mathsf{T}} \left[\nabla_{\boldsymbol{m}} f_0\right]^{\times} \underbrace{\boldsymbol{J}_{\boldsymbol{m}}(\boldsymbol{m})}_{=\boldsymbol{I}_3} \boldsymbol{m} - \underbrace{\boldsymbol{m}^{\mathsf{T}} [\boldsymbol{m}]^{\times}}_{=-(\boldsymbol{m}\times\boldsymbol{m})^{\mathsf{T}}=\boldsymbol{0}^{\mathsf{T}}} \boldsymbol{J}_{\nabla_{\boldsymbol{m}} f_0}(\boldsymbol{m})\boldsymbol{m} \\ &= \boldsymbol{m}^{\mathsf{T}} \left[\nabla_{\boldsymbol{m}} f_0\right]^{\times} \boldsymbol{m} = \boldsymbol{m}^{\mathsf{T}} \left(\nabla_{\boldsymbol{m}} f_0 \times \boldsymbol{m}\right) = 0\end{aligned}$$

and finally it is shown that

$$\operatorname{div}_{\mathbb{S}^2}\big(\left(\boldsymbol{H}_{\text{eff}} \times \boldsymbol{m}\right) f_0(\boldsymbol{m})\big) = 0$$

holds.

This proves that the Boltzmann distribution

$$f_0(\boldsymbol{m}) = \frac{1}{\mathcal{Z}} \mathrm{e}^{\beta\left(\boldsymbol{H}_0^{\mathsf{T}}\boldsymbol{m} + \frac{K_{\text{anis}} V_{\text{C}}}{m_0 \mu_0}\left(\boldsymbol{n}^{\mathsf{T}}\boldsymbol{m}\right)^2\right)} = \frac{1}{\mathcal{Z}} \mathrm{e}^{\beta \boldsymbol{H}_0^{\mathsf{T}}\boldsymbol{m} + \alpha_{\text{K}}\left(\boldsymbol{n}^{\mathsf{T}}\boldsymbol{m}\right)^2} \tag{3.17}$$

is a solution for the differential equation in (3.15) with $\alpha_{\text{K}} = \frac{\beta K_{\text{anis}} V_{\text{C}}}{m_0 \mu_0} = \frac{K_{\text{anis}} V_{\text{C}}}{k_{\text{B}} T_{\text{P}}}$. □

It is not surprising that the mean magnetic moment of (3.17) is generally not equal to the Langevin function. The Langevin function is part of the solution if the anisotropy constant K_{anis} is negligibly small in contrast to the general field strength of $\boldsymbol{H}$. In practice, general configurations of $\boldsymbol{n} \in \mathbb{S}^2$ should be considered. The single integral representation presented in the next Proposition 3.3 can also be found in a slightly different form in [18] and was also used in [F7]. A mention for the special case in which the easy axis is aligned with $\boldsymbol{n} = \boldsymbol{e}_{\boldsymbol{H}}$ is outlined, e.g., in [83].

Proposition 3.3. *The mean magnetic moment* $\tilde{\boldsymbol{m}}_0 : \mathbb{R}^3 \times \mathbb{S}^2 \to \mathbb{R}^3$ *derived from* (3.12) *is*

$$\tilde{\boldsymbol{m}}_0(\boldsymbol{H}; \boldsymbol{n}) = \boldsymbol{R}_{\boldsymbol{n}} \cdot \tilde{\boldsymbol{m}}_{\boldsymbol{n}}(\boldsymbol{R}_{\boldsymbol{n}}^{\mathsf{T}} \boldsymbol{H}),$$

where $\boldsymbol{n} \in \mathbb{S}^2$ *is the easy axis of a nanoparticle,* $\boldsymbol{H} \in \mathbb{R}^3$ *denotes the applied magnetic field,* $\boldsymbol{R}_{\boldsymbol{n}} \in \mathbb{R}^{3\times 3}$ *denotes a rotation matrix, such that* $\boldsymbol{e}_3 = \boldsymbol{R}_{\boldsymbol{n}}^{\mathsf{T}} \boldsymbol{n}$ *with* $\boldsymbol{e}_3$ *being the third Euclidean unit vector, and* $\tilde{\boldsymbol{H}} = \boldsymbol{R}_{\boldsymbol{n}}^{\mathsf{T}} \boldsymbol{H}$*. Note that* $\overline{\boldsymbol{m}}(\boldsymbol{x}, t) = \tilde{\boldsymbol{m}}_0(\boldsymbol{H}(\boldsymbol{x}, t); \boldsymbol{n})$ *can be used with the applied magnetic field* $\boldsymbol{H} : \mathbb{R}^3 \times \mathbb{R} \to \mathbb{R}^3$ *in* (2.6)*.*

The mean magnetic moment $\tilde{\boldsymbol{m}}_{\boldsymbol{n}} : \mathbb{R}^3 \to \mathbb{R}^3$ *in the rotated coordinate system is* $\tilde{\boldsymbol{m}}_{\boldsymbol{n}}(\tilde{\boldsymbol{H}}) = m_0 \frac{\left(z_j(\tilde{\boldsymbol{H}})\right)_{j=1}^3}{\mathcal{Z}(\boldsymbol{R}_{\boldsymbol{n}}\tilde{\boldsymbol{H}}, \boldsymbol{n})}$*, where the partition function* $\mathcal{Z} : \mathbb{R}^3 \times \mathbb{S}^2 \to \mathbb{R}_+$ *can be written as*

$$\mathcal{Z}(\boldsymbol{R}_{\boldsymbol{n}}\tilde{\boldsymbol{H}}, \boldsymbol{n}) = 2\pi \int_{-1}^{1} I_0\Big(\beta |\tilde{\boldsymbol{H}}|_{12} \sqrt{1 - x^2}\Big)\, \mathrm{e}^{\beta \tilde{H}_3 x + \alpha_{\mathrm{K}} x^2}\, \mathrm{d}x, \tag{3.18}$$

the vector elements $z_j : \mathbb{R}^3 \to \mathbb{R}$ *with* $j \in \{1, 2, 3\}$ *are*

$$z_3(\tilde{\boldsymbol{H}}) = 2\pi \int_{-1}^{1} x I_0\Big(\beta |\tilde{\boldsymbol{H}}|_{12} \sqrt{1 - x^2}\Big)\, \mathrm{e}^{\beta \tilde{H}_3 x + \alpha_{\mathrm{K}} x^2}\, \mathrm{d}x, \tag{3.19}$$

and for $i \in \{1, 2\}$

$$z_i(\tilde{\boldsymbol{H}}) = 2\pi \frac{\tilde{H}_i}{|\tilde{\boldsymbol{H}}|_{12}} \int_{-1}^{1} I_1\Big(\beta |\tilde{\boldsymbol{H}}|_{12} \sqrt{1 - x^2}\Big) \sqrt{1 - x^2} \mathrm{e}^{\beta \tilde{H}_3 x + \alpha_{\mathrm{K}} x^2}\, \mathrm{d}x, \tag{3.20}$$

with $\alpha_{\mathrm{K}} = \frac{\beta K_{\mathrm{anis}} V_{\mathrm{C}}}{m_0 \mu_0} = \frac{K_{\mathrm{anis}} V_{\mathrm{C}}}{k_{\mathrm{B}} T_{\mathrm{P}}}$*,* $|\tilde{\boldsymbol{H}}|_{12} = \sqrt{\tilde{H}_1^2 + \tilde{H}_2^2}$*, and* $I_\nu : \mathbb{R} \to \mathbb{R}$ *being the modified Bessel function of the first kind with order* $\nu \in \mathbb{R}$*. In particular, if the easy axis is* $\boldsymbol{n} = \boldsymbol{e}_{\boldsymbol{H}} = \frac{\boldsymbol{H}}{\|\boldsymbol{H}\|}$*, then*

$$\begin{aligned}
\tilde{\boldsymbol{m}}_0(\boldsymbol{H}; \boldsymbol{e}_{\boldsymbol{H}}) &= m_0 \left[\frac{1}{\sqrt{\pi \alpha_{\mathrm{K}}}} \frac{\mathrm{e}^{\frac{(2\alpha_{\mathrm{K}} + \beta\|\boldsymbol{H}\|)^2}{4\alpha_{\mathrm{K}}}} - \mathrm{e}^{\frac{(2\alpha_{\mathrm{K}} - \beta\|\boldsymbol{H}\|)^2}{4\alpha_{\mathrm{K}}}}}{\operatorname{erfi}\Big(\frac{2\alpha_{\mathrm{K}} + \beta\|\boldsymbol{H}\|}{2\sqrt{\alpha_{\mathrm{K}}}}\Big) + \operatorname{erfi}\Big(\frac{2\alpha_{\mathrm{K}} - \beta\|\boldsymbol{H}\|}{2\sqrt{\alpha_{\mathrm{K}}}}\Big)} - \frac{\beta\|\boldsymbol{H}\|}{2\alpha_{\mathrm{K}}} \right] \boldsymbol{e}_{\boldsymbol{H}} \\
&= m_0 \left[\frac{1}{2\sqrt{\alpha_{\mathrm{K}}}} \frac{1 - \mathrm{e}^{-2\beta\|\boldsymbol{H}\|}}{D_+\Big(\frac{2\alpha_{\mathrm{K}} + \beta\|\boldsymbol{H}\|}{2\sqrt{\alpha_{\mathrm{K}}}}\Big) + \mathrm{e}^{-2\beta\|\boldsymbol{H}\|} D_+\Big(\frac{2\alpha_{\mathrm{K}} - \beta\|\boldsymbol{H}\|}{2\sqrt{\alpha_{\mathrm{K}}}}\Big)} - \frac{\beta\|\boldsymbol{H}\|}{2\alpha_{\mathrm{K}}} \right] \boldsymbol{e}_{\boldsymbol{H}}
\end{aligned}$$

applies, where ($\operatorname{erfi} : \mathbb{R} \to \mathbb{R}$*)*

$$\operatorname{erfi}(\xi) = \frac{2}{\sqrt{\pi}} \int_0^{\xi} \mathrm{e}^{t^2}\, \mathrm{d}t = \frac{2}{\sqrt{\pi}} \mathrm{e}^{\xi^2} D_+(\xi)$$

and ($D_+ : \mathbb{R} \to \mathbb{R}$)

$$D_+(\xi) = \mathrm{e}^{-\xi^2} \int_0^\xi \mathrm{e}^{t^2}\,\mathrm{d}t$$

denote the imaginary error function and Dawson function, respectively.

Proof of Proposition 3.3. For the sake of simplicity, it is initially expected that the easy axis $\boldsymbol{n}$ of the particle coincides with the direction of the field strength $\boldsymbol{H}_0$, i.e., $\boldsymbol{n} = \boldsymbol{e}_{\boldsymbol{H}_0}$ with $\boldsymbol{e}_{\boldsymbol{H}_0} = \frac{\boldsymbol{H}_0}{\|\boldsymbol{H}_0\|}$. The partition function for $\boldsymbol{n} = \boldsymbol{e}_{\boldsymbol{H}_0}$ reads

$$\mathcal{Z} = \int_{\mathbb{S}^2} \mathrm{e}^{\beta \boldsymbol{H}_0^\mathsf{T}\boldsymbol{m} + \alpha_\mathrm{K}\left(\boldsymbol{n}^\mathsf{T}\boldsymbol{m}\right)^2}\,\mathrm{d}\boldsymbol{m} = \int_{\mathbb{S}^2} \mathrm{e}^{\beta \boldsymbol{H}_0^\mathsf{T}\boldsymbol{m} + \alpha_\mathrm{K}\left(\boldsymbol{e}_{\boldsymbol{H}_0}^\mathsf{T}\boldsymbol{m}\right)^2}\,\mathrm{d}\boldsymbol{m}. \tag{3.21}$$

Now $\boldsymbol{H}_0$ is rotated in such a way that $H_0\boldsymbol{e}_3 = \boldsymbol{R}^\mathsf{T}\boldsymbol{H}_0$ with $H_0 = \|\boldsymbol{H}_0\|$ and it follows that

$$\begin{aligned}
\mathcal{Z} &= \int_{\mathbb{S}^2} \mathrm{e}^{\beta \boldsymbol{H}_0^\mathsf{T}\boldsymbol{R}\boldsymbol{R}^\mathsf{T}\boldsymbol{m} + \alpha_\mathrm{K}\left(\boldsymbol{e}_{\boldsymbol{H}_0}^\mathsf{T}\boldsymbol{R}\boldsymbol{R}^\mathsf{T}\boldsymbol{m}\right)^2}\,\mathrm{d}\boldsymbol{m} \\
&= \int_{\mathbb{S}^2} \mathrm{e}^{\beta H_0 \boldsymbol{e}_3^\mathsf{T}\boldsymbol{R}^\mathsf{T}\boldsymbol{m} + \alpha_\mathrm{K}\left(\boldsymbol{e}_3^\mathsf{T}\boldsymbol{R}^\mathsf{T}\boldsymbol{m}\right)^2}\,\mathrm{d}\boldsymbol{m} = \int_{\mathbb{S}^2} \mathrm{e}^{\beta H_0 \boldsymbol{e}_3^\mathsf{T}\boldsymbol{r} + \alpha_\mathrm{K}\left(\boldsymbol{e}_3^\mathsf{T}\boldsymbol{r}\right)^2}\,\mathrm{d}\boldsymbol{r} \\
&= \int_0^\pi \int_0^{2\pi} \mathrm{e}^{\beta H_0 \cos(\theta) + \alpha_\mathrm{K}\cos^2(\theta)} \sin(\theta)\,\mathrm{d}\varphi\,\mathrm{d}\theta \\
&= 2\pi \int_0^\pi \mathrm{e}^{\beta H_0 \cos(\theta) + \alpha_\mathrm{K}\cos^2(\theta)} \sin(\theta)\,\mathrm{d}\theta = 2\pi \int_{-1}^1 \mathrm{e}^{\beta H_0 x + \alpha_\mathrm{K} x^2}\,\mathrm{d}x.
\end{aligned} \tag{3.22}$$

The resulting function cannot be expressed in a closed form by elementary functions, but can be written in the form of the imaginary error function or the Dawson function [83]. By completing the square and with $\xi = \beta H_0$, the exponent in (3.22) can be represented by

$$\mathcal{Z} = 2\pi \int_{-1}^1 \mathrm{e}^{\xi x + \alpha_\mathrm{K} x^2}\,\mathrm{d}x = 2\pi \mathrm{e}^{-\frac{\xi^2}{4\alpha_\mathrm{K}}} \int_{-1}^1 \mathrm{e}^{\frac{(2\alpha_\mathrm{K}x + \xi)^2}{4\alpha_\mathrm{K}}}\,\mathrm{d}x.$$

Using the substitutions $t = \frac{2\alpha_\mathrm{K}x + \xi}{2\sqrt{\alpha_\mathrm{K}}}$ and $t' = \frac{\mathrm{d}t}{\mathrm{d}x} = \sqrt{\alpha_\mathrm{K}}$,

$$\begin{aligned}
\mathcal{Z} &= 2\pi \mathrm{e}^{-\frac{\xi^2}{4\alpha_\mathrm{K}}} \int_{-1}^1 \mathrm{e}^{\frac{(2\alpha_\mathrm{K}x + \xi)^2}{4\alpha_\mathrm{K}}}\,\mathrm{d}x = \frac{\pi^{\frac{3}{2}}}{\sqrt{\alpha_\mathrm{K}}} \mathrm{e}^{-\frac{\xi^2}{4\alpha_\mathrm{K}}} \left[\frac{2}{\sqrt{\pi}} \int_{\frac{\xi - 2\alpha_\mathrm{K}}{2\sqrt{\alpha_\mathrm{K}}}}^{\frac{2\alpha_\mathrm{K} + \xi}{2\sqrt{\alpha_\mathrm{K}}}} \mathrm{e}^{t^2}\,\mathrm{d}t\right] \\
&= \frac{\pi^{\frac{3}{2}}}{\sqrt{\alpha_\mathrm{K}}} \mathrm{e}^{-\frac{\xi^2}{4\alpha_\mathrm{K}}} \left[\frac{2}{\sqrt{\pi}} \left(\int_0^{\frac{2\alpha_\mathrm{K} + \xi}{2\sqrt{\alpha_\mathrm{K}}}} \mathrm{e}^{t^2}\,\mathrm{d}t + \int_0^{\frac{2\alpha_\mathrm{K} - \xi}{2\sqrt{\alpha_\mathrm{K}}}} \mathrm{e}^{t^2}\,\mathrm{d}t\right)\right]
\end{aligned}$$

is obtained. The partition function can therefore be written as

$$\tilde{\mathcal{Z}}(H_0) = \mathcal{Z}(\boldsymbol{H}, \boldsymbol{e}_{\boldsymbol{H}_0}) = \frac{\pi^{\frac{3}{2}} \mathrm{e}^{-\frac{(\beta H_0)^2}{4\alpha_\mathrm{K}}}}{\sqrt{\alpha_\mathrm{K}}} \left[\operatorname{erfi}\left(\frac{2\alpha_\mathrm{K} + \beta H_0}{2\sqrt{\alpha_\mathrm{K}}} \right) + \operatorname{erfi}\left(\frac{2\alpha_\mathrm{K} - \beta H_0}{2\sqrt{\alpha_\mathrm{K}}} \right) \right] \tag{3.23}$$

or the Dawson function can be used, which results in

$$\tilde{\mathcal{Z}}(H_0) = \frac{2\pi \mathrm{e}^{\alpha_\mathrm{K} + \beta H_0}}{\sqrt{\alpha_\mathrm{K}}} \left[D_+\left(\frac{2\alpha_\mathrm{K} + \beta H_0}{2\sqrt{\alpha_\mathrm{K}}} \right) + \mathrm{e}^{-2\beta H_0} D_+\left(\frac{2\alpha_\mathrm{K} - \beta H_0}{2\sqrt{\alpha_\mathrm{K}}} \right) \right]. \tag{3.24}$$

The mean magnetic moment, which is thus given by

$$\tilde{\boldsymbol{m}}_0(\boldsymbol{H}_0; \boldsymbol{e}_{\boldsymbol{H}_0}) = 2\pi \boldsymbol{e}_{\boldsymbol{H}_0} \frac{m_0}{\tilde{\mathcal{Z}}(H_0)} \int_{-1}^{1} x \mathrm{e}^{\beta H_0 x + \alpha_\mathrm{K} x^2} \, \mathrm{d}x,$$

can be inferred in a similar way. First, $\xi = \beta H_0$ is used and then the integral is rewritten, thus obtaining

$$\begin{aligned} \tilde{\boldsymbol{m}}_0(\boldsymbol{H}_0; \boldsymbol{e}_{\boldsymbol{H}_0}) &= 2\pi \boldsymbol{e}_{\boldsymbol{H}_0} \frac{m_0}{\tilde{\mathcal{Z}}(H_0)} \int_{-1}^{1} x \mathrm{e}^{\xi x + \alpha_\mathrm{K} x^2} \, \mathrm{d}x \\ &= 2\pi \boldsymbol{e}_{\boldsymbol{H}_0} \frac{m_0}{\tilde{\mathcal{Z}}(H_0)} \int_{-1}^{1} \frac{\partial}{\partial \xi} \left[\mathrm{e}^{\xi x + \alpha_\mathrm{K} x^2} \right] \, \mathrm{d}x. \end{aligned} \tag{3.25}$$

Because $\mathrm{e}^{\xi x + \alpha_\mathrm{K} x^2}$ is continuous for all $\xi \in \mathbb{R}$, (3.25) can be written as

$$\begin{aligned} \tilde{\boldsymbol{m}}_0(\boldsymbol{H}_0; \boldsymbol{e}_{\boldsymbol{H}_0}) &= \boldsymbol{e}_{\boldsymbol{H}_0} \frac{m_0}{\tilde{\mathcal{Z}}(H_0)} \frac{\partial}{\partial \xi} \left[2\pi \int_{-1}^{1} \mathrm{e}^{\xi x + \alpha_\mathrm{K} x^2} \, \mathrm{d}x \right] = \boldsymbol{e}_{\boldsymbol{H}_0} \frac{m_0}{\tilde{\mathcal{Z}}(H_0)} \frac{\partial}{\partial \xi} \left[\tilde{\mathcal{Z}}\left(\frac{\xi}{\beta} \right) \right] \\ &= \frac{m_0}{\beta} \boldsymbol{e}_{\boldsymbol{H}_0} \frac{\tilde{\mathcal{Z}}'\left(\frac{\xi}{\beta} \right)}{\tilde{\mathcal{Z}}(H_0)}. \end{aligned}$$

Using the back substitution of $\xi = \beta H_0$ and the fact that for a differentiable function $f(z) > 0$ it is generally valid that $\frac{\mathrm{d}}{\mathrm{d}z} \ln(f(z)) = \frac{f'(z)}{f(z)}$, it follows that the mean magnetic moment can be calculated as the derivative of the logarithmic partition function as

$$\tilde{\boldsymbol{m}}_0(\boldsymbol{H}_0; \boldsymbol{e}_{\boldsymbol{H}_0}) = \frac{m_0}{\beta} \boldsymbol{e}_{\boldsymbol{H}_0} \frac{\mathrm{d}}{\mathrm{d}H_0} \ln\left(\tilde{\mathcal{Z}}(H_0) \right).$$

The derivative of $\tilde{\mathcal{Z}}\left(\frac{\xi}{\beta}\right)$ with respect to ξ can be derived as follows

$$\begin{aligned}
\mathrm{e}^{\frac{\xi^2}{4\alpha_\mathrm{K}}}\tilde{\mathcal{Z}}\left(\frac{\xi}{\beta}\right) &= \frac{\pi^{\frac{3}{2}}}{\sqrt{\alpha_\mathrm{K}}}\left(\operatorname{erfi}\left(\frac{2\alpha_\mathrm{K}+\xi}{2\sqrt{\alpha_\mathrm{K}}}\right)+\operatorname{erfi}\left(\frac{2\alpha_\mathrm{K}-\xi}{2\sqrt{\alpha_\mathrm{K}}}\right)\right), && \left|\cdot\mathrm{e}^{\frac{\xi^2}{4\alpha_\mathrm{K}}}\right.\\
\frac{\xi\mathrm{e}^{\frac{\xi^2}{4\alpha_\mathrm{K}}}}{2\alpha_\mathrm{K}}\tilde{\mathcal{Z}}\left(\frac{\xi}{\beta}\right)+\frac{\mathrm{e}^{\frac{\xi^2}{4\alpha_\mathrm{K}}}}{\beta}\tilde{\mathcal{Z}}'\left(\frac{\xi}{\beta}\right) &= \frac{\pi^{\frac{3}{2}}}{\sqrt{\alpha_\mathrm{K}}}\left(\mathrm{e}^{\frac{(2\alpha_\mathrm{K}+\xi)^2}{4\alpha_\mathrm{K}}}-\mathrm{e}^{\frac{(2\alpha_\mathrm{K}-\xi)^2}{4\alpha_\mathrm{K}}}\right)\frac{2}{2\sqrt{\alpha_\mathrm{K}}\sqrt{\pi}}, && \left|\frac{\mathrm{d}}{\mathrm{d}\xi}\cdot\right.\\
\frac{\mathrm{e}^{\frac{\xi^2}{4\alpha_\mathrm{K}}}}{\beta}\tilde{\mathcal{Z}}'\left(\frac{\xi}{\beta}\right) &= \frac{\pi}{\alpha_\mathrm{K}}\left(\mathrm{e}^{\frac{(2\alpha_\mathrm{K}+\xi)^2}{4\alpha_\mathrm{K}}}-\mathrm{e}^{\frac{(2\alpha_\mathrm{K}-\xi)^2}{4\alpha_\mathrm{K}}}\right)-\frac{\xi}{2\alpha_\mathrm{K}}\mathrm{e}^{\frac{\xi^2}{4\alpha_\mathrm{K}}}\tilde{\mathcal{Z}}\left(\frac{\xi}{\beta}\right),\\
\tilde{\mathcal{Z}}'\left(\frac{\xi}{\beta}\right) &= \frac{\beta\mathrm{e}^{-\frac{\xi^2}{4\alpha_\mathrm{K}}}\pi}{\alpha_\mathrm{K}}\left(\mathrm{e}^{\frac{(2\alpha_\mathrm{K}+\xi)^2}{4\alpha_\mathrm{K}}}-\mathrm{e}^{\frac{(2\alpha_\mathrm{K}-\xi)^2}{4\alpha_\mathrm{K}}}\right)-\frac{\beta\xi}{2\alpha_\mathrm{K}}\tilde{\mathcal{Z}}\left(\frac{\xi}{\beta}\right).
\end{aligned}$$

Consequently, the derivative with respect to H_0 is

$$\begin{aligned}
\tilde{\mathcal{Z}}'(H_0) &= \frac{\beta\mathrm{e}^{-\frac{(\beta H_0)^2}{4\alpha_\mathrm{K}}}\pi}{\alpha_\mathrm{K}}\left(\mathrm{e}^{\frac{(2\alpha_\mathrm{K}+\beta H_0)^2}{4\alpha_\mathrm{K}}}-\mathrm{e}^{\frac{(2\alpha_\mathrm{K}-\beta H_0)^2}{4\alpha_\mathrm{K}}}\right)-\frac{\beta^2 H_0}{2\alpha_\mathrm{K}}\tilde{\mathcal{Z}}(H_0)\\
&= \frac{\beta\pi\mathrm{e}^{\alpha_\mathrm{K}+\beta H_0}}{\alpha_\mathrm{K}}\left(1-\mathrm{e}^{-2\beta H_0}\right)-\frac{\beta^2 H_0}{2\alpha_\mathrm{K}}\tilde{\mathcal{Z}}(H_0).
\end{aligned}$$

The mean magnetic moment, calculated from the derivative of the logarithmic partition function according to H_0, finally leads to

$$\begin{aligned}
\tilde{\boldsymbol{m}}_0(\boldsymbol{H}_0;\boldsymbol{e}_{\boldsymbol{H}_0}) &= \frac{m_0}{\beta}\boldsymbol{e}_{\boldsymbol{H}_0}\frac{\mathrm{d}}{\mathrm{d}H_0}\ln\left(\tilde{\mathcal{Z}}(H_0)\right)\\
&= m_0\left[\frac{1}{\sqrt{\pi\alpha_\mathrm{K}}}\frac{\mathrm{e}^{\frac{(2\alpha_\mathrm{K}+\beta H_0)^2}{4\alpha_\mathrm{K}}}-\mathrm{e}^{\frac{(2\alpha_\mathrm{K}-\beta H_0)^2}{4\alpha_\mathrm{K}}}}{\operatorname{erfi}\left(\frac{2\alpha_\mathrm{K}+\beta H_0}{2\sqrt{\alpha_\mathrm{K}}}\right)+\operatorname{erfi}\left(\frac{2\alpha_\mathrm{K}-\beta H_0}{2\sqrt{\alpha_\mathrm{K}}}\right)}-\frac{\beta H_0}{2\alpha_\mathrm{K}}\right]\boldsymbol{e}_{\boldsymbol{H}_0}\\
&= m_0\left[\frac{1}{2\sqrt{\alpha_\mathrm{K}}}\frac{1-\mathrm{e}^{-2\beta H_0}}{D_+\left(\frac{2\alpha_\mathrm{K}+\beta H_0}{2\sqrt{\alpha_\mathrm{K}}}\right)+\mathrm{e}^{-2\beta H_0}D_+\left(\frac{2\alpha_\mathrm{K}-\beta H_0}{2\sqrt{\alpha_\mathrm{K}}}\right)}-\frac{\beta H_0}{2\alpha_\mathrm{K}}\right]\boldsymbol{e}_{\boldsymbol{H}_0}.
\end{aligned}$$

After the special case in which the easy axis $\boldsymbol{n}=\boldsymbol{e}_{\boldsymbol{H}_0}$ is aligned with the magnetic field $\boldsymbol{H}_0$, an arbitrary solution can also be found for the general Boltzmann distribution with $\boldsymbol{n}\in\mathbb{S}^2$. Unfortunately, the solution still has to be numerically integrated, but some simplifications are possible. A proof of a related expression can be found in [18].

Therefore, with recourse to the PDF (3.17), it seems helpful to apply a rotation matrix $\boldsymbol{R_n} \in \mathbb{R}^{3\times3}$ such that $\boldsymbol{e}_3 = \boldsymbol{R_n^\mathsf{T}}\boldsymbol{n}$. After these steps, the partition function is as follows

$$\begin{aligned}\mathcal{Z} &= \int_{\mathbb{S}^2} \mathrm{e}^{\beta \boldsymbol{H}_0^\mathsf{T}\boldsymbol{m}+\alpha_\mathrm{K}\left(\boldsymbol{n}^\mathsf{T}\boldsymbol{m}\right)^2}\,\mathrm{d}\boldsymbol{m} = \int_{\mathbb{S}^2} \mathrm{e}^{\beta \boldsymbol{H}_0^\mathsf{T}\boldsymbol{m}+\alpha_\mathrm{K}\left(\boldsymbol{n}^\mathsf{T}\boldsymbol{R_n}\boldsymbol{R_n^\mathsf{T}}\boldsymbol{m}\right)^2}\,\mathrm{d}\boldsymbol{m} \\ &= \int_{\mathbb{S}^2} \mathrm{e}^{\beta \boldsymbol{H}_0^\mathsf{T}\boldsymbol{m}+\alpha_\mathrm{K}\left(\boldsymbol{e}_3^\mathsf{T}\boldsymbol{R_n^\mathsf{T}}\boldsymbol{m}\right)^2}\,\mathrm{d}\boldsymbol{m}.\end{aligned} \tag{3.26}$$

At first, this does not seem particularly helpful. However, introducing the rotated magnetic field $\tilde{\boldsymbol{H}} = \boldsymbol{R_n^\mathsf{T}}\boldsymbol{H}_0$ and changing the integration variable $\tilde{\boldsymbol{r}} = \boldsymbol{R_n^\mathsf{T}}\boldsymbol{m}$, the integration in spherical coordinates $\tilde{\boldsymbol{r}}$ yields:

$$\begin{aligned}\mathcal{Z} &= \int_{\mathbb{S}^2} \mathrm{e}^{\beta \tilde{\boldsymbol{H}}^\mathsf{T}\tilde{\boldsymbol{r}}+\alpha_\mathrm{K}\left(\boldsymbol{e}_3^\mathsf{T}\tilde{\boldsymbol{r}}\right)^2}\,\mathrm{d}\tilde{\boldsymbol{r}} = \int_{\mathbb{S}^2} \mathrm{e}^{\beta \tilde{H}_1\tilde{r}_1+\beta \tilde{H}_2\tilde{r}_2+\beta \tilde{H}_3\tilde{r}_3+\alpha_\mathrm{K}\tilde{r}_3^2}\,\mathrm{d}\tilde{\boldsymbol{r}} \\ &= \int_0^\pi \int_0^{2\pi} \mathrm{e}^{\beta \tilde{H}_1\cos(\varphi)\sin(\theta)+\beta \tilde{H}_2\sin(\varphi)\sin(\theta)+\beta \tilde{H}_3\cos(\theta)+\alpha_\mathrm{K}\cos^2(\theta)}\sin(\theta)\,\mathrm{d}\varphi\,\mathrm{d}\theta.\end{aligned} \tag{3.27}$$

It should be noted that an equivalent form of (3.27) can also be found in [83]. With the substitution $\cos(\theta) = x$, (3.27) becomes

$$\begin{aligned}\mathcal{Z} &= \int_{-1}^1 \int_0^{2\pi} \mathrm{e}^{\beta \tilde{H}_1\cos(\varphi)\sqrt{1-x^2}+\beta \tilde{H}_2\sin(\varphi)\sqrt{1-x^2}+\beta \tilde{H}_3 x+\alpha_\mathrm{K}x^2}\,\mathrm{d}\varphi\,\mathrm{d}x \\ &= \int_{-1}^1 \int_0^{2\pi} \mathrm{e}^{\beta \tilde{H}_1\cos(\varphi)\sqrt{1-x^2}+\beta \tilde{H}_2\sin(\varphi)\sqrt{1-x^2}}\,\mathrm{d}\varphi\,\mathrm{e}^{\beta \tilde{H}_3 x+\alpha_\mathrm{K}x^2}\,\mathrm{d}x.\end{aligned} \tag{3.28}$$

When evaluating the inner integral, a relationship to the modified Bessel functions is revealed

$$\begin{aligned}&\int_0^{2\pi} \mathrm{e}^{\beta \tilde{H}_1\cos(\varphi)\sqrt{1-x^2}+\beta \tilde{H}_2\sin(\varphi)\sqrt{1-x^2}}\,\mathrm{d}\varphi \\ &\qquad = \int_0^{2\pi} \mathrm{e}^{\beta\sqrt{\tilde{H}_1^2+\tilde{H}_2^2}\cos\left(\varphi+\phi\left(\tilde{H}_1,\tilde{H}_2\right)\right)\sqrt{1-x^2}}\,\mathrm{d}\varphi,\end{aligned} \tag{3.29}$$

where each linear combination of a sine and cosine wave can be written as

$$a\cos(\xi) + b\sin(\xi) = \sqrt{a^2+b^2}\cos(\xi+\phi(a,b))$$

with $a, b \in \mathbb{R}$ and the phase shift $\phi : \mathbb{R}\times\mathbb{R} \to [0, 2\pi)$. However, since the integral over a full period length of a periodic function is invariant under any phase shift ϕ,

$$\int_0^{2\pi} \mathrm{e}^{\beta\sqrt{\tilde{H}_1^2+\tilde{H}_2^2}\sqrt{1-x^2}\cos(\varphi)}\,\mathrm{d}\varphi = 2\pi I_0\left(\beta\sqrt{\left(\tilde{H}_1^2+\tilde{H}_2^2\right)(1-x^2)}\right) \tag{3.30}$$

is obtained for (3.29), where the definition of modified Bessel functions of the first kind and order zero [1, §9.6.16]

$$I_0(\xi) = \frac{1}{\pi}\int_0^{\pi} \mathrm{e}^{\xi\cos\theta}\,\mathrm{d}\theta = \frac{1}{2\pi}\int_0^{2\pi} \mathrm{e}^{\xi\cos\theta}\,\mathrm{d}\theta$$

is used and it should be noted that the integration term is symmetric with respect to θ. Further information on Bessel functions can be found in Chapter 5. The combination of (3.29) and (3.30) with $\xi_1 = \beta\tilde{H}_1$ and $\xi_2 = \beta\tilde{H}_2$ also shows that

$$I_0\left(\sqrt{\left(\xi_1^2+\xi_2^2\right)\left(1-x^2\right)}\right) = \frac{1}{2\pi}\int_0^{2\pi} \mathrm{e}^{\xi_1\cos(\varphi)\sqrt{1-x^2}+\xi_2\sin(\varphi)\sqrt{1-x^2}}\,\mathrm{d}\varphi. \tag{3.31}$$

If (3.30) is inserted into (3.28), the partition function follows:

$$\mathcal{Z}(\boldsymbol{R_n}\tilde{\boldsymbol{H}}, \boldsymbol{n}) = 2\pi\int_{-1}^{1} I_0\left(\beta\sqrt{\left(\tilde{H}_1^2+\tilde{H}_2^2\right)\left(1-x^2\right)}\right)\mathrm{e}^{\beta\tilde{H}_3 x+\alpha_\mathrm{K}x^2}\,\mathrm{d}x. \tag{3.32}$$

This is the result from (3.18) in Proposition 3.3, which shows the partition function $\mathcal{Z}$. A similar result was also found in [18]. To obtain the third component of the mean magnetic moment in the rotated system, the vector element must be integrated, which yields

$$z_3(\tilde{\boldsymbol{H}}) = \int_0^{\pi}\int_0^{2\pi} \cos(\varphi)\mathrm{e}^{\beta\tilde{H}_1\cos(\theta)\sin(\theta)+\beta\tilde{H}_2\sin(\varphi)\sin(\theta)+\beta\tilde{H}_3\cos(\theta)+\alpha_\mathrm{K}\cos^2(\theta)} \times \sin(\theta)\,\mathrm{d}\varphi\,\mathrm{d}\theta. \tag{3.33}$$

If the derivative is calculated equivalently, as for (3.32), which is mathematically derived from (3.27), the simplified version reads

$$z_3(\tilde{\boldsymbol{H}}) = 2\pi\int_{-1}^{1} xI_0\left(\beta\sqrt{\left(\tilde{H}_1^2+\tilde{H}_2^2\right)\left(1-x^2\right)}\right)\mathrm{e}^{\beta\tilde{H}_3 x+\alpha_\mathrm{K}x^2}\,\mathrm{d}x. \tag{3.34}$$

The solutions for the other two vector components $z_1(\tilde{\boldsymbol{H}})$ and $z_2(\tilde{\boldsymbol{H}})$ are

$$z_i(\tilde{\boldsymbol{H}}) = 2\pi\int_{-1}^{1} \frac{\tilde{H}_i}{\sqrt{\tilde{H}_1^2+\tilde{H}_2^2}} I_1\left(\beta\sqrt{\left(\tilde{H}_1^2+\tilde{H}_2^2\right)\left(1-x^2\right)}\right)\sqrt{1-x^2}\mathrm{e}^{\beta\tilde{H}_3 x+\alpha_\mathrm{K}x^2}\,\mathrm{d}x \tag{3.35}$$

with $i \in \{1, 2\}$, where $I_1 : \mathbb{R} \to \mathbb{R}$ denotes the the modified Bessel function of the first kind with order one [1, §9.6.19]. These results require a somewhat more careful evaluation of the integrals using spherical coordinates:

$$z_1(\tilde{\boldsymbol{H}}) = \int_0^{\pi} \int_0^{2\pi} \cos(\varphi) \sin(\theta) \mathrm{e}^{\beta \tilde{H}_1 \cos(\varphi) \sin(\theta) + \beta \tilde{H}_2 \sin(\varphi) \sin(\theta) + \beta \tilde{H}_3 \cos(\theta) + \alpha_{\mathrm{K}} \cos^2(\theta)} \times \sin(\theta) \, \mathrm{d}\varphi \, \mathrm{d}\theta$$

and

$$z_2(\tilde{\boldsymbol{H}}) = \int_0^{\pi} \int_0^{2\pi} \sin(\varphi) \sin(\theta) \mathrm{e}^{\beta \tilde{H}_1 \cos(\varphi) \sin(\theta) + \beta \tilde{H}_2 \sin(\varphi) \sin(\theta) + \beta \tilde{H}_3 \cos(\theta) + \alpha_{\mathrm{K}} \cos^2(\theta)} \times \sin(\theta) \, \mathrm{d}\varphi \, \mathrm{d}\theta.$$

Without loss of generality, $i = 1$ is considered in the following. Using the substitution $\cos(\theta) = x$ one obtains

$$\begin{aligned} z_1(\tilde{\boldsymbol{H}}) &= \int_{-1}^{1} \int_0^{2\pi} \cos(\varphi) \mathrm{e}^{\beta \tilde{H}_1 \cos(\varphi) \sqrt{1-x^2} + \beta \tilde{H}_2 \sin(\varphi) \sqrt{1-x^2} + \beta \tilde{H}_3 x + \alpha_{\mathrm{K}} x^2} \sqrt{1-x^2} \, \mathrm{d}\varphi \, \mathrm{d}x \\ &= \int_{-1}^{1} \int_0^{2\pi} \cos(\varphi) \sqrt{1-x^2} \mathrm{e}^{\beta \tilde{H}_1 \cos(\varphi) \sqrt{1-x^2} + \beta \tilde{H}_2 \sin(\varphi) \sqrt{1-x^2}} \, \mathrm{d}\varphi \, \mathrm{e}^{\beta \tilde{H}_3 x + \alpha_{\mathrm{K}} x^2} \, \mathrm{d}x. \end{aligned} \tag{3.36}$$

An evaluation of the inner integral with $\xi_1 = \beta \tilde{H}_1$ and $\xi_2 = \beta \tilde{H}_2$ reveals

$$\begin{aligned} &\int_0^{2\pi} \cos(\varphi) \sqrt{1-x^2} \mathrm{e}^{\xi_1 \cos(\varphi) \sqrt{1-x^2} + \xi_2 \sin(\varphi) \sqrt{1-x^2}} \, \mathrm{d}\varphi \\ &\qquad = \int_0^{2\pi} \frac{\partial}{\partial \xi_1} \left[\mathrm{e}^{\xi_1 \cos(\varphi) \sqrt{1-x^2} + \xi_2 \sin(\varphi) \sqrt{1-x^2}} \right] \mathrm{d}\varphi \\ &\qquad \overset{\dagger}{=} \frac{\partial}{\partial \xi_1} \left[\int_0^{2\pi} \mathrm{e}^{\xi_1 \cos(\varphi) \sqrt{1-x^2} + \xi_2 \sin(\varphi) \sqrt{1-x^2}} \, \mathrm{d}\varphi \right] \\ &\qquad \overset{(3.31)}{=} 2\pi \frac{\partial}{\partial \xi_1} \left[I_0 \left(\sqrt{(\xi_1^2 + \xi_2^2)(1-x^2)} \right) \right] \\ &\qquad = 2\pi I_1 \left(\sqrt{(\xi_1^2 + \xi_2^2)(1-x^2)} \right) \sqrt{1-x^2} \frac{\xi_1}{\sqrt{\xi_1^2 + \xi_2^2}}, \end{aligned} \tag{3.37}$$

where † is valid because the modified Bessel function of the first kind and order zero is continuous in ξ_1. Inserting (3.37) into (3.36) leads to the desired equation (3.20). The solution for $z_2(\tilde{\boldsymbol{H}})$ follows in the same way. The only difference is to differentiate

in (3.37) † with respect to ξ_2 instead of ξ_1. The mean magnetic moment in the rotated coordinate system is finally

$$\tilde{\boldsymbol{m}}_{\boldsymbol{n}}(\tilde{\boldsymbol{H}}_0; \boldsymbol{n}) = m_0 \frac{\boldsymbol{z}(\tilde{\boldsymbol{H}})}{\mathcal{Z}(\boldsymbol{R}_{\boldsymbol{n}}\tilde{\boldsymbol{H}}, \boldsymbol{n})},$$

where $\boldsymbol{z}(\tilde{\boldsymbol{H}}) = \left(z_1(\tilde{\boldsymbol{H}}), z_2(\tilde{\boldsymbol{H}}), z_3(\tilde{\boldsymbol{H}})\right)^{\mathsf{T}}$. For the unrotated system of mean magnetic moments, the rotation must be reversed so that the final mean magnetic moment can be written as

$$\tilde{\boldsymbol{m}}_0(\boldsymbol{H}_0; \boldsymbol{n}) = \boldsymbol{R}_{\boldsymbol{n}} \cdot \tilde{\boldsymbol{m}}_{\boldsymbol{n}}(\boldsymbol{R}_{\boldsymbol{n}}^{\mathsf{T}}\boldsymbol{H}_0). \qquad \square$$

3.1.3 Series Expression for the Anisotropic Equilibrium Model

The single series expression from the next theorem was published without proof in [F7] and is, to the author's knowledge, the only single series expansion for the magnetization curve in the anisotropic case using elementary functions. In addition, a full numerical and experimental validation of the anisotropic equilibrium model in [F6] was recently performed, showing that it is suitable for both immobilized and fluid SPIO tracers. It should be noted that in [19] a double series expansion was derived.

Theorem 3.1

The integral expression in Proposition 3.3 for $\mathcal{Z} : \mathbb{R}^3 \times \mathbb{S}^2 \to \mathbb{R}_+$ and $z_i : \mathbb{R}^3 \to \mathbb{R}$ with $i \in \{1,2,3\}$ and $j \in \{1,2\}$ can be expressed as

$$\begin{aligned}
\mathcal{Z}(\boldsymbol{R_n}\tilde{\boldsymbol{H}}, \boldsymbol{n}) &= 4\pi \int_0^1 I_0\Big(\beta|\tilde{\boldsymbol{H}}|_{12}\sqrt{1-x^2}\Big)\cosh(\beta\tilde{H}_3 x)\mathrm{e}^{\alpha_\mathrm{K} x^2}\,\mathrm{d}x,\\
z_3(\tilde{\boldsymbol{H}}) &= 4\pi \int_0^1 x I_0\Big(\beta|\tilde{\boldsymbol{H}}|_{12}\sqrt{1-x^2}\Big)\sinh(\beta\tilde{H}_3 x)\mathrm{e}^{\alpha_\mathrm{K} x^2}\,\mathrm{d}x,\\
z_j(\tilde{\boldsymbol{H}}) &= 4\pi \frac{\tilde{H}_j}{|\tilde{\boldsymbol{H}}|_{12}} \int_0^1 \sqrt{1-x^2} I_1\Big(\beta|\tilde{\boldsymbol{H}}|_{12}\sqrt{1-x^2}\Big)\cosh(\beta\tilde{H}_3 x)\mathrm{e}^{\alpha_\mathrm{K} x^2}\,\mathrm{d}x
\end{aligned} \tag{3.38}$$

with $|\tilde{\boldsymbol{H}}|_{12} = \sqrt{\tilde{H}_1^2 + \tilde{H}_2^2}$ and has the single series expansion

$$\begin{aligned}
\mathcal{Z}(\boldsymbol{R_n}\tilde{\boldsymbol{H}}, \boldsymbol{n}) &= 4\pi^{\frac{3}{2}} \sum_{\ell=0}^{\infty} \alpha_\mathrm{K}^\ell L_\ell^{(-\frac{1}{2})}\left(-\frac{\beta^2\tilde{H}_3^2}{4\alpha_\mathrm{K}}\right) 2^{-\frac{1}{2}+\ell} \frac{I_{\frac{1}{2}+\ell}(\beta|\tilde{\boldsymbol{H}}|_{12})}{(\beta|\tilde{\boldsymbol{H}}|_{12})^{\frac{1}{2}+\ell}},\\
z_3(\tilde{\boldsymbol{H}}) &= 4\pi^{\frac{3}{2}} \beta\tilde{H}_3 \sum_{\ell=0}^{\infty} \alpha_\mathrm{K}^\ell L_\ell^{(\frac{1}{2})}\left(-\frac{\beta^2\tilde{H}_3^2}{4\alpha_\mathrm{K}}\right) 2^{-\frac{1}{2}+\ell} \frac{I_{\frac{3}{2}+\ell}(\beta|\tilde{\boldsymbol{H}}|_{12})}{(\beta|\tilde{\boldsymbol{H}}|_{12})^{\frac{3}{2}+\ell}},\\
z_j(\tilde{\boldsymbol{H}}) &= 4\pi^{\frac{3}{2}} \beta\tilde{H}_j \sum_{\ell=0}^{\infty} \alpha_\mathrm{K}^\ell L_\ell^{(-\frac{1}{2})}\left(-\frac{\beta^2\tilde{H}_3^2}{4\alpha_\mathrm{K}}\right) 2^{-\frac{1}{2}+\ell} \frac{I_{\frac{3}{2}+\ell}(\beta|\tilde{\boldsymbol{H}}|_{12})}{(\beta|\tilde{\boldsymbol{H}}|_{12})^{\frac{3}{2}+\ell}},
\end{aligned} \tag{3.39}$$

where $L_n^{(\alpha)} : \mathbb{R} \to \mathbb{R}$ denotes the generalized Laguerre polynomials with order $\alpha > -1$ and degree $n \in \mathbb{N}_0$. The function $I_\nu : \mathbb{R} \to \mathbb{R}$ denotes the modified Bessel function of the first kind with order $\nu \in \mathbb{C}$ and $\alpha_\mathrm{K} \neq 0$. In case of $\alpha_\mathrm{K} = 0$, the solution is given in Proposition 3.1. If $|\tilde{\boldsymbol{H}}|_{12} = 0$ then the solution is given in (3.23) or (3.24) with $H_0 = \tilde{H}_3$. The mean magnetic moment is given in Proposition 3.3.

Proof of Theorem 3.1. To prove (3.38) and (3.39), let $a = \beta|\tilde{\boldsymbol{H}}|_{12}$, $b = \beta\tilde{H}_3$, and $c = \alpha_{\mathrm{K}}$. Then we have the following for (3.18):

$$\begin{aligned}\mathcal{Z}(\boldsymbol{R_n}\tilde{\boldsymbol{H}}, \boldsymbol{n}) &= 2\pi \int_{-1}^{1} I_0\Big(a\sqrt{1-x^2}\Big)\, \mathrm{e}^{bx+cx^2}\, \mathrm{d}x, \\ &= 2\pi \left[\int_{0}^{1} I_0\Big(a\sqrt{1-x^2}\Big)\, \mathrm{e}^{bx+cx^2}\, \mathrm{d}x + \int_{-1}^{0} I_0\Big(a\sqrt{1-x^2}\Big)\, \mathrm{e}^{bx+cx^2}\, \mathrm{d}x\right].\end{aligned}$$

Substituting the second integral on the right-hand side with $x = -\tilde{x}$ and then factoring out the terms related to e in the integral leads to the results:

$$\begin{aligned}\mathcal{Z}(\boldsymbol{R_n}\tilde{\boldsymbol{H}}, \boldsymbol{n}) &= 2\pi \left[\int_{0}^{1} I_0\Big(a\sqrt{1-x^2}\Big)\, \mathrm{e}^{bx+cx^2}\, \mathrm{d}x + \int_{0}^{1} I_0\Big(a\sqrt{1-\tilde{x}^2}\Big)\, \mathrm{e}^{-b\tilde{x}+c\tilde{x}^2}\, \mathrm{d}\tilde{x}\right] \\ &= 2\pi \int_{0}^{1} I_0\Big(a\sqrt{1-x^2}\Big) \underbrace{\left[\mathrm{e}^{bx} + \mathrm{e}^{-bx}\right]}_{=2\cosh(bx)} \mathrm{e}^{cx^2}\, \mathrm{d}x. \qquad (3.40)\end{aligned}$$

Similarly, (3.19) and (3.20) follow as

$$\begin{aligned}z_3(\tilde{\boldsymbol{H}}) &= 2\pi \int_{-1}^{1} x I_0\Big(a\sqrt{1-x^2}\Big)\, \mathrm{e}^{bx+cx^2}\, \mathrm{d}x, \\ &= 2\pi \left[\int_{0}^{1} x I_0\Big(a\sqrt{1-x^2}\Big)\, \mathrm{e}^{bx+cx^2}\, \mathrm{d}x - \int_{0}^{1} \tilde{x} I_0\Big(a\sqrt{1-\tilde{x}^2}\Big)\, \mathrm{e}^{-b\tilde{x}+c\tilde{x}^2}\, \mathrm{d}\tilde{x}\right] \\ &= 2\pi \int_{0}^{1} x I_0\Big(a\sqrt{1-x^2}\Big) \underbrace{\left[\mathrm{e}^{bx} - \mathrm{e}^{-bx}\right]}_{=2\sinh(bx)} \mathrm{e}^{cx^2}\, \mathrm{d}x \\ z_j(\tilde{\boldsymbol{H}}) &= 2\pi \frac{\beta\tilde{H}_j}{a} \int_{-1}^{1} \sqrt{1-x^2} I_1\Big(a\sqrt{1-x^2}\Big)\, \mathrm{e}^{bx+cx^2}\, \mathrm{d}x, \qquad (3.41) \\ &= 2\pi \frac{\beta\tilde{H}_j}{a} \left[\int_{0}^{1} \sqrt{1-x^2} I_1\Big(a\sqrt{1-x^2}\Big)\, \mathrm{e}^{bx+cx^2}\, \mathrm{d}x \right. \\ &\qquad \left. + \int_{0}^{1} \sqrt{1-\tilde{x}^2} I_1\Big(a\sqrt{1-\tilde{x}^2}\Big)\, \mathrm{e}^{-b\tilde{x}+c\tilde{x}^2}\, \mathrm{d}\tilde{x}\right] \\ &= 2\pi \frac{\beta\tilde{H}_j}{a} \int_{0}^{1} \sqrt{1-x^2} I_1\Big(a\sqrt{1-x^2}\Big) \underbrace{\left[\mathrm{e}^{bx} + \mathrm{e}^{-bx}\right]}_{=2\cosh(bx)} \mathrm{e}^{cx^2}\, \mathrm{d}x.\end{aligned}$$

For the proof of the series in (3.39) some basic definitions are now given. To obtain a single series expression, generalized Laguerre polynomials are used, which are

briefly discussed in Section 5.1.2. Using the closed-form expression for the generalized Laguerre polynomials in (5.19) with $\alpha = -\frac{1}{2}$ yields

$$L_n^{(-\frac{1}{2})}(\xi) = \sum_{\ell=0}^{n} \frac{\Gamma(\frac{1}{2}+n)}{\Gamma(\frac{1}{2}+\ell)(n-\ell)!\ell!}(-\xi)^\ell = \frac{\Gamma(\frac{1}{2}+n)}{\sqrt{\pi}} \sum_{\ell=0}^{n} \frac{4^\ell}{(2\ell)!(n-\ell)!}(-\xi)^\ell \tag{3.42}$$

using $\Gamma(\frac{1}{2}+n) = \frac{(2n)!}{n!4^n}\sqrt{\pi}$, and consequently for $\alpha = \frac{1}{2}$ it is obtained that

$$L_n^{(\frac{1}{2})}(\xi) = \sum_{\ell=0}^{n} \frac{\Gamma(\frac{3}{2}+n)}{\Gamma(\frac{3}{2}+\ell)(n-\ell)!\ell!}(-\xi)^\ell = \frac{2\Gamma(\frac{3}{2}+n)}{\sqrt{\pi}} \sum_{\ell=0}^{n} \frac{4^\ell}{(2\ell+1)!(n-\ell)!}(-\xi)^\ell. \tag{3.43}$$

The Maclaurin series of functions used in the proof are

$$\mathrm{e}^\xi = \sum_{m=0}^{\infty} \frac{\xi^m}{m!}, \tag{3.44}$$

$$\cosh(\xi) = \sum_{m=0}^{\infty} \frac{\xi^{2m}}{(2m)!}, \tag{3.45}$$

and

$$\sinh(\xi) = \sum_{m=0}^{\infty} \frac{\xi^{2m+1}}{(2m+1)!}. \tag{3.46}$$

The integral formula from [1, §11.4.10] for Bessel functions of the first kind is used, which is

$$\begin{aligned} \int_0^1 I_0\big(a\sqrt{1-x^2}\big)x^n \,\mathrm{d}x &\overset{\dagger}{=} \int_0^{\frac{\pi}{2}} I_0(a\sin(\alpha))\cos^n(\alpha)\sin(\alpha)\,\mathrm{d}\alpha \\ &= 2^{\frac{n-1}{2}}\Gamma\left(\frac{n+1}{2}\right) a^{-\frac{n+1}{2}} I_{\frac{n+1}{2}}(a) \end{aligned} \tag{3.47}$$

with $n \in \mathbb{N}_0$. The equality denoted by the † can be shown by substitution with $x = \cos(\alpha)$ and $\mathrm{d}x = -\sin(\alpha)\,\mathrm{d}\alpha$. The following differentiation relationship [1, §9.6.28] applies to the modified Bessel function of the first kind:

$$\frac{\mathrm{d}}{\mathrm{d}\xi}[\xi^{-\alpha} I_\alpha(\xi)] = \xi^{-\alpha} I_{\alpha+1}(\xi) \quad \text{for } \alpha \geq 0. \tag{3.48}$$

The Cauchy product of $\mathrm{e}^{c\xi^2}$ and $\cosh(b\xi)$ with the power series in (3.44) and (3.45) is

$$\begin{aligned}\cosh(b\xi)\mathrm{e}^{c\xi^2} &= \sum_{\ell=0}^{\infty}\sum_{k=0}^{\ell}\frac{(b\xi)^{2k}}{(2k)!}\frac{(c\xi^2)^{\ell-k}}{(\ell-k)!} \\ &= \sum_{\ell=0}^{\infty}\xi^{2\ell}\underbrace{\sum_{k=0}^{\ell}\frac{b^{2k}}{(2k)!}\frac{c^{\ell-k}}{(\ell-k)!}}_{=d_\ell} = \sum_{\ell=0}^{\infty} d_\ell \xi^{2\ell}.\end{aligned} \tag{3.49}$$

If $c \neq 0$, the right hand side of the second equal sign d_ℓ can be further expressed by

$$\begin{aligned}d_\ell &= \sum_{k=0}^{\ell}\frac{b^{2k}}{(2k)!}\frac{c^{\ell-k}}{(\ell-k)!} = c^\ell\sum_{k=0}^{\ell}\frac{b^{2k}c^{-k}}{(2k)!(\ell-k)!} \\ &= c^\ell\sum_{k=0}^{\ell}\frac{\left(\frac{b^2}{c}\right)^k}{(2k)!(\ell-k)!} = c^\ell\sum_{k=0}^{\ell}4^k4^{-k}\frac{\left(\frac{b^2}{c}\right)^k}{(2k)!(\ell-k)!} \\ &= c^\ell\sum_{k=0}^{\ell}4^k\frac{\left(\frac{b^2}{4c}\right)^k}{(2k)!(\ell-k)!} \overset{(3.42)}{=} \frac{c^\ell\sqrt{\pi}}{\Gamma(\frac{1}{2}+\ell)}L_\ell^{(-\frac{1}{2})}\left(-\frac{b^2}{4c}\right).\end{aligned} \tag{3.50}$$

In the case that $c = 0$, the following results

$$d_\ell = \sum_{k=0}^{\ell}\frac{b^{2k}}{(2k)!}\frac{0^{\ell-k}}{(\ell-k)!} = \sum_{k=0}^{\ell}\frac{b^{2k}}{(2k)!}\frac{\delta_{\ell k}}{(\ell-k)!} = \frac{b^{2\ell}}{(2\ell)!}$$

with the definition $0^0 = 1$. The Cauchy product of the series representations of the functions in (3.44) and (3.46) multiplied by ξ is

$$\begin{aligned}\xi\sinh(b\xi)\mathrm{e}^{c\xi^2} &= \xi\sum_{\ell=0}^{\infty}\sum_{k=0}^{\ell}\frac{(b\xi)^{2k+1}}{(2k+1)!}\frac{(c\xi^2)^{\ell-k}}{(\ell-k)!} \\ &= \sum_{\ell=0}^{\infty}\xi^{2\ell+2}\underbrace{\sum_{k=0}^{\ell}\frac{b^{2k+1}}{(2k+1)!}\frac{c^{\ell-k}}{(\ell-k)!}}_{=e_\ell} \\ &= \sum_{\ell=0}^{\infty} e_\ell\xi^{2\ell+2}.\end{aligned} \tag{3.51}$$

Furthermore, e_ℓ can be simplified by

$$\begin{aligned} e_\ell &= \sum_{k=0}^{\ell} \frac{b^{2k+1}}{(2k+1)!} \frac{c^{\ell-k}}{(\ell-k)!} \\ &= bc^\ell \sum_{k=0}^{\ell} \frac{b^{2k} c^{-k}}{(2k+1)!(\ell-k)!} \\ &= bc^\ell \sum_{k=0}^{\ell} \frac{4^k}{(2k+1)!(\ell-k)!} \left(\frac{b^2}{4c}\right)^k \\ &\overset{(3.43)}{=} \frac{bc^\ell \sqrt{\pi}}{2\Gamma(\frac{3}{2}+\ell)} L_\ell^{(\frac{1}{2})}\left(-\frac{b^2}{4c}\right) \end{aligned} \tag{3.52}$$

under the assumption of $c \neq 0$. In the case of $c = 0$ this results in

$$e_\ell = \frac{b^{2\ell+1}}{(2\ell+1)!}.$$

The integrals involved in (3.38) can be integrated step by step by interchanging the summation of the series and the integration, which is allowed since all the functions involved are analytical functions and the series terms are absolutely convergent on the entire interval $[0, 1]$ to be integrated.

The essential component of the first integral in (3.38) is

$$\begin{aligned} \int_0^1 I_0\Big(a\sqrt{1-x^2}\Big) \cosh(bx) \mathrm{e}^{cx^2} \,\mathrm{d}x &\overset{(3.49)}{=} \int_0^1 I_0\Big(a\sqrt{1-x^2}\Big) \sum_{\ell=0}^{\infty} d_\ell x^{2\ell} \,\mathrm{d}x \\ &\overset{\dagger}{=} \sum_{\ell=0}^{\infty} d_\ell \int_0^1 I_0\Big(a\sqrt{1-x^2}\Big) x^{2\ell} \,\mathrm{d}x \\ &\overset{(3.47)}{=} \sum_{\ell=0}^{\infty} d_\ell 2^{\frac{2\ell-1}{2}} \Gamma\left(\frac{2\ell+1}{2}\right) a^{-\frac{2\ell+1}{2}} I_{\frac{2\ell+1}{2}}(a) \\ &\overset{(3.50)}{=} \sqrt{\pi} \sum_{\ell=0}^{\infty} c^\ell L_\ell^{(-\frac{1}{2})}\left(-\frac{b^2}{4c}\right) 2^{\ell-\frac{1}{2}} a^{-\ell-\frac{1}{2}} I_{\ell+\frac{1}{2}}(a). \end{aligned} \tag{3.53}$$

The essential component of the second integral in (3.38) is

$$\begin{aligned}
&\int_0^1 x I_0\Big(a\sqrt{1-x^2}\Big)\sinh(bx)\mathrm{e}^{cx^2}\,\mathrm{d}x \\
&\qquad \overset{(3.51)}{=} \int_0^1 I_0\Big(a\sqrt{1-x^2}\Big)\sum_{\ell=0}^{\infty} e_\ell x^{2\ell+2}\,\mathrm{d}x \\
&\qquad \overset{\dagger}{=} \sum_{\ell=0}^{\infty} e_\ell \int_0^1 I_0\Big(a\sqrt{1-x^2}\Big)\,x^{2\ell+2}\,\mathrm{d}x \\
&\qquad \overset{(3.47)}{=} \sum_{\ell=0}^{\infty} e_\ell 2^{\frac{2\ell+2-1}{2}}\Gamma\left(\frac{2\ell+2+1}{2}\right)a^{-\frac{2\ell+2+1}{2}} I_{\frac{2\ell+2+1}{2}}(a) \\
&\qquad \overset{(3.52)}{=} b\sqrt{\pi}\sum_{\ell=0}^{\infty} c^\ell L_\ell^{(\frac{1}{2})}\left(-\frac{b^2}{4c}\right)2^{\ell-\frac{1}{2}}a^{-\ell-\frac{3}{2}} I_{\ell+\frac{3}{2}}(a).
\end{aligned} \tag{3.54}$$

The following applies to the essential components of the third integral in (3.38):

$$\begin{aligned}
&\int_0^1 \sqrt{1-x^2} I_1\Big(a\sqrt{1-x^2}\Big)\cosh(bx)\mathrm{e}^{cx^2}\,\mathrm{d}x \\
&\qquad = \int_0^1 \frac{\partial I_0\big(a\sqrt{1-x^2}\big)}{\partial a}\cosh(bx)\mathrm{e}^{cx^2}\,\mathrm{d}x \\
&\qquad = \frac{\partial}{\partial a}\left[\int_0^1 I_0\Big(a\sqrt{1-x^2}\Big)\cosh(bx)\mathrm{e}^{cx^2}\,\mathrm{d}x\right].
\end{aligned}$$

It should be noted that this mathematical manipulation was also previously used in (3.37). This results in

$$\begin{aligned}
&\int_0^1 \sqrt{1-x^2} I_1\Big(a\sqrt{1-x^2}\Big)\cosh(bx)\mathrm{e}^{cx^2}\,\mathrm{d}x \\
&\qquad = \frac{\partial}{\partial a}\left[\int_0^1 I_0\Big(a\sqrt{1-x^2}\Big)\cosh(bx)\mathrm{e}^{cx^2}\,\mathrm{d}x\right] \\
&\qquad \overset{(3.54)}{=} \frac{\partial}{\partial a}\left[\sqrt{\pi}\sum_{\ell=0}^{\infty} c^\ell L_\ell^{(-\frac{1}{2})}\left(-\frac{b^2}{4c}\right)2^{\ell-\frac{1}{2}}a^{-\ell-\frac{1}{2}} I_{\ell+\frac{1}{2}}(a)\right] \\
&\qquad \overset{\ddagger}{=} \sqrt{\pi}\sum_{\ell=0}^{\infty} c^\ell L_\ell^{(-\frac{1}{2})}\left(-\frac{b^2}{4c}\right)2^{\ell-\frac{1}{2}}\frac{\partial}{\partial a}\Big[a^{-\ell-\frac{1}{2}} I_{\ell+\frac{1}{2}}(a)\Big] \\
&\qquad \overset{(3.48)}{=} \sqrt{\pi}\sum_{\ell=0}^{\infty} c^\ell L_\ell^{(-\frac{1}{2})}\left(-\frac{b^2}{4c}\right)2^{\ell-\frac{1}{2}}a^{-\ell-\frac{1}{2}} I_{\ell+\frac{3}{2}}(a),
\end{aligned} \tag{3.55}$$

where the step denoted by ‡ is allowed because all the functions involved are analytical and the series is absolutely convergent. By combining the results of (3.40) and (3.41) with the results of (3.53), (3.54), and (3.55), Theorem 3.1 is shown. □

4 Fourier Analysis

In this thesis, two types of Fourier analysis are used that are closely related, the Fourier series expansion and the continuous Fourier transform. This chapter covers the definition of the two transforms and some key properties. The Fourier series and the continuous Fourier transform are standard tools, and several descriptions in this chapter are based on the formulations in [15, 26, 37]. The interested reader is also referred to [25, 64]. Historically, the Fourier series is the older transform in the field of Fourier analysis. Joseph Fourier introduced the Fourier series named after him to study heat conduction and find basic solutions for the corresponding differential equations. From this starting point, various types of Fourier transforms were developed, which today have a wide range of applications in various fields of science and technology. In the Chapters 6 and 7 many of the properties of the Fourier series and the continuous Fourier transform are used. The Fourier series has already been briefly introduced in Chapter 2 in connection with the frequency representation of the periodic system function $s_\nu(\boldsymbol{x}, t)$ and the voltage signal $u_\nu^{\mathrm{P}}(t)$ in (2.35) and (2.36).

The Fourier series for a periodical function $f : \mathbb{R} \to \mathbb{C}$ with $f \in L^2([-\frac{T_\mathrm{D}}{2}, \frac{T_\mathrm{D}}{2}])$, $f(t) = f(t + T_\mathrm{D})$, and $T_\mathrm{D} \in \mathbb{R}$ is given by

$$f(t) = \sum_{k=-\infty}^{\infty} f_k \, \mathrm{e}^{\mathrm{i}2\pi k \frac{t}{T_\mathrm{D}}} = \sum_{k=-\infty}^{\infty} f_k \, \mathrm{e}^{\mathrm{i}\omega_k t}, \qquad \omega_k = 2\pi \tfrac{k}{T_\mathrm{D}}, \tag{4.1}$$

where the corresponding Fourier series coefficients $(f_k)_{k\in\mathbb{Z}} \in \ell^2(\mathbb{Z})$ of the function $f(t)$ can be calculated as follows:

$$f_k = \frac{1}{T_\mathrm{D}} \int_{-\frac{T_\mathrm{D}}{2}}^{\frac{T_\mathrm{D}}{2}} f(t) \mathrm{e}^{-\mathrm{i}2\pi k \frac{t}{T_\mathrm{D}}} \, \mathrm{d}t = \frac{1}{T_\mathrm{D}} \int_{-\frac{T_\mathrm{D}}{2}}^{\frac{T_\mathrm{D}}{2}} f(t) \mathrm{e}^{-\mathrm{i}\omega_k t} \, \mathrm{d}t. \tag{4.2}$$

However, since the focus of the thesis is not on the Fourier series, just the definition is given. It should be mentioned that many of the properties shown for the Fourier transform also hold for the Fourier series in a modified form. In addition, the two calculi can be unified into a more universal description in terms of generalized functions, also called distributions. The next part focuses on the continuous Fourier transform on $\mathbb{R}^N$.

4.1 Fourier Transform on $\mathbb{R}^N$

In this subchapter, the Fourier transform on $\mathbb{R}^N$ will be introduced and some properties will be discussed. First, the Fourier transform on $L^1(\mathbb{R}^N)$ is discussed and then an extension to $L^2(\mathbb{R}^N)$ is given.

4.1.1 Fourier Transform on $L^1(\mathbb{R}^N)$

At the beginning, the classical $L^1(\mathbb{R}^N)$ definition of the Fourier transform and the inverse Fourier transform will be introduced.

Definition 4.1: Fourier transform on $L^1(\mathbb{R}^N)$

The continuous Fourier transform of a function $f \in L^1(\mathbb{R}^N)$ is defined by

$$\hat{f}(\boldsymbol{\omega}_{\boldsymbol{x}}) = \mathcal{F}\{f(\boldsymbol{x})\} = \int_{\mathbb{R}^N} f(\boldsymbol{x}) \mathrm{e}^{-\mathrm{i}\boldsymbol{\omega}_{\boldsymbol{x}}^{\mathsf{T}}\boldsymbol{x}} \,\mathrm{d}\boldsymbol{x}, \tag{4.3}$$

where $\hat{f} \in C_0(\mathbb{R}^N)$ and $C_0(\mathbb{R}^N)$ denotes the space of functions which are continuous and vanish at infinity.
The inverse Fourier transform of a function $\hat{f} \in L^1(\mathbb{R}^N)$ is then defined by

$$f(\boldsymbol{x}) = \mathcal{F}^{-1}\left\{\hat{f}(\boldsymbol{\omega}_{\boldsymbol{x}})\right\} = \frac{1}{(2\pi)^N} \int_{\mathbb{R}^N} \hat{f}(\boldsymbol{\omega}_{\boldsymbol{x}}) \mathrm{e}^{\mathrm{i}\boldsymbol{x}^{\mathsf{T}}\boldsymbol{\omega}_{\boldsymbol{x}}} \,\mathrm{d}\boldsymbol{\omega}_{\boldsymbol{x}}, \tag{4.4}$$

where $f \in C_0(\mathbb{R}^N)$.

It should be noted here that slightly different definitions of the continuous Fourier transform exist in the literature, but fortunately these can easily be converted into one another.

There is no guarantee that for two arbitrary functions $f, \hat{g} \in L^1(\mathbb{R}^N)$ also $\hat{f}, g$ belong to $L^1(\mathbb{R}^N)$. Therefore, it is possible that the inverse Fourier transform of $\hat{f}$ or the forward Fourier transform of g does not exist.

Fortunately, the Fourier transform and the inverse Fourier transform on $L^1(\mathbb{R}^N)$ can be extended to a more general form. For this purpose, the forward Fourier transform of f is defined by

$$\hat{f}(\boldsymbol{\omega}_{\boldsymbol{x}}) = \lim_{n\to\infty} \int_{\mathbb{R}^N} f(\boldsymbol{x}) \mathrm{e}^{-\frac{1}{2n}\|\boldsymbol{x}\|^2} \mathrm{e}^{-\mathrm{i}\boldsymbol{\omega}_{\boldsymbol{x}}^{\mathsf{T}}\boldsymbol{x}} \,\mathrm{d}\boldsymbol{x} \tag{4.5}$$

and the inverse Fourier transform of $\hat{f}$ is defined by

$$f(\boldsymbol{x}) = \lim_{n\to\infty} \frac{1}{(2\pi)^N} \int_{\mathbb{R}^N} \hat{f}(\boldsymbol{\omega}_{\boldsymbol{x}}) \mathrm{e}^{-\frac{1}{2n}\|\boldsymbol{\omega}_{\boldsymbol{x}}\|^2} \mathrm{e}^{\mathrm{i}\boldsymbol{x}^{\mathsf{T}}\boldsymbol{\omega}_{\boldsymbol{x}}} \,\mathrm{d}\boldsymbol{\omega}_{\boldsymbol{x}}, \tag{4.6}$$

where f or $\hat{f}$ belongs to $L^1(\mathbb{R}^N)$. A brief proof for (4.5) and (4.6) and that the definition is compatible with the classical definition (4.3) and (4.4) is postponed. First, a lemma should be proved that helps later to generalize the definition of the Fourier transform on $L^1(\mathbb{R}^N)$.

Lemma 4.1. *The functions $f_n : \mathbb{R}^N \to \mathbb{C}$ and $\hat{f}_n : \mathbb{R}^N \to \mathbb{C}$ are represented by*

$$f_n(\boldsymbol{x}) = f(\boldsymbol{x}) \mathrm{e}^{-\frac{1}{2n}\|\boldsymbol{x}\|^2}$$

and

$$\hat{f}_n(\boldsymbol{\omega}_{\boldsymbol{x}}) = \hat{f}(\boldsymbol{\omega}_{\boldsymbol{x}}) \mathrm{e}^{-\frac{1}{2n}\|\boldsymbol{\omega}_{\boldsymbol{x}}\|^2},$$

where $n \in \mathbb{N}$ and $f : \mathbb{R}^N \to \mathbb{C}$ or $\hat{f} : \mathbb{R}^N \to \mathbb{C}$ belongs to $L^1(\mathbb{R}^N)$, then it holds that f_n and $\hat{f}_n$ both belong to $L^1(\mathbb{R}^N)$.

Proof of Lemma 4.1. Without loss of generality, let it be said that $f \in L^1(\mathbb{R}^N)$, then it is known that $\hat{f} \in C_0(\mathbb{R}^N) \subset L^\infty(\mathbb{R}^N)$. The multidimensional Gaussian function

$$g_n(\boldsymbol{x}) = \mathrm{e}^{-\frac{1}{2n}\|\boldsymbol{x}\|^2}$$

is in $L^p(\mathbb{R}^N)$ with $p \in [1, \infty]$, therefore with the Hölder inequality and $\frac{1}{r} = \frac{1}{q} + \frac{1}{p}$ it follows

$$\|f_n\|_{L^r} = \|f g_n\|_{L^r} \leq \|f\|_{L^q} \|g_n\|_{L^p} < \infty.$$

The selection of $r = 1$, $p = \infty$, and $q = 1$ shows that $f_n \in L^1(\mathbb{R}^N)$, since $\|g_n\|_{L^\infty} = 1$.

Let $\hat{f}$ be the Fourier transform of $f \in L^1(\mathbb{R}^N)$ and let

$$\hat{h}_n(\boldsymbol{\omega}_{\boldsymbol{x}}) = \mathrm{e}^{-\frac{1}{2n}\|\boldsymbol{\omega}_{\boldsymbol{x}}\|^2},$$

where $\hat{h}_n \in L^p(\mathbb{R}^N)$ for all $p \in [1, \infty]$. Hölder's inequality is now

$$\|\hat{f}_n\|_{L^r} = \|\hat{f}\hat{h}_n\|_{L^r} \leq \|\hat{f}\|_{L^\infty} \|\hat{h}_n\|_{L^p} < \infty.$$

With $\frac{1}{r} = \frac{1}{p} + \overbrace{\frac{1}{\infty}}^{=0}$ one has the desired form with $r = 1$ and $p = 1$, i.e., $\|\hat{h}_n\|_{L^1} = (2\pi n)^{\frac{N}{2}}$. This shows that $\hat{f}_n$ is actually also in $L^1(\mathbb{R}^N)$. Furthermore, it can be shown that $\hat{f}_n \in L^p(\mathbb{R}^N)$ for all $p \in [1, \infty]$. □

Properties in $L^1(\mathbb{R}^N)$

Property 1: Shift and modulation

Let $f \in L^1(\mathbb{R}^N)$ and $\hat{f}$ be its Fourier transform and let $\boldsymbol{x}_0 \in \mathbb{R}^N$. Then

$$\mathcal{F}\{f(\boldsymbol{x} - \boldsymbol{x}_0)\} = \hat{f}(\boldsymbol{\omega}_{\boldsymbol{x}}) \mathrm{e}^{-\mathrm{i}\boldsymbol{\omega}_{\boldsymbol{x}}^{\mathsf{T}} \boldsymbol{x}_0} \tag{4.7}$$

applies and, vice versa, for $\boldsymbol{\omega}_0 \in \mathbb{R}^N$ it holds

$$\mathcal{F}\left\{f(\boldsymbol{x}) \mathrm{e}^{\mathrm{i}\boldsymbol{\omega}_0^{\mathsf{T}} \boldsymbol{x}}\right\} = \hat{f}(\boldsymbol{\omega}_{\boldsymbol{x}} - \boldsymbol{\omega}_0). \tag{4.8}$$

Proof. The function $f \in L^1(\mathbb{R}^N)$ has the Fourier transform

$$\hat{f}(\boldsymbol{\omega}_{\boldsymbol{x}}) = \int_{\mathbb{R}^N} f(\boldsymbol{x}) \mathrm{e}^{-\mathrm{i}\boldsymbol{\omega}_{\boldsymbol{x}}^{\mathsf{T}} \boldsymbol{x}} \, \mathrm{d}\boldsymbol{x}.$$

Therefore, the function $g(\boldsymbol{x}) = f(\boldsymbol{x} - \boldsymbol{x}_0)$ with $\boldsymbol{x}_0 \in \mathbb{R}^N$ has the Fourier transform

$$\begin{aligned}\hat{g}(\boldsymbol{\omega}_{\boldsymbol{x}}) &= \int_{\mathbb{R}^N} g(\boldsymbol{x}) \mathrm{e}^{-\mathrm{i}\boldsymbol{\omega}_{\boldsymbol{x}}^\mathsf{T}\boldsymbol{x}} \,\mathrm{d}\boldsymbol{x} = \int_{\mathbb{R}^N} f(\boldsymbol{x} - \boldsymbol{x}_0) \mathrm{e}^{-\mathrm{i}\boldsymbol{\omega}_{\boldsymbol{x}}^\mathsf{T}\boldsymbol{x}} \,\mathrm{d}\boldsymbol{x} \\ &\underbrace{=}_{\boldsymbol{x}=\boldsymbol{z}+\boldsymbol{x}_0} \int_{\mathbb{R}^N} f(\boldsymbol{z}) \mathrm{e}^{-\mathrm{i}\boldsymbol{\omega}_{\boldsymbol{x}}^\mathsf{T}(\boldsymbol{z}+\boldsymbol{x}_0)} \,\mathrm{d}\boldsymbol{z} = \mathrm{e}^{-\mathrm{i}\boldsymbol{\omega}_{\boldsymbol{x}}^\mathsf{T}\boldsymbol{x}_0} \int_{\mathbb{R}^N} f(\boldsymbol{z}) \mathrm{e}^{-\mathrm{i}\boldsymbol{\omega}_{\boldsymbol{x}}^\mathsf{T}\boldsymbol{z}} \,\mathrm{d}\boldsymbol{z} = \mathrm{e}^{-\mathrm{i}\boldsymbol{\omega}_{\boldsymbol{x}}^\mathsf{T}\boldsymbol{x}_0} \hat{f}(\boldsymbol{\omega}_{\boldsymbol{x}}).\end{aligned}$$

If now $g(\boldsymbol{x}) = \mathrm{e}^{\mathrm{i}\boldsymbol{\omega}_0^\mathsf{T}\boldsymbol{x}} f(\boldsymbol{x})$ with $\boldsymbol{\omega}_0 \in \mathbb{R}^N$, then the Fourier transform results in

$$\begin{aligned}\hat{g}(\boldsymbol{\omega}_{\boldsymbol{x}}) &= \int_{\mathbb{R}^N} g(\boldsymbol{x}) \mathrm{e}^{-\mathrm{i}\boldsymbol{\omega}_{\boldsymbol{x}}^\mathsf{T}\boldsymbol{x}} \,\mathrm{d}\boldsymbol{x} = \int_{\mathbb{R}^N} \mathrm{e}^{\mathrm{i}\boldsymbol{\omega}_0^\mathsf{T}\boldsymbol{x}} f(\boldsymbol{x}) \mathrm{e}^{-\mathrm{i}\boldsymbol{\omega}_{\boldsymbol{x}}^\mathsf{T}\boldsymbol{x}} \,\mathrm{d}\boldsymbol{x} \\ &= \int_{\mathbb{R}^N} \mathrm{e}^{\mathrm{i}\boldsymbol{\omega}_0^\mathsf{T}\boldsymbol{x}} f(\boldsymbol{x}) \mathrm{e}^{-\mathrm{i}\boldsymbol{\omega}_{\boldsymbol{x}}^\mathsf{T}\boldsymbol{x}} \,\mathrm{d}\boldsymbol{x} = \int_{\mathbb{R}^N} \mathrm{e}^{\mathrm{i}\boldsymbol{\omega}_0^\mathsf{T}\boldsymbol{x}} f(\boldsymbol{x}) \mathrm{e}^{-\mathrm{i}\boldsymbol{\omega}_{\boldsymbol{x}}^\mathsf{T}\boldsymbol{x}} \,\mathrm{d}\boldsymbol{x} \\ &= \int_{\mathbb{R}^N} f(\boldsymbol{x}) \mathrm{e}^{-\mathrm{i}(\boldsymbol{\omega}_{\boldsymbol{x}} - \boldsymbol{\omega}_0)^\mathsf{T}\boldsymbol{x}} \,\mathrm{d}\boldsymbol{x} = \hat{f}(\boldsymbol{\omega}_{\boldsymbol{x}} - \boldsymbol{\omega}_0). \qquad \square\end{aligned}$$

Property 2: Affine transform

Let $f \in L^1(\mathbb{R}^N)$ and let the corresponding Fourier transform be denoted by $\hat{f}(\boldsymbol{\omega}_{\boldsymbol{x}}) = \mathcal{F}\{f(\boldsymbol{x})\}$. If the matrix $\boldsymbol{A} \in \mathbb{R}^{N\times N}$ is invertible, then the Fourier transform of $f(\boldsymbol{A}\boldsymbol{x})$ is as follows:

$$\mathcal{F}\{f(\boldsymbol{A}\boldsymbol{x})\} = \frac{1}{|\det(\boldsymbol{A})|} \hat{f}(\boldsymbol{A}^{-\mathsf{T}}\boldsymbol{\omega}_{\boldsymbol{x}}). \tag{4.9}$$

Alternatively, if $\hat{f} \in L^1(\mathbb{R}^N)$, then

$$\mathcal{F}^{-1}\Big\{\hat{f}(\boldsymbol{A}^{-\mathsf{T}}\boldsymbol{\omega}_{\boldsymbol{x}})\Big\} = |\det(\boldsymbol{A})| f(\boldsymbol{A}\boldsymbol{x}). \tag{4.10}$$

Proof. Let $f \in L^1(\mathbb{R}^N)$ and $\hat{f}$ be the corresponding Fourier transform. Since $\boldsymbol{A} \in \mathbb{R}^{N\times N}$ is an arbitrary but invertible matrix, it holds

$$\mathcal{F}\{f(\boldsymbol{A}\boldsymbol{x})\} = \int_{\mathbb{R}^N} f(\boldsymbol{A}\boldsymbol{x}) \mathrm{e}^{-\mathrm{i}\boldsymbol{\omega}_{\boldsymbol{x}}^\mathsf{T}\boldsymbol{x}} \,\mathrm{d}\boldsymbol{x}.$$

Using integration by substitution with $\boldsymbol{z} = \boldsymbol{A}\boldsymbol{x}$, $\boldsymbol{x} = \boldsymbol{A}^{-1}\boldsymbol{z}$, $\mathrm{d}\boldsymbol{x} = |\det(\boldsymbol{A}^{-1})|\,\mathrm{d}\boldsymbol{z}$, and $\mathrm{d}\boldsymbol{x} = \frac{\mathrm{d}\boldsymbol{z}}{|\det(\boldsymbol{A})|}$ results in

$$\begin{aligned}\int_{\mathbb{R}^N} f(\boldsymbol{A}\boldsymbol{x})\mathrm{e}^{-\mathrm{i}\boldsymbol{\omega}_x^\mathsf{T}\boldsymbol{x}}\,\mathrm{d}\boldsymbol{x} &= \int_{\mathbb{R}^N} f(\boldsymbol{z})\mathrm{e}^{-\mathrm{i}\boldsymbol{\omega}_x^\mathsf{T}\boldsymbol{A}^{-1}\boldsymbol{z}}\frac{1}{|\det(\boldsymbol{A})|}\,\mathrm{d}\boldsymbol{z} \\ &= \frac{1}{|\det(\boldsymbol{A})|}\int_{\mathbb{R}^N} f(\boldsymbol{z})\mathrm{e}^{-\mathrm{i}\left(\boldsymbol{A}^{-\mathsf{T}}\boldsymbol{\omega}_x\right)^\mathsf{T}\boldsymbol{z}}\,\mathrm{d}\boldsymbol{z} \\ &= \frac{1}{|\det(\boldsymbol{A})|}\hat{f}(\boldsymbol{A}^{-\mathsf{T}}\boldsymbol{\omega}_x).\end{aligned}$$

Equation (4.10) for the inverse Fourier transform follows in a similar manner. □

Property 3: Duality

If $f \in C_0(\mathbb{R}^N)$ and its Fourier transform is given by $\hat{f} \in L^1(\mathbb{R}^N)$, then the Fourier transform of $g(\boldsymbol{x}) = \hat{f}(\boldsymbol{x})$ is

$$\hat{g}(\boldsymbol{\omega}_x) = \mathcal{F}\left\{\hat{f}(\boldsymbol{x})\right\} = (2\pi)^N f(-\boldsymbol{\omega}_x). \tag{4.11}$$

Proof. For $\hat{f} \in L^1(\mathbb{R}^N)$, it holds

$$\begin{aligned}\hat{g}(\boldsymbol{\omega}_x) &= \mathcal{F}\left\{\hat{f}(\boldsymbol{x})\right\} \\ &= \int_{\mathbb{R}^N} \hat{f}(\boldsymbol{x})\mathrm{e}^{-\mathrm{i}\boldsymbol{\omega}_x^\mathsf{T}\boldsymbol{x}}\,\mathrm{d}\boldsymbol{x} \\ &= \int_{\mathbb{R}^N} \hat{f}(-\boldsymbol{z})\mathrm{e}^{\mathrm{i}\boldsymbol{\omega}_x^\mathsf{T}\boldsymbol{z}}\,\mathrm{d}\boldsymbol{z} \\ &= (2\pi)^N\mathcal{F}^{-1}\left\{\hat{f}(-\boldsymbol{x})\right\} \\ &\overset{(4.10)}{=} (2\pi)^N f(-\boldsymbol{\omega}_x).\end{aligned}$$

□

Property 4: Complex conjugate of a function

Let $f \in L^1(\mathbb{R}^N)$ and let $\hat{f} \in C_0(\mathbb{R}^N)$ denote its Fourier transform, then the Fourier transform of the complex conjugate f^* of f is

$$\mathcal{F}\{f^*(\boldsymbol{x})\} = \hat{f}^*(-\boldsymbol{\omega}_{\boldsymbol{x}}). \tag{4.12}$$

For $\hat{f} \in L^1(\mathbb{R}^N)$ with the inverse Fourier transform $f \in C_0(\mathbb{R}^N)$, the following is obtained for the complex conjugate $\hat{f}^*$:

$$\mathcal{F}^{-1}\left\{\hat{f}^*(\boldsymbol{\omega}_{\boldsymbol{x}})\right\} = f^*(-\boldsymbol{x}). \tag{4.13}$$

Proof. Since both directions are similar, only one direction is shown. Let, therefore, $f \in L^1(\mathbb{R}^N)$. Then the Fourier transform of the complex conjugate is

$$\begin{aligned}\mathcal{F}\{f^*(\boldsymbol{x})\} &= \int_{\mathbb{R}^N} f^*(\boldsymbol{x}) \mathrm{e}^{-\mathrm{i}\boldsymbol{\omega}_{\boldsymbol{x}}^{\mathsf{T}}\boldsymbol{x}} \,\mathrm{d}\boldsymbol{x} = \left(\int_{\mathbb{R}^N} f(\boldsymbol{x}) \mathrm{e}^{\mathrm{i}\boldsymbol{\omega}_{\boldsymbol{x}}^{\mathsf{T}}\boldsymbol{x}} \,\mathrm{d}\boldsymbol{x}\right)^* \\ &= \left(\int_{\mathbb{R}^N} f(\boldsymbol{x}) \mathrm{e}^{-\mathrm{i}(-\boldsymbol{\omega}_{\boldsymbol{x}})^{\mathsf{T}}\boldsymbol{x}} \,\mathrm{d}\boldsymbol{x}\right)^* = (\hat{f}(-\boldsymbol{\omega}_{\boldsymbol{x}}))^* = \hat{f}^*(-\boldsymbol{\omega}_{\boldsymbol{x}}). \qquad \square\end{aligned}$$

Property 5: Convolution and multiplication

If $f, g \in L^1(\mathbb{R}^N)$, then, for the convolution

$$(f * g)(\boldsymbol{x}) = \int_{\mathbb{R}^N} f(\boldsymbol{z}) g(\boldsymbol{x} - \boldsymbol{z}) \,\mathrm{d}\boldsymbol{z} = \int_{\mathbb{R}^N} f(\boldsymbol{x} - \boldsymbol{z}) g(\boldsymbol{z}) \,\mathrm{d}\boldsymbol{z}, \tag{4.14}$$

the continuous Fourier transform is given by

$$\mathcal{F}\{(f * g)(\boldsymbol{x})\} = \hat{f}(\boldsymbol{\omega}_{\boldsymbol{x}}) \hat{g}(\boldsymbol{\omega}_{\boldsymbol{x}}) \tag{4.15}$$

with $f * g \in L^1(\mathbb{R}^N)$. Equivalently, the inverse Fourier transform of convolution $(\hat{f} * \hat{g})(\boldsymbol{\omega}_{\boldsymbol{x}})$ for $\hat{f}, \hat{g} \in L^1(\mathbb{R}^N)$ is given by

$$\mathcal{F}^{-1}\left\{(\hat{f} * \hat{g})(\boldsymbol{\omega}_{\boldsymbol{x}})\right\} = (2\pi)^N f(\boldsymbol{x}) g(\boldsymbol{x}) \tag{4.16}$$

with $\hat{f} * \hat{g} \in L^1(\mathbb{R}^N)$.

Proof. The continuous Fourier transform (4.3) is to be calculated for the function given in (4.14), i.e., the transform is given by

$$\begin{aligned}\mathcal{F}\{(f*g)(\boldsymbol{x})\} &= \int_{\mathbb{R}^N} (f*g)(\boldsymbol{x}) \mathrm{e}^{\mathrm{i}\boldsymbol{\omega}_x^\mathsf{T}\boldsymbol{x}}\,\mathrm{d}\boldsymbol{x} \\ &= \int_{\mathbb{R}^N}\int_{\mathbb{R}^N} f(\boldsymbol{z})g(\boldsymbol{x}-\boldsymbol{z})\,\mathrm{d}\boldsymbol{z}\,\mathrm{e}^{-\mathrm{i}\boldsymbol{\omega}_x^\mathsf{T}\boldsymbol{x}}\,\mathrm{d}\boldsymbol{x}.\end{aligned}$$

Since f and g belong to $L^1(\mathbb{R}^N)$, Fubini's theorem can be applied and the iterated integrals can be interchanged as follows:

$$\begin{aligned}\mathcal{F}\{(f*g)(\boldsymbol{x})\} &= \int_{\mathbb{R}^N} f(\boldsymbol{z}) \underbrace{\int_{\mathbb{R}^N} g(\boldsymbol{x}-\boldsymbol{z})\mathrm{e}^{-\mathrm{i}\boldsymbol{\omega}_x^\mathsf{T}\boldsymbol{x}}\,\mathrm{d}\boldsymbol{x}}_{=\hat{g}(\boldsymbol{\omega}_x)\mathrm{e}^{-\mathrm{i}\boldsymbol{\omega}_x^\mathsf{T}\boldsymbol{z}}}\,\mathrm{d}\boldsymbol{z} \\ &= \int_{\mathbb{R}^N} f(\boldsymbol{z})\hat{g}(\boldsymbol{\omega}_x)\mathrm{e}^{-\mathrm{i}\boldsymbol{\omega}_x^\mathsf{T}\boldsymbol{z}}\,\mathrm{d}\boldsymbol{z} \\ &= \hat{g}(\boldsymbol{\omega}_x)\underbrace{\int_{\mathbb{R}^N} f(\boldsymbol{z})\mathrm{e}^{-\mathrm{i}\boldsymbol{\omega}_x^\mathsf{T}\boldsymbol{z}}\,\mathrm{d}\boldsymbol{z}}_{=\hat{f}(\boldsymbol{\omega}_x)} = \hat{g}(\boldsymbol{\omega}_x)\hat{f}(\boldsymbol{\omega}_x).\end{aligned}$$

□

Property 6: Correlation

For $f, g \in L^1(\mathbb{R}^N)$,

$$(g \star f)(\boldsymbol{x}) = \int_{\mathbb{R}^N} f(\boldsymbol{z}+\boldsymbol{x})g^*(\boldsymbol{z})\,\mathrm{d}\boldsymbol{z} \tag{4.17}$$

denotes the correlation and

$$\mathcal{F}\{(g \star f)(\boldsymbol{x})\} = \hat{f}(\boldsymbol{\omega}_x)\hat{g}^*(\boldsymbol{\omega}_x) \tag{4.18}$$

is the continuous Fourier transform. Besides, $f \star g \in L^1(\mathbb{R}^N)$. Equivalently, the inverse Fourier transform of the correlation $(\hat{f} \star \hat{g})(\boldsymbol{\omega}_x)$ for $\hat{f}, \hat{g} \in L^1(\mathbb{R}^N)$ is given by

$$\mathcal{F}^{-1}\Big\{(\hat{g} \star \hat{f})(\boldsymbol{\omega}_x)\Big\} = (2\pi)^N f(\boldsymbol{x})g^*(\boldsymbol{x}) \tag{4.19}$$

with $\hat{f} \star \hat{g} \in L^1(\mathbb{R}^N)$.

Proof. The cross-correlation can be expressed by the convolution between $g(\boldsymbol{x})$ and the complex-conjugate and inverted signal $f^*(-\boldsymbol{x})$ of $f(\boldsymbol{x})$, so that the Fourier transform reads

$$\mathcal{F}\{(g \star f)(\boldsymbol{x})\} = \mathcal{F}\{(f(\boldsymbol{x}) * g^*(-\boldsymbol{x}))(\boldsymbol{x})\} = \mathcal{F}\{f(\boldsymbol{x})\} \cdot \underbrace{\mathcal{F}\{g^*(-\boldsymbol{x})\}}_{\text{(4.9) and (4.12)}} = \hat{f}(\boldsymbol{\omega}_{\boldsymbol{x}})\hat{g}^*(\boldsymbol{\omega}_{\boldsymbol{x}}).$$

□

Property 7: Differentiation

Let f be in $L^1(\mathbb{R}^N)$, $g(\boldsymbol{x}) = \frac{\partial}{\partial x_i} f(\boldsymbol{x})$ be the continuous partial derivative of f with respect to x_i, and $g \in L^1(\mathbb{R}^N)$. Let the Fourier transform of f be denoted by $\hat{f}$. Then, the Fourier transform of g is

$$\hat{g}(\boldsymbol{\omega}_{\boldsymbol{x}}) = \mathcal{F}\left\{ \frac{\partial}{\partial x_i} f(\boldsymbol{x}) \right\} = \mathrm{i}\omega_{x_i} \hat{f}(\boldsymbol{\omega}_{\boldsymbol{x}}) \tag{4.20}$$

with $i \in \{1, 2, \ldots, N\}$.

Proof. Since f lies in $L^1(\mathbb{R}^N)$, the decay behavior of $f(\boldsymbol{x})$ is $\lim_{x_i \to \pm\infty} f(\boldsymbol{x}) = 0$. The desired property is obtained by integration by parts and exploiting the decay behavior of $f(\boldsymbol{x})$ and the fact that $f(\boldsymbol{x})$ is continuously differentiable in x_i, resulting in

$$\begin{aligned}
\hat{g}(\boldsymbol{\omega}_{\boldsymbol{x}}) &= \int_{\mathbb{R}^N} \left[\frac{\partial}{\partial x_i} f(\boldsymbol{x}) \right] \mathrm{e}^{-\mathrm{i}\boldsymbol{\omega}_{\boldsymbol{x}}^{\mathsf{T}} \boldsymbol{x}} \, \mathrm{d}\boldsymbol{x} = \mathrm{i}\omega_{x_i} \hat{f}(\boldsymbol{\omega}_{\boldsymbol{x}}) \\
&= \int_{\mathbb{R}^{N-1}} \int_{-\infty}^{\infty} \left[\frac{\partial}{\partial x_i} f(\boldsymbol{x}) \right] \mathrm{e}^{-\mathrm{i}\boldsymbol{\omega}_{\boldsymbol{x}}^{\mathsf{T}} \boldsymbol{x}} \, \mathrm{d}x_i \, \mathrm{d}\boldsymbol{x}' = \mathrm{i}\omega_{x_i} \hat{f}(\boldsymbol{\omega}_{\boldsymbol{x}}) \\
&= \int_{\mathbb{R}^{N-1}} \underbrace{f(\boldsymbol{x}) \mathrm{e}^{-\mathrm{i}\boldsymbol{\omega}_{\boldsymbol{x}}^{\mathsf{T}} \boldsymbol{x}} \Big|_{x_i=-\infty}^{\infty}}_{=0} \, \mathrm{d}\boldsymbol{x}' - \int_{\mathbb{R}^N} f(\boldsymbol{x}) \left[\frac{\partial}{\partial x_i} \mathrm{e}^{-\mathrm{i}\boldsymbol{\omega}_{\boldsymbol{x}}^{\mathsf{T}} \boldsymbol{x}} \right] \mathrm{d}\boldsymbol{x} \\
&= \mathrm{i}\omega_{x_i} \hat{f}(\boldsymbol{\omega}_{\boldsymbol{x}}),
\end{aligned}$$

where $\boldsymbol{x}' = (x_j)_{j \in \{1,2,\ldots,N\} \setminus \{i\}}$. □

Theorem 4.1: Plancherel theorem 1

If $f, g \in L^1(\mathbb{R}^N)$, then

$$\int_{\mathbb{R}^N} f(\boldsymbol{z})\hat{g}(\boldsymbol{z})\,\mathrm{d}\boldsymbol{z} = \int_{\mathbb{R}^N} \hat{f}(\boldsymbol{x})g(\boldsymbol{x})\,\mathrm{d}\boldsymbol{x} \tag{4.21}$$

holds with $f\hat{g}, \hat{f}g \in L^1(\mathbb{R}^N)$.

Proof of Theorem 4.1. Since $f, g \in L^1(\mathbb{R}^N)$ it follows that $\hat{f}, \hat{g} \in C_0(\mathbb{R}^N)$. The function space $C_0(\mathbb{R}^N)$ is a subset of $L^\infty(\mathbb{R}^N)$, therefore Hölder's inequality holds, i.e.,

$$\|f\hat{g}\|_{L^1} = \int_{\mathbb{R}^N} |f(\boldsymbol{z})\hat{g}(\boldsymbol{z})|\,\mathrm{d}\boldsymbol{z} \leq \|f\|_{L^1}\|\hat{g}\|_{L^\infty} < +\infty.$$

Equivalently, it holds that

$$\|\hat{f}g\|_{L^1} \leq \|\hat{f}\|_{L^\infty}\|g\|_{L^1} < +\infty.$$

It remains to show that the equality in (4.21) holds

$$\begin{aligned}
\int_{\mathbb{R}^N} f(\boldsymbol{z})\hat{g}(\boldsymbol{z})\,\mathrm{d}\boldsymbol{z} &= \int_{\mathbb{R}^N} f(\boldsymbol{z}) \int_{\mathbb{R}^N} g(\boldsymbol{x})\mathrm{e}^{-\mathrm{i}\boldsymbol{z}^\mathsf{T}\boldsymbol{x}}\,\mathrm{d}\boldsymbol{x}\,\mathrm{d}\boldsymbol{z} \\
&\overset{\dagger}{=} \int_{\mathbb{R}^N} g(\boldsymbol{x}) \int_{\mathbb{R}^N} f(\boldsymbol{z})\mathrm{e}^{-\mathrm{i}\boldsymbol{z}^\mathsf{T}\boldsymbol{x}}\,\mathrm{d}\boldsymbol{z}\,\mathrm{d}\boldsymbol{x} \\
&= \int_{\mathbb{R}^N} \hat{f}(\boldsymbol{x})g(\boldsymbol{x})\,\mathrm{d}\boldsymbol{x}.
\end{aligned}$$

The step labeled with † is allowed as the Fubini-Tonelli theorem applies. □

Theorem 4.2: Forward theorem

Let $\hat{f} \in L^1(\mathbb{R}^N)$ and f denote the inverse Fourier transform of $\hat{f}$. Then,

$$\hat{f}(\boldsymbol{\omega}_{\boldsymbol{x}}) = \lim_{n\to\infty} \int_{\mathbb{R}^N} f(\boldsymbol{x})\mathrm{e}^{-\frac{1}{2n}\|\boldsymbol{x}\|^2}\mathrm{e}^{-\mathrm{i}\boldsymbol{\omega}_{\boldsymbol{x}}^\mathsf{T}\boldsymbol{x}}\,\mathrm{d}\boldsymbol{x} \tag{4.22}$$

denotes the forward Fourier transform in the L^1-mean.

Theorem 4.3: Inversion theorem

Let $f \in L^1(\mathbb{R}^N)$ and $\hat{f}$ denote the Fourier transform of f. Then,

$$f(\boldsymbol{x}) = \lim_{n\to\infty} \frac{1}{(2\pi)^N} \int_{\mathbb{R}^N} \hat{f}(\boldsymbol{\omega_x}) \mathrm{e}^{-\frac{1}{2n}\|\boldsymbol{\omega_x}\|^2} \mathrm{e}^{\mathrm{i}\boldsymbol{x}^\mathsf{T}\boldsymbol{\omega_x}} \,\mathrm{d}\boldsymbol{\omega_x} \tag{4.23}$$

denotes the inverse Fourier transform in the L^1-mean.

Proof of Theorem 4.3. Only the inverse Fourier transform in the Theorem 4.3 is to be proved here. The reverse direction in Theorem 4.2 follows in a similar way by switching from the forward to the inverse Fourier transform. If $f \in L^1(\mathbb{R}^N)$, the convolution integral is given by

$$h_n(\boldsymbol{x}) = (f * g_n)(\boldsymbol{x})$$

with

$$g_n(\boldsymbol{x}) = \left(\frac{n}{2\pi}\right)^{\frac{N}{2}} \mathrm{e}^{-\frac{n\|\boldsymbol{x}\|^2}{2}}.$$

The Gaussian function g_n is a function in $L^1(\mathbb{R}^N) \cap L^\infty(\mathbb{R}^N)$. In addition, the Fourier transform of g_n is

$$\hat{g}_n(\boldsymbol{\omega_x}) = \mathcal{F}\{g_n(\boldsymbol{x})\} = \mathrm{e}^{-\frac{1}{2n}\|\boldsymbol{\omega_x}\|^2}.$$

The function $h_n(\boldsymbol{x})$ is in $L^1(\mathbb{R}^N)$ as the convolution of two functions is in $L^1(\mathbb{R}^N)$. Since $g_n \in L^p(\mathbb{R}^N)$ applies to all $p \in [1, +\infty]$, h_n inherits this property, which can be shown with Young's convolution inequality. Another important property of $g_n(\boldsymbol{x})$ is the fact that for all $n \in \mathbb{N}$ it holds that

$$\int_{\mathbb{R}^N} g_n(\boldsymbol{x}) \,\mathrm{d}\boldsymbol{x} = 1.$$

Due to the convolution property of the Fourier transform that a convolution in the spatial domain is a multiplication in the frequency domain (see Property 5), it follows

$$\hat{h}_n(\boldsymbol{\omega_x}) = \hat{f}(\boldsymbol{\omega_x})\hat{g}_n(\boldsymbol{\omega_x})$$

and, therefore,

$$\hat{h}_n(\boldsymbol{\omega_x}) = \hat{f}(\boldsymbol{\omega_x})\mathrm{e}^{-\frac{1}{2n}\|\boldsymbol{\omega_x}\|^2}.$$

For the limit of $\hat{g}_n(\boldsymbol{\omega_x})$ as n approaches infinity, we obtain

$$\lim_{n\to+\infty} \hat{g}_n(\boldsymbol{\omega_x}) = \lim_{n\to+\infty} \mathrm{e}^{-\frac{1}{2n}\|\boldsymbol{\omega_x}\|^2} = \mathrm{e}^{-0} = 1$$

and, consequently,

$$\lim_{n\to+\infty} \hat{h}_n(\boldsymbol{\omega_x}) = \lim_{n\to+\infty} \hat{f}(\boldsymbol{\omega_x})\hat{g}_n(\boldsymbol{\omega_x}) = \hat{f}(\boldsymbol{\omega_x}).$$

Thus, it also appears to be the case that

$$\lim_{n\to+\infty} h_n(\boldsymbol{x}) = \lim_{n\to+\infty} (f * g_n)(\boldsymbol{x}) = f(\boldsymbol{x})$$

in L^1-mean, which means that

$$\lim_{n\to\infty} \|f * g_n - f\|_{L^1} = 0.$$

Therefore, the L^1-convergence should now be checked. The first step is to rewrite $h_n - f$ slightly:

$$\begin{aligned}
(f * g_n)(\boldsymbol{x}) - f(\boldsymbol{x}) &= (f * g_n)(\boldsymbol{x}) - \Big(f(\boldsymbol{x}) \cdot \underbrace{1}_{\int_{\mathbb{R}^N} g_n(\boldsymbol{z})\,\mathrm{d}\boldsymbol{z}}\Big) \\
&= \int_{\mathbb{R}^N} \Big(f(\boldsymbol{x}-\boldsymbol{z}) - f(\boldsymbol{x})\Big) g_n(\boldsymbol{z})\,\mathrm{d}\boldsymbol{z} \\
&= \int_{\mathbb{R}^N} \Big(f(\boldsymbol{x}-\boldsymbol{z}) - f(\boldsymbol{x})\Big) \left(\frac{n}{2\pi}\right)^{\frac{N}{2}} \mathrm{e}^{-\frac{n\|\boldsymbol{z}\|^2}{2}}\,\mathrm{d}\boldsymbol{z} \\
&\underbrace{=}_{\boldsymbol{z}=\frac{1}{\sqrt{n}}\boldsymbol{\nu}} \int_{\mathbb{R}^N} \left(f\left(\boldsymbol{x} - \frac{\boldsymbol{\nu}}{\sqrt{n}}\right) - f(\boldsymbol{x})\right) \left(\frac{1}{2\pi}\right)^{\frac{N}{2}} \mathrm{e}^{-\frac{\|\boldsymbol{\nu}\|^2}{2}}\,\mathrm{d}\boldsymbol{\nu}.
\end{aligned}$$

From this it follows for $\|f * g_n - f\|_{L^1}$ that

$$\begin{aligned}
\|f * g_n - f\|_{L^1} &= \int_{\mathbb{R}^N} \left| \int_{\mathbb{R}^N} \left(f\left(\boldsymbol{x} - \frac{\boldsymbol{\nu}}{\sqrt{n}}\right) - f(\boldsymbol{x}) \right) \left(\frac{1}{2\pi}\right)^{\frac{N}{2}} \mathrm{e}^{-\frac{\|\boldsymbol{\nu}\|^2}{2}} \,\mathrm{d}\boldsymbol{\nu} \right| \mathrm{d}\boldsymbol{x} \\
&\leq \int_{\mathbb{R}^N} \int_{\mathbb{R}^N} \left| f\left(\boldsymbol{x} - \frac{\boldsymbol{\nu}}{\sqrt{n}}\right) - f(\boldsymbol{x}) \right| \left(\frac{1}{2\pi}\right)^{\frac{N}{2}} \mathrm{e}^{-\frac{\|\boldsymbol{\nu}\|^2}{2}} \,\mathrm{d}\boldsymbol{\nu} \,\mathrm{d}\boldsymbol{x} \\
&= \int_{\mathbb{R}^N} \underbrace{\int_{\mathbb{R}^N} \left| f\left(\boldsymbol{x} - \frac{\boldsymbol{\nu}}{\sqrt{n}}\right) - f(\boldsymbol{x}) \right| \mathrm{d}\boldsymbol{x}}_{\leq 2\|f\|_{L^1}} \left(\frac{1}{2\pi}\right)^{\frac{N}{2}} \mathrm{e}^{-\frac{\|\boldsymbol{\nu}\|^2}{2}} \,\mathrm{d}\boldsymbol{\nu} \\
&\leq 2\|f\|_{L^1} \underbrace{\|g_1\|_{L^1}}_{=1} = 2\|f\|_{L^1},
\end{aligned}$$

i.e., $\|f * g_n - f\|_{L^1}$ is upper bounded and it additionally holds that

$$\lim_{n\to+\infty} \int_{\mathbb{R}^N} \left| f\left(\boldsymbol{x} - \frac{\boldsymbol{\nu}}{\sqrt{n}}\right) - f(\boldsymbol{x}) \right| \mathrm{d}\boldsymbol{x} = 0.$$

Consequently, $\lim_{n\to\infty} \|f * g_n - f\|_{L^1} = 0$ holds. Therefore, the Lebesgue's dominated convergence theorem can be applied, which implies that

$$\lim_{n\to\infty} \int_{\mathbb{R}^N} (f * g_n)(\boldsymbol{x}) \,\mathrm{d}\boldsymbol{x} = \int_{\mathbb{R}^N} f(\boldsymbol{x}) \,\mathrm{d}\boldsymbol{x}.$$

Consequently, one has

$$\lim_{n\to\infty} (f * g_n)(\boldsymbol{x}) = f(\boldsymbol{x})$$

almost everywhere.

It remains to show that (4.23) is indeed an inversion formula. Therefore, the auxiliary function

$$G_{n,\boldsymbol{x}}(\boldsymbol{\omega}_{\boldsymbol{z}}) = \mathcal{F}^{-1}\{g_n(\boldsymbol{x} - \boldsymbol{z})\} = \frac{1}{(2\pi)^N} \mathrm{e}^{-\frac{\|\boldsymbol{\omega}_{\boldsymbol{z}}\|^2}{2n}} \mathrm{e}^{\mathrm{i}\boldsymbol{\omega}_{\boldsymbol{z}}^{\mathsf{T}}\boldsymbol{x}}$$

is defined. Consequently,

$$g_n(\boldsymbol{x} - \boldsymbol{z}) = \hat{G}_{n,\boldsymbol{x}}(\boldsymbol{z}).$$

With the help of Theorem 4.1 the following is obtained:

$$\begin{aligned} h_n(\boldsymbol{x}) = (f * g_n)(\boldsymbol{x}) &= \int_{\mathbb{R}^N} f(\boldsymbol{z}) g_n(\boldsymbol{x} - \boldsymbol{z}) \,\mathrm{d}\boldsymbol{z} \\ &= \int_{\mathbb{R}^N} f(\boldsymbol{z}) \hat{G}_{n,\boldsymbol{x}}(\boldsymbol{z}) \,\mathrm{d}\boldsymbol{z} = \int_{\mathbb{R}^N} \hat{f}(\boldsymbol{\omega}_z) G_{n,\boldsymbol{x}}(\boldsymbol{\omega}_z) \,\mathrm{d}\boldsymbol{\omega}_z \\ &= \int_{\mathbb{R}^N} \hat{f}(\boldsymbol{\omega}_z) \frac{1}{(2\pi)^N} \mathrm{e}^{-\frac{\|\boldsymbol{\omega}_z\|^2}{2n}} \mathrm{e}^{\mathrm{i}\boldsymbol{\omega}_z^\mathsf{T}\boldsymbol{x}} \,\mathrm{d}\boldsymbol{\omega}_z \\ &= \frac{1}{(2\pi)^N} \int_{\mathbb{R}^N} \hat{f}(\boldsymbol{\omega}_z) \mathrm{e}^{-\frac{\|\boldsymbol{\omega}_z\|^2}{2n}} \mathrm{e}^{\mathrm{i}\boldsymbol{\omega}_z^\mathsf{T}\boldsymbol{x}} \,\mathrm{d}\boldsymbol{\omega}_z. \end{aligned}$$

Finally, the limit of h_n as n approaches infinity is

$$\begin{aligned} f(\boldsymbol{x}) &= \lim_{n\to\infty} h_n(\boldsymbol{x}) \\ &= \lim_{n\to\infty} \frac{1}{(2\pi)^N} \int_{\mathbb{R}^N} \hat{f}(\boldsymbol{\omega}_x) \mathrm{e}^{-\frac{\|\boldsymbol{\omega}_x\|^2}{2n}} \mathrm{e}^{\mathrm{i}\boldsymbol{\omega}_x^\mathsf{T}\boldsymbol{x}} \,\mathrm{d}\boldsymbol{\omega}_x. \end{aligned}$$

□

Definition 4.2: Delta distribution

A sequence for $n \in \mathbb{N}$ defined by $g_n(\boldsymbol{x})$ which has the properties

$$\lim_{n\to\infty} \int_{\mathbb{R}^N} g_n(\boldsymbol{x}) \,\mathrm{d}\boldsymbol{x} = 1,$$

$$\lim_{n\to\infty} (f * g_n)(\boldsymbol{x}) = f(\boldsymbol{x}),$$

and

$$\lim_{n\to\infty} \int_{\mathbb{R}^N} f(\boldsymbol{x}) g_n(\boldsymbol{x}) \,\mathrm{d}\boldsymbol{x} = f(\boldsymbol{0}),$$

is commonly called Dirac sequence, delta distribution, or Dirac distribution. It is often simply denoted as $\delta_{\boldsymbol{0}}(\boldsymbol{x})$ with the properties

$$\int_{\mathbb{R}^N} \delta_{\boldsymbol{0}}(\boldsymbol{x}) \,\mathrm{d}\boldsymbol{x} = 1,$$

$$(f * \delta_{\boldsymbol{0}})(\boldsymbol{x}) = f(\boldsymbol{x}),$$

$$\int_{\mathbb{R}^N} f(\boldsymbol{x}) \delta_{\boldsymbol{0}}(\boldsymbol{x}) \,\mathrm{d}\boldsymbol{x} = f(\boldsymbol{0}).$$

A common, but not the only function that implies such a sequence is the Gaussian function with

$$g_n(\boldsymbol{x}) = \left(\frac{n}{2\pi}\right)^{\frac{N}{2}} \mathrm{e}^{-\frac{n\|\boldsymbol{x}\|^2}{2}}. \tag{4.24}$$

But even if the delta distribution $\delta_{\mathbf{0}}(\boldsymbol{x})$ is often used like calculating with a classical function, there is no function that behaves like the delta distribution.

4.1.2 Fourier Transform on $L^2(\mathbb{R}^N)$

The Fourier transform can be extended to functions that lie in $L^2(\mathbb{R}^N)$. The trick here is to use the fact that $L^2(\mathbb{R}^N)$ is a Hilbert space and therefore, for two functions $f, g \in L^2(\mathbb{R}^N)$, the scalar product

$$\langle f, g\rangle_{L^2(\mathbb{R}^N)} = \int_{\mathbb{R}^N} f^*(\boldsymbol{x}) g(\boldsymbol{x})\,\mathrm{d}\boldsymbol{x}$$

exists. As a shorthand notation the scalar product is also written in the following as $\langle f, g\rangle_{L^2}$. The induced L^2-norm associated with the scalar product is written as

$$\|f\|_{L^2} = \sqrt{\langle f, f\rangle_{L^2}}.$$

Let $\tilde{f}(\boldsymbol{x}) = f(\boldsymbol{x})\mathrm{e}^{-\mathrm{i}\boldsymbol{\omega}_x^{\mathsf{T}}\boldsymbol{x}}$ and $f \in L^2(\mathbb{R}^N)$, where $\boldsymbol{\omega}_{\boldsymbol{x}} \in \mathbb{R}^N$ is a fixed vector. This choice for $\tilde{f}(\boldsymbol{x})$ therefore results in the norm

$$\begin{aligned}\|\tilde{f}\|_{L^2}^2 = \langle \tilde{f}, \tilde{f}\rangle_{L^2} &= \int_{\mathbb{R}^N} f^*(\boldsymbol{x})\mathrm{e}^{\mathrm{i}\boldsymbol{\omega}_x^{\mathsf{T}}\boldsymbol{x}} f(\boldsymbol{x})\mathrm{e}^{-\mathrm{i}\boldsymbol{\omega}_x^{\mathsf{T}}\boldsymbol{x}}\,\mathrm{d}\boldsymbol{x} \\ &= \int_{\mathbb{R}^N} f^*(\boldsymbol{x}) f(\boldsymbol{x})\,\mathrm{d}\boldsymbol{x} = \langle f, f\rangle_{L^2} = \|f\|_{L^2}^2,\end{aligned}$$

and, thus, $\tilde{f} \in L^2(\mathbb{R}^N)$ actually also holds. For functions in $L^2(\mathbb{R}^N)$ it is therefore sufficient to use a convergent sequence of functions $f_n \in L^1(\mathbb{R}^N) \cap L^2(\mathbb{R}^N)$ so that the function f_n converges to $f \in L^2(\mathbb{R}^N)$ [37], which means that

$$\lim_{n\to\infty} \|f - f_n\|_{L^2} = 0$$

or, as a shorthand, $f_n \to f$. Since $L^2(\mathbb{R}^N)$ is a Hilbert space and $L^1(\mathbb{R}^N) \cap L^2(\mathbb{R}^N)$ is dense in $L^2(\mathbb{R}^N)$, any function $f \in L^2(\mathbb{R}^N)$ can be approximated by a Cauchy sequence

of functions $f_n \in L^1(\mathbb{R}^N) \cap L^2(\mathbb{R}^N)$. For functions in $L^1(\mathbb{R}^N) \cap L^2(\mathbb{R}^N)$ the Fourier transform maps to $L^2(\mathbb{R}^N)$. Consequently, the sequence $f_n \in L^1(\mathbb{R}^N) \cap L^2(\mathbb{R}^N)$ is mapped to the sequence $\hat{f}_n \in L^2(\mathbb{R}^N)$, which in turn must be a Cauchy sequence. However, since L^2 is a Hilbert space, the space is closed and all Cauchy sequences must therefore converge in L^2. The L^2 Fourier transform is unique in the sense that a second sequence $g_\ell \to f$, with $g_\ell \in L^1(\mathbb{R}^N) \cap L^2(\mathbb{R}^N)$ and $\hat{g}_\ell \in L^2(\mathbb{R}^N)$, converges almost everywhere to the same function in the L^2-mean, i.e.,

$$\lim_{n,\ell\to\infty} \|\hat{f}_n - \hat{g}_\ell\|_{L^2} = 0.$$

The forward Fourier transform of a function $f \in L^2(\mathbb{R}^N)$, with $f_n \in L^1(\mathbb{R}^N) \cap L^2(\mathbb{R}^N)$ and $f_n \to f$, is given by

$$\hat{f}(\boldsymbol{\omega}_{\boldsymbol{x}}) = \lim_{n\to\infty} \int_{\mathbb{R}^N} f_n(\boldsymbol{x}) \mathrm{e}^{-\mathrm{i}\boldsymbol{\omega}_{\boldsymbol{x}}^\mathsf{T}\boldsymbol{x}} \,\mathrm{d}\boldsymbol{x}, \tag{4.25}$$

and the inverse Fourier transform of a function $\hat{f} \in L^2(\mathbb{R}^N)$, with $\hat{f}_n \in L^1(\mathbb{R}^N) \cap L^2(\mathbb{R}^N)$ and $\hat{f}_n \to \hat{f}$, is given by

$$f(\boldsymbol{x}) = \lim_{n\to\infty} \frac{1}{(2\pi)^N} \int_{\mathbb{R}^N} \hat{f}_n(\boldsymbol{\omega}_{\boldsymbol{x}}) \mathrm{e}^{\mathrm{i}\boldsymbol{x}^\mathsf{T}\boldsymbol{\omega}_x} \,\mathrm{d}\boldsymbol{\omega}_{\boldsymbol{x}}. \tag{4.26}$$

For example, two possible sequences for $f, \hat{f} \in L^2(\mathbb{R}^N)$ could be

$$f_n(\boldsymbol{x}) = f(\boldsymbol{x}) \mathrm{e}^{-\frac{1}{2n}\|\boldsymbol{x}\|_2^2} \qquad \text{and} \qquad \hat{f}_n(\boldsymbol{\omega}_{\boldsymbol{x}}) = \hat{f}(\boldsymbol{\omega}_{\boldsymbol{x}}) \mathrm{e}^{-\frac{1}{2n}\|\boldsymbol{\omega}_x\|_2^2},$$

leading to equivalent cases as for $L^1(\mathbb{R}^N)$. It can be verified that f_n and $\hat{f}_n$ are indeed in $L^1(\mathbb{R}^N) \cap L^2(\mathbb{R}^N)$.

Properties in $L^2(\mathbb{R}^N)$

Theorem 4.4: Parseval's theorem

If f and $\hat{g}^*$ belong to $L^1(\mathbb{R}^N) \cap L^2(\mathbb{R}^N)$, and $\hat{f}$ and g denote their Fourier transform and inverse Fourier transform, respectively, then the following holds

$$\int_{\mathbb{R}^N} f(\boldsymbol{x}) g^*(\boldsymbol{x}) \, \mathrm{d}\boldsymbol{x} = \frac{1}{(2\pi)^N} \int_{\mathbb{R}^N} \hat{f}(\boldsymbol{\omega}_{\boldsymbol{x}}) \hat{g}^*(\boldsymbol{\omega}_{\boldsymbol{x}}) \, \mathrm{d}\boldsymbol{\omega}_{\boldsymbol{x}}. \tag{4.27}$$

Proof of Theorem 4.4. The functions f and $\hat{g}$ belong to $L^1(\mathbb{R}^N) \cap L^2(\mathbb{R}^N)$, therefore $\hat{f}$ and g are well defined. The following is valid for the cross-correlation with a fixed $\boldsymbol{x}_0 \in \mathbb{R}^N$:

$$\begin{aligned}
(f \star g)(\boldsymbol{x}_0) &= \int_{\mathbb{R}^N} f^*(\boldsymbol{z}) g(\boldsymbol{z} + \boldsymbol{x}_0) \, \mathrm{d}\boldsymbol{z} \\
&= \int_{\mathbb{R}^N} f^*(\boldsymbol{z}) \frac{1}{(2\pi)^N} \int_{\mathbb{R}^N} \hat{g}(\boldsymbol{\omega}_{\boldsymbol{x}}) \mathrm{e}^{\mathrm{i}(\boldsymbol{z}+\boldsymbol{x}_0)^{\mathsf{T}} \boldsymbol{\omega}_{\boldsymbol{x}}} \, \mathrm{d}\boldsymbol{\omega}_{\boldsymbol{x}} \, \mathrm{d}\boldsymbol{z} \\
&\overset{\dagger}{=} \frac{1}{(2\pi)^N} \int_{\mathbb{R}^N} \hat{g}(\boldsymbol{\omega}_{\boldsymbol{x}}) \mathrm{e}^{\mathrm{i}\boldsymbol{x}_0^{\mathsf{T}} \boldsymbol{\omega}_{\boldsymbol{x}}} \underbrace{\int_{\mathbb{R}^N} f^*(\boldsymbol{z}) \mathrm{e}^{\mathrm{i}\boldsymbol{z}^{\mathsf{T}} \boldsymbol{\omega}_{\boldsymbol{x}}} \, \mathrm{d}\boldsymbol{z}}_{=\hat{f}^*(\boldsymbol{\omega}_{\boldsymbol{x}})} \, \mathrm{d}\boldsymbol{\omega}_{\boldsymbol{x}} \\
&= \frac{1}{(2\pi)^N} \int_{\mathbb{R}^N} \hat{g}(\boldsymbol{\omega}_{\boldsymbol{x}}) \hat{f}^*(\boldsymbol{\omega}_{\boldsymbol{x}}) \mathrm{e}^{\mathrm{i}\boldsymbol{x}_0^{\mathsf{T}} \boldsymbol{\omega}_{\boldsymbol{x}}} \, \mathrm{d}\boldsymbol{\omega}_{\boldsymbol{x}}.
\end{aligned}$$

The Fubini theorem is used in the † step. The desired result is obtained for $\boldsymbol{x}_0 = \boldsymbol{0}$. □

Theorem 4.5: Plancherel theorem 2

If f or $\hat{f}$ belongs to $L^1(\mathbb{R}^N) \cap L^2(\mathbb{R}^N)$, then it holds that

$$\|f\|_{L^2}^2 = \int_{\mathbb{R}^N} |f(\boldsymbol{x})|^2 \, \mathrm{d}\boldsymbol{x} = \frac{1}{(2\pi)^N} \int_{\mathbb{R}^N} \left|\hat{f}(\boldsymbol{\omega}_{\boldsymbol{x}})\right|^2 \, \mathrm{d}\boldsymbol{\omega}_{\boldsymbol{x}} = \frac{1}{(2\pi)^N} \|\hat{f}\|_{L^2}^2 \tag{4.28}$$

and, consequently, that $\hat{f} \in L^2(\mathbb{R}^N)$ and $f \in L^2(\mathbb{R}^N)$.

Proof of Theorem 4.5. Let the function $f \in L^1(\mathbb{R}^N) \cap L^2(\mathbb{R}^N)$ and let a second function be defined as $g(\boldsymbol{x}) = f^*(-\boldsymbol{x})$. Furthermore, the function $h(\boldsymbol{x}) = (f * g)(\boldsymbol{x})$ is defined.

The Fourier transform of $h(\boldsymbol{x})$ is

$$\hat{h}(\boldsymbol{\omega}_x) = \mathcal{F}\{h(\boldsymbol{x})\} = \hat{f}(\boldsymbol{\omega}_x)\hat{g}(\boldsymbol{\omega}_x) = \hat{f}(\boldsymbol{\omega}_x)\hat{f}^*(\boldsymbol{\omega}_x) = \left|\hat{f}(\boldsymbol{\omega}_x)\right|^2.$$

The function $h \in L^1(\mathbb{R}^N)$ is continuous in $\boldsymbol{x} = \boldsymbol{0}$ and the result is $\hat{h}(\boldsymbol{\omega}_x) \geq 0$, from which it follows that $\hat{h} \in L^1(\mathbb{R}^N)$ also holds, i.e.,

$$\begin{aligned}\int_{\mathbb{R}^N} \left|\hat{f}(\boldsymbol{\omega}_x)\right|^2 \mathrm{d}\boldsymbol{\omega}_x &= \int_{\mathbb{R}^N} \hat{h}(\boldsymbol{\omega}_x)\,\mathrm{d}\boldsymbol{\omega}_x = (2\pi)^N h(\boldsymbol{0}) \\ &= (2\pi)^N \int_{\mathbb{R}^N} f(\boldsymbol{0}-\boldsymbol{z}) f^*(-\boldsymbol{z})\,\mathrm{d}\boldsymbol{z} = (2\pi)^N \int_{\mathbb{R}^N} f(\boldsymbol{x}) f^*(\boldsymbol{x})\,\mathrm{d}\boldsymbol{z} \\ &= (2\pi)^N \int_{\mathbb{R}^N} |f(\boldsymbol{x})|^2\,\mathrm{d}\boldsymbol{x}.\end{aligned}$$

It therefore follows that $\hat{f} \in L^2(\mathbb{R}^N)$ also holds. The mathematical claim for the function $\hat{f} \in L^1(\mathbb{R}^N) \cap L^2(\mathbb{R}^N)$ follows in a similar way. □

4.1.3 Fourier Transform of Radial Functions

In this section, a correspondence between the N-dimensional Fourier transform of a radial function and the Hankel transform is introduced. The Hankel transform is used to calculate the two-dimensional Fourier transform of the normalized Langevin function in Chapter 6. First, a definition of the radial function will be given.

Definition 4.3: Radial function

A function $f : \mathbb{R}^N \to \mathbb{C}$ is a radial (rotational invariant) function if a one-dimensional function $F : \mathbb{R}_+ \to \mathbb{C}$ exist such that

$$f(\boldsymbol{x}) = F(\|\boldsymbol{x}\|). \tag{4.29}$$

The following lemma helps to check under which conditions a radial function is integrable.

Lemma 4.2. *If $f : \mathbb{R}^N \to \mathbb{C}$ with $f(\boldsymbol{x}) = F(\|\boldsymbol{x}\|)$ is a radial function, then the identity*

$$\int_{\mathbb{R}^N} f(\boldsymbol{x})\,\mathrm{d}\boldsymbol{x} = \int_{\mathbb{R}^N} F(\|\boldsymbol{x}\|)\,\mathrm{d}\boldsymbol{x} = S_{N-1}\int_0^\infty F(r)r^{N-1}\,\mathrm{d}r \tag{4.30}$$

holds, where

$$S_{N-1} = \frac{2\pi^{\frac{N}{2}}}{\Gamma\left(\frac{N}{2}\right)} \tag{4.31}$$

denotes the surface of the unit $(N-1)$-dimensional sphere.

A proof can be found in [98].

The following corollary could be derived as a direct consequence of Lemma 4.2.

Corollary 4.3. *Let a radial function $f : \mathbb{R}^N \to \mathbb{C}$ be defined by*

$$f(\boldsymbol{x}) = F(\|\boldsymbol{x}\|),$$

with $F : \mathbb{R}_+ \to \mathbb{C}$. Then $f \in L^p(\mathbb{R}^N)$ with $p \in [1, \infty)$ if and only if

$$r^{\frac{N-1}{p}} F \in L^p(\mathbb{R}_+).$$

For $p = \infty$, it follows that $f \in L^\infty(\mathbb{R}^N)$ if and only if $F \in L^\infty(\mathbb{R}_+)$.

Proof of Corollary 4.3. If the radial function $f : \mathbb{R}^N \to \mathbb{R}$ is given by $f(\boldsymbol{x}) = F(\|\boldsymbol{x}\|)$ in $L^p(\mathbb{R}^N)$, then the following holds:

$$\int_{\mathbb{R}^N} |f(\boldsymbol{x})|^p\,\mathrm{d}\boldsymbol{x} < \infty.$$

When $f(\boldsymbol{x})$ is radial, then $|f(\boldsymbol{x})|^p = |F(\|\boldsymbol{x}\|)|^p$ is also radial and Lemma 4.2 can be applied, resulting in

$$\int_{\mathbb{R}^N} |f(\boldsymbol{x})|^p\,\mathrm{d}\boldsymbol{x} = S_{N-1}\int_0^\infty |F(r)|^p r^{N-1}\,\mathrm{d}r = S_{N-1}\int_0^\infty |F(r)r^{\frac{N-1}{p}}|^p\,\mathrm{d}r < \infty.$$

It follows that $r^{\frac{N-1}{p}} F \in L^p(\mathbb{R}_+)$. The reverse direction follows in a similar manner. □

The next definition refers to the Hankel transform [77] and relates it to the N-dimensional Fourier transform of radial functions. The relationship of the radial function to the Fourier transform can be found, for example, in [37, Ch. B5] and is used in Chapter 6 to derive the two-dimensional Fourier transform of the "normalized" Langevin function. Note that there are different but related definitions of the Hankel transform in the literature.

Definition 4.4: Hankel transform and N-dimensional Fourier transform

The Hankel transform with order $\mu > -\frac{1}{2}$ of a function $g : \mathbb{R}_+ \to \mathbb{C}$ is defined as

$$g_\mu(s) = \mathcal{H}_\mu \{g(r)\} = \int_0^\infty J_\mu(sr) g(r) r \, \mathrm{d}r,$$

where $J_\mu : \mathbb{R} \to \mathbb{R}$ denotes the μ-th Bessel function of the first kind.
The Hankel transform is self-inverse, i.e., $g(r) = \mathcal{H}_\mu \{\mathcal{H}_\mu \{g(r)\}\}$, for functions that are piecewise continuous, of bounded variation in $(0, \infty)$, and fulfill the following condition:

$$\int_0^\infty r^{\frac{1}{2}} |g(r)| \, \mathrm{d}r < \infty.$$

If $f : \mathbb{R}^N \to \mathbb{C}$ is a radial function such that

$$f(\boldsymbol{x}) = F(\|\boldsymbol{x}\|) = F(r),$$

where $F : \mathbb{R}_+ \to \mathbb{C}$ denotes a one-dimensional function, then the N-dimensional Fourier transform reads

$$\hat{f}(\boldsymbol{\omega_x}) = \hat{F}_N(s) = \hat{F}_N(\|\boldsymbol{\omega_x}\|),$$

with

$$\hat{F}_N(s) = (2\pi)^{\frac{N}{2}} \, s^{-\frac{N-2}{2}} \mathcal{H}_{\frac{N-2}{2}} \left\{ r^{\frac{N-2}{2}} F(r) \right\}.$$

5 Orthogonal Polynomials and Bessel Functions

This chapter covers a group of orthogonal polynomials and Bessel functions that are used in the analytical Fourier representation of MPI as well as in the representation of the magnetization curves of SPIOs. For this purpose, central properties of these functions are presented and the connection between Chebyshev polynomials and Bessel functions via a Fourier transform is demonstrated. Most of the properties shown are known from the literature.

5.1 Orthogonal Polynomials

Orthogonal polynomials are a special class of functions that can be used to build up a function space related to an inner product. In general, classical polynomials are of the form

$$p_n(\xi) = \sum_{k=0}^{n} c_{nk} \xi^k, \tag{5.1}$$

where $c_{nk} \in \mathbb{R}$ are real-valued coefficients and $n \in \mathbb{N}$ denotes the degree of the polynomial with the definition that $0^0 = 1$.

A sequence of polynomials $(p_\ell)_{\ell \in \mathbb{N}_0}$ is orthogonal on an open interval $\Omega = (a, b)$ with $a, b \in \mathbb{R}$, where it is also allowed that $a = -\infty$ or $b = \infty$ and with respect to a

non-negative weighting function $w : \Omega \to \mathbb{R}_+ \backslash \{0\}$, if the following orthogonality relationship applies for any two polynomials from the sequence

$$\langle p_n, p_m \rangle_w = \int_\Omega p_n(t) p_m^*(t) w(t)\,\mathrm{d}t = \begin{cases} h_n, & \text{if } n = m, \\ 0, & \text{if } n \neq m, \end{cases}$$

with the positive and finite weights

$$h_n = \int_\Omega |p_n(t)|^2 w(t)\,\mathrm{d}t > 0.$$

Let a function $f : \Omega \to \mathbb{C}$ has the formal series expansion

$$f(\xi) = \sum_{k=0}^{\infty} f_k p_k(\xi), \tag{5.2}$$

with the coefficients $f_k \in \mathbb{C}$, then the ℓ-th coefficient of the series can be formally calculated by

$$f_\ell = \frac{1}{h_\ell} \int_\Omega f(t) p_\ell(t) w(t)\,\mathrm{d}t. \tag{5.3}$$

For any function f, however, the question arises under which conditions the formal series in (5.2) with the calculated coefficients from (5.3) converges pointwise to the function f in a norm.

To ensure that the coefficients exist, $f(\xi)p_\ell(\xi)w(\xi)$ must be integrable for all $\ell \in \mathbb{N}_0$ on the interval $\Omega = (a, b)$. Unfortunately, this does not guarantee that the series in (5.2) is convergent, and if it is, there is no certainty that the series will converge to the original function f. For a class of classical orthogonal polynomials of the Jacobi polynomial type, i.e., Chebyshev polynomials, this question was answered in [78, 79, 114]. For Hermite and generalized Laguerre polynomials, similar results are presented in [7].

Be

$$L_w^2(\Omega) = \left\{ f : \Omega \to \mathbb{C} \;\middle|\; \left(\int_\Omega |f(t)|^2 w(t)\,\mathrm{d}t \right)^{\frac{1}{2}} < \infty \right\},$$

the associated square-integrable Hilbert space with respect to the weighting function w and the interval $\Omega = (a, b)$. For functions from $f \in L_w^2(\Omega)$, the mean convergence in terms of $L_w^2(\Omega)$ for the series in (5.2) with the coefficients from (5.3) can be derived directly from the Hilbert space. If $f \in L_w^2(\Omega)$ is valid, then $w^{\frac{1}{2}} f \in L^2(\Omega)$ is also true in the "classical" unweighted L^2-function space.

In particular, the Chebyshev polynomials of the first and second kind and the generalized Laguerre polynomials will be briefly introduced here, as they are required as central components of the work.

5.1.1 Chebyshev Polynomials

Both kinds of Chebyshev polynomials – first and second kind – are orthogonal on the interval $(-1, 1)$ with the corresponding weighting functions. In case of Chebyshev polynomials of the first kind, the weighting function reads

$$w_I(\xi) = \frac{1}{\sqrt{1 - \xi^2}},$$

while the Chebyshev polynomials of the second kind will have the weighting function

$$w_{II}(\xi) = \sqrt{1 - \xi^2}.$$

Let us denote the Chebyshev polynomial of the first kind with order n by $T_n : \mathbb{R} \to \mathbb{R}$ and the Chebyshev polynomial of the second kind with order n by $U_n : \mathbb{R} \to \mathbb{R}$.

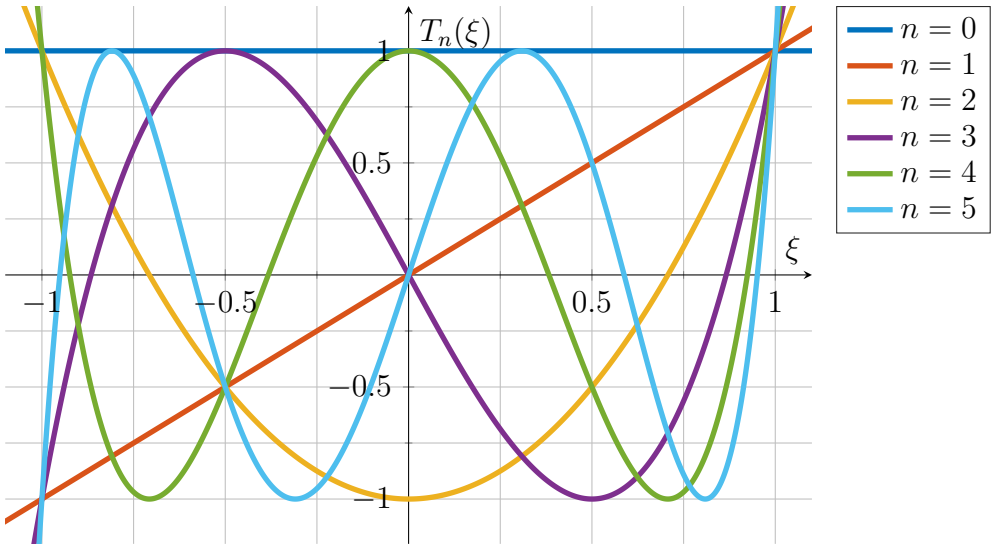

Figure 5.1: The Chebyshev polynomials of the first kind with orders $n \in \{0, 1, \ldots, 5\}$.

Chebyshev Polynomials of the First Kind

The Chebyshev polynomials of the first kind exemplarily shown in Figure 5.1 with the orders $n \in \{0, 1, \ldots, 5\}$ can be obtained by the recurrence relation [1, §22.2.4, §22.4.4]

$$\begin{aligned} T_0(\xi) &= 1 \\ T_1(\xi) &= \xi \\ T_{n+1}(\xi) &= 2\xi T_n(\xi) - T_{n-1}(\xi). \end{aligned} \tag{5.4}$$

An important property of Chebyshev polynomials of the first kind is the function composition with the cosine function [1, §22.3.15]

$$T_n(\cos\theta) = \cos(n\theta), \tag{5.5}$$

which in turn can be used to define the Chebyshev polynomials of the first kind by

$$T_n(\xi) = \begin{cases} \cos(n \arccos \xi), & \text{if } |\xi| \leq 1, \\ \cosh(n \operatorname{arcosh} \xi), & \text{if } \xi > 1, \\ (-1)^n \cosh(n \operatorname{arcosh}(-\xi)) & \text{if } \xi < -1. \end{cases} \tag{5.6}$$

The orthogonality relation for Chebyshev polynomials of the first kind is given by

$$\int_{-1}^{1} T_n(t)T_m(t)\frac{\mathrm{d}t}{\sqrt{1-t^2}} = \begin{cases} \pi, & \text{if } n = m = 0, \\ \frac{\pi}{2}, & \text{if } n = m \neq 0, \\ 0, & \text{if } n \neq m. \end{cases}$$

Let the function $f : [-1, 1] \to \mathbb{C}$ be represented by the series coefficients $f_k : \mathbb{N}_0 \to \mathbb{C}$ with the help of Chebyshev polynomials of the first kind, i.e.,

$$f(\xi) = \sum_{k\in\mathbb{N}_0} f_k T_k(\xi), \tag{5.7}$$

where

$$f_\ell = \frac{2-\delta_{0\ell}}{\pi}\int_{-1}^{1} f(t)T_\ell(t)\frac{\mathrm{d}t}{\sqrt{1-t^2}}. \tag{5.8}$$

The calculation of the coefficients f_ℓ can therefore also be calculated using the substitution $t = \cos\theta$, $\mathrm{d}t = -\sin\theta\,\mathrm{d}\theta$ by

$$\begin{aligned} f_\ell &= \frac{2-\delta_{0\ell}}{\pi}\int_{-1}^{1} f(t)T_\ell(t)\frac{\mathrm{d}t}{\sqrt{1-t^2}} \\ &= \frac{2-\delta_{0\ell}}{\pi}\int_{\pi}^{0} f(\cos\theta)T_\ell(\cos\theta)\frac{-\sin\theta\,\mathrm{d}\theta}{\sqrt{1-\cos^2\theta}} \\ &= \frac{2-\delta_{0\ell}}{\pi}\int_{0}^{\pi} f(\cos\theta)\cos(\ell\theta)\,\mathrm{d}\theta. \end{aligned} \tag{5.9}$$

Consequently, the coefficients of $f(\xi)$ to represent f by a series of Chebyshev polynomials of the first kind can be calculated by the Fourier cosine series of $f(\cos\theta)$.

The formal series in (5.7) is closely related to the Fourier cosine series, which can be verified by substituting $\xi = \cos\theta$ with $\theta \in [0, \pi]$. By performing this substitution and using the relationship (5.5), one obtains

$$\begin{aligned} f(\cos(\theta)) &= \sum_{k\in\mathbb{N}_0} f_k T_k(\cos\theta) \\ &= \sum_{k\in\mathbb{N}_0} f_k \cos(k\theta). \end{aligned} \tag{5.10}$$

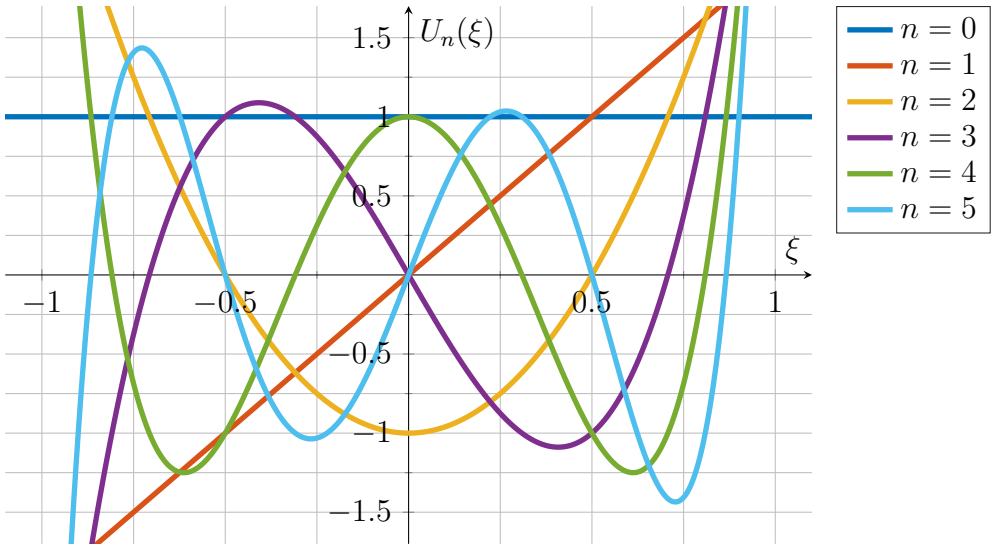

Figure 5.2: The Chebyshev polynomials of the second kind for different orders $n \in \{0, 1, \ldots, 5\}$.

Chebyshev Polynomials of the Second Kind

The Chebyshev polynomials of the second kind can be calculated by the recurrence relation [1, §22.2.5, §22.4.5]

$$\begin{aligned} U_0(\xi) &= 1 \\ U_1(\xi) &= 2\xi \\ U_{n+1}(\xi) &= 2\xi U_n(\xi) - U_{n-1}(\xi). \end{aligned} \tag{5.11}$$

The recurrence relation is almost the same as for (5.4). The only difference lies in the initial conditions, i.e., for Chebyshev polynomials of the second kind one has $U_1(\xi) = 2\xi$, while for Chebyshev polynomials of the first kind one has $T_1(\xi) = \xi$. The first six Chebyshev polynomials of the second kind are shown as examples in Figure 5.2.

The Chebyshev polynomials of the second kind also fulfill a relation to trigonometric functions by [1, §22.3.16]

$$U_n(\cos\theta) = \frac{\sin((n+1)\theta)}{\sin\theta}, \tag{5.12}$$

thus, the Chebyshev polynomials of the second kind can also be written as

$$U_n(\xi) = \begin{cases} \frac{\sin((n+1)\arccos\xi)}{\sqrt{1-\xi^2}}, & \text{if } |\xi| < 1, \\ \frac{\sinh((n+1)\operatorname{arcosh}\xi)}{\sqrt{\xi^2-1}}, & \text{if } |\xi| > 1, \end{cases} \tag{5.13}$$

using the fact that $\sin(\arccos\xi) = \sqrt{1-\xi^2}$.

The orthogonality relationship for Chebyshev polynomial of the second kind is

$$\int_{-1}^{1} U_n(t)U_m(t)\sqrt{1-t^2}\,\mathrm{d}t = \begin{cases} \frac{\pi}{2}, & \text{if } n = m, \\ 0, & \text{if } n \neq m. \end{cases}$$

Formally, the series expansion with Chebyshev polynomials of the second kind for a function $f : [-1, 1] \to \mathbb{C}$ reads

$$f(\xi) = \sum_{k\in\mathbb{N}_0} f_k U_k(\xi), \tag{5.14}$$

where

$$f_\ell = \frac{2}{\pi}\int_{-1}^{1} f(t)U_\ell(t)\sqrt{1-t^2}\,\mathrm{d}t. \tag{5.15}$$

As well as for the Chebyshev polynomials of the first kind, the series in (5.14) is closely related to the Fourier series, in particular to the Fourier sine series, which in turn can be verified by the substitution $\xi = \cos\theta$, resulting in

$$\begin{aligned} f(\cos\theta) &= \sum_{k\in\mathbb{N}_0} f_k U_k(\cos\theta) \\ &= \sum_{k\in\mathbb{N}_0} f_k \frac{\sin((k+1)\theta)}{\sin\theta}, \end{aligned} \tag{5.16}$$

where it is used that $U_n(\cos\theta) = \frac{\sin((n+1)\theta)}{\sin\theta}$ for $n \in \mathbb{N}_0$.

Consequently, the coefficients can be calculated with $t = \cos\theta$, $\mathrm{d}t = -\sin\theta\,\mathrm{d}\theta$ by

$$\begin{aligned} f_\ell &= \frac{2}{\pi}\int_{-1}^{1} f(t)U_\ell(t)\sqrt{1-t^2}\,\mathrm{d}t \\ &= \frac{2}{\pi}\int_{\pi}^{0} f(\cos\theta)\underbrace{U_\ell(\cos\theta)}_{=\frac{\sin((\ell+1)\theta)}{\sin\theta}}\underbrace{\sqrt{1-\cos^2\theta}}_{=\sin\theta}(-\sin\theta)\,\mathrm{d}\theta \\ &= \frac{2}{\pi}\int_{0}^{\pi} f(\cos\theta)\sin((\ell+1)\theta)\sin\theta\,\mathrm{d}\theta \\ &= \frac{2}{\pi}\int_{0}^{\pi} f(\cos\theta)\sin\theta\sin((\ell+1)\theta)\,\mathrm{d}\theta. \end{aligned} \tag{5.17}$$

The coefficients f_ℓ for $f(\xi)$ can therefore be calculated from the Fourier sine series of $f(\cos\theta)\sin\theta$.

5.1.2 Generalized Laguerre Polynomials

Since generalized Laguerre polynomials are also important in the context of the magnetization process of SPIOs, a brief introduction to them will be given. Laguerre polynomials with $\alpha > -1$ are obtained by the recurrence relation [1, §22.2.12]

$$\begin{aligned} L_0^{(\alpha)}(\xi) &= 1 \\ L_1^{(\alpha)}(\xi) &= 1+\alpha-\xi \\ L_{n+1}^{(\alpha)}(\xi) &= \frac{(2n+1+\alpha-\xi)L_n^{(\alpha)}(\xi) - (n+\alpha)L_{n-1}^{(\alpha)}(\xi)}{n+1}. \end{aligned} \tag{5.18}$$

As an example, the Laguerre polynomials with $\alpha \in \{-0.5, 0.5\}$ and $n \in \{0, 1, \ldots, 3\}$ are shown in Figure 5.3.

The generalized Laguerre polynomials $L_n^{(\alpha)}(\xi)$ with $\alpha > -1$ and $n \in \mathbb{N}_0$ could also defined by the explicit representation [1, §22.3.9]

$$L_n^{(\alpha)}(\xi) = \sum_{\ell=0}^{n}\binom{n+\alpha}{n-\ell}\frac{1}{\ell!}(-\xi)^\ell = \sum_{\ell=0}^{n}\frac{\Gamma(\alpha+n+1)}{\Gamma(\alpha+\ell+1)(n-\ell)!\ell!}(-\xi)^\ell. \tag{5.19}$$

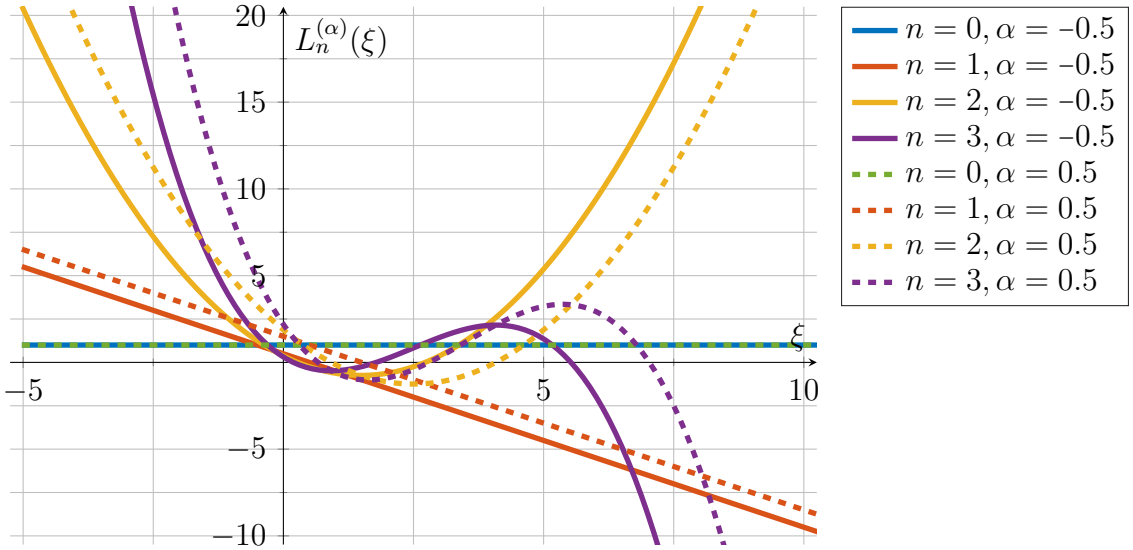

Figure 5.3: The generalized Laguerre polynomials with orders $n \in \{0, 1, \ldots, 3\}$ and $\alpha \in \{-0.5, 0.5\}$.

Generalized Laguerre polynomials are a family of orthogonal polynomials on the interval $(a, b) = (0, +\infty)$ with the weighting function $w_L^{(\alpha)}(\xi) = \mathrm{e}^{-\xi}\xi^\alpha$, i.e., the orthogonality relation between two generalized Laguerre polynomials $L_n^{(\alpha)}(\xi)$ and $L_m^{(\alpha)}(\xi)$ with $n, m \in \mathbb{N}_0$ is

$$\int_0^\infty L_n^{(\alpha)}(t) L_m^{(\alpha)}(t) \mathrm{e}^{-t} t^\alpha \,\mathrm{d}t = \begin{cases} \frac{\Gamma(n+\alpha+1)}{n!}, & \text{if } n = m, \\ 0, & \text{if } n \neq m. \end{cases}$$

Formally, the series expansion of a function $f : [0, +\infty) \to \mathbb{C}$ is related to generalized Laguerre polynomials by

$$f(\xi) = \sum_{k \in \mathbb{N}_0} f_k L_k^{(\alpha)}(\xi), \tag{5.20}$$

where

$$f_\ell = \frac{n!}{\Gamma(n+\alpha+1)} \int_0^\infty f(t) L_\ell^{(\alpha)}(t) \mathrm{e}^{-t} t^\alpha \,\mathrm{d}t. \tag{5.21}$$

5.2 Bessel Functions

This section introduces Bessel functions that are used throughout the work. Particular attention will therefore be paid to Bessel functions of the first kind $J_\alpha(\xi)$ and modified Bessel functions of the first kind $I_\alpha(\xi)$.

5.2.1 Bessel Function of the First Kind

The Bessel functions of the first kind are used in conjunction with the Chebyshev polynomials to obtain the spatio-temporal frequency representation of MPI in Chapter 7. At the beginning, a definition of the Bessel function of the first kind in series and integral form will be presented. The Bessel function of the first kind $J_\alpha : \mathbb{C} \to \mathbb{C}$ with order $\alpha \in \mathbb{R}$ is defined by [1, §9.1.10]

$$J_\alpha(\xi) = \sum_{m=0}^{\infty} \frac{(-1)^m}{m!\Gamma(m+\alpha+1)} \left(\frac{\xi}{2}\right)^{2m+\alpha}. \tag{5.22}$$

If $\alpha = n$ and $n \in \mathbb{Z}$ is restricted to integer values, then the following integral representation also applies [108, p. 20, eq. (5)]

$$J_n(\xi) = \frac{1}{2\pi} \int_{-\pi}^{\pi} \mathrm{e}^{\mathrm{i}(n\theta - \xi\sin(\theta))}\,\mathrm{d}\theta = \frac{1}{2\pi} \int_{-\pi}^{\pi} \mathrm{e}^{\mathrm{i}\left(\xi\sin(\tilde{\theta}) - n\tilde{\theta}\right)}\,\mathrm{d}\tilde{\theta}. \tag{5.23}$$

The first five Bessel functions of the first kind are shown in Figure 5.4.

The modified Bessel function of the first kind is directly connected to the standard Bessel function of the first kind by [1, §9.6.3, §9.6.10]

$$I_\alpha(\xi) = \mathrm{i}^{-\alpha} J_\alpha(\mathrm{i}\xi) = \sum_{m=0}^{\infty} \frac{1}{m!\Gamma(m+\alpha+1)} \left(\frac{\xi}{2}\right)^{2m+\alpha} \tag{5.24}$$

and therefore the following applies for the integer $\alpha = n$

$$I_n(\xi) = \frac{1}{2\pi} \int_{-\pi}^{\pi} \mathrm{e}^{-\xi\sin(\theta) - \mathrm{i}n\theta}\,\mathrm{d}\theta. \tag{5.25}$$

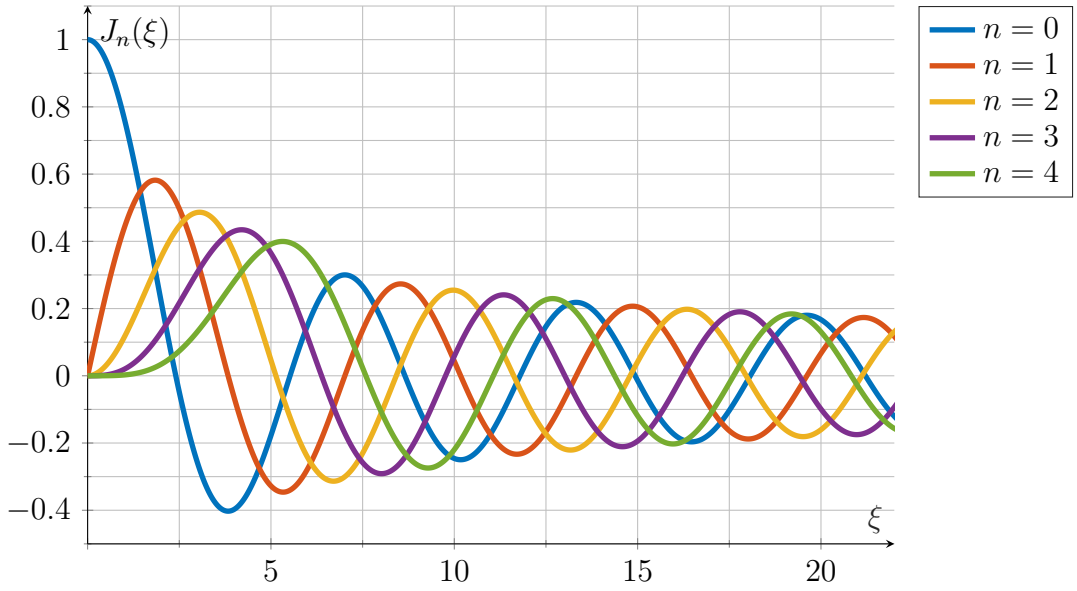

Figure 5.4: The Bessel functions of the first kind with orders $n \in \{0, 1, \ldots, 4\}$.

The first five modified Bessel functions of the first kind are shown in Figure 5.5. The modified Bessel functions of the first kind have already been used in Section 3.1.3 to obtain the series representation of the anisotropic equilibrium model for the mean magnetic moment of the SPIO.

Bessel functions of the first kind with integer order $\alpha = n \in \mathbb{Z}$ are entire functions, i.e., the series in (5.22) converges uniformly for each compact set in $\mathbb{C}$. This property is necessarily also transferred to the modified version in (5.24), as this is only a special case of the unmodified version. The integral representations in (5.23) and (5.25) also reveal a direct relationship to the Fourier series coefficients of $\mathrm{e}^{\mathrm{i}\xi \sin\theta}$ and $\mathrm{e}^{-\xi \sin\theta}$, respectively.

In the following, and since it is necessary for the later proofs in this thesis, one is interested in finding upper bounds on the real axis $\xi \in \mathbb{R}$ for the Bessel functions of the first kind.

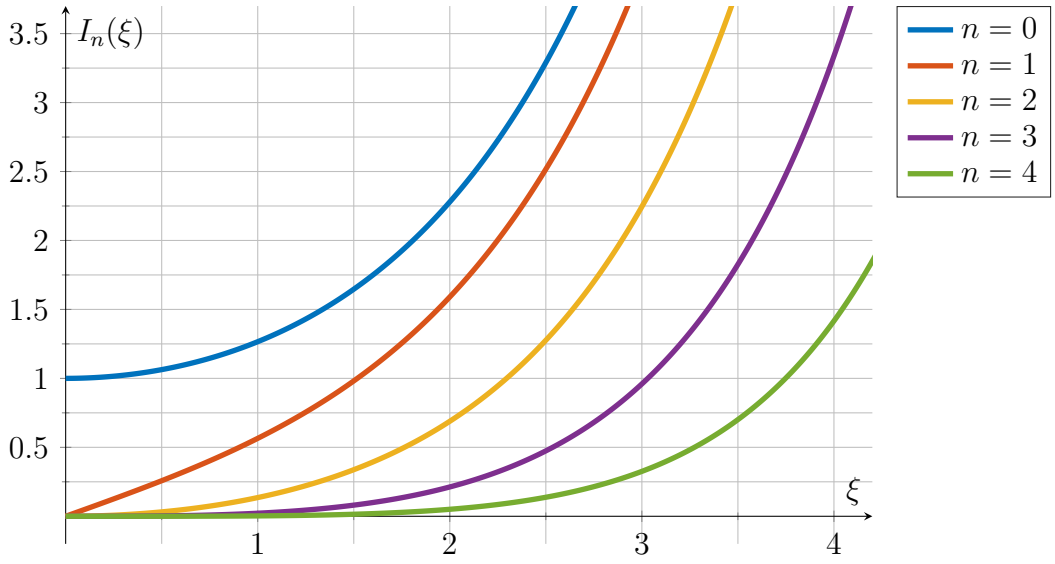

Figure 5.5: The modified Bessel functions of first kind with orders $n \in \{0, 1, \ldots, 4\}$.

Corollary 5.1. *For Bessel functions of the first kind $J_n : \mathbb{R} \to \mathbb{R}$ with order $n \geq 2$ the following upper bounds are given*

$$|J_n(\xi)| \leq \begin{cases} \frac{1}{n!}\left(\frac{\xi}{2}\right)^n, & 0 \leq \xi < n/2, \\ Cn^{-1/4}\left(|\xi - n| + n^{1/3}\right)^{-1/4}, & n/2 \leq \xi \leq 2n, \\ C\xi^{-1/2}, & 2n < \xi \end{cases} \tag{5.26}$$

with the constant $C > 0$ [95]. Additionally, according to [61] it holds that

$$|J_n(\xi)| \leq \min(1, bn^{-\frac{1}{3}}, c|\xi|^{-\frac{1}{3}}) \tag{5.27}$$

with constants $b = 0.674885\ldots$ and $c = 0.7857468704\ldots$.

If now the Bessel function of the first kind is weighted with the weighting function $\frac{1}{\xi}$, the following corollary can be proved [F1].

Corollary 5.2. *The function $\frac{J_n(\xi)}{\xi}$ is in $L^1(\mathbb{R}) \cap L^\infty(\mathbb{R})$, and the L^∞-norm has an upper bound of*

$$\left\| \frac{J_n(\xi)}{\xi} \right\|_{L^\infty} \leq C \frac{1}{n^{\frac{4}{3}}} \tag{5.28}$$

with a constant $C > 0$ and $n \in \mathbb{Z}\backslash\{0\}$.

Proof of Corollary 5.2. With the help of the Corollary 5.1 (5.26) and the fact that $|J_n(\xi)|$ is an even symmetric function for all $n \in \mathbb{Z}$, it is only necessary to check the positive half of the real axis. Since $J_{-n}(\xi) = (-1)^n J_n(\xi)$, the Corollary 5.1 is also valid for negative integer values n. The proof is therefore only provided for positive arguments, i.e., $n \in \mathbb{N}$ and $\xi \in \mathbb{R}_+$.

Thus, it should be started with the intervals $0 \leq \xi < n/2$ and $2n < \xi$ and finally the interval $n/2 \leq \xi \leq 2n$ should be investigated.

C1: $0 \leq \xi < n/2$

Using the inequality one obtains:

$$\left|\frac{J_n(\xi)}{\xi}\right| \leq \frac{1}{n!}\frac{\xi^{n-1}}{2^n},$$

which also holds for all $n \geq 1$ and $\xi \in \mathbb{R}_+$. For the beginning, however, one is only interested in $n \geq 2$, so that the upper bound is a monotonically increasing polynomial and therefore the maximizer can be found on the upper bound of the interval $\xi \to n/2$. Insertion of $\xi = n/2$ leads to

$$\left|\frac{J_n(\xi)}{\xi}\right| \leq \frac{1}{n!}\frac{n^{n-1}}{2^{2n-1}}.$$

To simplify the expression, the Sterling inequality [85] is used

$$\frac{\sqrt{2\pi n}n^n}{n!\mathrm{e}^n} < \mathrm{e}^{-\frac{1}{12n+1}} < 1,$$

which then leads to the following results

$$\left|\frac{J_n(\xi)}{\xi}\right| \leq \frac{2}{n\sqrt{2\pi n}}\frac{\sqrt{2\pi n}n^n}{n!2^{2n}} < \frac{2}{n\sqrt{2\pi n}}\frac{\sqrt{2\pi n}n^n}{n!\mathrm{e}^n} < \sqrt{\frac{2}{\pi}}\frac{1}{n^{3/2}}.$$

C2: $2n < \xi$

In this interval, the upper bound for $\left|\frac{J_n(\xi)}{\xi}\right|$ is given by the lower bound $\xi \to 2n$, since $C\xi^{-\frac{3}{2}}$ is monotonically decreasing and $1 < \xi$ and thus

$$\left|\frac{J_n(\xi)}{\xi}\right| < \frac{C}{2^{3/2}}\frac{1}{n^{3/2}}.$$

C3: $n/2 \leq \xi \leq 2n$

For the last interval the following inequality holds

$$\left|\frac{J_n(\xi)}{\xi}\right| \leq C\frac{1}{\xi n^{1/4}\left(|\xi - n| + n^{1/3}\right)^{1/4}} = C\frac{1}{n^{1/4}\left(\xi^4|\xi - n| + n^{1/3}\xi^4\right)^{1/4}}.$$

Hence, the upper bound for all $\xi \in [n/2, 2n]$ is given whenever

$$f(\xi) = \xi^4|\xi - n| + n^{1/3}\xi^4$$

is minimal. Since $\xi \in [n/2, n]$,

$$f(\xi) = -\xi^5 + (n + n^{1/3})\xi^4$$

is obtained. The $f(\xi)$ is a continuous and differentiable function and, therefore, the minimizer is either a zero point of $f'(\xi)$, or one of the boundary values $\xi^{(1)} = n/2$ or $\xi^{(2)} = n$. Let us first examine the zero points of

$$f'(\xi) = -5\xi^4 + 4(n + n^{1/3})\xi^3 = 0 \Leftrightarrow \xi^{(3)} = 0 \text{ or } \xi^{(4)} = \frac{4}{5}(n + n^{1/3}).$$

The point $\xi^{(3)}$ does not lie in $[n/2, 2n]$. Using the second derivative of $f(\xi)$, the sufficient condition yields that $\xi^{(4)}$ is a maximizer, because

$$\begin{aligned} f''(\xi^{(4)}) &= -5 \cdot 4\left(\frac{4}{5}\left(n + n^{1/3}\right)\right)^3 + 4 \cdot 3\left(n + n^{1/3}\right)\left(\frac{4}{5}\left(n + n^{1/3}\right)\right)^2 \\ &= -\frac{64}{25}\left(n + n^{1/3}\right)^3 < 0. \end{aligned}$$

The evaluation of the function $f(\xi)$ for $\xi^{(1)} = n/2$ and $\xi^{(2)} = n$ results in

$$\begin{aligned} f(\xi^{(1)}) &= -\frac{n^5}{32} + (n + n^{1/3})\frac{n^4}{16} = \frac{n^5}{32} + \frac{n^{13/3}}{16}, \\ f(\xi^{(2)}) &= -n^5 + (n + n^{1/3})n = n^{13/3}. \end{aligned}$$

By checking

$$f(\xi^{(1)}) = \frac{n^5}{32} + \frac{n^{13/3}}{16} < f(\xi^{(2)}) = n^{13/3} \Rightarrow n < 30\sqrt{30} \approx 164.317,$$

it follows that for large n $\xi^{(2)}$ is the minimizer. For $n > 164$,

$$\left|\frac{J_n(\xi)}{\xi}\right| \leq C\frac{1}{n^{1/4}\left(n^{13/3}\right)^{1/4}} = C\frac{1}{\left(n^{16/3}\right)^{1/4}} = C\frac{1}{n^{4/3}}$$

is obtained and for $n \leq 164$,

$$\left|\frac{J_n(\xi)}{\xi}\right| \leq C\frac{1}{n^{1/4}\left(\frac{n^5}{32}+\frac{n^{13/3}}{16}\right)^{1/4}} < 2C\frac{1}{\left(n^{16/3}\right)^{1/4}} = 2C\frac{1}{n^{4/3}}$$

is obtained. Thus, all $n \geq 2$ can be upper bounded by

$$\left|\frac{J_n(\xi)}{\xi}\right| < \tilde{C}\frac{1}{n^{4/3}}$$

with $\tilde{C} = 2C$.

The following applies to the subinterval $\xi \in (n, 2n]$:

$$f(\xi) = \xi^5 + (n^{1/3} - n)\xi^4.$$

The function $f(\xi)$ is strictly monotonically increasing, since for each $\xi = \alpha n$ with $\alpha \in (1, 2]$ the derivative

$$f'(\xi) = 5\alpha^4 n^4 + 4(n^{1/3} - n)\alpha^3 n^3 = (5\alpha - 4)\alpha^3 n^4 + 4\alpha^3 n^{10/3} > 0$$

is fulfilled and thus the minimizer $\xi \to n$ corresponds to the previously calculated minimizer.

By comparing all cases and choosing a correspondingly large constant $C > 0$, the following result is obtained:

$$\left\|\frac{J_n(\xi)}{\xi}\right\|_{L^\infty} \leq C\frac{1}{n^{4/3}}.$$

The upper bound is also valid for $n = 1$ as $\left|\frac{J_1(\xi)}{\xi}\right| \leq \frac{1}{2}$, which corresponds to the calculated upper limit.

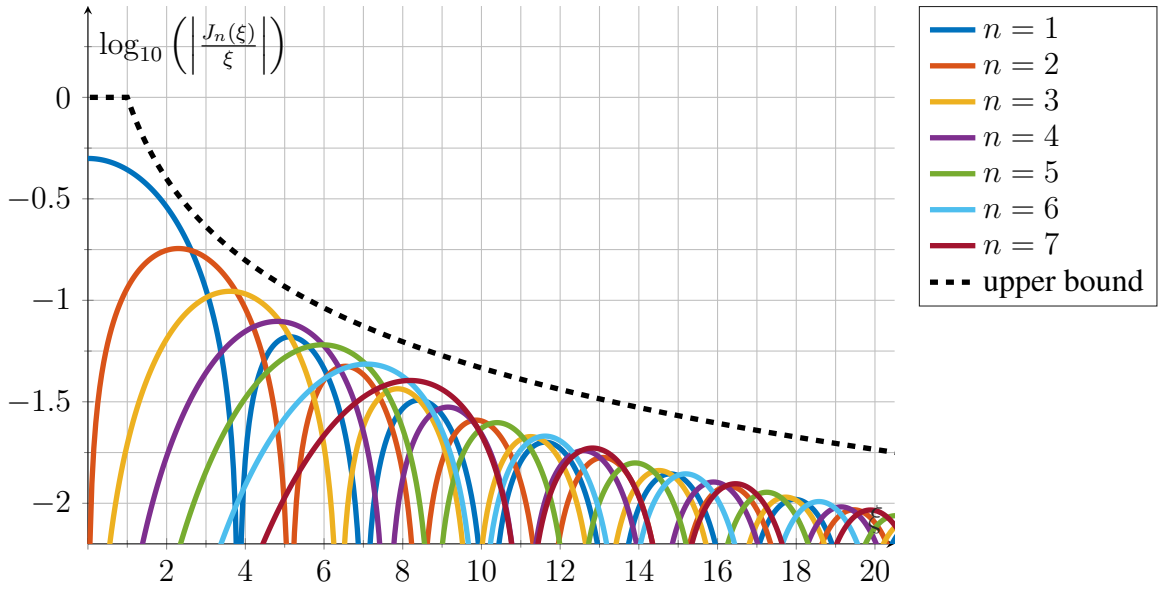

Figure 5.6: The upper bound and $\left|\frac{J_n(\xi)}{\xi}\right|$ with $n \in \{1, \ldots, 7\}$ in $\log_{10}$-scale.

Thus, it remains to prove that $\frac{J_n(\xi)}{\xi}$ is in $L^1(\mathbb{R})$. According to the Corollary 5.1 (5.27) and taking into account the fact that the function can be upper bounded for all $n \in \mathbb{N}$ by

$$\left|\frac{J_n(\xi)}{\xi}\right| \leq \operatorname{rect}\left(\frac{\xi}{2}\right) + \left(1 - \operatorname{rect}\left(\frac{\xi}{2}\right)\right) \frac{1}{|\xi|^{\frac{4}{3}}}$$

it holds that

$$\begin{aligned}\int_{-\infty}^{\infty} \left|\frac{J_n(\xi)}{\xi}\right| \mathrm{d}\xi &\leq 2 + 2\int_{1}^{\infty} \frac{1}{|\xi|^{\frac{4}{3}}} \mathrm{d}\xi \\ &= 2 - \left.\frac{2}{(\frac{4}{3}-1)|\xi|^{\frac{4}{3}-1}}\right|_{1}^{\infty} = 8 < \infty.\end{aligned}$$

The upper bound construction is shown for $n \in \{1, 2, \ldots, 7\}$ in Figure 5.6. □

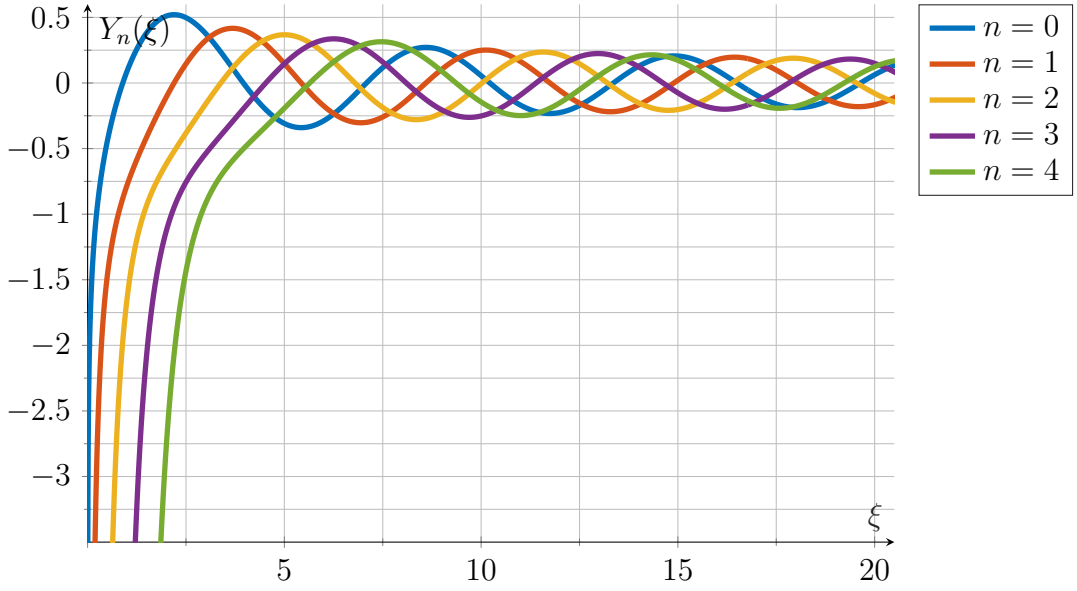

Figure 5.7: The Bessel functions of the second kind with orders $n \in \{0, 1, \ldots, 4\}$.

5.2.2 Bessel Functions of the Second Kind

For the sake of completeness, the Bessel functions of the second kind $Y_\alpha : \mathbb{C} \to \mathbb{C}$ with $\alpha \in \mathbb{R}$ are defined by [1, §9.1.2]

$$Y_\alpha(\xi) = \frac{J_\alpha(\xi)\cos(\alpha\pi) - J_{-\alpha}(\xi)}{\sin(\alpha\pi)}, \quad \text{if } \alpha \neq \mathbb{Z} \tag{5.29}$$

and for the integer case $n \in \mathbb{Z}$ by the limit

$$Y_n(\xi) = \lim_{\alpha \to n} Y_\alpha(\xi).$$

The Bessel functions of the second kind can also be written as a series or integrals for $Y_n(\xi)$ with $n \in \mathbb{Z}$, but since this kind of Bessel functions plays a subordinate role in this work, reference should be made to [1, Ch. 9]. An illustration with the first five Bessel functions of the second kind is shown in Figure 5.7.

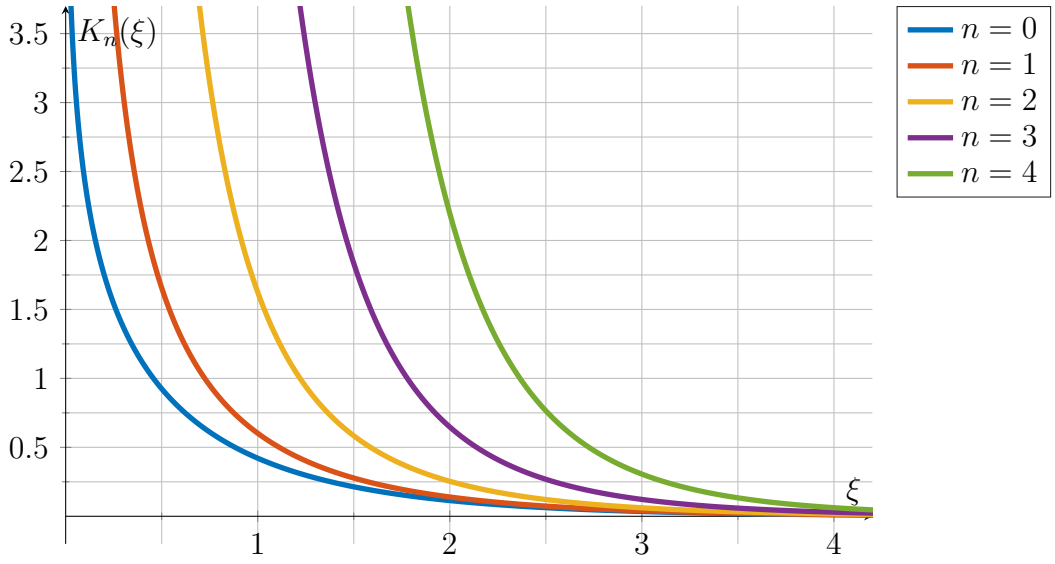

Figure 5.8: The modified Bessel functions of the second kind with orders $n \in \{0, 1, \ldots, 4\}$.

The modified Bessel functions of the second kind $K_\alpha : \mathbb{C} \to \mathbb{C}$ are given by [1, §9.6.2]

$$K_\alpha(\xi) = \frac{\pi}{2} \frac{I_{-\alpha}(\xi) - I_\alpha(\xi)}{\sin(\alpha\pi)}, \quad \text{if } \alpha \neq \mathbb{Z} \tag{5.30}$$

and for the integer case $n \in \mathbb{Z}$ by the limit

$$K_n(\xi) = \lim_{\alpha \to n} K_\alpha(\xi).$$

Since the case $n = 0$ with $K_0 : \mathbb{R} \to \mathbb{R}$ is of particular interest in this work, the following integral representations are given in [1, §9.6.4] and [8, Ch. 8.2 , (45)] as

$$K_0(\xi) = \int_0^\infty \mathrm{e}^{-\xi \cosh(t)} \, \mathrm{d}t \quad = \int_0^\infty J_0(\xi t) \frac{t}{1 + t^2} \, \mathrm{d}t. \tag{5.31}$$

The modified Bessel functions of the second kind are used in this work to calculate the Fourier transform of the multidimensional Langevin function. A figure with the first five modified Bessel functions of the second kind is shown in Figure 5.8.

5.3 Fourier Transforms of Chebyshev Polynomials

The Chebyshev polynomials and Bessel functions of the first kind are closely related to each other via a Fourier transform. The results presented here are helpful for the representation of MPI in the spatial frequency domain. It is assumed that the Chebyshev polynomials lie in the spatial domain with the variable x and ω_x denotes the corresponding frequency. The following lemma was used to prove the MPI frequency domain representation in [F1].

Lemma 5.3. *The Fourier transform of weighted Chebyshev polynomials of the first kind*

$$\mathrm{i}^n \frac{T_{|n|}(x)}{\pi\sqrt{1-x^2}} \operatorname{rect}\Big(\frac{x}{2}\Big) = \begin{cases} \frac{\mathrm{i}^n T_{|n|}(x)}{\pi\sqrt{1-x^2}} & \textit{for } |x| < 1 \\ 0 & \textit{else}, \end{cases} \tag{5.32}$$

with order $n \in \mathbb{Z}$ is

$$J_n(\omega_x) = \mathcal{F}\left\{ \mathrm{i}^n \frac{T_{|n|}(x)}{\pi\sqrt{1-x^2}} \operatorname{rect}\Big(\frac{x}{2}\Big) \right\}, \tag{5.33}$$

where $J_k(\xi)$ denotes the Bessel function of the first kind with order k.

The Fourier transform of

$$\frac{\mathrm{i}^n}{\pi} V_n(\xi) = \frac{\mathrm{i}^n}{\pi} \begin{cases} \operatorname{rect}\big(\frac{\xi}{2}\big) \left(-\frac{U_{|n|-1}(\xi)\sqrt{1-\xi^2}}{|n|} \right) & \textit{if } |n| > 0 \\ \frac{\pi}{2} \operatorname{sgn}(\xi+1) - \operatorname{rect}\big(\frac{\xi}{2}\big) \arccos(\xi) & \textit{if } n = 0, \end{cases} \tag{5.34}$$

and $n \in \mathbb{Z}\backslash\{0\}$, where $U_k(\xi)$ denotes the Chebyshev polynomial of the second kind with order k [1] is

$$\frac{J_n(\omega_x)}{\mathrm{i}\omega_x} = \mathcal{F}\left\{ \frac{\mathrm{i}^n}{\pi} V_n(x) \right\}. \tag{5.35}$$

Moreover, $V_k(\xi)$ and $T_k(\xi)$ have for all $k \in \mathbb{Z}$ the mutual relationship

$$v_k(\xi) = \frac{\mathrm{d}}{\mathrm{d}\xi} V_k(\xi) = \operatorname{rect}\left(\frac{\xi}{2}\right) \frac{T_{|k|}(\xi)}{\sqrt{1-\xi^2}}. \tag{5.36}$$

Proof of Lemma 5.3. A proof for (5.33) can be found in the literature [9] or in tabular form in [1, §11.4.24]. The forward Fourier transform for (5.32) reads

$$\begin{aligned}\mathcal{F}\left\{\frac{\mathrm{i}^n \operatorname{rect}\left(\frac{x}{2}\right) T_{|n|}(x)}{\pi\sqrt{1-x^2}}\right\} &= \int_{-\infty}^{\infty} \frac{\mathrm{i}^n \operatorname{rect}\left(\frac{x}{2}\right) T_{|n|}(x)}{\pi\sqrt{1-x^2}} \mathrm{e}^{-\mathrm{i}\omega_x x}\,\mathrm{d}x \\ &= \int_{-1}^{1} \frac{\mathrm{i}^n T_{|n|}(x)}{\pi\sqrt{1-x^2}} \mathrm{e}^{-\mathrm{i}\omega_x x}\,\mathrm{d}x.\end{aligned}$$

Applying the substitution $x = \cos u$ with $\frac{\mathrm{d}x}{\mathrm{d}u} = -\sin u$ yields

$$\int_{\pi}^{0} \frac{\mathrm{i}^n T_{|n|}(\cos u)}{\pi\sqrt{1-\cos^2(u)}} \mathrm{e}^{-\mathrm{i}\omega_x \cos(u)}(-\sin u)\,\mathrm{d}u = \int_{0}^{\pi} \frac{\mathrm{i}^n T_{|n|}(\cos u)}{\pi} \mathrm{e}^{-\mathrm{i}\omega_x \cos(u)}\,\mathrm{d}u.$$

If (5.5) is used and then Euler's formula is applied, the following is obtained

$$\begin{aligned}\frac{\mathrm{i}^n}{\pi}\int_0^{\pi} \cos(|n|u)\mathrm{e}^{-\mathrm{i}\omega_x \cos(u)}\,\mathrm{d}u &= \frac{\mathrm{i}^n}{2\pi}\int_0^{\pi} \left(\mathrm{e}^{\mathrm{i}|n|u} + \mathrm{e}^{-\mathrm{i}|n|u}\right)\mathrm{e}^{-\mathrm{i}\omega_x \cos(u)}\,\mathrm{d}u \\ &= \frac{\mathrm{i}^n}{2\pi}\left[\int_0^{\pi} \mathrm{e}^{\mathrm{i}|n|u-\mathrm{i}\omega_x \cos(u)}\,\mathrm{d}u + \int_0^{\pi} \mathrm{e}^{-\mathrm{i}|n|u-\mathrm{i}\omega_x \cos(u)}\,\mathrm{d}u\right] \\ &= \frac{\mathrm{i}^n}{2\pi}\left[\int_{-\pi}^{0} \mathrm{e}^{-\mathrm{i}|n|u-\mathrm{i}\omega_x \cos(u)}\,\mathrm{d}u + \int_0^{\pi} \mathrm{e}^{-\mathrm{i}|n|u-\mathrm{i}\omega_x \cos(u)}\,\mathrm{d}u\right] \\ &= \frac{\mathrm{i}^n}{2\pi}\int_{-\pi}^{\pi} \mathrm{e}^{-\mathrm{i}|n|u-\mathrm{i}\omega_x \cos(u)}\,\mathrm{d}u.\end{aligned}$$

Using $\mathrm{i}^n = \mathrm{e}^{\mathrm{i}\frac{\pi}{2}n}$, it now follows that

$$\frac{1}{2\pi}\int_{-\pi}^{\pi} \mathrm{e}^{-\mathrm{i}\omega_x \cos(u)-\mathrm{i}|n|u+\mathrm{i}\frac{\pi}{2}n}\,\mathrm{d}u.$$

Finally, from $-\cos(u) = \sin(u - \frac{\pi}{2})$ and the substitution $z = u - \frac{\pi}{2}$ one obtains

$$\frac{1}{2\pi}\int_{-\pi}^{\pi} \mathrm{e}^{\mathrm{i}\omega_x \sin(z)-\mathrm{i}|n|z+\mathrm{i}\frac{\pi}{2}n-\mathrm{i}|n|\frac{\pi}{2}}\,\mathrm{d}z = \frac{\mathrm{e}^{\mathrm{i}\frac{\pi}{2}(n-|n|)}}{2\pi}\int_{-\pi}^{\pi} \mathrm{e}^{\mathrm{i}\omega_x \sin(z)-\mathrm{i}|n|z}\,\mathrm{d}z.$$

First of all, it should be noted that $n \geq 0$ is only the definition (5.23) of a Bessel function of the first kind and therefore one has

$$\mathcal{F}\left\{\frac{\mathrm{i}^n \operatorname{rect}\left(\frac{x}{2}\right) T_{|n|}(x)}{\pi\sqrt{1-x^2}}\right\} = \frac{1}{2\pi}\int_{-\pi}^{\pi} \mathrm{e}^{\mathrm{i}\omega_x \sin(z)-\mathrm{i}nz}\,\mathrm{d}z = J_n\left(\omega_x\right).$$

For $n < 0$ one gets

$$\mathcal{F}\left\{\frac{\mathrm{i}^n \operatorname{rect}\left(\frac{x}{2}\right) T_{|n|}(x)}{\pi\sqrt{1-x^2}}\right\} = \frac{(-1)^n}{2\pi}\int_{-\pi}^{\pi} \mathrm{e}^{\mathrm{i}\omega_x \sin(z) - \mathrm{i}|n|z}\,\mathrm{d}z$$
$$= (-1)^n J_{|n|}(\omega_x) = J_{-|n|}(\omega_x) = J_n(\omega_x).$$

To prove (5.36) for $k \geq 1$, the derivative $\frac{\mathrm{d}}{\mathrm{d}\xi}V_k(\xi)$ with $V_k(\xi)$ is taken according to (5.34) and (5.13):

$$\frac{\mathrm{d}}{\mathrm{d}\xi}V_k(\xi) = -\frac{\mathrm{d}}{\mathrm{d}\xi}\frac{\sin\left(k \cdot \arccos(\xi)\right)}{k}$$
$$= \frac{\cos(k\arccos(\xi))}{\sqrt{1-\xi^2}}.$$

The comparison with (5.6) confirms (5.36) for $k \geq 1$. If $k = 0$ one has

$$V_0(\xi) = \frac{\pi}{2} - \arccos(\xi) = \arcsin(\xi), \qquad |\xi| < 1.$$

A derivative of $V_0(\xi)$ with respect to ξ then results in

$$\frac{\mathrm{d}}{\mathrm{d}\xi}V_0(\xi) = \frac{1}{\sqrt{1-\xi^2}} = \frac{T_0(\xi)}{\sqrt{1-\xi^2}},$$

which confirms (5.36) for $k = 0$. For $|\xi| > 1$ it can be proven that $\frac{\mathrm{d}}{\mathrm{d}\xi}V_k(\xi) = 0$.

It remains to be shown that (5.35) is valid. Based on the Fourier correspondence in (5.33) and the property $J_n(0) = 0$, whenever $|n| \geq 1$, the Fourier integration theorem is

$$\int_{-\infty}^{x} f(\tau)\,\mathrm{d}\tau \longleftrightarrow \frac{1}{\mathrm{i}\omega}F(\omega) \quad \text{if} \quad F(0) = 0$$

and thus

$$\frac{\mathrm{i}^n}{\pi}\int_{-\infty}^{x} \operatorname{rect}\left(\frac{y}{2}\right)\frac{T_{|n|}(y)}{\sqrt{1-y^2}}\,\mathrm{d}y \longleftrightarrow \frac{1}{\mathrm{i}\omega_x}J_n(\omega_x)$$

results. Fortunately, it only remains to show that

$$g(x) := \frac{\mathrm{i}^n}{\pi}\int_{-\infty}^{x} \operatorname{rect}\left(\frac{y}{2}\right)\frac{T_{|n|}(y)}{\sqrt{1-y^2}}\,\mathrm{d}y \stackrel{!}{=} \frac{\mathrm{i}^n}{\pi}V_n(x).$$

For $x \in [-1, 1]$ one gets

$$g(x) = \frac{\mathrm{i}^n}{\pi} V_n(y)\Big|_{-1}^{x} = \frac{\mathrm{i}^n}{\pi}\left(V_n(x) - \underbrace{V_n(-1)}_{=0}\right) = \frac{\mathrm{i}^n}{\pi} V_n(x).$$

For $x < -1$ it is obvious that $g(x) = 0$. For $x > 1$ follows

$$\begin{aligned} g(x) &= \frac{\mathrm{i}^n}{\pi} \int_{-\infty}^{x} \operatorname{rect}\Big(\frac{y}{2}\Big) \frac{T_{|n|}(y)}{\sqrt{1-y^2}}\,\mathrm{d}y \\ &= \left[\frac{\mathrm{i}^n}{\pi} \int_{-\infty}^{\infty} \operatorname{rect}\Big(\frac{y}{2}\Big) \frac{T_{|n|}(y)}{\sqrt{1-y^2}} \mathrm{e}^{-\mathrm{i}\omega_x y}\,\mathrm{d}y\right]_{\omega_x=0} \\ &= J_n(0) = 0. \end{aligned}$$

Overall, for $|n| \geq 1$ this validates that $g(x) = \frac{\mathrm{i}^n}{\pi} V_n(x)$. The case $n = 0$ in (5.34) is more involved and is treated in the next Lemma 5.4. □

As mentioned in the proof of Lemma 5.3, the case $n = 0$ in (5.34) is more complicated since the inverse Fourier transform of $\frac{J_0(\omega_x)}{\mathrm{i}\omega_x}$ exist only in the distributional sense and neither $\frac{J_0(\omega_x)}{\mathrm{i}\omega_x}$ nor the one identified with its inverse Fourier transform is an $L^1(\mathbb{R})$ function. However, it is possible to use a convolution property in spatial x-space to obtain a similar result.

Lemma 5.4. *The convolution of a function $F \in L^\infty(\mathbb{R})$ that have the properties*

$$\lim_{x\to\pm\infty} F(x) = \pm c \quad \textit{and} \quad f(x) = \tfrac{\mathrm{d}}{\mathrm{d}x} F(x) \qquad (c \in \mathbb{R})$$

with a scaled version of the function

$$v_0(x) = \tfrac{\mathrm{d}}{\mathrm{d}x} V_0(x),$$

where $V_0(x)$ is defined in (5.34), yields

$$\begin{aligned} &\int_{-\infty}^{\infty} F(x-y) \frac{1}{|\alpha|} v_0\left(\frac{y}{\alpha}\right)\,\mathrm{d}y \\ &\qquad = \int_{-\infty}^{\infty} f(x-y) \frac{\alpha}{|\alpha|} V_0\left(\frac{y}{\alpha}\right)\,\mathrm{d}y, \quad \alpha \in \mathbb{R}\backslash\{0\}. \end{aligned} \tag{5.37}$$

Proof of Lemma 5.4. We aim to prove the convolution correspondence in Lemma 5.4, which helps us to unify the notation in this work. First, we rewrite the left term in (5.37) with

$$v_0\left(\tfrac{x}{\alpha}\right) = \operatorname{rect}\left(\tfrac{x}{2\alpha}\right) \frac{T_0\left(\frac{x}{\alpha}\right)}{\sqrt{1-\left(\frac{x}{\alpha}\right)^2}}, \qquad \alpha \in \mathbb{R}\backslash\{0\}$$

from (5.36) as

$$\begin{aligned} &\int_{-\infty}^{\infty} F(x-y)\frac{1}{|\alpha|}\operatorname{rect}\left(\frac{y}{2\alpha}\right)\frac{1}{\sqrt{1-\left(\frac{y}{\alpha}\right)^2}}\,\mathrm{d}y \\ &\quad = \int_{-|\alpha|}^{|\alpha|} F(x-y)\frac{1}{|\alpha|}\frac{1}{\sqrt{1-\left(\frac{y}{\alpha}\right)^2}}\,\mathrm{d}y. \end{aligned} \tag{5.38}$$

Partial integration yields

$$\begin{aligned} &\int_{-|\alpha|}^{|\alpha|} F(x-y)\frac{1}{|\alpha|}\frac{1}{\sqrt{1-\left(\frac{y}{\alpha}\right)^2}}\,\mathrm{d}y \\ &\quad = F(x-y)\frac{\alpha}{|\alpha|}\arcsin\left(\frac{y}{\alpha}\right)\Big|_{-|\alpha|}^{|\alpha|} \\ &\qquad + \int_{-|\alpha|}^{|\alpha|} f(x-y)\frac{\alpha}{|\alpha|}\arcsin\left(\frac{y}{\alpha}\right)\,\mathrm{d}y \\ &\quad = \frac{\pi}{2}\left(F(x-|\alpha|)+F(x+|\alpha|)\right) \\ &\qquad + \int_{-|\alpha|}^{|\alpha|} f(x-y)\frac{\alpha}{|\alpha|}\arcsin\left(\frac{y}{\alpha}\right)\,\mathrm{d}y. \end{aligned} \tag{5.39}$$

Now notice that because of $\lim_{x\to\pm\infty} F(x) = \pm c$ with $c \in \mathbb{R}$ and $F \in L^\infty(\mathbb{R})$, it holds that

$$\begin{aligned} &\int_{-\infty}^{\infty} f(x-\tau)\operatorname{sgn}(\tau-y)\,\mathrm{d}\tau \\ &\qquad = \int_{y}^{\infty} f(x-\tau)\,\mathrm{d}\tau - \int_{-\infty}^{y} f(x-\tau)\,\mathrm{d}\tau \\ &\qquad = -F(x-\tau)\Big|_{\tau=y}^{\infty} + F(x-\tau)\Big|_{\tau=-\infty}^{y} \\ &\qquad = 2F(x-y) - \underbrace{\lim_{\tau\to\infty}\left[F(x-\tau)+F(x+\tau)\right]}_{=0} = 2F(x-y). \end{aligned}$$

Using this relationship inside the convolution integral in (5.39), we get

$$\begin{aligned}\int_{-\infty}^{\infty} F(x-y)\frac{1}{|\alpha|}v_0\Big(\frac{y}{\alpha}\Big)\,\mathrm{d}y \\ = \int_{-\infty}^{\infty} f(x-y)\Bigg(\frac{\pi}{4}\big(\operatorname{sgn}(y-|\alpha|)+\operatorname{sgn}(y+|\alpha|)\big) \\ + \operatorname{rect}\Big(\frac{y}{2\alpha}\Big)\,\frac{\alpha}{|\alpha|}\arcsin\Big(\frac{y}{\alpha}\Big)\Bigg)\,\mathrm{d}y.\end{aligned}$$

The term

$$\frac{\pi}{4}\left(\operatorname{sgn}(y-|\alpha|)+\operatorname{sgn}(y+|\alpha|)\right)+\operatorname{rect}\Big(\frac{y}{2\alpha}\Big)\,\frac{\alpha}{|\alpha|}\arcsin\Big(\frac{y}{\alpha}\Big)$$

is equivalent to

$$\frac{1}{\operatorname{sgn}(\alpha)}\left(\frac{\pi}{2}\operatorname{sgn}\Big(\frac{y}{\alpha}+1\Big)-\operatorname{rect}\Big(\frac{y}{2\alpha}\Big)\arccos\Big(\frac{y}{\alpha}\Big)\right)=\frac{1}{\operatorname{sgn}(\alpha)}V_0\Big(\frac{y}{\alpha}\Big)$$

with $\operatorname{sgn}(\alpha)=\frac{\alpha}{|\alpha|}=\frac{|\alpha|}{\alpha}$. Thus, we have obtained the expression on the right-hand side of (5.37). □

The last lemma shows a remarkable connection between Bessel functions of the first kind and functions of the form $(1-x^2)^{n-\frac{1}{2}}\operatorname{rect}(x/2)\quad(n\in\mathbb{N}_0)$.

Lemma 5.5. *The Fourier transform of*

$$f(x)=\frac{(1-x^2)^{n-1/2}}{\Gamma\big(n+\frac{1}{2}\big)\sqrt{\pi}2^n}\operatorname{rect}\Big(\frac{x}{2}\Big) \tag{5.40}$$

with $f\in L^1(\mathbb{R})$ and $n\in\mathbb{N}_0$ is

$$\hat{f}(\omega_x)=\frac{J_n(\omega_x)}{\omega_x^n}=\mathcal{F}\left\{\frac{(1-x^2)^{n-1/2}}{\Gamma\big(n+\frac{1}{2}\big)\sqrt{\pi}2^n}\operatorname{rect}\Big(\frac{x}{2}\Big)\right\}\quad\textit{with}\quad\hat{f}\in C_0(\mathbb{R})\subset L^\infty(\mathbb{R}), \tag{5.41}$$

where $J_k(\xi)$ denotes the Bessel function of the first kind with order $k\in\mathbb{Z}$.

Proof of Lemma 5.5. For $n \in \mathbb{N}$ the following applies to the function $f(x)$ in (5.40)

$$\begin{aligned}\int_{-\infty}^{\infty} |f(x)| \, \mathrm{d}x &= \frac{1}{\Gamma\left(n+\frac{1}{2}\right)\sqrt{\pi}2^n} \int_{-1}^{1} \left(1-x^2\right)^{n-1/2} \, \mathrm{d}x \\ &< \frac{1}{\Gamma\left(n+\frac{1}{2}\right)\sqrt{\pi}2^n} \int_{-1}^{1} 1 \, \mathrm{d}x = \frac{1}{\Gamma\left(n+\frac{1}{2}\right)\sqrt{\pi}2^{n-1}} < \infty\end{aligned}$$

and therefore $f \in L^1(\mathbb{R})$ holds true. For $n = 0$ the following substitution $x = \cos(t)$ is applied and the result is

$$\int_{-\infty}^{\infty} |f(x)| \, \mathrm{d}x = \frac{1}{\pi} \int_{-1}^{1} \frac{1}{\sqrt{1-x^2}} \, \mathrm{d}x = \frac{1}{\pi} \int_{0}^{\pi} \frac{1}{\sin(t)} \sin(t) \, \mathrm{d}t = \frac{1}{\pi} \int_{0}^{\pi} 1 \, \mathrm{d}t = 1.$$

By carrying out the Fourier transform, we obtain

$$\begin{aligned}\mathcal{F}\left\{ \frac{(1-x^2)^{n-1/2}}{\Gamma\left(n+\frac{1}{2}\right)\sqrt{\pi}2^n} \operatorname{rect}\left(\frac{x}{2}\right) \right\} &= \int_{-\infty}^{\infty} \frac{(1-x^2)^{n-1/2}}{\Gamma\left(n+\frac{1}{2}\right)\sqrt{\pi}2^n} \operatorname{rect}\left(\frac{x}{2}\right) \mathrm{e}^{-\mathrm{i}\omega_x x} \, \mathrm{d}x \\ &= \frac{1}{\Gamma\left(n+\frac{1}{2}\right)\sqrt{\pi}2^n} \int_{-1}^{1} \left(1-x^2\right)^{n-1/2} \mathrm{e}^{-\mathrm{i}\omega_x x} \, \mathrm{d}x \\ &= \frac{2}{\Gamma\left(n+\frac{1}{2}\right)\sqrt{\pi}2^n} \int_{0}^{1} \left(1-x^2\right)^{n-1/2} \cos(\omega_x x) \, \mathrm{d}x.\end{aligned}$$

Using the formula

$$J_\nu(z) = \frac{2(\frac{1}{2}z)^\nu}{\pi^{\frac{1}{2}}\Gamma(\nu+\frac{1}{2})} \int_0^1 \left(1-t^2\right)^{\nu-\frac{1}{2}} \cos(zt) \, \mathrm{d}t, \qquad \nu > -\frac{1}{2}$$

from [1, §9.1.20], it holds that

$$\mathcal{F}\left\{ \frac{(1-x^2)^{n-1/2}}{\Gamma\left(n+\frac{1}{2}\right)\sqrt{\pi}2^n} \operatorname{rect}\left(\frac{x}{2}\right) \right\} = \frac{J_n(\omega_x)}{\omega_x^n}$$

for all $n \in \mathbb{N}_0$, which corresponds to the expression in (5.41). □

6 Fourier Analytical Representation of Magnetic Particle Imaging

After discussing the Langevin model and its relation to the theory of MPI in the previous chapters, introducing the Fourier transform, in particular Chebyshev polynomials and Bessel functions, a detailed Fourier-analytical investigation of the system function of MPI will now be carried out. Therefore, in the first section the spatio-temporal Fourier representation of the MPI system function is derived and in the second section the multidimensional Fourier-transformed Langevin function is discussed.

In contrast to the previous chapters, a vectorial notation will also be used here; the voltage signals caused by an N-dimensional SPIO distribution and received at N' receive coils can be written as a vector-valued T_{D}-periodic voltage function $\boldsymbol{u}^{\mathrm{P}} : \mathbb{R} \to \mathbb{R}^{N'}$ [48, 81, 92] and is

$$\boldsymbol{u}^{\mathrm{P}}(t) = \boldsymbol{M}_0 \boldsymbol{g}(t)$$

with $\boldsymbol{M}_0 = \mu_0 m_0 \boldsymbol{P}$, where matrix $\boldsymbol{P} \in \mathbb{R}^{N' \times N}$ with $\boldsymbol{P} = (\boldsymbol{\rho}_\ell^{\mathsf{T}})_{\ell=1}^{N'}$ denotes the homogeneous coil sensitivities. The vector-valued auxiliary function $\boldsymbol{g} : \mathbb{R} \to \mathbb{R}^N$ represents the essential content of the voltage signal $\boldsymbol{u}^{\mathrm{P}}(t)$. Consequently, instead of the voltage signals the auxiliary function $\boldsymbol{g}(t)$ is used in the following section. The auxiliary function $\boldsymbol{g}(t)$ is connected to the voltage signals $\boldsymbol{u}^{\mathrm{P}}(t)$ by the linear transformation matrix $\boldsymbol{M}_0$. The function $\boldsymbol{g}(t)$ is calculated with help of a component-wise integration of the vector-valued components by (cf. (2.27))

$$\begin{aligned}
\boldsymbol{g}(t) &= \frac{\mathrm{d}}{\mathrm{d}t} \int_{\mathbb{R}^N} c(\boldsymbol{x})\, \mathscr{L}\big(\beta \|\boldsymbol{G}(\boldsymbol{x}_{\mathrm{FFP}}(t) - \boldsymbol{x})\|\big) \frac{\boldsymbol{G}\left(\boldsymbol{x}_{\mathrm{FFP}}(t) - \boldsymbol{x}\right)}{\|\boldsymbol{G}(\boldsymbol{x}_{\mathrm{FFP}}(t) - \boldsymbol{x})\|}\, \mathrm{d}\boldsymbol{x}, \\
&= \frac{\mathrm{d}}{\mathrm{d}t} \int_{\mathbb{R}^N} c(\boldsymbol{x})\, \mathscr{L}_{\mathrm{n}}\big(\beta \|\boldsymbol{G}(\boldsymbol{x}_{\mathrm{FFP}}(t) - \boldsymbol{x})\|\big) \beta \boldsymbol{G}\left(\boldsymbol{x}_{\mathrm{FFP}}(t) - \boldsymbol{x}\right) \mathrm{d}\boldsymbol{x}, \qquad (6.1) \\
&= \frac{\mathrm{d}}{\mathrm{d}t} \int_{\mathbb{R}^N} c(\boldsymbol{x})\, \boldsymbol{\mathscr{L}}\big(\beta(\boldsymbol{G}(\boldsymbol{x}_{\mathrm{FFP}}(t) - \boldsymbol{x}))\big)\, \mathrm{d}\boldsymbol{x}
\end{aligned}$$

with $\beta = \frac{\mu_0 m_0}{k_\mathrm{B} T_\mathrm{P}}$. The vector $\boldsymbol{x} \in \mathbb{R}^N$ denotes the spatial position, and $c : \Omega \to \mathbb{R}_+$ is the spatial SPIO distribution with the bounded support $\Omega \subset \mathbb{R}^N$. Moreover, the bounded support of the SPIO distribution is essential for the existence of the integral in (6.1), since otherwise the integral may become divergent as the Langevin function is only a bounded function in $L^\infty(\mathbb{R}^N)$.

The vector-valued version of (2.32) is written as an inner product between the SPIO distribution $c(\boldsymbol{x})$ and a system function $\boldsymbol{s} : \mathbb{R}^N \times \mathbb{R} \to \mathbb{R}^N$ that includes all terms that are independent of $c(\boldsymbol{x})$:

$$\boldsymbol{g}(t) = \int_{\mathbb{R}^N} \boldsymbol{s}(\boldsymbol{x}, t) c(\boldsymbol{x}) \, \mathrm{d}\boldsymbol{x}. \tag{6.2}$$

By comparing (6.2) with (6.1), it can be obtained that the vector-valued system function itself can be written in the following form

$$\boldsymbol{s}(\boldsymbol{x}, t) = \frac{\partial}{\partial t} \left[\mathscr{L} \left(\beta \left(\boldsymbol{G}(\boldsymbol{x}_\mathrm{FFP}(t) - \boldsymbol{x}) \right) \right) \right]. \tag{6.3}$$

The vector-valued version of (2.36) for $\boldsymbol{g}(t)$ reads

$$\begin{aligned} \boldsymbol{g}_k &= \frac{1}{T_\mathrm{D}} \int_{-\frac{T_\mathrm{D}}{2}}^{\frac{T_\mathrm{D}}{2}} \boldsymbol{g}(t) \mathrm{e}^{-\mathrm{i}\omega_k t} \, \mathrm{d}t \\ &= \int_{\mathbb{R}^N} \boldsymbol{s}_k(\boldsymbol{x}) c(\boldsymbol{x}) \, \mathrm{d}\boldsymbol{x} \end{aligned} \tag{6.4}$$

with $\omega_k = \frac{2\pi k}{T_\mathrm{D}} = 2\pi k f_\mathrm{D}$ and

$$\boldsymbol{s}_k(\boldsymbol{x}) = \frac{1}{T_\mathrm{D}} \int_{-\frac{T_\mathrm{D}}{2}}^{\frac{T_\mathrm{D}}{2}} \boldsymbol{s}(\boldsymbol{x}, t) \mathrm{e}^{-\mathrm{i}\omega_k t} \, \mathrm{d}t \tag{6.5}$$

being the k-th Fourier series component of the system function $\boldsymbol{s}(\boldsymbol{x}, t)$.

6.1 The MPI System Equation in Spatio-Temporal Fourier Space

The following theorem states that it is possible to separate the SPIO- and the trajectory-dependent terms in the system equation in (6.4) using the spatial Fourier transform. This result was first published in [F1].

Theorem 6.1

Let $c(\boldsymbol{x})$ be of bounded support and in $L^1(\mathbb{R}^N) \cap L^2(\mathbb{R}^N)$, then the Fourier series coefficients $\boldsymbol{g}_k$ of $\boldsymbol{g}(t)$ in (6.4) can be expressed using the spatial Fourier transform by

$$\boldsymbol{g}_k = \frac{\mathrm{i}\omega_k}{(2\pi)^n} \int_{\mathbb{R}^N} \hat{\boldsymbol{h}}(\boldsymbol{\omega}_{\boldsymbol{x}}) P(\boldsymbol{\omega}_{\boldsymbol{x}}, k) \, \mathrm{d}\boldsymbol{\omega}_{\boldsymbol{x}}, \tag{6.6}$$

where the function

$$P(\boldsymbol{\omega}_{\boldsymbol{x}}, k) = \frac{1}{2\pi} \int_{-\pi}^{\pi} \mathrm{e}^{\mathrm{i}\boldsymbol{\omega}_{\boldsymbol{x}}^{\mathsf{T}} \boldsymbol{x}_{\mathrm{FFP}}\left(\frac{z}{2\pi f_D}\right)} \mathrm{e}^{-\mathrm{i}kz} \, \mathrm{d}z \tag{6.7}$$

only depends on the used FFP-trajectory $\boldsymbol{x}_{\mathrm{FFP}}(t)$ with period length $T_D = \frac{1}{f_D}$. The term $\hat{\boldsymbol{h}}(\boldsymbol{\omega}_{\boldsymbol{x}})$ is given by

$$\hat{\boldsymbol{h}}(\boldsymbol{\omega}_{\boldsymbol{x}}) = \hat{c}(\boldsymbol{\omega}_{\boldsymbol{x}}) \frac{1}{|\det(\beta \boldsymbol{G})|} \hat{\mathscr{L}}\left(\frac{\boldsymbol{G}^{-\mathsf{T}} \boldsymbol{\omega}_{\boldsymbol{x}}}{\beta}\right), \tag{6.8}$$

where $\hat{\mathscr{L}}(\boldsymbol{\omega}_{\boldsymbol{x}})$ and $\hat{c}(\boldsymbol{\omega}_{\boldsymbol{x}})$ are the continuous spatial Fourier transforms of the Langevin function $\mathscr{L}(\boldsymbol{x})$ and the SPIO distribution $c(\boldsymbol{x})$, respectively.

Proof of Theorem 6.1. Note that a vector-valued notation for the convolution is used within the proof:

$$\boldsymbol{h}(\boldsymbol{x}) = \int_{\mathbb{R}^N} c(\boldsymbol{u}) \, \mathscr{L}\left(\beta \boldsymbol{G}(\boldsymbol{x} - \boldsymbol{u})\right) \mathrm{d}\boldsymbol{u}. \tag{6.9}$$

In a first step, the Fourier series expansion of $\frac{\mathrm{d}}{\mathrm{d}t}\boldsymbol{h}(\boldsymbol{x}_{\mathrm{FFP}}(t))$ is to be calculated. The Fourier series coefficients of $\frac{\mathrm{d}}{\mathrm{d}t}\boldsymbol{h}(\boldsymbol{x}_{\mathrm{FFP}}(t))$ are given by

$$\boldsymbol{g}_k = \mathrm{i}\omega_k f_D \int_{-\frac{T_D}{2}}^{\frac{T_D}{2}} \boldsymbol{h}(\boldsymbol{x}_{\mathrm{FFP}}(t)) \mathrm{e}^{-\mathrm{i}\omega_k t} \, \mathrm{d}t, \tag{6.10}$$

where $\omega_k = 2\pi f_k = 2\pi \frac{k}{T_D} = 2\pi k f_D$ and T_D is the duration of one period of the motion of the FFP over the entire trajectory (cf. (2.47)).

The convolution in (6.9) is equivalent to a multiplication in the Fourier domain (Property 5) and applying the Fourier transform rules for an affine transform with $\boldsymbol{A} = \beta \boldsymbol{G}$ (Property 2) leads to

$$\hat{\boldsymbol{h}}(\boldsymbol{\omega}_{\boldsymbol{x}}) = \hat{c}(\boldsymbol{\omega}_{\boldsymbol{x}}) \frac{1}{|\det(\beta \boldsymbol{G})|} \hat{\mathscr{L}}\left(\frac{\boldsymbol{G}^{-\mathsf{T}} \boldsymbol{\omega}_{\boldsymbol{x}}}{\beta}\right). \tag{6.11}$$

A formal proof of this has to be performed within the distribution theory. As $c(\boldsymbol{x})$ has a bounded support, is in $L^1(\mathbb{R}^N) \cap L^2(\mathbb{R}^N)$, and the locally integrable function $\mathscr{L}(\boldsymbol{x})$ is in $L^\infty(\mathbb{R}^N)$, the integral in (6.9) exists and, consequently, $\boldsymbol{h}(\boldsymbol{x})$ is locally integrable. The latter makes it possible to define a distributional forward Fourier transform on $\boldsymbol{h}(\boldsymbol{x})$, which is given by $\hat{\boldsymbol{h}}(\boldsymbol{\omega}_{\boldsymbol{x}})$ in (6.11).

By using the ideas in [13], $\boldsymbol{h}(\boldsymbol{x}_{\mathrm{FFP}}(t))$ is represented by the inverse Fourier transform with respect to $\boldsymbol{\omega}_{\boldsymbol{x}}$:

$$\boldsymbol{h}(\boldsymbol{x}_{\mathrm{FFP}}(t)) = \frac{1}{(2\pi)^N} \int_{\mathbb{R}^N} \hat{\boldsymbol{h}}(\boldsymbol{\omega}_{\boldsymbol{x}}) \mathrm{e}^{\mathrm{i}\boldsymbol{\omega}_{\boldsymbol{x}}^{\mathsf{T}} \boldsymbol{x}_{\mathrm{FFP}}(t)} \, \mathrm{d}\boldsymbol{\omega}_{\boldsymbol{x}}. \tag{6.12}$$

By substituting $t = \frac{z}{2\pi f_D}$ in (6.10), inserting (6.12), and changing the order of integration, it is possible to obtain

$$\begin{aligned} \boldsymbol{g}_k &= \frac{\mathrm{i}\omega_k}{2\pi} \int_{-\pi}^{\pi} \boldsymbol{h}\left(\boldsymbol{x}_{\mathrm{FFP}}\left(\frac{z}{2\pi f_D}\right)\right) \mathrm{e}^{-\mathrm{i}kz} \, \mathrm{d}z, \\ &= \frac{\mathrm{i}\omega_k}{(2\pi)^{N+1}} \int_{-\pi}^{\pi} \int_{\mathbb{R}^N} \hat{\boldsymbol{h}}(\boldsymbol{\omega}_{\boldsymbol{x}}) \mathrm{e}^{\mathrm{i}\boldsymbol{\omega}_{\boldsymbol{x}}^{\mathsf{T}} \boldsymbol{x}_{\mathrm{FFP}}\left(\frac{z}{2\pi f_D}\right)} \, \mathrm{d}\boldsymbol{\omega}_{\boldsymbol{x}} \, \mathrm{e}^{-\mathrm{i}kz} \, \mathrm{d}z, \\ &= \frac{\mathrm{i}\omega_k}{(2\pi)^N} \int_{\mathbb{R}^N} \hat{\boldsymbol{h}}(\boldsymbol{\omega}_{\boldsymbol{x}}) \left[\frac{1}{2\pi} \int_{-\pi}^{\pi} \mathrm{e}^{\mathrm{i}\boldsymbol{\omega}_{\boldsymbol{x}}^{\mathsf{T}} \boldsymbol{x}_{\mathrm{FFP}}\left(\frac{z}{2\pi f_D}\right)} \mathrm{e}^{-\mathrm{i}kz} \, \mathrm{d}z\right] \mathrm{d}\boldsymbol{\omega}_{\boldsymbol{x}}. \end{aligned} \tag{6.13}$$

The comparison of (6.13) with (6.6) and (6.7) confirms Theorem 6.1. □

6.2 Fourier Transform of the Langevin Function

In the following, the Fourier transform of the multidimensional Langevin function is presented, which occurs in the MPI context when the Langevin model of paramagnetism is used. The results are based on the results published for the case of one-dimensional excitation in [F8] and for the case of multidimensional excitation in [F1]. Some of the central results are generalized in this thesis, if this is the case, it is mentioned separately. Note that the related one-dimensional Fourier transform of the derivative of the Langevin function (6.34) can also be found in the independent works [17, 24].

On the basis of a series expansion for $\mathscr{L}(x)$, which is given in the next lemma, the Fourier transform of the Langevin function will be established.

Lemma 6.1. *The Langevin function $\mathscr{L} : \mathbb{R} \to \mathbb{R}$ has the uniformly convergent series expansion*

$$\begin{aligned} \mathscr{L}(x) &= \sum_{k=1}^{\infty} \frac{2x}{k^2\pi^2 + x^2} \\ &= \frac{1}{\mathrm{i}} \sum_{k=1}^{\infty} \left(\frac{1}{k\pi - \mathrm{i}x} - \frac{1}{k\pi + \mathrm{i}x} \right) \end{aligned} \tag{6.14}$$

and in consequence the normalized version $\mathscr{L}_{\mathrm{n}} : \mathbb{R} \to \mathbb{R}$ has the uniformly convergent series expansion

$$\mathscr{L}_{\mathrm{n}}(x) = \sum_{k=1}^{\infty} \frac{2}{k^2\pi^2 + x^2}. \tag{6.15}$$

Proof of Lemma 6.1. With the help of the gamma function $\Gamma : \mathbb{C} \to \mathbb{C}$, the uniform convergence of the series (6.14) is shown here. The gamma function is given by

$$\Gamma(z) = \int_0^{\infty} t^{z-1} \mathrm{e}^{-t} \, \mathrm{d}t,$$

and based on this, the digamma function reads

$$\psi(z) = \frac{\mathrm{d}}{\mathrm{d}z} \ln\left(\Gamma(z)\right) = \frac{\Gamma'(z)}{\Gamma(z)}.$$

The digamma function has the following properties that are useful for the proof [1, §6.3.5, §6.3.7]:

$$\psi(z+1) - \psi(z) = \frac{1}{z},$$
$$\psi(1-z) - \psi(z) = \pi \cot(\pi z).$$

Using these properties and subtracting these equations from each other gives

$$\psi(1-z) - \psi(z+1) = \pi \cot(\pi z) - \frac{1}{z}. \tag{6.16}$$

Using the complex argument $z = \frac{\mathrm{i}x}{\pi}$ ($x \in \mathbb{R}$) for (6.16) and multiplying it by the factor $\frac{\mathrm{i}}{\pi}$ the following representation for the Langevin function is obtained:

$$\begin{aligned}
\mathscr{L}(x) &= \coth(x) - \frac{1}{x} \\
&= \mathrm{i}\cot(\mathrm{i}x) - \frac{1}{x} \\
&= \frac{\mathrm{i}}{\pi}\left(\pi\cot(\mathrm{i}x) + \frac{\mathrm{i}\pi}{x}\right) \\
&= \frac{\mathrm{i}}{\pi}\left(\pi\cot\left(\pi\frac{\mathrm{i}x}{\pi}\right) - \frac{\pi}{\mathrm{i}x}\right) \\
&= \frac{\mathrm{i}}{\pi}\left(\psi\left(1 - \frac{\mathrm{i}x}{\pi}\right) - \psi\left(\frac{\mathrm{i}x}{\pi} + 1\right)\right).
\end{aligned} \tag{6.17}$$

The digamma function has the series expansion [1, §6.3.16]

$$\psi(z+1) = -\gamma + \sum_{k=1}^{\infty} \frac{z}{k(k+z)}, \quad z \neq -1, -2, -3, \ldots \tag{6.18}$$

with γ being the Euler–Mascheroni constant. The substitution of (6.18) in (6.17) leads to

$$\begin{aligned}
\mathscr{L}(x) &= \frac{\mathrm{i}}{\pi}\left(-\gamma + \sum_{k=1}^{\infty} \frac{-\frac{\mathrm{i}x}{\pi}}{k(k-\frac{\mathrm{i}x}{\pi})} + \gamma - \sum_{k=1}^{\infty} \frac{\frac{\mathrm{i}x}{\pi}}{k(k+\frac{\mathrm{i}x}{\pi})}\right) \\
&= \frac{\mathrm{i}}{\pi}\left(\sum_{k=1}^{\infty} \frac{-\frac{\mathrm{i}x}{\pi}}{k(k-\frac{\mathrm{i}x}{\pi})} - \sum_{k=1}^{\infty} \frac{\frac{\mathrm{i}x}{\pi}}{k(k+\frac{\mathrm{i}x}{\pi})}\right) \\
&= \frac{\mathrm{i}}{\pi}\left[-\frac{\mathrm{i}x}{\pi}\left(\sum_{k=1}^{\infty} \frac{1}{k(k-\frac{\mathrm{i}x}{\pi})} + \sum_{k=1}^{\infty} \frac{1}{k(k+\frac{\mathrm{i}x}{\pi})}\right)\right].
\end{aligned} \tag{6.19}$$

In the further derivation of the series expansion the pointwise convergence to $\mathscr{L}(x)$ is used. Since for fixed $x \in \mathbb{R}$ it holds that $|\frac{1}{k(k\pm\mathrm{i}x/\pi)}| = \mathcal{O}(\frac{1}{k^2})$, the series in (6.19) are

absolutely convergent, and thus a pointwise convergence is given. This allows the two series to be combined into a single one:

$$\begin{aligned}\mathscr{L}(x) &= \frac{x}{\pi^2}\left(\sum_{k=1}^{\infty}\frac{1}{k(k-\frac{\mathrm{i}x}{\pi})}+\sum_{k=1}^{\infty}\frac{1}{k(k+\frac{\mathrm{i}x}{\pi})}\right)\\ &= \frac{x}{\pi^2}\sum_{k=1}^{\infty}\left(\frac{1}{k(k-\frac{\mathrm{i}x}{\pi})}+\frac{1}{k(k+\frac{\mathrm{i}x}{\pi})}\right)\\ &= \frac{x}{\pi^2}\sum_{k=1}^{\infty}\frac{k+\frac{\mathrm{i}x}{\pi}+k-\frac{\mathrm{i}x}{\pi}}{k\left(k-\frac{\mathrm{i}x}{\pi}\right)\left(k+\frac{\mathrm{i}x}{\pi}\right)}\\ &= \sum_{k=1}^{\infty}\frac{2x}{\pi^2k^2+x^2}.\end{aligned} \tag{6.20}$$

The series is uniformly convergent on every finite closed interval $\Omega = [-\alpha, \alpha]$ with $\alpha \in \mathbb{R}$. This is proved by the Weierstrass M-test:

$$\begin{aligned}&\forall k \in \mathbb{N} \quad \forall x \in \Omega \quad \exists c_k > 0 :\\ &|f_k(x)| \leq c_k \wedge \sum_{k=1}^{\infty} c_k < \infty\\ &\Rightarrow \sum_{k=1}^{\infty} f_k(x) \text{ is uniformly convergent.}\end{aligned}$$

Therefore, let $f_k : \mathbb{R} \to \mathbb{R}$ be given as $f_k(x) = \frac{2x}{\pi^2k^2+x^2}$. Then, due to the odd symmetry $f_k(x) = -f_k(-x)$, it is sufficient to find the maximizer $x_{\max}$ for the function $f_k(x)$ on the interval $[0, \alpha]$. The function term $f_k(x)$ and its derivatives are

$$\begin{aligned}f_k(x) &= \frac{2x}{\pi^2k^2+x^2},\\ f_k'(x) &= \frac{2\left(\pi^2k^2-x^2\right)}{\left(\pi^2k^2+x^2\right)^2},\\ f_k''(x) &= \frac{4x\left(x^2-3\pi^2k^2\right)}{\left(\pi^2k^2+x^2\right)^3}.\end{aligned}$$

There is a $K \in \mathbb{N}$ such that for all $k \leq K-1 \leq \alpha\pi < K$, the maximizer on the interval $[0, \alpha]$ of $|f_k(x)|$ is $x_{\max}^k = \pi k$. This can be checked by observing that $|f_k'(x_{\max}^k)| = 0$ and $f_k''(x_{\max}^k) = \frac{-1}{\pi^3k^3} < 0$. For all $k \geq K$ and $\tau \in [0, \alpha]$, $f_k'(\tau) > 0$ holds. Hence, the continuous function $f_k(x)$ on the interval $[0, \alpha]$ is strictly increasing and the maximal

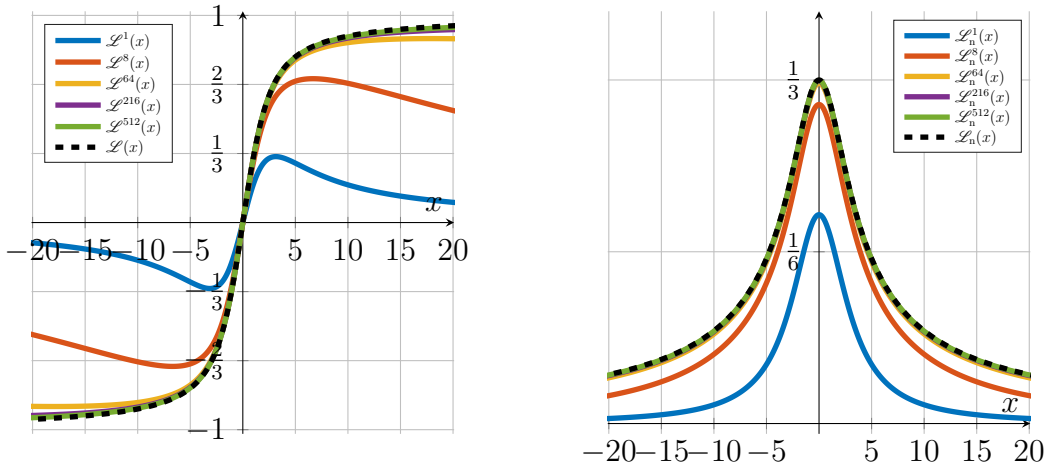

(a) (b)

Figure 6.1: The partial sums $\mathscr{L}^K(x)$ and $\mathscr{L}_{\mathrm{n}}^K(x)$ (6.21) of the Langevin function $\mathscr{L}(x)$ and normalized Langevin function $\mathscr{L}_{\mathrm{n}}(x)$ are shown for $K \in \{1, 8, 64, 216, 512\}$. In (a) the partial sum with convergence to $\mathscr{L}(x)$ is shown and (b) shows the partial sum with convergence to $\mathscr{L}_{\mathrm{n}}(x)$.

value is reached on the upper boundary of the interval: $x_{\max}^k = \alpha$. Therefore, the following inequality is obtained

$$\begin{aligned}
\sum_{k=1}^{\infty} |f_k(x)| &= \sum_{k=1}^{K-1} |f_k(x)| + \sum_{k=K}^{\infty} |f_k(x)| \\
&\leq \sum_{k=1}^{K-1} |f_k(\pi k)| + \sum_{k=K}^{\infty} |f_k(\alpha)| \\
&= \sum_{k=1}^{K-1} \frac{1}{\pi k} + \sum_{k=K}^{\infty} \frac{2\alpha}{\pi^2 k^2 + \alpha^2} \\
&< c + 2\alpha \sum_{k=1}^{\infty} \frac{1}{\pi^2 k^2 + \alpha^2} \quad \text{with} \quad c \in \mathbb{R} \\
&< c + 2\frac{\alpha}{\pi^2} \sum_{k=1}^{\infty} \frac{1}{k^2} = c + \frac{\alpha}{3} < \infty.
\end{aligned}$$

The Weierstrass M-test is fulfilled and it follows that the series is uniformly convergent on every finite closed interval $[-\alpha, \alpha]$. Due the pointwise convergence in (6.20), it is uniformly convergent to $\mathscr{L}(x)$ on every finite interval on $\mathbb{R}$. □

The K-th partial sums of the series for $\mathscr{L}_{\mathrm{n}}(x)$ from Lemma 6.1 are used to derive the different Fourier transform version of the Langevin function. The K-th partial sums for the series of $\mathscr{L}(x)$ and $\mathscr{L}_{\mathrm{n}}(x)$ are given by

$$\mathscr{L}^K(x) = \sum_{k=1}^{K} \frac{2x}{k^2\pi^2 + x^2} \quad \text{and} \quad \mathscr{L}_{\mathrm{n}}^K(x) = \sum_{k=1}^{K} \frac{2}{k^2\pi^2 + x^2}. \tag{6.21}$$

The partial sums are presented in Figure 6.1.

Using the series expansion, the Fourier transform of the one-dimensional normalized Langevin function $\mathscr{L}_{\mathrm{n}}(x)$ can be derived, which is formulated in the next theorem. Note that in the following theorem an auxiliary function $\Lambda_1 : \mathbb{R}_+ \to \mathbb{R}$ is introduced, which later helps to formulate the N-dimensional Fourier transform of the Langevin function in a generalized form.

Theorem 6.2

The one-dimensional Fourier transform of the normalized Langevin function $\mathscr{L}_{\mathrm{n}} : \mathbb{R} \to \mathbb{R}_+$ is given by

$$\hat{\mathscr{L}}_{\mathrm{n}}(\omega_x) = \Lambda_1(s) \qquad \text{with} \qquad s = |\omega_x|, \qquad \omega_x \neq 0, \tag{6.22}$$

$$\Lambda_1(s) = -2\ln\left(1 - \mathrm{e}^{-\pi s}\right), \quad s > 0, \tag{6.23}$$

and $\hat{\mathscr{L}}_{\mathrm{n}} \in L^1(\mathbb{R})$.

Proof of Theorem 6.2. Using the K-th partial sum for the series of $\mathscr{L}_{\mathrm{n}}(x)$ (cf. (6.21)) yields

$$\mathscr{L}_{\mathrm{n}}^K(x) = \sum_{k=1}^{K} \frac{2}{k^2\pi^2 + x^2},$$

which is for all $K \in \mathbb{N}$ in $L^1(\mathbb{R}) \cap L^2(\mathbb{R})$. The application of L^2-convergence according to (4.25) enforces that

$$\begin{aligned}\hat{\mathscr{L}}_{\mathrm{n}}^K(\omega_x) &= \mathcal{F}\left\{\mathscr{L}_{\mathrm{n}}^K(x)\right\} \\ &= \mathcal{F}\left\{\sum_{k=1}^{K} \frac{2}{k^2\pi^2 + x^2}\right\} = \sum_{k=1}^{K} \mathcal{F}\left\{\frac{2}{k^2\pi^2 + x^2}\right\}\end{aligned}$$

is a sequence in $L^2(\mathbb{R})$, i.e., the series will converge pointwise for all $K \to +\infty$ and $\omega_x \neq 0$ towards the Fourier transform of $\mathscr{L}_\mathrm{n}(x)$ in L^2-mean. Taking advantage of the fact that the Fourier transform of $\frac{2}{k^2\pi^2+x^2}$ is

$$\mathcal{F}\left\{\frac{2}{k^2\pi^2+x^2}\right\} = \frac{2}{k}\mathrm{e}^{-k\pi|\omega_x|}$$

and that [1, §4.1.24]

$$\sum_{k=1}^{\infty}\frac{1}{k}z^{-k} = -\ln\left(1-\frac{1}{z}\right) \quad \text{for} \quad |z|>1,$$

holds, the result is

$$\hat{\mathscr{L}}_\mathrm{n}(\omega_x) = \sum_{k=1}^{\infty}\frac{2}{k}\mathrm{e}^{-k\pi|\omega_x|} = -2\ln\left(1-\mathrm{e}^{-\pi|\omega_x|}\right), \quad |\omega_x|>0. \tag{6.24}$$

It remains to show that $\hat{\mathscr{L}}_\mathrm{n}(\omega_x)$ is in $L^1(\mathbb{R})$. Due to the singularity at $\omega_x = 0$ and the property that $\hat{\mathscr{L}}_\mathrm{n}(\omega_x)$ is symmetric and non-negative for all ω_x, the integration over $|\hat{\mathscr{L}}_\mathrm{n}(\omega_x)|$ is performed by taking limits in the following form:

$$\int_{-\infty}^{\infty}\left|\hat{\mathscr{L}}_\mathrm{n}(\omega_x)\right|\,\mathrm{d}\omega_x = 2\lim_{\epsilon^+\to 0}\int_{\epsilon}^{\frac{1}{\epsilon}}\hat{\mathscr{L}}_\mathrm{n}(\omega_x)\,\mathrm{d}\omega_x.$$

Using the series expansion in (6.24) and the fact that the series is absolutely convergent for all $\omega_x > 0$, the limit and the integration can be interchanged. Thus, it follows

$$\begin{aligned}
\int_{-\infty}^{\infty}\left|\hat{\mathscr{L}}_\mathrm{n}(\omega_x)\right|\,\mathrm{d}\omega_x &= 2\lim_{\epsilon^+\to 0}\int_{\epsilon}^{\frac{1}{\epsilon}}\sum_{k=1}^{\infty}\frac{2}{k}\mathrm{e}^{-k\pi\omega_x}\,\mathrm{d}\omega_x \\
&= 2\lim_{\epsilon^+\to 0}\sum_{k=1}^{\infty}\int_{\epsilon}^{\frac{1}{\epsilon}}\frac{2}{k}\mathrm{e}^{-k\pi\omega_x}\,\mathrm{d}\omega_x = 2\lim_{\epsilon^+\to 0}\sum_{k=1}^{\infty}\frac{-2}{\pi k^2}\mathrm{e}^{-k\pi\omega_x}\Big|_{\epsilon}^{\frac{1}{\epsilon}} \\
&= 2\sum_{k=1}^{\infty}\left(\frac{-2}{\pi k^2}\mathrm{e}^{-k\pi\infty} - \frac{-2}{\pi k^2}\mathrm{e}^{-k\pi 0}\right) \\
&= 2\sum_{k=1}^{\infty}\frac{2}{\pi k^2} = \frac{2\pi}{3} < \infty
\end{aligned}$$

and therefore an inverse Fourier transform exists that converges to $\mathscr{L}_\mathrm{n}(x)$. □

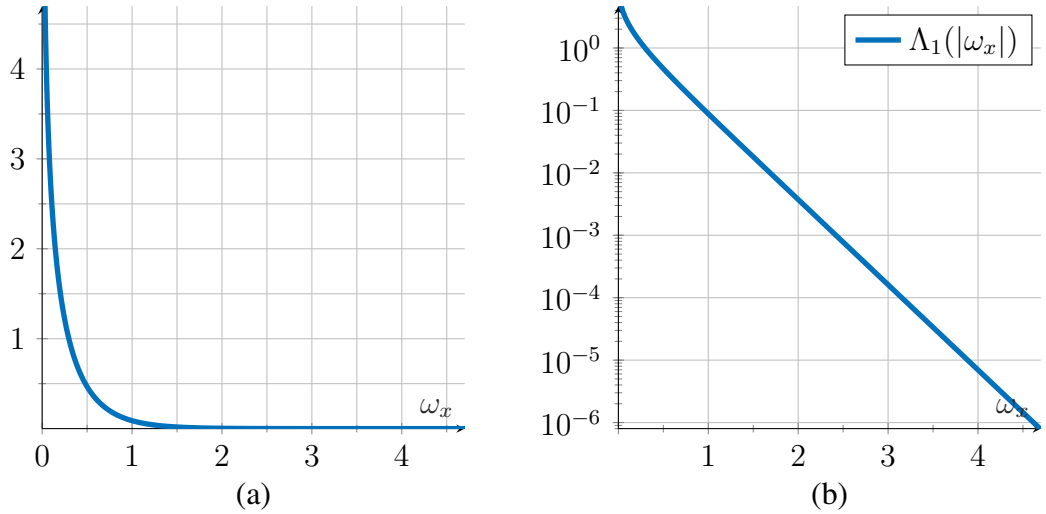

Figure 6.2: The Fourier transform $\hat{\mathscr{L}}_{\mathrm{n}}(\omega_x) = \Lambda_1(|\omega_x|)$ of the one-dimensional normalized Langevin function in normal scale (a) and log-scale (b).

The function $\hat{\mathscr{L}}_{\mathrm{n}}(\omega_x) = \Lambda_1(|\omega_x|)$ is plotted in Figure 6.2. In Figure 6.2 (a) it can be seen that there is a singularity at $\omega_x = 0$. The log-scale plot in Figure 6.2 (b) shows for $\Lambda_1(\omega_x)$ an exponential decay, if $\omega_x \to \infty$. The singularity at $\omega_x^+ \to 0$ is a logarithmic singularity, which can be verified by the fact that $f(\xi) = -\ln(1 - \mathrm{e}^{-\xi})$ is an involution.

The one-dimensional correspondence between $\mathscr{L}_{\mathrm{n}}(x)$ and $\hat{\mathscr{L}}_{\mathrm{n}}(\omega_x)$ should also be extended to higher dimensions. For this purpose, it is helpful to use Definition 4.3 of radial functions in (4.29). From the definition for radial functions in (4.29) it can be concluded that the function $\ell_{\mathrm{n}} : \mathbb{R}^N \to \mathbb{R}$ with $\ell_{\mathrm{n}}(\boldsymbol{x}) = \mathscr{L}_{\mathrm{n}}(\|\boldsymbol{x}\|)$ is a radial function.

In the following, the two- and three-dimensional Fourier transforms of $\mathscr{L}_{\mathrm{n}}(\|\boldsymbol{x}\|)$ are calculated, where $\|\boldsymbol{x}\|$ denotes either the two- or three-dimensional Euclidean norm of a vector $\boldsymbol{x}$.

Theorem 6.3

The two-dimensional Fourier transform of $\ell_{\mathrm{n}} : \mathbb{R}^2 \to \mathbb{R}$ with $\ell_{\mathrm{n}}(\boldsymbol{x}) = \mathscr{L}_{\mathrm{n}}(\|\boldsymbol{x}\|)$ results in

$$\hat{\mathscr{L}}_{\mathrm{n}}(\boldsymbol{\omega}_{\boldsymbol{x}}) = \Lambda_2(s) \qquad \text{with} \qquad s = \|\boldsymbol{\omega}_{\boldsymbol{x}}\| \qquad \text{and} \qquad \boldsymbol{\omega}_{\boldsymbol{x}} \neq \mathbf{0} \tag{6.25}$$

and

$$\Lambda_2(s) = 4\pi \int_0^\infty \frac{1}{\mathrm{e}^{\pi s \cosh(t)} - 1} \, \mathrm{d}t. \tag{6.26}$$

Proof of Theorem 6.3. The Hankel transform (see Definition 4.4) is used to derive the two-dimensional Fourier transform of $\ell_{\mathrm{n}}(\boldsymbol{x}) = \mathscr{L}_{\mathrm{n}}(\|\boldsymbol{x}\|)$. For two dimensions, i.e., $N = 2$, the following is obtained

$$\hat{F}_2(s) = 2\pi \mathcal{H}_0 \left\{ F(r) \right\} = 2\pi \int_0^\infty J_0(sr) F(r) r \, \mathrm{d}r.$$

Using the K-th partial sum of the series for $\mathscr{L}_{\mathrm{n}}(r)$ in Lemma 6.1 yields

$$\mathscr{L}_{\mathrm{n}}^K(r) = \sum_{k=1}^{K} \frac{2}{k^2\pi^2 + r^2}.$$

It should be briefly noted that

$$\begin{aligned} \int_0^\infty r^{\frac{1}{2}} \mathscr{L}_{\mathrm{n}}^K(r) \, \mathrm{d}r &\leq 2K \int_0^\infty r^{\frac{1}{2}} \frac{1}{\pi^2 + r^2} \, \mathrm{d}r \\ &< 2K \left(\int_0^1 1 \, \mathrm{d}r + \int_1^\infty r^{-1.5} \, \mathrm{d}r \right) = 6K < \infty, \end{aligned}$$

which shows that the Hankel transform exists. Thus, the Hankel transform with order zero of $\mathscr{L}_{\mathrm{n}}^K(r)$ reads

$$\begin{aligned} \mathcal{H}_0 \left\{ \mathscr{L}_{\mathrm{n}}^K(r) \right\} &= \mathcal{H}_0 \left\{ \sum_{k=1}^{K} \frac{2}{k^2\pi^2 + r^2} \right\} = \sum_{k=1}^{K} \mathcal{H}_0 \left\{ \frac{2}{k^2\pi^2 + r^2} \right\} = \sum_{k=1}^{K} 2K_0(k\pi s) \\ &= 2 \sum_{k=1}^{K} \int_0^\infty \mathrm{e}^{-k\pi s \cosh(t)} \, \mathrm{d}t = 2 \int_0^\infty \sum_{k=1}^{K} \mathrm{e}^{-k\pi s \cosh(t)} \, \mathrm{d}t \\ &= 2 \int_0^\infty \frac{\mathrm{e}^{-(K+1)\pi s \cosh(t)} - \mathrm{e}^{-\pi s \cosh(t)}}{\mathrm{e}^{-\pi s \cosh(t)} - 1} \, \mathrm{d}t \qquad s > 0 \end{aligned}$$

with $K_0(k\pi s)$ being the modified Bessel function of the second kind and zero order (5.31), where

$$K_0(\alpha\xi) = \int_0^\infty J_0(\alpha\xi t)\frac{t}{1+t^2}\,\mathrm{d}t = \int_0^\infty J_0(\xi u)\frac{u}{\alpha^2+u^2}\,\mathrm{d}u$$

with the substitution $u = \alpha t$ and $\alpha > 0$.

The function

$$S_K(s,t) = \sum_{k=1}^{K} \mathrm{e}^{-k\pi s\cosh(t)} = \frac{\mathrm{e}^{-(K+1)\pi s\cosh(t)} - \mathrm{e}^{-\pi s\cosh(t)}}{\mathrm{e}^{-\pi s\cosh(t)} - 1}$$

is non-negative for $s \geq 0$ and $0 < S_K(s,t) < S_{K+1}(s,t)$ holds. The sequence $(S_K)_{K\in\mathbb{N}}$ is converting pointwise to

$$S(s,t) = \lim_{K\to+\infty} \frac{\mathrm{e}^{-(K+1)\pi s\cosh(t)} - \mathrm{e}^{-\pi s\cosh(t)}}{\mathrm{e}^{-\pi s\cosh(t)} - 1} = \frac{-\mathrm{e}^{-\pi s\cosh(t)}}{\mathrm{e}^{-\pi s\cosh(t)} - 1} = \frac{1}{\mathrm{e}^{\pi s\cosh(t)} - 1}.$$

This makes it possible to apply the monotone convergence theorem and leads to the following result

$$\lim_{K\to+\infty} \int_0^\infty S_K(s,t)\,\mathrm{d}t = \int_0^\infty S(s,t)\,\mathrm{d}t.$$

The use of the previous result confirms that the sequence of Hankel transforms for all $s > 0$ converges pointwise to

$$\mathcal{H}_0\left\{\mathscr{L}_\mathrm{n}(r)\right\} = \lim_{K\to+\infty} \mathcal{H}_0\left\{\mathscr{L}_\mathrm{n}^K(r)\right\} = 2\int_0^\infty \frac{1}{\mathrm{e}^{\pi s\cosh(t)} - 1}\,\mathrm{d}t.$$

The result is then used to calculate the radial Fourier transforms of $\mathscr{L}_\mathrm{n}(r)$ with $r = \|\boldsymbol{x}\|$ in two dimensions. This results in

$$\hat{\mathscr{L}}_\mathrm{n}(\boldsymbol{\omega}_{\boldsymbol{x}}) = \Lambda_2(s) = 4\pi\int_0^\infty \frac{1}{\mathrm{e}^{\pi s\cosh(t)} - 1}\,\mathrm{d}t$$

with $s = \|\boldsymbol{\omega}_{\boldsymbol{x}}\|$ and $\boldsymbol{\omega}_{\boldsymbol{x}} \neq \mathbf{0}$. □

In Figure 6.3 the function $\Lambda_2(s)$ is shown, which correspond to the two-dimensional Fourier transform $\hat{\mathscr{L}}_\mathrm{n} : \mathbb{R}^2 \to \mathbb{R}$ by $s = \|\boldsymbol{\omega}_{\boldsymbol{x}}\|$. The Figure 6.3 shows an exponential decay for $s \to \infty$. The singularity at $s = 0$ is of the form $\lim_{s^+\to 0} s\Lambda_2(s) = 2\pi$.

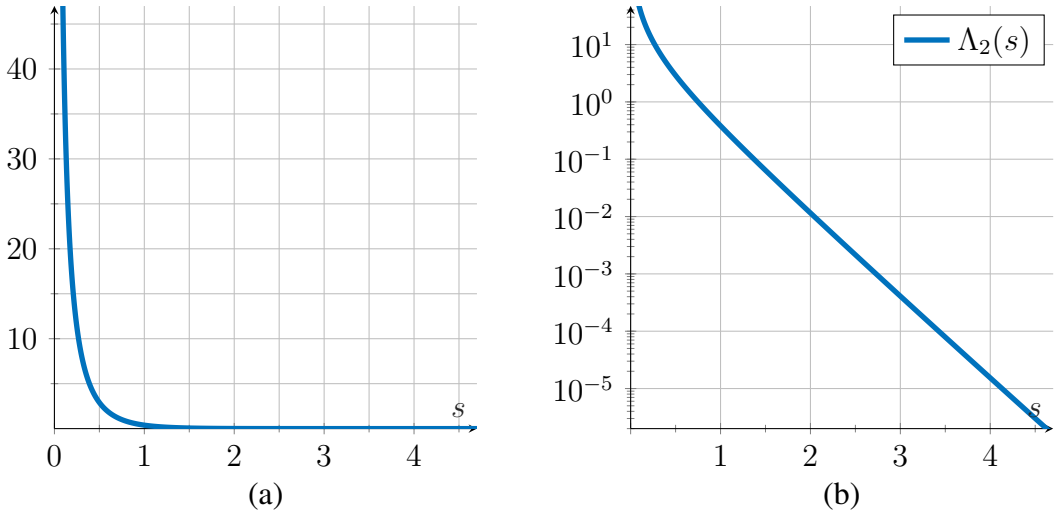

Figure 6.3: The function $\Lambda_2(s)$ in normal scale (a) and log-scale (b). Note, the relationship $\hat{\mathscr{L}}_{\mathrm{n}}(\boldsymbol{\omega}_x) = \Lambda_2(s)$ with $\boldsymbol{\omega}_x \in \mathbb{R}^2$ and $s = \|\boldsymbol{\omega}_x\|$.

Although the function has the singularity at zero, $\hat{\mathscr{L}}_{\mathrm{n}} \in L^1(\mathbb{R}^2)$ is valid as shown in the following lemma.

Lemma 6.2. *The two-dimensional Fourier transform of the normalized Langevin function $\hat{\mathscr{L}}_{\mathrm{n}} : \mathbb{R}^2 \to \mathbb{R}$ is in $L^1(\mathbb{R}^2)$.*

Proof of Lemma 6.2. The function $\hat{\mathscr{L}}_{\mathrm{n}}(\boldsymbol{\omega}_x)$ is positive for all $\boldsymbol{\omega}_x \in \mathbb{R}^2$ and $s = \|\boldsymbol{\omega}_x\|$, i.e.,

$$\hat{\mathscr{L}}_{\mathrm{n}}(\boldsymbol{\omega}_x) = \Lambda_2(s) = 4\pi \int_0^\infty \frac{1}{\mathrm{e}^{\pi s \cosh(t)} - 1} > 0.$$

Equivalent to the proof of Theorem 6.3, a monotonically increasing sequence $(S_K(s))_{K\in\mathbb{N}}$ with $\lim_{K\to\infty} S_K(s) = \Lambda_2(s)$ and $0 < S_K(s) < S_{K+1}(s)$ is defined by

$$S_K(s) = 4\pi \sum_{k=1}^{K} K_0(k\pi s). \tag{6.27}$$

With the help of Lemma 4.2 and Corollary 4.3 it can be shown that $S_K(\|\boldsymbol{\omega}_x\|)$ is in $L^1(\mathbb{R}^2)$. Therefore, the integral of the partial sum in (6.27) is given by

$$\int_{\mathbb{R}^2} S_K(\|\boldsymbol{\omega}_x\|)\,\mathrm{d}\boldsymbol{\omega}_x = 2\pi \int_0^\infty s S_K(s)\,\mathrm{d}s = 8\pi^2 \sum_{k=1}^{K} \int_0^\infty s K_0(k\pi s)\,\mathrm{d}s. \tag{6.28}$$

Using the identity

$$\int_0^z tK_0(t)\,\mathrm{d}t = -zK_1(z) + 1,$$

which can be found in [1, §11.3.27] and performing the substitutions $z = k\pi s$ and $t = k\pi u$, it is obtained that

$$k^2\pi^2 \int_0^s uK_0(k\pi u)\,\mathrm{d}u = -k\pi sK_1(k\pi s) + 1.$$

Using

$$\lim_{s\to\infty} sK_1(k\pi s) = 0$$

the result for (6.28) is

$$\int_{\mathbb{R}^2} S_K(\|\boldsymbol{\omega_x}\|)\,\mathrm{d}\boldsymbol{\omega_x} = 2\pi \int_0^\infty sS_K(s)\,\mathrm{d}s = 8\pi^2 \sum_{k=1}^{K} \frac{1}{\pi^2 k^2}$$

and finally, the limit of (6.28) as K approaches infinity is

$$\begin{aligned}\int_{\mathbb{R}^2} \left|\hat{\mathscr{L}}_{\mathrm{n}}(\boldsymbol{\omega_x})\right|\,\mathrm{d}\boldsymbol{\omega_x} &= 2\pi \int_0^\infty s\Lambda_2(s)\,\mathrm{d}s \\ &= \lim_{K\to+\infty} 2\pi \int_0^\infty sS_K(s)\,\mathrm{d}s \\ &= 8\pi^2 \frac{1}{6} = \frac{4}{3}\pi^2 < +\infty.\end{aligned}$$

and therefore $\hat{\mathscr{L}}_{\mathrm{n}} \in L^1(\mathbb{R}^2)$. □

It should be mentioned that the result about the two-dimensional Fourier transform in the Theorem 6.3 is not necessary for the structure of the proofs of the next theorems, which mostly use the physically motivated three spatial dimensions, i.e., $N = 3$. The two-dimensional result was only given for the sake of completeness.

In contrast to the two-dimensional Fourier transform of the normalized Langevin function, there is a closed-form solution for the three-dimensional version.

Theorem 6.4

The three-dimensional Fourier transform of $\ell_{\mathrm{n}} : \mathbb{R}^3 \to \mathbb{R}$ with $\ell_{\mathrm{n}}(\boldsymbol{x}) = \mathscr{L}_{\mathrm{n}}(\|\boldsymbol{x}\|)$ results in

$$\hat{\mathscr{L}}_{\mathrm{n}}(\boldsymbol{\omega}_{\boldsymbol{x}}) = \Lambda_3(s) \qquad \text{with} \qquad s = \|\boldsymbol{\omega}_{\boldsymbol{x}}\|, \qquad \boldsymbol{\omega}_{\boldsymbol{x}} \neq \mathbf{0}, \tag{6.29}$$

and

$$\Lambda_3(s) = \frac{4\pi^2}{s} \frac{1}{\mathrm{e}^{\pi s} - 1}. \tag{6.30}$$

Proof of Theorem 6.4. The results of [38] are used in this proof, where it was shown that there is a connection between different dimensionalities of the Fourier transforms of radial functions. There it was shown that for $\hat{f}_N(s)$ with $s : \mathbb{R}^N \to \mathbb{R}_+$, $s(\boldsymbol{\omega}_{\boldsymbol{x}}) = \|\boldsymbol{\omega}_{\boldsymbol{x}}\|$, and $\hat{f}_N(s)$ being the N-dimensional Fourier transform of a radial function $f(r)$, the $(N+2)$-dimensional Fourier transform is given by

$$\hat{f}_{N+2}(s) = -\frac{2\pi \hat{f}'_N(s)}{s}. \tag{6.31}$$

If the result from Theorem 6.2 is now used and $\Lambda_1(s) = -2\ln\left(1 - \mathrm{e}^{-\pi s}\right)$ is set for the three-dimensional case, it can be derived that

$$\Lambda_3(s) = -\frac{2\pi}{s}\Lambda'_1(s) = 2\frac{2\pi}{s}\frac{\pi \mathrm{e}^{-\pi s}}{1 - \mathrm{e}^{-\pi s}} = \frac{4\pi^2}{s}\frac{1}{\mathrm{e}^{\pi s} - 1}.$$

This thus confirms (6.29) and (6.30). □

The Figure 6.4 shows the function $\Lambda_3(s)$. This function is the radial representation of the three-dimensional Fourier transform of $\hat{\mathscr{L}}_{\mathrm{n}} : \mathbb{R}^3 \to \mathbb{R}$ with $s = \|\boldsymbol{\omega}_{\boldsymbol{x}}\|$. As for $\Lambda_1(s)$ and $\Lambda_2(s)$, the function shows an exponential decay for $s \to \infty$ (see Figure 6.4 (b)). The singularity at $s = 0$ is of the form $\lim_{s^+ \to 0} s^2 \Lambda_3(s) = 4\pi$.

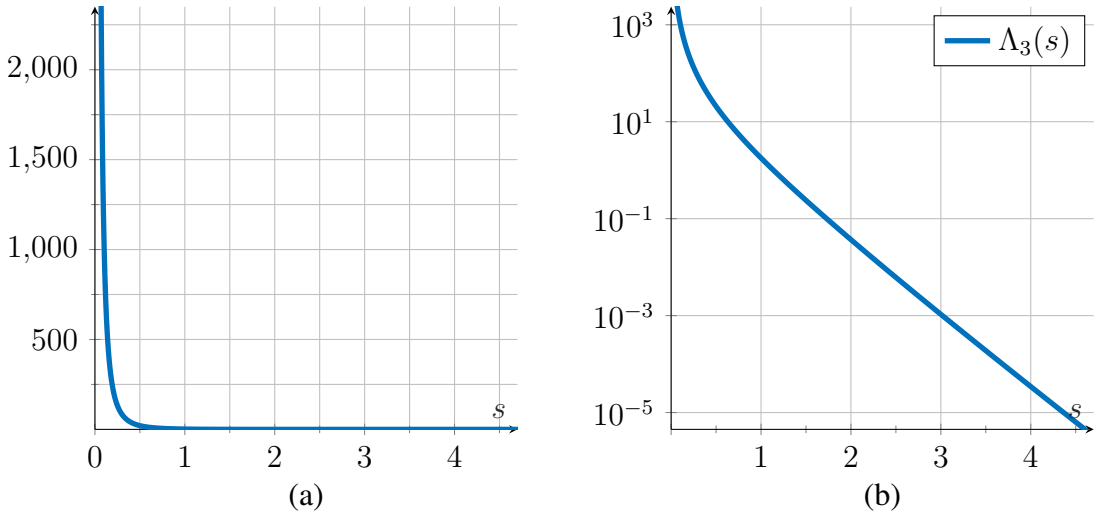

Figure 6.4: The function $\Lambda_3(s)$ in normal scale (a) and log-scale (b). Note, the relationship $\hat{\mathscr{L}}_{\mathrm{n}}(\boldsymbol{\omega}_{\boldsymbol{x}}) = \Lambda_3(s)$ with $\boldsymbol{\omega}_{\boldsymbol{x}} \in \mathbb{R}^3$ and $s = \|\boldsymbol{\omega}_{\boldsymbol{x}}\|$.

Lemma 6.3. *The three-dimensional Fourier transform of the normalized Langevin function* $\hat{\mathscr{L}}_{\mathrm{n}} : \mathbb{R}^3 \to \mathbb{R}$ *is in* $L^1(\mathbb{R}^3)$.

Proof 1 of Lemma 6.3. According to Lemma 4.2 for radial functions and $\Lambda_3(s) > 0$ for all $s \in \mathbb{R}$ follows

$$\int_{\mathbb{R}^3} \left| \hat{\mathscr{L}}_{\mathrm{n}}(\boldsymbol{\omega}_{\boldsymbol{x}}) \right| \, \mathrm{d}\boldsymbol{\omega}_{\boldsymbol{x}} = 4\pi \int_0^\infty \Lambda_3(r) r^2 \, \mathrm{d}r = 16\pi^3 \int_0^\infty \frac{r}{\mathrm{e}^{\pi r} - 1} \, \mathrm{d}r.$$

By using the substitution $s = \pi r$ as well as the definition of the product of the gamma function $\Gamma : \mathbb{R} \to \mathbb{R}$ and the zeta function $\zeta : \mathbb{R} \to \mathbb{R}$ [1, §23.2.7]

$$\Gamma(x)\zeta(x) = \int_0^\infty \frac{t^{x-1}}{\mathrm{e}^t - 1} \, \mathrm{d}t,$$

the following can be obtained

$$\begin{aligned} \int_{\mathbb{R}^3} \left| \hat{\mathscr{L}}_{\mathrm{n}}(\boldsymbol{\omega}_{\boldsymbol{x}}) \right| \, \mathrm{d}\boldsymbol{\omega}_{\boldsymbol{x}} &= 16\pi \int_0^\infty \frac{s}{\mathrm{e}^s - 1} \, \mathrm{d}s \\ &= 16\pi\Gamma(2)\zeta(2) \\ &= \frac{8\pi^3}{3} < \infty. \end{aligned}$$

□

A second proof, which was not included in [F1], should also be given here, as it reveals a lot about the rule for radial functions in (6.31) in connection with the integration of radial functions in Lemma 4.2 and could potentially pave the way for a future proof of $\hat{\mathscr{L}}_{\mathrm{n}} \in L^1(\mathbb{R}^N)$ for all $N \in \mathbb{N}$ by induction.

Proof 2 of Lemma 6.3. Using (6.31) and Lemma 4.2 the following is obtained

$$\begin{aligned}\int_{\mathbb{R}^3} \left|\hat{\mathscr{L}}_{\mathrm{n}}(\boldsymbol{\omega}_{\boldsymbol{x}})\right| \,\mathrm{d}\boldsymbol{\omega}_{\boldsymbol{x}} = 4\pi \int_0^\infty \Lambda_3(r) r^2 \,\mathrm{d}r &\overset{(6.31)}{=} -4\pi \int_0^\infty \frac{2\pi\,\Lambda_1'(r)}{r} r^2 \,\mathrm{d}r \\ &= -8\pi^2 \int_0^\infty \Lambda_1'(r) r \,\mathrm{d}r.\end{aligned}$$

Utilizing the integration by parts holds

$$\begin{aligned}\int_{\mathbb{R}^3} \left|\hat{\mathscr{L}}_{\mathrm{n}}(\boldsymbol{\omega}_{\boldsymbol{x}})\right| \,\mathrm{d}\boldsymbol{\omega}_{\boldsymbol{x}} &= -8\pi^2 \int_0^\infty \Lambda_1'(r) r \,\mathrm{d}r \\ &= -8\pi^2 \Bigg[\underbrace{\Lambda_1(r) r\Big|_{r=0}^{\infty}}_{\dagger} - \underbrace{\int_0^\infty \Lambda_1(r)\,\mathrm{d}r}_{=\frac{\pi}{3}}\Bigg].\end{aligned}$$

The part marked with † is equal to zero, which remains to be shown. Therefore,

$$\begin{aligned}\lim_{r^+\to 0} r\Lambda_1(r) &= \lim_{r^+\to 0} -2r\ln(1-\mathrm{e}^{-\pi r}) \\ &= \lim_{r^+\to 0} -2\frac{\ln(1-\mathrm{e}^{-\pi r})}{\frac{1}{r}}\end{aligned}$$

should be examined. The L'Hôpital's rule is used twice for $r^+ \to 0$, resulting in

$$\begin{aligned}\lim_{r^+\to 0} r\Lambda_1(r) &= \lim_{r^+\to 0} -2\frac{\left(\ln(1-\mathrm{e}^{-\pi r})\right)'}{\left(\frac{1}{r}\right)'} = \lim_{r^+\to 0} -2\frac{\frac{\pi}{\mathrm{e}^{\pi r}-1}}{-\frac{1}{r^2}} = \lim_{r^+\to 0} \frac{\pi r^2}{\mathrm{e}^{\pi r}-1} \\ &= \lim_{r^+\to 0} \frac{(\pi r^2)'}{(\mathrm{e}^{\pi r}-1)'} = \lim_{r^+\to 0} \frac{2\pi r}{\pi \mathrm{e}^{\pi r}} = 0,\end{aligned}$$

and for $r \to \infty$

$$\lim_{r\to+\infty} r\Lambda_1(r) = \lim_{r\to+\infty} -2\ln(1-\mathrm{e}^{-\pi r}) = \lim_{r\to+\infty} -2r\ln\left(\underbrace{\left(1-\mathrm{e}^{-\pi r}\right)^r}_{\to 1}\right) = 0$$

can be obtained. When all sub-results are combined, the final result is

$$\int_{\mathbb{R}^3} \left|\hat{\mathscr{L}}_{\mathrm{n}}(\boldsymbol{\omega}_{\boldsymbol{x}})\right| \,\mathrm{d}\boldsymbol{\omega}_{\boldsymbol{x}} = \frac{8\pi^3}{3}. \qquad \square$$

The fact $\hat{\mathscr{L}}_{\mathrm{n}} \in L^1(\mathbb{R}^3)$ implies the existence of the inverse Fourier transform according to the Definition 4.1 and is given by

$$\mathscr{L}_{\mathrm{n}}(\|\boldsymbol{x}\|) = \frac{1}{(2\pi)^3} \int_{\mathbb{R}^3} \hat{\mathscr{L}}_{\mathrm{n}}(\boldsymbol{\omega}_{\boldsymbol{x}}) \mathrm{e}^{\mathrm{i}\boldsymbol{x}^{\mathsf{T}}\boldsymbol{\omega}_{\boldsymbol{x}}} \, \mathrm{d}\boldsymbol{\omega}_{\boldsymbol{x}},$$

where $\hat{\mathscr{L}}_{\mathrm{n}}(\boldsymbol{\omega}_{\boldsymbol{x}}) = \Lambda_3(\|\boldsymbol{\omega}_{\boldsymbol{x}}\|)$.

This allows one to define a forward and an inverse Fourier transform $\hat{\boldsymbol{\mathscr{L}}}(\boldsymbol{\omega}_{\boldsymbol{x}})$ for the N-dimensional Langevin function. The forward transform is formulated in the next theorem.

Theorem 6.5

The Fourier transform of $\boldsymbol{\mathscr{L}} : \mathbb{R}^N \to \mathbb{R}^N$ is

$$\hat{\boldsymbol{\mathscr{L}}}(\boldsymbol{\omega}_{\boldsymbol{x}}) = \mathrm{i}\, \Lambda_N'(\|\boldsymbol{\omega}_{\boldsymbol{x}}\|) \frac{\boldsymbol{\omega}_{\boldsymbol{x}}}{\|\boldsymbol{\omega}_{\boldsymbol{x}}\|}, \tag{6.32}$$

with $\hat{\boldsymbol{\mathscr{L}}} : \mathbb{R}^N \to \mathbb{C}^N$, $\Lambda_N'(s) = \frac{\mathrm{d}}{\mathrm{d}s}\Lambda_N(s)$, and $\Lambda_N : \mathbb{R}_+ \to \mathbb{R}$ denoting the N-dimensional Fourier transform of $\mathscr{L}_{\mathrm{n}}(\|\boldsymbol{x}\|)$:

$$\Lambda_N\left(\|\boldsymbol{\omega}_{\boldsymbol{x}}\|\right) = \hat{\mathscr{L}}_{\mathrm{n}}(\boldsymbol{\omega}_{\boldsymbol{x}}) = \mathcal{F}\{\mathscr{L}_{\mathrm{n}}\left(\|\boldsymbol{x}\|\right)\}.$$

Proof of Theorem 6.5. The N-dimensional formulation of the Langevin function in (2.28) has the form $\boldsymbol{\mathscr{L}}(\boldsymbol{x}) = \mathscr{L}_{\mathrm{n}}(\|\boldsymbol{x}\|)\boldsymbol{x}$. The Fourier-transform correspondence $(-\mathrm{i}x)f(x) \overset{\mathcal{F}}{\longleftrightarrow} \frac{\mathrm{d}}{\mathrm{d}\omega_x}\hat{f}(\omega_x)$ for a derivative in frequency domain leads to the correspondence

$$\boldsymbol{\mathscr{L}}(\boldsymbol{x}) = \mathscr{L}_{\mathrm{n}}(\|\boldsymbol{x}\|)\boldsymbol{x} \overset{\mathcal{F}}{\longleftrightarrow} \mathrm{i}\, \nabla_{\boldsymbol{\omega}_{\boldsymbol{x}}} \hat{\mathscr{L}}_{\mathrm{n}}(\boldsymbol{\omega}_{\boldsymbol{x}}),$$

where $\nabla_{\boldsymbol{\omega}_{\boldsymbol{x}}} = \left[\frac{\partial}{\partial\omega_{x_1}}, \frac{\partial}{\partial\omega_{x_2}}, \ldots, \frac{\partial}{\partial\omega_{x_N}}\right]^{\mathsf{T}}$ is the gradient operator with respect to $\boldsymbol{\omega}_{\boldsymbol{x}}$. Considering that $\hat{\mathscr{L}}_{\mathrm{n}}(\boldsymbol{\omega}_{\boldsymbol{x}}) = \Lambda_N(\|\boldsymbol{\omega}_{\boldsymbol{x}}\|)$ and applying the chain-rule, the Fourier transform of $\boldsymbol{\mathscr{L}}(\boldsymbol{x})$ finally becomes

$$\hat{\boldsymbol{\mathscr{L}}}(\boldsymbol{\omega}_{\boldsymbol{x}}) = \mathcal{F}\{\boldsymbol{\mathscr{L}}(\boldsymbol{x})\} = \mathrm{i}\, \nabla_{\boldsymbol{\omega}_{\boldsymbol{x}}} \left[\Lambda_N(\|\boldsymbol{\omega}_{\boldsymbol{x}}\|)\right] = \mathrm{i}\, \Lambda_N'(\|\boldsymbol{\omega}_{\boldsymbol{x}}\|) \frac{\boldsymbol{\omega}_{\boldsymbol{x}}}{\|\boldsymbol{\omega}_{\boldsymbol{x}}\|},$$

which proves (6.32). □

The Euclidean norm for the vector-valued Fourier transform of the multidimensional Langevin function from Theorem 6.5 will be given first, as it is helpful in the following proofs, since it in turn forms a radial function. The following corollary is formulated for the first time in this thesis and was not part of [F1].

Corollary 6.4. *The Euclidean norm of* $\hat{\boldsymbol{\mathscr{L}}} : \mathbb{R}^N \to \mathbb{C}^N$ *in* (6.32) *is given by*

$$\left\| \hat{\boldsymbol{\mathscr{L}}}(\boldsymbol{\omega_x}) \right\| = \left| \Lambda_N'(\|\boldsymbol{\omega_x}\|) \right|, \tag{6.33}$$

hence it holds that

$$\left| \hat{\mathscr{L}}_\nu(\boldsymbol{\omega_x}) \right| \leq \left\| \hat{\boldsymbol{\mathscr{L}}}(\boldsymbol{\omega_x}) \right\| = \left| \Lambda_N'(\|\boldsymbol{\omega_x}\|) \right|,$$

where $\hat{\mathscr{L}}_\nu : \mathbb{R}^N \to \mathbb{C}^N$ *are the components of* $\hat{\boldsymbol{\mathscr{L}}}(\boldsymbol{\omega_x})$ *with* $\nu \in \{1, 2, \ldots, N\}$ *and*

$$\left\| \hat{\boldsymbol{\mathscr{L}}}(\boldsymbol{\omega_x}) \right\| = \left| \Lambda_N'(s) \right|$$

is a radial function with $s = \|\boldsymbol{\omega_x}\|$.

The function $\Lambda_N(s)$ was derived for different $N \in \mathbb{N}$. Especially, for $N = 1$ it is given by $\Lambda_1(s) = \hat{\mathscr{L}}_{\mathrm{n}}(s)$ in (6.23), for $N = 2$ the result is shown in (6.26), and for $N = 3$ it is given by (6.30). Note, the function $\Lambda_N(s)$ can also be determined for any dimension $N \in \mathbb{N}$ by using the recursive relation in (6.31), which comes from [38], i.e., with the framework in this work, the multidimensional Fourier transform of the Langevin function $\hat{\mathscr{L}}_{\mathrm{n}}(\boldsymbol{\omega_x})$ (cf. Theorem 6.5) can be determined for any dimension.

Consequently, the expression for the Fourier transform of the multidimensional Langevin function can be explicitly specified for $N \in \{1, 2, 3\}$, which is formulated in the next three corollaries.

Corollary 6.5. *The one-dimensional Fourier transform (*$N = 1$*) of* $\mathscr{L} : \mathbb{R} \to \mathbb{R}$ *is*

$$\hat{\mathscr{L}}(\omega_x) = -2\pi \mathrm{i} \operatorname{sgn}(\omega_x) \frac{1}{\mathrm{e}^{\pi|\omega_x|} - 1}, \qquad \omega_x \neq 0. \tag{6.34}$$

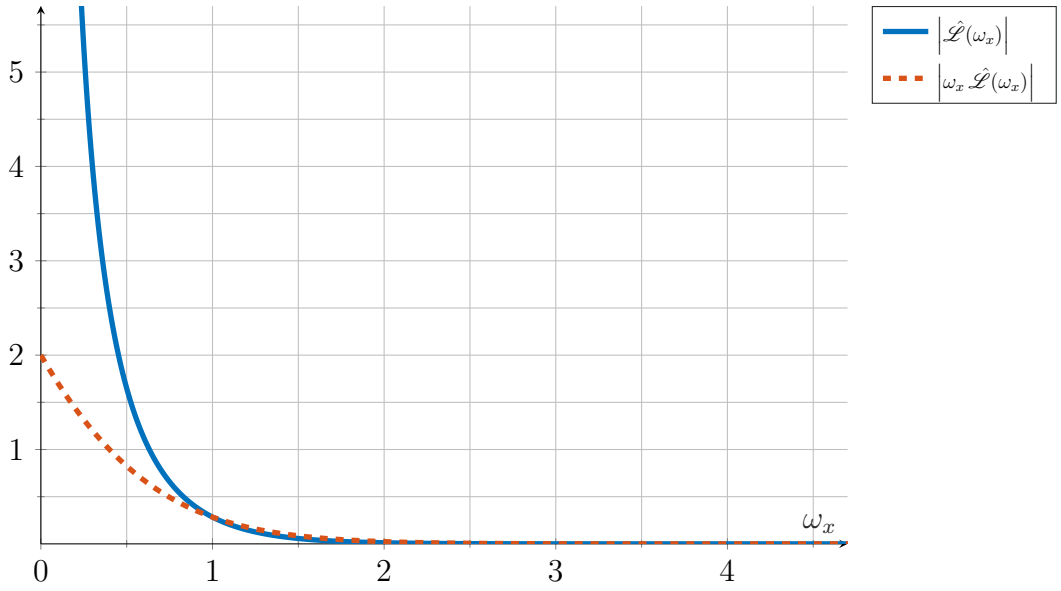

Figure 6.5: The magnitude $\left|\hat{\mathscr{L}}(\omega_x)\right|$ is shown as a solid blue line and the magnitude $\left|\omega_x\,\hat{\mathscr{L}}(\omega_x)\right|$ is shown as a dashed red line.

In Figure 6.5, the magnitude of the one-dimensional Fourier transform $\hat{\mathscr{L}}(\omega_x)$ for $\omega_x > 0$ is illustrated. It can be observed that there is a singularity at $\omega_x = 0$ and $|\omega_x\,\hat{\mathscr{L}}(\omega_x)|$ is continuous in $\omega_x = 0$ with $\lim_{\omega_x^+ \to 0} |\omega_x\,\hat{\mathscr{L}}(\omega_x)| = 2$. Consequently, $\hat{\mathscr{L}}(\omega_x)$ has a pole of order one at $\omega_x = 0$.

Corollary 6.6. *The two-dimensional Fourier transform ($N = 2$) of $\mathscr{L} : \mathbb{R}^2 \to \mathbb{R}^2$ is*

$$\begin{aligned}\hat{\mathscr{L}}(\boldsymbol{\omega_x}) &= -4\pi^2\mathrm{i}\left(\int_0^\infty \frac{\cosh(t)\mathrm{e}^{\pi\|\boldsymbol{\omega_x}\|\cosh(t)}}{\left(\mathrm{e}^{\pi\|\boldsymbol{\omega_x}\|\cosh(t)}-1\right)^2}\,\mathrm{d}t\right)\frac{\boldsymbol{\omega_x}}{\|\boldsymbol{\omega_x}\|} \\ &= \frac{-\pi^2\mathrm{i}\boldsymbol{\omega_x}}{\|\boldsymbol{\omega_x}\|}\left(\int_0^\infty \cosh(t)\,\mathrm{csch}^2\left(\frac{\pi}{2}\|\boldsymbol{\omega_x}\|\cosh(t)\right)\,\mathrm{d}t\right),\end{aligned} \tag{6.35}$$

where $\mathrm{csch}(x) = \frac{1}{\sinh(x)}$ *denotes the hyperbolic cosecant with* $\boldsymbol{\omega_x} \neq \mathbf{0}$.

Different substitutions lead to different integral expressions:

1. *The substitution* $y = \cosh(t)$ *results in*

$$\hat{\mathscr{L}}(\boldsymbol{\omega_x}) = \frac{-\pi^2\mathrm{i}\boldsymbol{\omega_x}}{\|\boldsymbol{\omega_x}\|}\int_1^\infty \frac{y}{\sqrt{y^2-1}}\,\mathrm{csch}^2\left(\frac{\pi}{2}\|\boldsymbol{\omega_x}\|y\right)\,\mathrm{d}y. \tag{6.36}$$

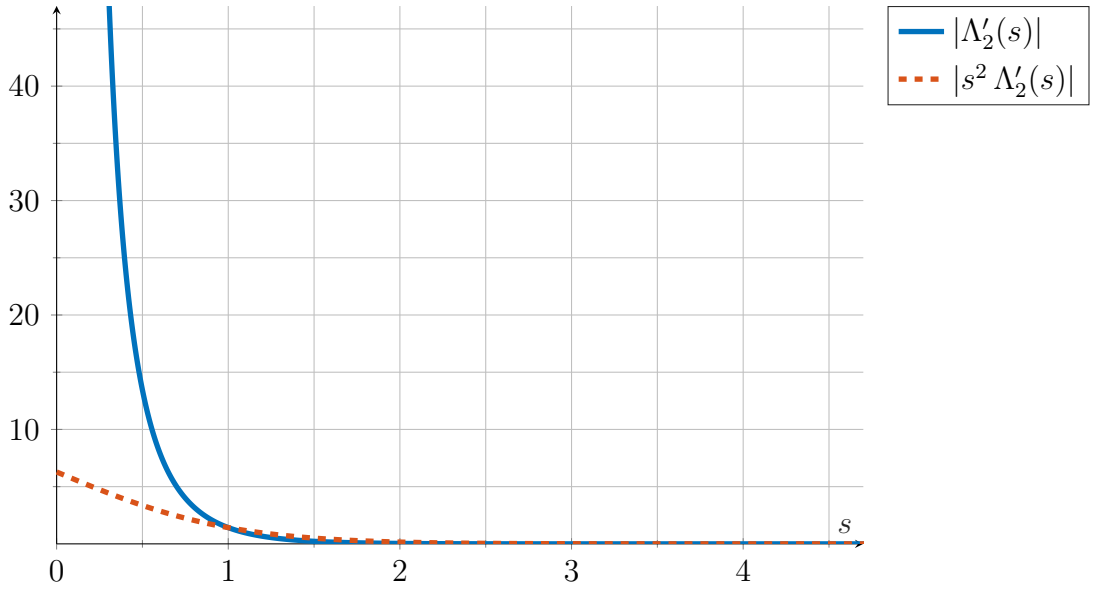

Figure 6.6: The magnitude $|\Lambda_2'(s)|$ is shown as a solid blue line and the magnitude of $|s^2\,\Lambda_2'(s)|$ is shown as a dashed red line. Note, $|\Lambda_2'(s)|$ is directly related to the Euclidean norm of the two-dimensional Fourier transform of the two-dimensional Langevin function by $\|\hat{\mathscr{L}}(\boldsymbol{\omega}_x)\| = |\Lambda_2'(s)|$ with $s = \|\boldsymbol{\omega}_x\|$.

2. *The substitution* $t = \tanh^{-1}(z)$ *yields*

$$\hat{\mathscr{L}}(\boldsymbol{\omega}_x) = \frac{-\pi^2 \mathrm{i}\boldsymbol{\omega}_x}{\|\boldsymbol{\omega}_x\|} \int_0^1 \frac{\operatorname{csch}^2\left(\frac{\frac{1}{2}\pi\|\boldsymbol{\omega}_x\|}{\sqrt{1-z^2}}\right)}{(1-z^2)^{\frac{3}{2}}}\,\mathrm{d}z. \tag{6.37}$$

3. *Using the substitution* $z = \sin(u)$ *gives*

$$\begin{aligned}\hat{\mathscr{L}}(\boldsymbol{\omega}_x) &= \frac{-\pi^2 \mathrm{i}\boldsymbol{\omega}_x}{\|\boldsymbol{\omega}_x\|} \int_0^{\frac{\pi}{2}} \frac{\operatorname{csch}^2\left(\frac{\pi\|\boldsymbol{\omega}_x\|}{2\cos(u)}\right)}{\cos^2(u)}\,\mathrm{d}u \\ &= \frac{-\pi^2 \mathrm{i}\boldsymbol{\omega}_x}{\|\boldsymbol{\omega}_x\|^3} \int_0^{\frac{\pi}{2}} \left(\|\boldsymbol{\omega}_x\| \operatorname{csch}\left(\frac{\pi}{2}\|\boldsymbol{\omega}_x\| \sec(u)\right) \sec(u)\right)^2 \mathrm{d}u,\end{aligned} \tag{6.38}$$

where $\sec(u) = \frac{1}{\cos(u)}$.

Equation (6.38) is well suited for numerical integration, as the integrand

$$i(\|\boldsymbol{\omega}_x\|, u) = \left(\|\boldsymbol{\omega}_x\| \operatorname{csch}\left(\frac{\pi}{2}\|\boldsymbol{\omega}_x\| \sec(u)\right) \sec(u)\right)^2$$

is fully defined for all $\boldsymbol{\omega_x} \in \mathbb{R}^2$. It can be shown that

$$\lim_{u^- \to \frac{\pi}{2}} i(\|\boldsymbol{\omega_x}\|, u) = 0$$

is the only point singularity on the finite interval $\left[0, \frac{\pi}{2}\right]$, which can be continuously removed. The other formulations have either a non-closed infinite interval, a singularity at the boundary of the interval, or even both. Moreover, the integrand fulfills

$$\lim_{\|\boldsymbol{\omega_x}\| \to 0} i(\|\boldsymbol{\omega_x}\|, u) = \frac{4}{\pi^2}, \qquad u \in [0, \tfrac{\pi}{2}).$$

Thus, with (6.38) follows $\| \hat{\boldsymbol{\mathscr{L}}}(\boldsymbol{\omega_x})\| = |\Lambda_2'(\|\boldsymbol{\omega_x}\|)|$, which has a second-order pole at $\|\boldsymbol{\omega_x}\| = 0$. The behavior of $\| \hat{\boldsymbol{\mathscr{L}}}(\boldsymbol{\omega_x})\| = |\Lambda_2'(s)|$ and $\|\boldsymbol{\omega_x}\|^2 \| \hat{\boldsymbol{\mathscr{L}}}(\boldsymbol{\omega_x})\| = s^2 \, |\Lambda_2'(s)|$ is shown for $s \geq 0$ in Figure 6.6.

Corollary 6.7. *The three-dimensional Fourier transform ($N = 3$) of $\boldsymbol{\mathscr{L}} : \mathbb{R}^3 \to \mathbb{R}^3$ is*

$$\hat{\boldsymbol{\mathscr{L}}}(\boldsymbol{\omega_x}) = -4\pi^2 \mathrm{i} \frac{(\pi\|\boldsymbol{\omega_x}\| + 1)\, \mathrm{e}^{\pi\|\boldsymbol{\omega_x}\|} - 1}{\|\boldsymbol{\omega_x}\|^2 \left(\mathrm{e}^{\pi\|\boldsymbol{\omega_x}\|} - 1\right)^2} \frac{\boldsymbol{\omega_x}}{\|\boldsymbol{\omega_x}\|}, \qquad \boldsymbol{\omega_x} \neq \mathbf{0}. \tag{6.39}$$

The behavior of the Euclidean norm $\| \hat{\boldsymbol{\mathscr{L}}}(\boldsymbol{\omega_x})\| = |\Lambda_3'(s)|$ and $\|\boldsymbol{\omega_x}\|^3 \| \hat{\boldsymbol{\mathscr{L}}}(\boldsymbol{\omega_x})\| = s^3 \, |\Lambda_3'(s)|$ for the three-dimensional function $\hat{\boldsymbol{\mathscr{L}}} : \mathbb{R}^3 \to \mathbb{C}^3$ is shown in Figure 6.7. It can be observed that $\lim_{s^+ \to 0} s^3 \| \Lambda_3'(s)\| = 8\pi \approx 25.1327$ applies.

In physical context, the Langevin function $\boldsymbol{\mathscr{L}}(\boldsymbol{x})$ has to be treated in a three-dimensional way due to the three-dimensional structure of SPIO distributions.

In the following, conditions for the existence of an inverse Fourier transform in the classical $L^1(\mathbb{R}^3)$ sense are to be established with the function $\hat{\boldsymbol{\mathscr{L}}}(\boldsymbol{\omega_x})$ serving as a subargument of the Fourier transform. The following lemma is helpful for this. Note that the next lemma is a generalized version of [F1, Lem. 4.8].

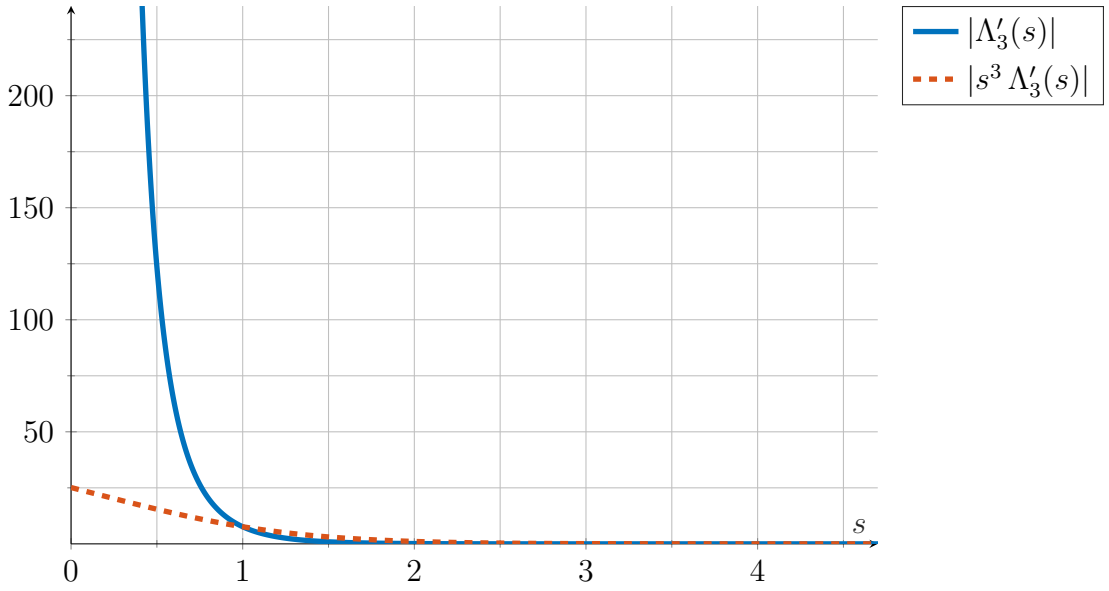

Figure 6.7: The magnitude $|\Lambda_3'(s)|$ is shown as a solid blue line and the magnitude $|s^3\,\Lambda_3'(s)|$ is shown as a dashed red line. Note, $|\Lambda_3'(s)|$ is directly related to the Euclidean norm of the three-dimensional Fourier transform of the three-dimensional Langevin function by $\|\hat{\mathscr{L}}(\boldsymbol{\omega}_{\boldsymbol{x}})\| = |\Lambda_3'(s)|$ with $s = \|\boldsymbol{\omega}_{\boldsymbol{x}}\|$.

Lemma 6.8. *Products of the form*

$$\omega_{x_1}^{\ell}\omega_{x_2}^{m}\omega_{x_3}^{n}\,\hat{\mathscr{L}}_{\nu}(\boldsymbol{\omega}_{\boldsymbol{x}}), \qquad \ell, m, n \in \mathbb{N}_0, \tag{6.40}$$

where $\hat{\mathscr{L}}_{\nu} : \mathbb{R}^3 \to \mathbb{C}$, $\nu \in \{1,2,3\}$ *are the components of* $\hat{\mathscr{L}}(\boldsymbol{\omega}_{\boldsymbol{x}})$,

- *are in* $L^p(\mathbb{R}^3)$, *if* $\ell + m + n = 1$ *with* $p \in [1, \frac{3}{2})$.
- *are in* $L^p(\mathbb{R}^3)$, *if* $\ell + m + n = 2$ *with* $p \in [1, 3)$.
- *are in* $L^1(\mathbb{R}^3) \cap L^{\infty}(\mathbb{R}^3)$, *if* $\ell + m + n \geq 3$.

Proof of Lemma 6.8. Let $\hat{\mathscr{L}}_{\nu}(\boldsymbol{\omega}_{\boldsymbol{x}})$ with $\nu \in \{1,2,3\}$ denote a vector entry in $\hat{\mathscr{L}}(\boldsymbol{\omega}_{\boldsymbol{x}})$. The function $\omega_{x_1}^{\ell}\omega_{x_2}^{m}\omega_{x_3}^{n}\,\hat{\mathscr{L}}_{\nu}(\boldsymbol{\omega}_{\boldsymbol{x}})$ is in $L^p(\mathbb{R}^3)$ with $p \in [1, +\infty)$ when there is a $C \in \mathbb{R}_+$ such that

$$\int_{\mathbb{R}^3} \left|\omega_{x_1}^{\ell}\omega_{x_2}^{m}\omega_{x_3}^{n}\,\hat{\mathscr{L}}_{\nu}(\boldsymbol{\omega}_{\boldsymbol{x}})\right|^p \,\mathrm{d}\boldsymbol{\omega}_{\boldsymbol{x}} = C < \infty$$

is true. Using the integration in spherical coordinates

$$\boldsymbol{\omega}_{\boldsymbol{x}}(s,\varphi,\theta) = \begin{pmatrix} \omega_{x_1} \\ \omega_{x_2} \\ \omega_{x_3} \end{pmatrix} = \begin{pmatrix} s\sin(\theta)\cos(\varphi) \\ s\sin(\theta)\sin(\varphi) \\ s\cos(\theta) \end{pmatrix}$$

for all $\ell, m, n \in \mathbb{N}_0$ it turns out that

$$\int_{\mathbb{R}^3} \left| \omega_{x_1}^{\ell} \omega_{x_2}^{m} \omega_{x_3}^{n} \, \hat{\mathscr{L}}_{\nu}(\boldsymbol{\omega}_{\boldsymbol{x}}) \right|^p \mathrm{d}\boldsymbol{\omega}_{\boldsymbol{x}} = \int_0^{\infty} \int_0^{\pi} \int_0^{2\pi} \left| s^{\ell+m+n} \sin^{\ell+m}(\theta) \cos^{\ell}(\varphi) \sin^{m}(\varphi) \right. \\ \left. \times \cos^{n}(\theta) \, \hat{\mathscr{L}}_{\nu} \left(\boldsymbol{\omega}_{\boldsymbol{x}}(s, \varphi, \theta) \right) \right|^p s^2 \sin(\theta) \, \mathrm{d}\varphi \, \mathrm{d}\theta \, \mathrm{d}s,$$

where $\| \boldsymbol{\omega}_{\boldsymbol{x}}(s, \varphi, \theta) \| = s$ with $p \geq 1$ is used.

According to Corollary 6.4 with $N = 3$ the inequality

$$\left| \hat{\mathscr{L}}_{\nu} \left(\boldsymbol{\omega}_{\boldsymbol{x}}(s, \varphi, \theta) \right) \right| \leq \left| \Lambda_3'(s) \right|,$$

holds and one obtains

$$\int_{\mathbb{R}^3} \left| \omega_{x_1}^{\ell} \omega_{x_2}^{m} \omega_{x_3}^{n} \, \hat{\mathscr{L}}_{\nu}(\boldsymbol{\omega}_{\boldsymbol{x}}) \right|^p \mathrm{d}\boldsymbol{\omega}_{\boldsymbol{x}} \leq \int_0^{\infty} \int_0^{\pi} \int_0^{2\pi} \left| s^{\ell+m+n} \sin^{\ell+m}(\theta) \cos^{\ell}(\varphi) \sin^{m}(\varphi) \right. \\ \left. \times \cos^{n}(\theta) \left| \Lambda_3'(s) \right| \right|^p s^2 \sin(\theta) \, \mathrm{d}\varphi \, \mathrm{d}\theta \, \mathrm{d}s.$$

Using the inequalities $|\cos(\xi)| \leq 1$ and $|\sin(\xi)| \leq 1$, which hold for all $\xi \in \mathbb{R}$, an upper bound for the integral can be given as follows:

$$\begin{aligned} \int_{\mathbb{R}^3} \left| \omega_{x_1}^{\ell} \omega_{x_2}^{m} \omega_{x_3}^{n} \, \hat{\mathscr{L}}_{\nu}(\boldsymbol{\omega}_{\boldsymbol{x}}) \right|^p \mathrm{d}\boldsymbol{\omega}_{\boldsymbol{x}} &\leq \int_0^{\infty} \int_0^{\pi} \int_0^{2\pi} \left| s^{\ell+m+n} \left| \Lambda_3'(s) \right| \right|^p s^2 \sin(\theta) \, \mathrm{d}\varphi \, \mathrm{d}\theta \, \mathrm{d}s \\ &\leq 4\pi \int_0^{\infty} \left| s^{\ell+m+n} \left| \Lambda_3'(s) \right| \right|^p s^2 \, \mathrm{d}s. \end{aligned}$$

The calculations holds for all $\nu \in \{1, 2, 3\}$. For $\hat{\mathscr{L}}_{\nu} \in L^p(\mathbb{R}^3)$ it remains to be verified that $\left| s^{\ell+m+n+\frac{2}{p}} \left| \Lambda_3'(s) \right| \right|^p = \left| s^{\ell+m+n+\frac{2}{p}} \, \Lambda_3'(s) \right|^p$ is absolutely integrable on the interval $[0, +\infty)$. Consequently, one gets

$$\begin{aligned} &\int_0^{\infty} \left| s^{\ell+m+n+\frac{2}{p}} \, \Lambda_3'(s) \right|^p \mathrm{d}s \\ &\quad = \left(4\pi^2\right)^p \int_0^{\infty} \left| s^{\ell+m+n+\frac{2}{p}-2} \frac{(\pi s + 1) \, \mathrm{e}^{\pi s} - 1}{\left(\mathrm{e}^{\pi s} - 1\right)^2} \right|^p \mathrm{d}s \\ &\quad = \left(4\pi^2\right)^p \int_0^{\infty} \left| s^{\ell+m+n+\frac{2}{p}-2} \frac{\left((\pi s + 1) - \mathrm{e}^{-\pi s}\right) \mathrm{e}^{\pi s}}{\mathrm{e}^{2\pi s} \left(1 - \mathrm{e}^{-\pi s}\right)^2} \right|^p \mathrm{d}s \\ &\quad = \left(4\pi^2\right)^p \int_0^{\infty} \left| s^{\ell+m+n+\frac{2}{p}-2} \frac{\left((\pi s + 1) - \mathrm{e}^{-\pi s}\right) \mathrm{e}^{-\pi s}}{\left(1 - \mathrm{e}^{-\pi s}\right)^2} \right|^p \mathrm{d}s. \end{aligned} \tag{6.41}$$

To simplify the problem, the function

$$F(s) = \begin{cases} \dfrac{s^{\mu}\left(\pi s + 1 - \mathrm{e}^{-\pi s}\right)\mathrm{e}^{-\pi s}}{\left(1-\mathrm{e}^{-\pi s}\right)^2}, & s \geq 0 \\ 0, & s < 0 \end{cases}$$

with $\mu = \ell + m + n + \frac{2}{p} - 2$ is defined and the constraints under which $F(s)$ is in $L^p(\mathbb{R})$ for $\mu > 0$ are investigated.

In a first step, the limit of $F(s)$ as s approaches zero should be derived, given that $\mu \geq 1$ and $s \geq 0$. Thus, $F(s)$ is rewritten:

$$\begin{aligned} \frac{s^{\mu}\left(\pi s + 1 - \mathrm{e}^{-\pi s}\right)\mathrm{e}^{-\pi s}}{\left(1-\mathrm{e}^{-\pi s}\right)^2} &= \frac{s^{\mu}\left(\pi s + 1 - \mathrm{e}^{-\pi s}\right)}{\left(1-\mathrm{e}^{-\pi s}\right)^2 \mathrm{e}^{\pi s}} = \frac{s^{\mu}\left(\pi s + 1 - \mathrm{e}^{-\pi s}\right)}{\left(\mathrm{e}^{\frac{\pi s}{2}} - \mathrm{e}^{-\frac{\pi s}{2}}\right)^2} \\ &= \frac{s^{\mu}\left(\pi s + 1 - \mathrm{e}^{-\pi s}\right)}{4\sinh^2\left(\frac{\pi s}{2}\right)} = \frac{s^{\mu-2}\left(\pi s + 1 - \mathrm{e}^{-\pi s}\right)\frac{1}{\pi^2}}{\left(\frac{\sinh\left(\frac{\pi s}{2}\right)}{\frac{\pi s}{2}}\right)^2} = \frac{s^{\mu-1}\left(\frac{1}{\pi} + \mathrm{e}^{-\frac{\pi s}{2}}\frac{\mathrm{e}^{\frac{\pi s}{2}} - \mathrm{e}^{-\frac{\pi s}{2}}}{\pi^2 s}\right)}{\left(\frac{\sinh\left(\frac{\pi s}{2}\right)}{\frac{\pi s}{2}}\right)^2} \\ &= \frac{s^{\mu-1}\left(\frac{1}{\pi} + \mathrm{e}^{-\frac{\pi s}{2}}\frac{\sinh\left(\frac{\pi s}{2}\right)}{\frac{\pi^2 s}{2}}\right)}{\left(\frac{\sinh\left(\frac{\pi s}{2}\right)}{\frac{\pi s}{2}}\right)^2} = s^{\mu-1}\left(\frac{1}{\pi\left(\frac{\sinh\left(\frac{\pi s}{2}\right)}{\frac{\pi s}{2}}\right)^2} + \mathrm{e}^{-\frac{\pi s}{2}}\frac{1}{\pi\left(\frac{\sinh\left(\frac{\pi s}{2}\right)}{\frac{\pi s}{2}}\right)}\right). \end{aligned}$$

The limit of $F(s)$ as s approaches zero with $\mu \geq 1$ is calculated as follows

$$\lim_{s\to 0^+} s^{\mu-1}\left(\frac{1}{\pi\left(\frac{\sinh\left(\frac{\pi s}{2}\right)}{\frac{\pi s}{2}}\right)^2} + \mathrm{e}^{-\frac{\pi s}{2}}\frac{1}{\pi\left(\frac{\sinh\left(\frac{\pi s}{2}\right)}{\frac{\pi s}{2}}\right)}\right) = 2\frac{\delta_{(\mu,1)}}{\pi},$$

where $\delta_{(\mu,1)}$ denotes the Kronecker delta and the following holds

$$\lim_{s\to 0^+} \frac{\sinh\left(\frac{\pi s}{2}\right)}{\frac{\pi s}{2}} = \lim_{s\to 0^+} \frac{\sin\left(\mathrm{i}\frac{\pi s}{2}\right)}{\mathrm{i}\frac{\pi s}{2}} = \lim_{s\to 0^+} \mathrm{si}\left(\mathrm{i}\frac{\pi s}{2}\right) = \mathrm{si}(0) = 1.$$

This means that the value at zero for $\mu \geq 1$ is well-defined and there is no singularity, which is an important constraint for the infinity-norm. However, for $\mu \in (0, 1)$ it can be observed that there is a singularity at $s = 0$, i.e., $F \notin L^\infty(\mathbb{R})$. By reformulating $F(s)$ as

$$F(s) = \frac{s^\mu}{1 - \mathrm{e}^{-\pi s}} \left(\frac{\pi s}{1 - \mathrm{e}^{-\pi s}} + 1 \right) \mathrm{e}^{-\pi s}, \qquad s \geq 0,$$

it can be seen that $F(s) \geq 0$ holds. An upper bound on $F(s)$ can be found by starting with the inequality

$$\pi s + 1 \leq \mathrm{e}^{\pi s},$$

which can be derived from the linearization of $\mathrm{e}^{\pi s}$ at the point $s = 0$. If this expression is multiplied by $\mathrm{e}^{-\pi s}$ and the order is changed, the result is

$$\begin{aligned} \mathrm{e}^{-\pi s}(\pi s + 1) &\leq 1 \\ 0 &\leq 1 - \pi s \mathrm{e}^{-\pi s} - \mathrm{e}^{-\pi s} \\ \pi s &\leq \pi s + 1 - \pi s \mathrm{e}^{-\pi s} - \mathrm{e}^{-\pi s} = (\pi s + 1)(1 - \mathrm{e}^{-\pi s}) \\ \frac{\pi s}{1 - \mathrm{e}^{-\pi s}} &\leq \pi s + 1, \end{aligned}$$

which is valid for $s \geq 0$, since

$$\lim_{s \to 0} \frac{\pi s}{1 - \mathrm{e}^{-\pi s}} = \lim_{s \to 0} \frac{(\pi s)'}{(1 - \mathrm{e}^{-\pi s})'} = \lim_{s \to 0} \frac{\pi}{\pi \mathrm{e}^{-\pi s}} = 1.$$

The functions $\pi s + 1$ and $\frac{\pi s}{1 - \mathrm{e}^{-\pi s}}$ are visualized in Figure 6.8.

The final upper bound for $s \geq 0$ is given by

$$\begin{aligned} F(s) &= \frac{s^{\mu-1}}{\pi} \frac{\pi s}{1 - \mathrm{e}^{-\pi s}} \left(\frac{\pi s}{1 - \mathrm{e}^{-\pi s}} + 1 \right) \mathrm{e}^{-\pi s} \\ &\leq \frac{1}{\pi} s^{\mu-1} (\pi s + 1) (\pi s + 2) \mathrm{e}^{-\pi s} \\ &= \frac{1}{\pi} s^{\mu-1} (\pi^2 s^2 + 3\pi s + 2) \mathrm{e}^{-\pi s} \\ &= \pi \underbrace{s^{\mu+1} \mathrm{e}^{-\pi s}}_{=f(s)} + 3 \underbrace{s^\mu \mathrm{e}^{-\pi s}}_{=g(s)} + \frac{2}{\pi} \underbrace{s^{\mu-1} \mathrm{e}^{-\pi s}}_{=h(s)}. \end{aligned} \tag{6.42}$$

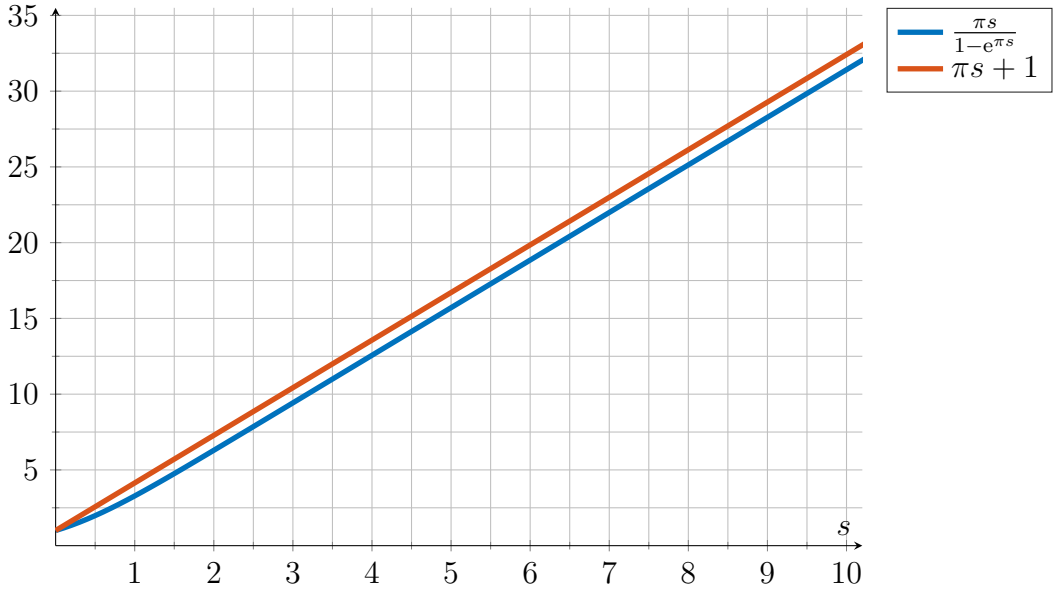

Figure 6.8: The visualization of the two function $\pi s + 1$ and $\frac{\pi s}{1-e^{-\pi s}}$. It is shown that $\frac{\pi s}{1-e^{-\pi s}} \leq \pi s + 1$ for $s \in [0, 10.2]$.

The previous inequality can be used to determine for which $p \in [1, \infty)$ and $\mu > 0$ the function $F(s)$ is in $L^p(\mathbb{R})$. Therefore, it can be observed that the auxiliary functions $f : \mathbb{R}_+ \to \mathbb{R}$, $g : \mathbb{R}_+ \to \mathbb{R}$, and $h : \mathbb{R}_+ \to \mathbb{R}$ are of the form

$$v(\xi, \nu) = \xi^\nu e^{-\pi\xi}$$

and the corresponding $L^p(\mathbb{R}_+)$-norm with respect to ξ is

$$\begin{aligned}
\|v(\cdot, \nu)\|_{L^p} &= \left(\int_0^\infty \xi^{p\nu} e^{-\pi p\xi} \, d\xi \right)^{\frac{1}{p}} \\
&\underbrace{=}_{z=\pi p\xi} \left(\int_0^\infty \left(\frac{z}{\pi p} \right)^{p\nu} e^{-z} \frac{dz}{\pi p} \right)^{\frac{1}{p}} \\
&= \frac{1}{(\pi p)^{\nu+\frac{1}{p}}} \left(\int_0^\infty z^{p\nu} e^{-z} \, dz \right)^{\frac{1}{p}} \\
&= \frac{1}{(\pi p)^\nu} \left(\frac{\Gamma(p\nu + 1)}{\pi p} \right)^{\frac{1}{p}}.
\end{aligned}$$

With the help of the Minkowski inequality it can be determined that

$$\begin{aligned}
\|F\|_{L^p} &\leq \left\|\pi f + 3g + \tfrac{2}{\pi}h\right\|_{L^p} \\
&\leq \pi\|f\|_{L^p} + 3\|g\|_{L^p} + \frac{2}{\pi}\|h\|_{L^p} \\
&= \pi\|v(\cdot,\mu+1)\|_{L^p} + 3\|v(\cdot,\mu)\|_{L^p} + \frac{2}{\pi}\|v(\cdot,\mu-1)\|_{L^p} \\
&= \frac{\pi}{(\pi p)^{\mu+1}}\left(\frac{\Gamma(p(\mu+1)+1)}{\pi p}\right)^{\frac{1}{p}} + \frac{3}{(\pi p)^{\mu}}\left(\frac{\Gamma(p\mu+1)}{\pi p}\right)^{\frac{1}{p}} \\
&\qquad + \frac{2}{\pi(\pi p)^{\mu-1}}\left(\frac{\Gamma(p(\mu-1)+1)}{\pi p}\right)^{\frac{1}{p}}.
\end{aligned}$$

Since $p \geq 1$ and with $\mu > 0$, the important subterm is $\Gamma(p(\mu-1)+1)$, which implies that

$$p(\mu-1)+1 > 0 \tag{6.43}$$

to ensure that $F \in L^p(\mathbb{R})$. By reinserting $\mu = \ell + m + n + \frac{2}{p} - 2$ into (6.43), the constraint

$$p(\ell+m+n-3)+3 > 0 \tag{6.44}$$

is obtained.

For the special case $p \to \infty$, it should first be noted that $\mu \geq 1$ must apply, so that $F(s)$ is bounded as

$$\begin{aligned}
F(s) &= \frac{s^{\mu}}{1-\mathrm{e}^{-\pi s}}\left(\frac{\pi s}{1-\mathrm{e}^{-\pi s}}+1\right)\mathrm{e}^{-\pi s} \\
&\leq \frac{1}{\pi}s^{\mu-1}(\pi s+1)\,(\pi s+2)\,\mathrm{e}^{-\pi s} \\
&< w(s) = \frac{1}{\pi}(\pi s+2)^{\mu+1}\mathrm{e}^{-\pi s}.
\end{aligned}$$

The supremum of $w(s)$ with $s \geq 0$ is reached either at one of boundaries $s \to 0$ and $s \to \infty$ or at $w'(s^*) = 0$. The derivative of $w(s)$ reads

$$w'(s) = (\pi s+2)^{\mu}(\mu-1-\pi s)\mathrm{e}^{-\pi s}.$$

The only zero point s^* within the interval $[0,\infty)$ is $s^* = \frac{\mu-1}{\pi}$. Since $\lim_{s\to 0} w'(s) = 2^{\mu}(\mu-1) > 0$, the function $w(s)$ is locally increasing for $\mu > 1$ in the vicinity of

$s = 0$ and thus $s = 0$ cannot be a maximizer and for $\lim_{s\to\infty} w(s) = 0$ the value is even smaller than $w(0)$, so

$$|F(s)| < w(s^*) = \frac{(\mu+1)^{\mu+1}\mathrm{e}^{-(\mu-1)}}{\pi}$$

is proofed and, therefore, the value for $p \to \infty$ exists. It should be remembered that $\mu = \ell + m + n + \frac{2}{p} - 2 \geq 1$ must be fulfilled, which is only valid for $p \to \infty$ and $\ell + m + n \geq 3$.

To solve the original problem stated in (6.41), (6.44) for $p \in [1, \infty)$ must be satisfied, i.e.,

$$p(\ell + m + n - 3) + 3 > 0.$$

From $m + n + \ell = 1$ one obtains $p(-2) + 3 > 0$, i.e., $F \in L^p(\mathbb{R})$ for all $p \in [1, \frac{3}{2})$. It follows that $\omega_{x_1}^{\ell}\omega_{x_2}^{m}\omega_{x_3}^{n}\,\hat{\mathscr{L}}_\nu(\boldsymbol{\omega_x})$ is in $L^p(\mathbb{R}^3)$ with $p \in [1, \frac{3}{2})$.

If $m + n + \ell = 2$, it can be proven that the value p must lie in $p \in [1, 3)$ and that $\omega_{x_1}^{\ell}\omega_{x_2}^{m}\omega_{x_3}^{n}\,\hat{\mathscr{L}}_\nu(\boldsymbol{\omega_x})$ is in $L^p(\mathbb{R}^3)$ with $p \in [1, 3)$.

If $m + n + \ell \geq 3$, one can choose $p \in [1, \infty]$ arbitrarily and thus $\omega_{x_1}^{\ell}\omega_{x_2}^{m}\omega_{x_3}^{n}\,\hat{\mathscr{L}}_\nu(\boldsymbol{\omega_x})$ is in $L^p(\mathbb{R}^3)$ with $p \in [1, \infty]$. □

Lemma 6.8 shows that an inverse Fourier transform exists whenever $\hat{\mathscr{L}}(\boldsymbol{\omega_x})$ occurs in a product with a second function $f(\boldsymbol{\omega_x})$ for which $g(\boldsymbol{\omega_x}) = \frac{1}{\omega_{x_i}} f(\boldsymbol{\omega_x})$ and $g \in L^\infty(\mathbb{R}^3)$. Interestingly, Bessel functions of the first kind with an order that is higher than zero are of this type. These functions naturally occur in Fourier-domain representations of the MPI measurement process.

6.2.1 Product of Bessel Function and Fourier Transformed Langevin Function

In the following, a central result of this thesis is presented. The product of the Fourier-transformed Langevin function with the Bessel function of the first kind is deducted. First, a corollary is formulated that uses Lemma 5.5 as well as Lemma 6.8 and generalizes the lemma in [F1, Lem. 4.11].

Corollary 6.9. *Let $\hat{\mathscr{L}}_\nu(\boldsymbol{\omega_x})$ denote the components of $\hat{\boldsymbol{\mathscr{L}}} : \mathbb{R}^3 \to \mathbb{C}^3$ as well as $J_\ell(\alpha_1\omega_{x_1})$, $J_m(\alpha_2\omega_{x_2})$, $J_n(\alpha_3\omega_{x_3})$ be the Bessel functions of the first kind with at least one $\alpha_i \neq 0$. The function*

$$l_\nu^{\text{3D}}(\boldsymbol{\omega_x}) = J_\ell(\alpha_1\omega_{x_1})J_m(\alpha_2\omega_{x_2})J_n(\alpha_3\omega_{x_3})\,\hat{\mathscr{L}}_\nu(\boldsymbol{\omega_x}), \tag{6.45}$$

is in $L^p(\mathbb{R}^3)$ with

- $p \in [1, \frac{3}{2})$, *if* $|\ell| + |m| + |n| = 1$.
- $p \in [1, 3)$, *if* $|\ell| + |m| + |n| = 2$.
- $p \in [1, \infty]$, *if* $|\ell| + |m| + |n| \geq 3$.

Proof of Corollary 6.9. For two functions $f \in L^p(\mathbb{R}^3)$ and $g \in L^q(\mathbb{R}^3)$, the Hölder inequality is given by

$$\|f \cdot g\|_{L^r} \leq \|f\|_{L^p}\|g\|_{L^q}$$

with $\frac{1}{r} = \frac{1}{p} + \frac{1}{q}$, $p, q, r \in [1, \infty]$, and the convention $\frac{1}{\infty} = 0$. It follows that the product $f \cdot g \in L^r(\mathbb{R}^3)$. Without loss of generality, it is assumed that $n, m, \ell \geq 0$, otherwise $J_{-n}(x) = (-1)^n J_n(x)$ could be applied. The function $l_\nu^{\text{3D}}(\boldsymbol{\omega_x})$ can be split into two parts

$$\begin{aligned} l_\nu^{\text{3D}}(\boldsymbol{\omega_x}) &= J_\ell(\alpha_1\omega_{x_1})J_m(\alpha_2\omega_{x_2})J_n(\alpha_3\omega_{x_3})\,\hat{\mathscr{L}}_\nu(\boldsymbol{\omega_x}) \\ &= \underbrace{\left(\frac{J_\ell(\alpha_1\omega_{x_1})}{\omega_{x_1}^\ell}\frac{J_m(\alpha_2\omega_{x_2})}{\omega_{x_2}^m}\frac{J_n(\alpha_1\omega_{x_3})}{\omega_{x_3}^n}\right)}_{=f(\boldsymbol{\omega_x})}\underbrace{\left(\omega_{x_1}^\ell\omega_{x_2}^m\omega_{x_3}^n\,\hat{\mathscr{L}}_\nu(\boldsymbol{\omega_x})\right)}_{g(\boldsymbol{\omega_x})}, \end{aligned}$$

therefore the two functions $f(\boldsymbol{\omega_x})$ and $g(\boldsymbol{\omega_x})$ are chosen as

$$f(\boldsymbol{\omega_x}) := \frac{J_\ell(\alpha_1\omega_{x_1})}{\omega_{x_1}^\ell}\frac{J_m(\alpha_2\omega_{x_2})}{\omega_{x_2}^m}\frac{J_n(\alpha_3\omega_{x_3})}{\omega_{x_3}^n},$$
$$g(\boldsymbol{\omega_x}) := \omega_{x_1}^\ell\omega_{x_2}^m\omega_{x_3}^n\,\hat{\mathscr{L}}_\nu(\boldsymbol{\omega_x}).$$

The function $\frac{J_\ell(\alpha_1\omega_{x_1})}{\omega_{x_1}^\ell}$ is in $L^\infty(\mathbb{R})$, which follows from Lemma 5.5 and due to the tensor product structure in $f(\boldsymbol{\omega_x})$, thus $f \in L^\infty(\mathbb{R}^3)$ holds. Consequently, in the Hölder inequality $p = \infty$ and $r = q$ are chosen, which yields

$$\|f \cdot g\|_{L^q} \leq \|f\|_{L^\infty}\|g\|_{L^q} = C\|g\|_{L^q} \quad \text{with} \quad \|f\|_{L^\infty} \leq C.$$

Since $g(\boldsymbol{\omega_x})$ is exactly the function from Lemma 6.8, the conditions in the mentioned lemma are transferred to $l_\nu^{3\mathrm{D}}(\boldsymbol{\omega_x})$. □

The next lemma is formulated to obtain an upper bound for the L^1-norm of the function $l_\nu^{3\mathrm{D}}(\boldsymbol{\omega_x})$ and, thus, ensure that an inverse Fourier transform exists.

Lemma 6.10. *The function*

$$l_\nu^{3\mathrm{D}}(\boldsymbol{\omega_x}) = J_\ell(\alpha_1\omega_{x_1})J_m(\alpha_2\omega_{x_2})J_n(\alpha_3\omega_{x_3})\,\hat{\mathscr{L}}_\nu(\boldsymbol{\omega_x}), \tag{6.46}$$

where $\hat{\mathscr{L}}_\nu(\boldsymbol{\omega_x})$ denotes the components of $\hat{\boldsymbol{\mathscr{L}}} : \mathbb{R}^3 \to \mathbb{C}^3$ and $J_\ell(\alpha_1\omega_{x_1})$, $J_m(\alpha_2\omega_{x_2})$, $J_n(\alpha_3\omega_{x_3})$ are Bessel functions of the first kind with at least one $\alpha_i \neq 0$, is in $L^1(\mathbb{R}^3)$ if $|\ell| + |m| + |n| \geq 1$. An upper bound for the L^1-norm is given by

$$\|l_\nu^{3\mathrm{D}}\|_{L^1} \leq \frac{C}{(\max(1,|\ell|)\max(1,|m|)\max(1,|n|))^{\frac{4}{3}}} \tag{6.47}$$

with $C > 0$. Similarly, the bounds for the L^1-norms of

$$l_\nu^{2\mathrm{D}}(\boldsymbol{\omega_x}) = J_\ell(\alpha_1\omega_{x_1})J_m(\alpha_2\omega_{x_2})\,\hat{\mathscr{L}}_\nu(\boldsymbol{\omega_x}) = \left[l_\nu^{3\mathrm{D}}(\boldsymbol{\omega_x})\right]_{\substack{\alpha_3=0\\ n=0}} \tag{6.48}$$

and

$$l_\nu^{1\mathrm{D}}(\boldsymbol{\omega_x}) = J_\ell(\alpha_1\omega_{x_1})\,\hat{\mathscr{L}}_\nu(\boldsymbol{\omega_x}) = \left[l_\nu^{3\mathrm{D}}(\boldsymbol{\omega_x})\right]_{\substack{\alpha_2=\alpha_3=0\\ n=m=0}} \tag{6.49}$$

are given by (6.47) *with the appropriate choice of $\ell, m \in \mathbb{Z}$.*

Proof of Lemma 6.10. The function $l_\nu^{3\mathrm{D}}(\boldsymbol{\omega_x})$ from (6.46) is considered. At the beginning of the proof, the case with $|\ell| \geq 1$ and $n = m = 0$ is considered for which

$$f(\boldsymbol{\omega_x}) := \frac{J_\ell(\alpha_1 \omega_{x_1})}{\omega_{x_1}} J_m(\alpha_2 \omega_{x_2}) J_n(\alpha_3 \omega_{x_3}),$$
$$g(\boldsymbol{\omega_x}) := \omega_{x_1} \hat{\mathscr{L}}_\nu(\boldsymbol{\omega_x})$$

is defined. By Lemma 6.8, $\|g\|_{L^1}$ is bounded by a constant c_1 with $0 < c_1 < \infty$. With Corollary 5.2 and using $\|J_0\|_{L^\infty} = 1$ the inequality $\|f\|_{L^\infty} \leq C_1/|\ell|^{\frac{4}{3}}$ results. From the Hölder inequality it follows that

$$\|l_\nu^{3\mathrm{D}}\|_{L^1} = \|f \cdot g\|_{L^1} \leq \|f\|_{L^\infty} \|g\|_{L^1} \leq \frac{C_1}{|\ell|^{\frac{4}{3}}} c_1 < \infty. \tag{6.50}$$

Secondly, it is considered that $|\ell| \geq 1$, $|m| \geq 1$ and $n = 0$. The function $l_\nu^{3\mathrm{D}}(\boldsymbol{\omega_x}) = f(\boldsymbol{\omega_x}) g(\boldsymbol{\omega_x})$ is split into

$$f(\boldsymbol{\omega_x}) := \frac{J_\ell(\alpha_1 \omega_{x_1})}{\omega_{x_1}} \frac{J_m(\alpha_2 \omega_{x_2})}{\omega_{x_2}} J_n(\alpha_3 \omega_{x_3}),$$
$$g(\boldsymbol{\omega_x}) := \omega_{x_1} \omega_{x_2} \hat{\mathscr{L}}_\nu(\boldsymbol{\omega_x}).$$

Using Lemma 6.8, Corollary 5.2, and $\|J_0\|_\infty = 1$ the Hölder inequality then yields

$$\|l_\nu^{3\mathrm{D}}\|_{L^1} = \|f \cdot g\|_{L^1} \leq \|f\|_{L^\infty} \|g\|_{L^1} \leq \frac{C_2}{|\ell|^{\frac{4}{3}} |m|^{\frac{4}{3}}} c_2 < \infty. \tag{6.51}$$

Finally, it is assumed that $|\ell|$, $|m|$, and $|n|$ are larger than zero. In this case the function $l_\nu^{3\mathrm{D}}(\boldsymbol{\omega_x}) = f(\boldsymbol{\omega_x}) g(\boldsymbol{\omega_x})$ is split into

$$f(\boldsymbol{\omega_x}) := \frac{J_\ell(\alpha_1 \omega_{x_1})}{\omega_{x_1}} \frac{J_m(\alpha_2 \omega_{x_2})}{\omega_{x_2}} \frac{J_n(\alpha_3 \omega_{x_3})}{\omega_{x_3}},$$
$$g(\boldsymbol{\omega_x}) := \omega_{x_1} \omega_{x_2} \omega_{x_3} \hat{\mathscr{L}}_\nu(\boldsymbol{\omega_x}).$$

Using Lemma 6.8 and Corollary 5.2, the Hölder inequality reads

$$\|l_\nu^{3\mathrm{D}}\|_{L^1} = \|f \cdot g\|_{L^1} \leq \|f\|_{L^\infty} \|g\|_{L^1} \leq \frac{C_3}{|\ell|^{\frac{4}{3}} |m|^{\frac{4}{3}} |n|^{\frac{4}{3}}} c_3 < \infty. \tag{6.52}$$

Expressions similar to (6.50), (6.51), and (6.52) can be derived for the other possible combinations of general $\ell, n, m \in \mathbb{Z}$ with $|\ell| + |m| + |n| \geq 1$. These confirm (6.47) in Lemma 6.10 for all $\ell, m, n \in \mathbb{Z}$. □

Lemma 6.10 ensures the existence of an inverse Fourier transform from products of $\hat{\mathscr{L}}_\nu(\boldsymbol{\omega}_{\boldsymbol{x}})$ and Bessel functions of the first kind. Therefore, the inverse Fourier transform of products from $\hat{\mathscr{L}}_\nu(\boldsymbol{\omega}_{\boldsymbol{x}})$ with Bessel functions of the first kind are introduced now and will be used to derive the MPI system function components later.

Lemma 6.11. *The inverse Fourier transforms of products*

$$\hat{a}_\nu^{1\mathrm{D}}(\boldsymbol{\omega}_{\boldsymbol{x}}) := \frac{J_n(\alpha_1\omega_{x_1})\,\mathrm{e}^{-\mathrm{i}\omega_{x_2}c_2}\mathrm{e}^{-\mathrm{i}\omega_{x_3}c_3}\,\hat{\mathscr{L}}_\nu\left(\frac{\boldsymbol{G}^{-\mathsf{T}}\boldsymbol{\omega}_{\boldsymbol{x}}}{\beta}\right)}{|\det(\beta\boldsymbol{G})|},$$

$$\hat{a}_\nu^{2\mathrm{D}}(\boldsymbol{\omega}_{\boldsymbol{x}}) := \frac{J_n(\alpha_1\omega_{x_1})\,J_m(\alpha_2\omega_{x_2})\,\mathrm{e}^{-\mathrm{i}\omega_{x_3}c_3}\,\hat{\mathscr{L}}_\nu\left(\frac{\boldsymbol{G}^{-\mathsf{T}}\boldsymbol{\omega}_{\boldsymbol{x}}}{\beta}\right)}{|\det(\beta\boldsymbol{G})|},$$

$$\hat{a}_\nu^{3\mathrm{D}}(\boldsymbol{\omega}_{\boldsymbol{x}}) := \frac{J_n(\alpha_1\omega_{x_1})\,J_m(\alpha_2\omega_{x_2})\,J_\ell(\alpha_3\omega_{x_3})\,\hat{\mathscr{L}}_\nu\left(\frac{\boldsymbol{G}^{-\mathsf{T}}\boldsymbol{\omega}_{\boldsymbol{x}}}{\beta}\right)}{|\det(\beta\boldsymbol{G})|},$$

of $\hat{\mathscr{L}}_\nu : \mathbb{R}^3 \to \mathbb{C}$ *with the Bessel functions of the first kind* $J_n(\alpha_1\omega_{x_1})$*,* $J_m(\alpha_2\omega_{x_2})$*, and* $J_\ell(\alpha_3\omega_{x_3})$ *with* $\alpha_i \neq 0$*,* $c_2, c_3 \in \mathbb{R}$ *as well as* $|n| + |m| + |\ell| \geq 1$ *are given by*

$$\mathcal{F}^{-1}\{\hat{a}_\nu^{1\mathrm{D}}(\boldsymbol{\omega}_{\boldsymbol{x}})\} = \frac{\mathrm{i}^n}{\pi\,\mathrm{sgn}(\alpha_1)}\int_{\mathbb{R}}\left[\frac{\partial}{\partial z_1}\mathscr{L}_\nu\left(\beta\boldsymbol{G}\begin{pmatrix} z_1 \\ x_2-c_2 \\ x_3-c_3\end{pmatrix}\right)\right]_{z_1=x_1-u_1} V_n\left(\frac{u_1}{\alpha_1}\right)\mathrm{d}u_1, \tag{6.53}$$

$$\mathcal{F}^{-1}\{\hat{a}_\nu^{2\mathrm{D}}(\boldsymbol{\omega}_{\boldsymbol{x}})\} = \frac{\mathrm{i}^{n+m}}{\pi^2\,\mathrm{sgn}(\alpha_1\alpha_2)}\int_{\mathbb{R}^2}\left[\frac{\partial^2}{\partial z_1\partial z_2}\mathscr{L}_\nu\left(\beta\boldsymbol{G}\begin{pmatrix} z_1 \\ z_2 \\ x_3-c_3\end{pmatrix}\right)\right]_{\substack{z_1=x_1-u_1\\ z_2=x_2-u_2}} \times V_n\left(\frac{u_1}{\alpha_1}\right)V_m\left(\frac{u_2}{\alpha_2}\right)\mathrm{d}u_1\,\mathrm{d}u_2, \tag{6.54}$$

and

$$\mathcal{F}^{-1}\{\hat{a}_\nu^{3\mathrm{D}}(\boldsymbol{\omega}_{\boldsymbol{x}})\} = \frac{\mathrm{i}^{n+m+\ell}}{\pi^3\,\mathrm{sgn}(\alpha_1\alpha_2\alpha_3)}\int_{\mathbb{R}^3}\left[\frac{\partial^3}{\partial z_1\partial z_2\partial z_3}\mathscr{L}_\nu(\beta\boldsymbol{G}\boldsymbol{z})\right]_{\boldsymbol{z}=\boldsymbol{x}-\boldsymbol{u}} \times V_n\left(\frac{u_1}{\alpha_1}\right)V_m\left(\frac{u_2}{\alpha_2}\right)V_\ell\left(\frac{u_3}{\alpha_3}\right)\mathrm{d}\boldsymbol{u}, \tag{6.55}$$

respectively.

Proof of Lemma 6.11. According to Lemma 5.3 with $|n| \geq 1$ and the scaling property of the Fourier transform (Property 2) with $\alpha \neq 0$ it results that

$$\begin{aligned}
\mathcal{F}^{-1}\left\{ \frac{J_n(\alpha\omega_x)}{\mathrm{i}\omega_x} \right\} &= \frac{\mathrm{i}^n}{\pi\,\mathrm{sgn}(\alpha)} V_n\Big(\frac{x}{\alpha}\Big)\,, \\
\mathcal{F}^{-1}\left\{ \frac{\mathrm{i}\omega_{x_1}\,\hat{\mathscr{L}}_\nu\Big(\frac{\boldsymbol{G}^{-\mathsf{T}}\boldsymbol{\omega}_{\boldsymbol{x}}}{\beta}\Big)}{|\det(\beta\boldsymbol{G})|} \right\} &= \tfrac{\partial}{\partial x_1}\,\mathscr{L}_\nu(\beta\boldsymbol{G}\boldsymbol{x})\,, \\
\mathcal{F}^{-1}\left\{ \frac{\mathrm{i}\omega_{x_1}\mathrm{i}\omega_{x_2}\,\hat{\mathscr{L}}_\nu\Big(\frac{\boldsymbol{G}^{-\mathsf{T}}\boldsymbol{\omega}_{\boldsymbol{x}}}{\beta}\Big)}{|\det(\beta\boldsymbol{G})|} \right\} &= \tfrac{\partial^2}{\partial x_1\partial x_2}\,\mathscr{L}_\nu(\beta\boldsymbol{G}\boldsymbol{x})\,, \\
\mathcal{F}^{-1}\left\{ \frac{\mathrm{i}\omega_{x_1}\mathrm{i}\omega_{x_2}\mathrm{i}\omega_{x_3}\,\hat{\mathscr{L}}_\nu\Big(\frac{\boldsymbol{G}^{-\mathsf{T}}\boldsymbol{\omega}_{\boldsymbol{x}}}{\beta}\Big)}{|\det(\beta\boldsymbol{G})|} \right\} &= \tfrac{\partial^3}{\partial x_1\partial x_2\partial x_3}\,\mathscr{L}_\nu(\beta\boldsymbol{G}\boldsymbol{x})\,.
\end{aligned}$$

Moreover, there is the well-known relationship

$$\mathcal{F}^{-1}\big\{\mathrm{e}^{-\mathrm{i}\omega_x c}\big\} = \delta_0(x-c)$$

with $\delta_0(x)$ being the Dirac delta distribution and $c \in \mathbb{R}$. Since a multiplication in the Fourier domain is equivalent to a convolution in the spatial domain (Property 5), one gets (term by term) the results for $a_\nu^{1\mathrm{D}}(\boldsymbol{x}) = \mathcal{F}^{-1}\{\hat{a}_\nu^{1\mathrm{D}}(\boldsymbol{\omega}_{\boldsymbol{x}})\}$, $a_\nu^{2\mathrm{D}}(\boldsymbol{x}) = \mathcal{F}^{-1}\{\hat{a}_\nu^{2\mathrm{D}}(\boldsymbol{\omega}_{\boldsymbol{x}})\}$, and $a_\nu^{3\mathrm{D}}(\boldsymbol{x}) = \mathcal{F}^{-1}\{\hat{a}_\nu^{3\mathrm{D}}(\boldsymbol{\omega}_{\boldsymbol{x}})\}$. These convolutions generally occur in all three dimensions. However, for $a_\nu^{1\mathrm{D}}(\boldsymbol{x})$ and $a_\nu^{2\mathrm{D}}(\boldsymbol{x})$, they reduce to one- and two-dimensional ones, respectively, since the convolutions with Dirac delta distributions along the unused dimensions result in phase shifts.

In the case that either n, m or ℓ is zero, there is still the Fourier correspondence

$$\begin{aligned}
\mathcal{F}^{-1}\big\{J_0\big(\alpha_j\omega_{x_j}\big)\big\} &= \frac{1}{\pi}\frac{1}{|\alpha_j|}\,\mathrm{rect}\left(\frac{x_j}{\alpha_j}\right)\frac{1}{\sqrt{1-\left(\frac{x_j}{\alpha_j}\right)^2}} \\
&= \frac{1}{\pi}\frac{1}{|\alpha_j|}v_0\left(\frac{x_j}{\alpha_j}\right)
\end{aligned}$$

with $v_0(x) = \frac{\mathrm{d}}{\mathrm{d}x}V(x)$ defined in Lemma 5.3 and Lemma 5.4.

For $|n|, |m| > 0$ and $\ell = 0$, the following inverse Fourier transform of $\hat{a}_\nu^{\mathrm{3D}}(\boldsymbol{\omega}_{\boldsymbol{x}})$ is given by

$$a_\nu^{\mathrm{3D}}(\boldsymbol{x}) = \frac{\mathrm{i}^{n+m}}{\pi^3 \operatorname{sgn}(\alpha_1\alpha_2)} \int_{\mathbb{R}^3} \left[\frac{\partial^2}{\partial z_1 \partial z_2} \mathscr{L}_\nu(\beta \boldsymbol{G}\boldsymbol{z}) \right]_{\boldsymbol{z}=\boldsymbol{x}-\boldsymbol{u}} \times V_n\left(\frac{u_1}{\alpha_1}\right) V_m\left(\frac{u_2}{\alpha_2}\right) \frac{1}{|\alpha_3|} v_0\left(\frac{u_3}{\alpha_3}\right) \mathrm{d}\boldsymbol{u}.$$

Due to Lemma 6.8 it is known that $\omega_{x_1}\omega_{x_2}\, \hat{\mathscr{L}}_\nu\left(\frac{\boldsymbol{G}^{-\mathsf{T}}\boldsymbol{\omega}_{\boldsymbol{x}}}{\beta}\right)$ is in $L^1(\mathbb{R}^3)$. Hence, the function $\frac{\partial^2}{\partial x_1 \partial x_2} \mathscr{L}_\nu(\beta \boldsymbol{G}\boldsymbol{x})$ vanishes as its argument goes to plus or minus infinity and, thus, it is in $L^\infty(\mathbb{R}^3)$. Therefore, Lemma 5.4 can be used, resulting in

$$a_\nu^{\mathrm{3D}}(\boldsymbol{x}) = \frac{\mathrm{i}^{n+m}}{\pi^3 \operatorname{sgn}(\alpha_1\alpha_2\alpha_3)} \int_{\mathbb{R}^3} \left[\frac{\partial^3}{\partial z_1 \partial z_2 \partial z_3} \mathscr{L}_\nu(\beta \boldsymbol{G}\boldsymbol{z}) \right]_{\boldsymbol{z}=\boldsymbol{x}-\boldsymbol{u}} \times V_n\left(\frac{u_1}{\alpha_1}\right) V_m\left(\frac{u_2}{\alpha_2}\right) V_0\left(\frac{u_3}{\alpha_3}\right) \mathrm{d}\boldsymbol{u}.$$

The expressions for $a_\nu^{\mathrm{3D}}(\boldsymbol{x})$ and $a_\nu^{\mathrm{2D}}(\boldsymbol{x})$ with other combinations of $|m| + |n| + |\ell| \geq 1$ follow analogously. Note, for $a_\nu^{\mathrm{1D}}(\boldsymbol{x})$ the case $n = 0$ is not required and was, thus, excluded from the proof and the lemma. □

Another novelty in this work is the utilization of a convolution property to obtain a more direct formulation of $a_\nu^{\mathrm{3D}}(\boldsymbol{x})$:

$$\begin{aligned} a_\nu^{\mathrm{3D}}(\boldsymbol{x}) &= \frac{\mathrm{i}^{n+m+\ell}}{\pi^3 \operatorname{sgn}(\alpha_1\alpha_2\alpha_3)} \int_{\mathbb{R}^3} \left[\frac{\partial^3}{\partial z_1 \partial z_2 \partial z_3} \mathscr{L}_\nu(\beta \boldsymbol{G}\boldsymbol{z}) \right]_{\boldsymbol{z}=\boldsymbol{x}-\boldsymbol{u}} P_{nm\ell}\left(\frac{u_1}{\alpha_1}, \frac{u_2}{\alpha_2}, \frac{u_3}{\alpha_3}\right) \mathrm{d}\boldsymbol{u} \\ &= \frac{\mathrm{i}^{n+m+\ell}}{\pi^3 |\alpha_1\alpha_2\alpha_3|} \int_{\mathbb{R}^3} \mathscr{L}_\nu\big(\beta \boldsymbol{G}(\boldsymbol{x}-\boldsymbol{u})\big) p_{nm\ell}\left(\frac{u_1}{\alpha_1}, \frac{u_2}{\alpha_2}, \frac{u_3}{\alpha_3}\right) \mathrm{d}\boldsymbol{u} \end{aligned} \tag{6.56}$$

with $P_{nm\ell}(\boldsymbol{\xi}) = V_n(\xi_1)V_m(\xi_2)V_\ell(\xi_3)$, $p_{nm\ell}(\boldsymbol{\xi}) = v_n(\xi_1)v_m(\xi_2)v_\ell(\xi_3)$, as well as $\boldsymbol{\xi} \in \mathbb{R}^3$. Thereby, $V_n(\xi)$ refers to a weighted Chebyshev polynomial of the second kind and $v_n(\xi)$ refers to a weighted Chebyshev polynomial of the first kind and they are defined in (5.34) and (5.36), respectively. This fact can be derived from the property that the

partial derivative operator can be transferred from one function to another within the convolution. This fact is shown in Lemma 5.4 for $n = 0$, which is the most difficult case to show. For general $n \in \mathbb{Z}$ this property is much easier to show, but for the sake of simplicity the proof is omitted.

Moreover, using the differential operator $\mathrm{D}_{\boldsymbol{\xi}}^{\mathbb{I}} = \prod_{i \in \mathbb{I}} \frac{\partial}{\partial \xi_i}$ with $\mathbb{I} \subseteq \mathbb{\Omega} = \{1, 2, 3\}$ and $\mathrm{D}_{\boldsymbol{\xi}}^{\emptyset} = 1$. Equation (6.56) can be expressed by

$$a_{\nu}^{\mathrm{3D}}(\boldsymbol{x}) = \frac{\mathrm{i}^{n+m+\ell}}{\pi^3 \operatorname{sgn}(\alpha_1\alpha_2\alpha_3)} \int_{\mathbb{R}^3} \left[\mathrm{D}_{\boldsymbol{z}}^{\mathbb{K}} \mathscr{L}_{\nu}(\beta \boldsymbol{G}\boldsymbol{z})\right]_{\boldsymbol{z}=\boldsymbol{x}-\boldsymbol{y}} \times \left[\mathrm{D}_{\boldsymbol{u}}^{\mathbb{\Omega}\setminus\mathbb{K}} P_{nm\ell}\left(\frac{u_1}{\alpha_1}, \frac{u_2}{\alpha_2}, \frac{u_3}{\alpha_3}\right)\right] \mathrm{d}\boldsymbol{u} \tag{6.57}$$

with $\mathbb{K} \subseteq \mathbb{\Omega}$. Equation (6.57) states that the partial derivatives in a convolution between the kernel $\mathscr{L}_{\nu}(\beta \boldsymbol{G}\boldsymbol{z})$ and the tensor product of the weighted Chebyshev polynomials $P_{nm\ell}(\frac{u_1}{\alpha_1}, \frac{u_2}{\alpha_2}, \frac{u_3}{\alpha_3})$ can be interchanged arbitrarily.

The property in (6.57) can be used to mathematically motivate the system matrix compression algorithm proposed in [C2], which uses a combination of Chebyshev polynomials of the first and second kind. Furthermore, the direct Chebyshev polynomial reconstruction in [C1] is based on Chebyshev polynomials of the second kind, but can possibly be transformed into a reconstruction with Chebyshev polynomials of the first kind with the help of (6.56). This would have the advantage that all frequency components u_k^{P} could be used, which is not possible in the current form. However, this remains a task to be investigated in the future.

7 Fourier Representation for Different FFP-Trajectories

This chapter deals with the MPI system function for various FFP-trajectories. In the first three sections, the results from [F1] on Lissajous FFP-trajectories are recapitulated and supplemented by the possibility of phase shifts. In addition, a general strategy for arbitrary periodic FFP-trajectories is introduced for the first time. It is a direct consequence of the model derived in Theorem 6.1 and is applied to various other FFP-trajectories from the literature.

7.1 Fourier Representation for a One-Dimensional FFP-Trajectory

For a one-dimensional excitation with a three-dimensional SPIO distribution, a closed-form representation of the temporal Fourier series coefficients has been derived in [81], see also Theorem 2.1 in this thesis. Since the proof from Theorem 2.1 cannot simply be extended to the case of a multidimensional excitation, a different proof strategy for a one-dimensional excitation and a one-dimensional SPIO distribution was outlined in [F8]. The first theorem of this chapter was formulated in [F1]. In addition to the known relationships for $\boldsymbol{s}_k(\boldsymbol{x})$, a spatial Fourier transform $\hat{\boldsymbol{s}}_k(\boldsymbol{\omega}_x)$ was also introduced.

Definition 7.1: One-dimensional excitation

Let $f_1 = f_\mathrm{B}$ be an arbitrary excitation frequency of an MPI scanner with $f_\mathrm{B} > 0$. Then the drive field along the x_1-axis has the form

$$\boldsymbol{H}^\mathrm{D}(t) = \begin{pmatrix} -A_1 \sin(\omega_1 t + \varphi_1) \\ -c_2 \\ -c_3 \end{pmatrix},$$

where $\omega_1 = 2\pi f_1$ denotes the angular frequency, A_1 is the amplitude, $\varphi_1 \in [0, 2\pi)$ is a phase shift, and $c_2, c_3 \in \mathbb{R}$ are time independent drive-field offsets. The homogeneous selection field $\boldsymbol{H}^\mathrm{S}(\boldsymbol{x}) = \boldsymbol{G}\boldsymbol{x}$ of the MPI scanner is, without loss of generality, assumed to be diagonal:

$$\boldsymbol{G} = \begin{pmatrix} G_1 & 0 & 0 \\ 0 & G_2 & 0 \\ 0 & 0 & G_3 \end{pmatrix}. \tag{7.1}$$

According to Maxwell's equations, the magnetic field must fulfill the following condition: $G_1 + G_2 + G_3 = 0$.

Following (2.25), the position of the FFP is given by [48, 70, 92]

$$\boldsymbol{x}_\mathrm{FFP}(t) = -\boldsymbol{G}^{-1}\boldsymbol{H}^\mathrm{D}(t) \tag{7.2}$$

and has the period length $T_\mathrm{D} = \frac{1}{f_1}$ with $f_\mathrm{D} = f_1$. By this definition, the Fourier representation for MPI with a one-dimensional trajectory can be formulated in a theorem.

Theorem 7.1

The Fourier series coefficients $\boldsymbol{s}_k : \mathbb{R}^3 \to \mathbb{C}^3$ of the MPI system function for a one-dimensional FFP-trajectory with the phase shift $\varphi_1 \in [0, 2\pi)$ and $k \in \mathbb{Z}\backslash\{0\}$ can be expressed in terms of $V_\ell : \mathbb{R} \to \mathbb{R}$ convolved along the spatial dimension with the spatial derivative of the Langevin function $\mathscr{L} : \mathbb{R}^3 \to \mathbb{R}^3$ by

$$\begin{aligned}\boldsymbol{s}_k(\boldsymbol{x}) = \frac{(-\mathrm{i})^{k+1}\omega_k \mathrm{e}^{\mathrm{i}\varphi_1 k}}{\pi} \frac{\operatorname{sgn}(A_1)}{\operatorname{sgn}(G_1)} \\ \times \int_{\mathbb{R}} \left[\frac{\partial}{\partial z_1} \mathscr{L}\left(\beta \boldsymbol{G} \begin{pmatrix} z_1 \\ x_2 - \frac{c_2}{G_2} \\ x_3 - \frac{c_3}{G_3} \end{pmatrix} \right) \right]_{z_1 = x_1 - u_1} V_k\left(\frac{G_1}{A_1} u_1 \right) \mathrm{d}u_1,\end{aligned} \tag{7.3}$$

with

$$V_n(\xi) = \operatorname{rect}\left(\frac{\xi}{2}\right) \left(-\frac{U_{|n|-1}(\xi)\sqrt{1-\xi^2}}{|n|} \right), \qquad |n| > 0$$

and $U_\ell(\xi)$ being the Chebyshev polynomial of the second kind with degree $\ell \in \mathbb{N}_0$. Equivalently, the spatial Fourier domain representation of $\boldsymbol{s}_k(\boldsymbol{x})$ is given by

$$\hat{\boldsymbol{s}}_k(\boldsymbol{\omega_x}) = (-1)^{k+1}\mathrm{i}\omega_k \mathrm{e}^{\mathrm{i}\varphi_1 k} \frac{\hat{\mathscr{L}}\left(\frac{\boldsymbol{G}^{-\mathsf{T}}\boldsymbol{\omega_x}}{\beta}\right)}{|\det(\beta \boldsymbol{G})|} J_k\left(\omega_{x_1} \frac{A_1}{G_1} \right) \mathrm{e}^{-\mathrm{i}\frac{c_2}{G_2}\omega_{x_2}} \mathrm{e}^{-\mathrm{i}\frac{c_3}{G_3}\omega_{x_3}}, \tag{7.4}$$

where $J_\ell(\xi)$ denotes the ℓ-th Bessel function of the first kind and $\hat{\mathscr{L}} : \mathbb{R}^3 \to \mathbb{C}^3$ reads

$$\hat{\mathscr{L}}(\boldsymbol{\omega_x}) = -4\pi^2 \mathrm{i} \frac{(\pi\|\boldsymbol{\omega_x}\| + 1)\,\mathrm{e}^{\pi\|\boldsymbol{\omega_x}\|} - 1}{\|\boldsymbol{\omega_x}\|^2 \left(\mathrm{e}^{\pi\|\boldsymbol{\omega_x}\|} - 1\right)^2} \frac{\boldsymbol{\omega_x}}{\|\boldsymbol{\omega_x}\|}.$$

For $k = 0$ it holds that $\boldsymbol{s}_0(\boldsymbol{x}) = \boldsymbol{0}$ and $\hat{\boldsymbol{s}}_0(\boldsymbol{\omega_x}) = \boldsymbol{0}$.

Note that the expression for $\boldsymbol{s}_k(\boldsymbol{x})$ in (7.3) is the same as in [81] when the phase shift is set to $\varphi_1 = \frac{\pi}{2}$ and it is used that $c_2 = c_3 = 0$.

Proof of Theorem 7.1. The position of the FFP with the substitution $t = \frac{z}{2\pi f_\mathrm{D}}$ is

$$\boldsymbol{x}_\mathrm{FFP}\left(\frac{z}{2\pi f_\mathrm{D}}\right) = \begin{pmatrix} \frac{A_1}{G_1}\sin(z + \varphi_1) \\ \frac{c_2}{G_2} \\ \frac{c_3}{G_3} \end{pmatrix}.$$

To compute the mapping function

$$P(\boldsymbol{\omega}_{\boldsymbol{x}}, k) = \frac{1}{2\pi} \int_{-\pi}^{\pi} \mathrm{e}^{\mathrm{i}\boldsymbol{\omega}_{\boldsymbol{x}}^{\mathsf{T}} \boldsymbol{x}_{\mathrm{FFP}}\left(\frac{z}{2\pi f_{\mathrm{D}}}\right)} \mathrm{e}^{-\mathrm{i}kz} \,\mathrm{d}z \tag{7.5}$$

defined in Theorem 6.1, the term $\mathrm{e}^{\mathrm{i}\boldsymbol{\omega}_{\boldsymbol{x}}^{\mathsf{T}} \boldsymbol{x}_{\mathrm{FFP}}\left(\frac{z}{2\pi f_{\mathrm{D}}}\right)}$ is rewritten as

$$\mathrm{e}^{\mathrm{i}\boldsymbol{\omega}_{\boldsymbol{x}}^{\mathsf{T}} \boldsymbol{x}_{\mathrm{FFP}}\left(\frac{z}{2\pi f_{\mathrm{D}}}\right)} = \mathrm{e}^{\mathrm{i}\omega_{x_1} \frac{A_1}{G_1} \sin(z+\varphi_x)} \mathrm{e}^{\mathrm{i}\frac{c_2}{G_2}\omega_{x_2}} \mathrm{e}^{\mathrm{i}\frac{c_3}{G_3}\omega_{x_3}}$$

and by using the Jacobi-Anger expansion [8, Ch. 7.2.4, (26)]

$$\mathrm{e}^{\mathrm{i}z\sin(\theta)} = \sum_{n=-\infty}^{\infty} J_n(z) \mathrm{e}^{\mathrm{i}n\theta},$$

as

$$\mathrm{e}^{\mathrm{i}\boldsymbol{\omega}_{\boldsymbol{x}}^{\mathsf{T}} \boldsymbol{x}_{\mathrm{FFP}}\left(\frac{z}{2\pi f_{\mathrm{D}}}\right)} = \sum_{n=-\infty}^{\infty} J_n\left(\omega_{x_1} \frac{A_1}{G_1}\right) \mathrm{e}^{\mathrm{i}n(z+\varphi_1)} \mathrm{e}^{\mathrm{i}\frac{c_2}{G_2}\omega_{x_2}} \mathrm{e}^{\mathrm{i}\frac{c_3}{G_3}\omega_{x_3}}. \tag{7.6}$$

Inserting (7.6) into (7.5), reordering the terms, and carrying out the integration yields

$$\begin{aligned} P(\boldsymbol{\omega}_{\boldsymbol{x}}, k) &= \sum_{n=-\infty}^{\infty} \mathrm{e}^{\mathrm{i}\varphi_1 n} J_n\left(\omega_{x_1} \frac{A_1}{G_1}\right) \mathrm{e}^{\mathrm{i}\frac{c_2}{G_2}\omega_{x_2}} \mathrm{e}^{\mathrm{i}\frac{c_3}{G_3}\omega_{x_3}} \\ &\qquad \times \underbrace{\frac{1}{2\pi} \int_{-\pi}^{\pi} \mathrm{e}^{\mathrm{i}(n-k)z} \,\mathrm{d}z}_{=\delta_{(n,k)}} \\ &= \mathrm{e}^{\mathrm{i}\varphi_1 k} J_k\left(\omega_{x_1} \frac{A_1}{G_1}\right) \mathrm{e}^{\mathrm{i}\frac{c_2}{G_2}\omega_{x_2}} \mathrm{e}^{\mathrm{i}\frac{c_3}{G_3}\omega_{x_3}}, \end{aligned} \tag{7.7}$$

where

$$\delta_{(n,k)} = \begin{cases} 1 & \text{if } k = n \\ 0 & \text{otherwise} \end{cases}$$

denotes the Kronecker delta.

By considering $\boldsymbol{g}_k$ from (6.6) with $\hat{\boldsymbol{h}}(\boldsymbol{\omega}_{\boldsymbol{x}})$ from (6.8), one obtains

$$\boldsymbol{g}_k = \frac{\mathrm{i}\omega_k}{(2\pi)^3} \int_{\mathbb{R}^3} \hat{c}(\boldsymbol{\omega}_{\boldsymbol{x}}) \frac{\hat{\mathscr{L}}\left(\frac{\boldsymbol{G}^{-\mathsf{T}}\boldsymbol{\omega}_{\boldsymbol{x}}}{\beta}\right)}{|\det(\beta \boldsymbol{G})|} P(\boldsymbol{\omega}_{\boldsymbol{x}}, k) \,\mathrm{d}\boldsymbol{\omega}_{\boldsymbol{x}}. \tag{7.8}$$

Inserting $P(\boldsymbol{\omega_x}, k)$ from (7.7) into (7.8) and comparing the obtained expression with (7.4) under the use of $\hat{\mathscr{L}}(-\boldsymbol{\omega_x}) = -\hat{\mathscr{L}}(\boldsymbol{\omega_x})$ and $J_k(-\omega) = (-1)^k J_k(\omega)$ yields

$$\boldsymbol{g}_k = \frac{1}{(2\pi)^3} \int_{\mathbb{R}^3} \hat{c}(\boldsymbol{\omega_x}) \hat{\boldsymbol{s}}_k(-\boldsymbol{\omega_x}) \, \mathrm{d}\boldsymbol{\omega_x} = \frac{1}{(2\pi)^3} \int_{\mathbb{R}^3} \hat{c}(-\boldsymbol{\omega_x}) \hat{\boldsymbol{s}}_k(\boldsymbol{\omega_x}) \, \mathrm{d}\boldsymbol{\omega_x} \tag{7.9}$$

with

$$\hat{\boldsymbol{s}}_k(\boldsymbol{\omega_x}) = (-1)^{k+1} \mathrm{i}\omega_k \mathrm{e}^{\mathrm{i}\varphi_1 k} \frac{\hat{\mathscr{L}}\left(\frac{\boldsymbol{G}^{-\mathsf{T}}\boldsymbol{\omega_x}}{\beta}\right)}{|\det(\beta \boldsymbol{G})|} J_k\left(\omega_{x_1} \frac{A_1}{G_1}\right) \mathrm{e}^{-\mathrm{i}\frac{c_2}{G_2}\omega_{x_2}} \mathrm{e}^{-\mathrm{i}\frac{c_3}{G_3}\omega_{x_3}}.$$

Using that $c(\boldsymbol{x})$ is real-valued and that its Fourier transform has the conjugate symmetry $\hat{c}(-\boldsymbol{\omega_x}) = \hat{c}^*(\boldsymbol{\omega_x})$, Parseval's Theorem 4.4 can be applied to obtain the original relationship (6.4):

$$\boldsymbol{g}_k = \int_{\mathbb{R}^3} c(\boldsymbol{x}) \boldsymbol{s}_k(\boldsymbol{x}) \, \mathrm{d}\boldsymbol{x}. \tag{7.10}$$

This proves that $\hat{\boldsymbol{s}}_k(\boldsymbol{\omega_x})$ according to (7.4) is the spatial-frequency representation of $\boldsymbol{s}_k(\boldsymbol{x})$.

Using Lemma 6.11 and by observing that the expression in $\hat{a}_\nu^{\mathrm{1D}}(\boldsymbol{\omega_x})$ is equivalent to (7.4) up to a factor, one gets $\boldsymbol{s}_k(\boldsymbol{x})$ according to (7.3) as the inverse Fourier transform of (7.4), which was to be proven. □

Figure 7.1 shows functions from Theorem 7.1 for a sinusoidal drive field, i.e., $\varphi_1 = \frac{\pi}{2}$ and $c_2 = c_3 = 0$. The parameters for the simulation not mentioned here can be found in the Table 7.1 in the next section. For the one-dimensional excitation, f_2 was set to zero and $T_\mathrm{D} = \frac{1}{f_1}$. Two different particle diameters were simulated, namely $D \in \{20\,\mathrm{nm}, 30\,\mathrm{nm}\}$. From left to right, the weighted Chebyshev polynomial $-V_k\left(\frac{G_1}{A_1}x_1\right)$ is shown in blue, the imaginary part of $\tilde{s}_k(x_1) = s_{1k}(x_1, 0, 0)$ (see (7.3)) is shown in red in the middle column and the absolute value of the one-dimensional Fourier transform $\tilde{s}_k(x_1) = s_{1k}(x_1, 0, 0)$ (see (7.4)) is shown in green in the right column. The one-dimensional Fourier transform can be calculated by replacing the three-dimensional Fourier transform $\hat{\mathscr{L}} : \mathbb{R}^3 \to \mathbb{C}^3$ from (6.39) with the one-dimensional version $\hat{\mathscr{L}} : \mathbb{R} \to \mathbb{C}$ from (6.34). By comparing the blue function curves with the red ones, it can be seen that the system function components in the one-dimensional excited MPI are weighted Chebyshev polynomials of the second kind, which are blurred by the convolution with the kernel $\frac{\partial}{\partial x_1}\mathscr{L}(\beta G_1 x_1, 0, 0)$. This observation was first reported in [81]. A smaller particle diameter D leads to a

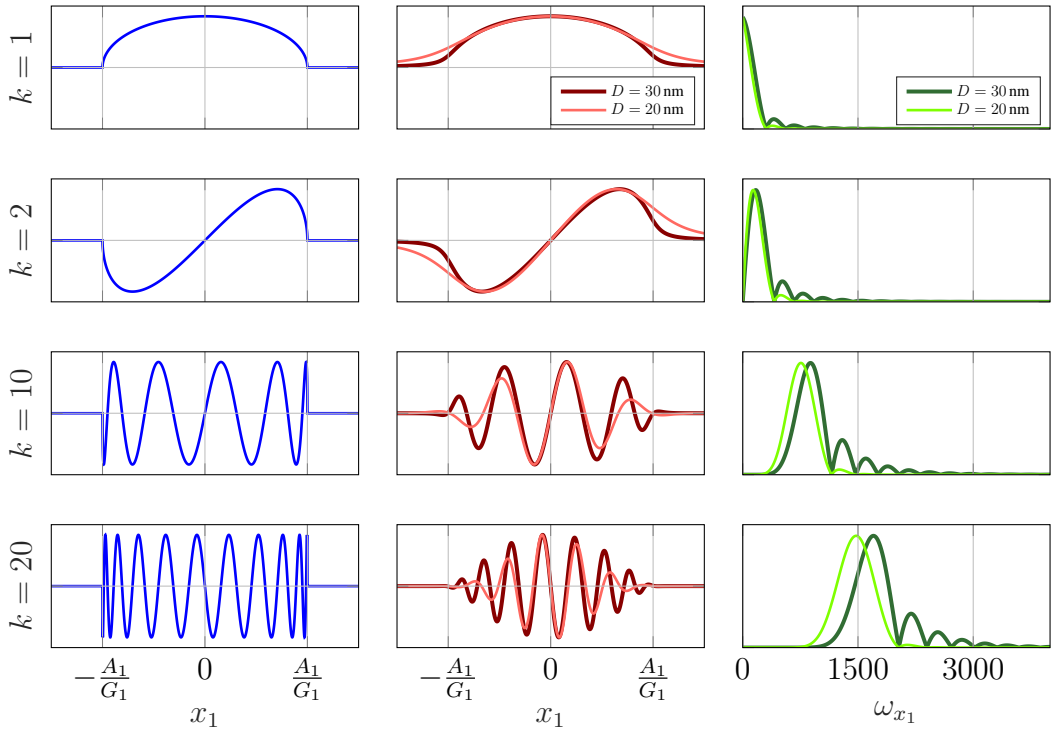

Figure 7.1: Different functions (from left to right) related to the MPI system function are shown for different particle diameters $D \in \{20\,\text{nm}, 30\,\text{nm}\}$ and different $k \in \mathbb{N}$ (from top to bottom). In blue: The weighted Chebyshev polynomials of the second kind $-V_k(\frac{G_1}{A_1}x_1)$ are shown. In red: The imaginary part of the system function components $\tilde{s}_k(x_1) = s_{1k}(x_1, 0, 0)$ is shown for a sinusoidal drive field $\boldsymbol{H}^{\text{D}}(t)$. In green: The one-dimensional magnitude spectra, i.e., $\hat{\tilde{s}}_k(\omega_{x_1}) = \mathcal{F}\{\tilde{s}_k(x_1)\}$. Please note that all the functions shown have been normalized so that the maximum absolute value is one.

stronger blurring. This can also be seen in the corresponding magnitude spectra, which show that a larger particle diameter leads to a less pronounced drop in the spatial frequency spectra. It can also be observed that the system function components $k > 1$ have a bandpass characteristic and the passband shifts to a higher frequency range as k increases. A similar figure was first shown in [F8].

7.2 Fourier Representation for Two-Dimensional Lissajous Trajectories

In this section, two-dimensional Lissajous FFP-trajectories are considered. This is the first multidimensional excitation studied in this thesis for MPI. In [81] it was conjectured that the system function components of MPI are related to tensor products of Chebyshev polynomials of the second kind. With the proof in [F1] the exact connection could be uncovered. This proof is shown here, with included phase shifts.

Definition 7.2: Two-dimensional excitation

Let $N_\mathrm{B} \in \mathbb{N}$ be a frequency divider with $N_\mathrm{B} \geq 2$ and let $f_\mathrm{B} > 0$ be an arbitrary basis frequency of an MPI scanner. Then the excitation frequencies for the two-dimensional Lissajous FFP-trajectory are given by $f_1 = \frac{f_\mathrm{B}}{N_\mathrm{B}}$ and $f_2 = \frac{f_\mathrm{B}}{N_\mathrm{B}-1}$. The corresponding angular frequencies are $\omega_1 = 2\pi f_1$ and $\omega_2 = 2\pi f_2$, respectively. The two-dimensional drive field can be expressed as

$$\boldsymbol{H}^\mathrm{D}(t) = \begin{pmatrix} -A_1 \sin(\omega_1 t + \varphi_1) \\ -A_2 \sin(\omega_2 t + \varphi_2) \\ -c_3 \end{pmatrix}, \tag{7.11}$$

where $A_1, A_2 \in \mathbb{R}$ denote the drive-field amplitudes, $\varphi_1, \varphi_2 \in [0, 2\pi)$ are the phase shifts, and $c_3 \in \mathbb{R}$ is a time-independent drive-field offset in the third dimension. The homogeneous selection field $\boldsymbol{H}^\mathrm{S}(\boldsymbol{x}) = \boldsymbol{G}\boldsymbol{x}$ of the MPI scanner has a gradient matrix $\boldsymbol{G} \in \mathbb{R}^{3\times 3}$ as in (7.1).

Following (2.25), the position of the FFP is given by

$$\boldsymbol{x}_\mathrm{FFP}(t) = -\boldsymbol{G}^{-1}\boldsymbol{H}^\mathrm{D}(t), \tag{7.12}$$

where the trajectory is periodic with period length $T_\mathrm{D} = \frac{1}{f_\mathrm{D}} = \frac{N_\mathrm{B}(N_\mathrm{B}-1)}{f_\mathrm{B}}$.

A direct expression for Fourier series coefficients of the MPI system function $\boldsymbol{s}(\boldsymbol{x}, t)$ is given in the following theorem.

Theorem 7.2

The Fourier series coefficients $\boldsymbol{s}_k : \mathbb{R}^3 \to \mathbb{C}^3$ of the MPI system function for a two-dimensional Lissajous FFP-trajectory with the phase shifts $\varphi_1, \varphi_2 \in [0, 2\pi)$ and $k \in \mathbb{Z}\backslash\{0\}$ can be expressed in terms of tensor products of $V_\ell : \mathbb{R} \to \mathbb{R}$ convolved along each spatial dimension with the spatial derivative of the Langevin function $\mathscr{L} : \mathbb{R}^3 \to \mathbb{R}^3$ by

$$\begin{aligned}\boldsymbol{s}_k(\boldsymbol{x}) = \sum_{\lambda\in\mathbb{Z}} \frac{(-\mathrm{i})^{\lambda+1}\omega_k \mathrm{e}^{\mathrm{i}\theta_k(\lambda)}}{\pi^2} \frac{\operatorname{sgn}(A_1A_2)}{\operatorname{sgn}(G_1G_2)} \\ \times \int_{\mathbb{R}^2} \left[\frac{\partial^2}{\partial z_1 \partial z_2} \mathscr{L}\left(\beta \boldsymbol{G} \begin{pmatrix} z_1 \\ z_2 \\ x_3 - \frac{c_3}{G_3} \end{pmatrix} \right) \right]_{\substack{z_1 = x_1 - u_1 \\ z_2 = x_2 - u_2}} \\ \times V_{n_k(\lambda)}\left(\frac{G_1}{A_1}u_1\right) V_{m_k(\lambda)}\left(\frac{G_2}{A_2}u_2\right) \mathrm{d}u_1 \, \mathrm{d}u_2,\end{aligned} \tag{7.13}$$

where $n_k(\lambda) = -k + \lambda N_\mathrm{B}$, $m_k(\lambda) = k - \lambda(N_\mathrm{B} - 1)$, $\theta_k(\lambda) = n_k(\lambda)\varphi_1 + m_k(\lambda)\varphi_2$,

$$V_n(\xi) = \begin{cases} \operatorname{rect}\left(\frac{\xi}{2}\right) \left(-\frac{U_{|n|-1}(\xi)\sqrt{1-\xi^2}}{|n|} \right) & \text{if } |n| > 0 \\ \frac{\pi}{2} \operatorname{sgn}(\xi + 1) - \operatorname{rect}\left(\frac{\xi}{2}\right) \arccos(\xi) & \text{if } n = 0, \end{cases}$$

and $U_\ell(\xi)$ denotes the Chebyshev polynomial of the second kind with degree $\ell \in \mathbb{N}_0$.

Equivalently, the spatial Fourier domain representation of $\boldsymbol{s}_k(\boldsymbol{x})$ can be expressed as

$$\begin{aligned}\hat{\boldsymbol{s}}_k(\boldsymbol{\omega_x}) = \sum_{\lambda=-\infty}^{\infty} (-1)^{\lambda+1} \mathrm{i}\omega_k \mathrm{e}^{\mathrm{i}\theta_k(\lambda)} \frac{\hat{\mathscr{L}}\left(\frac{\boldsymbol{G}^{-\mathsf{T}}\boldsymbol{\omega_x}}{\beta}\right)}{|\det(\beta \boldsymbol{G})|} \\ \times J_{n_k(\lambda)}\left(\omega_{x_1}\frac{A_1}{G_1}\right) J_{m_k(\lambda)}\left(\omega_{x_2}\frac{A_2}{G_2}\right) \mathrm{e}^{-\mathrm{i}\omega_{x_3}\frac{c_z}{G_z}},\end{aligned} \tag{7.14}$$

where $J_\ell(\xi)$ denotes the ℓ-th Bessel function of the first kind and $\hat{\mathscr{L}} : \mathbb{R}^3 \to \mathbb{C}^3$ is given by

$$\hat{\mathscr{L}}(\boldsymbol{\omega_x}) = -4\pi^2 \mathrm{i} \frac{(\pi\|\boldsymbol{\omega_x}\| + 1)\,\mathrm{e}^{\pi\|\boldsymbol{\omega_x}\|} - 1}{\|\boldsymbol{\omega_x}\|^2 \left(\mathrm{e}^{\pi\|\boldsymbol{\omega_x}\|} - 1\right)^2} \frac{\boldsymbol{\omega_x}}{\|\boldsymbol{\omega_x}\|}.$$

For $k = 0$ it holds that $\boldsymbol{s}_0(\boldsymbol{x}) = \boldsymbol{0}$ and $\hat{\boldsymbol{s}}_0(\boldsymbol{\omega_x}) = \boldsymbol{0}$.

This theorem is proven in several steps. First, an expression for the mapping function $P(\boldsymbol{\omega}_{\boldsymbol{x}}, k)$ introduced in (6.7) is derived for the special case of a two-dimensional Lissajous FFP-trajectory. The result is contained in the following lemma.

Lemma 7.1. *The mapping function $P : \mathbb{R}^3 \times \mathbb{Z} \to \mathbb{C}$ for the two-dimensional Lissajous FFP-trajectory $\boldsymbol{x}_{\mathrm{FFP}} : \mathbb{R} \to \mathbb{R}^3$ in Theorem 6.1 is given by*

$$P(\boldsymbol{\omega}_{\boldsymbol{x}}, k) = \sum_{n,m\in\mathbb{Z}} \left[\mathrm{e}^{\mathrm{i}(n\varphi_1 + m\varphi_2)} J_n\left(\omega_{x_1}\frac{A_1}{G_1}\right) J_m\left(\omega_{x_2}\frac{A_2}{G_2}\right) \times \delta_{(n(N_{\mathrm{B}}-1)+mN_{\mathrm{B}},\, k)} \right] \mathrm{e}^{\mathrm{i}\omega_{x_3}\frac{c_3}{G_3}}. \tag{7.15}$$

Proof of Lemma 7.1. To confirm (7.15), $P(\boldsymbol{\omega}_{\boldsymbol{x}}, k)$ is considered according to (6.7),

$$P(\boldsymbol{\omega}_{\boldsymbol{x}}, k) = \frac{1}{2\pi}\int_{-\pi}^{\pi} \mathrm{e}^{\mathrm{i}\boldsymbol{\omega}_{\boldsymbol{x}}^{\mathsf{T}}\boldsymbol{x}_{\mathrm{FFP}}\left(\frac{z}{2\pi f_{\mathrm{D}}}\right)} \mathrm{e}^{-\mathrm{i}kz}\,\mathrm{d}z. \tag{7.16}$$

Using the particular Lissajous FFP-trajectory from (7.12), it turns out for the position of the FFP that

$$\boldsymbol{x}_{\mathrm{FFP}}\left(\frac{z}{2\pi f_{\mathrm{D}}}\right) = \begin{pmatrix} \frac{A_1}{G_1}\sin\left(\frac{f_1}{f_{\mathrm{D}}}z + \varphi_1\right) \\ \frac{A_2}{G_2}\sin\left(\frac{f_2}{f_{\mathrm{D}}}z + \varphi_2\right) \\ \frac{c_3}{G_3} \end{pmatrix} = \begin{pmatrix} \frac{A_1}{G_1}\sin((N_{\mathrm{B}}-1)z + \varphi_1) \\ \frac{A_2}{G_2}\sin(N_{\mathrm{B}}z + \varphi_2) \\ \frac{c_3}{G_3} \end{pmatrix}. \tag{7.17}$$

With help of the Jacobi-Anger expansion [8, Ch. 7.2.4, (26)]

$$\mathrm{e}^{\mathrm{i}z\sin(\theta)} = \sum_{n=-\infty}^{\infty} J_n(z)\mathrm{e}^{\mathrm{i}n\theta},$$

the term to be integrated in (7.16) can be reformulated as

$$\begin{aligned} \mathrm{e}^{\mathrm{i}\boldsymbol{\omega}_{\boldsymbol{x}}^{\mathsf{T}}\boldsymbol{x}_{\mathrm{FFP}}\left(\frac{z}{2\pi f_{\mathrm{D}}}\right)}\mathrm{e}^{-\mathrm{i}kz} &= \mathrm{e}^{\mathrm{i}\omega_{x_1}\frac{A_1}{G_1}\sin((N_{\mathrm{B}}-1)z+\varphi_1)}\mathrm{e}^{\mathrm{i}\omega_{x_2}\frac{A_2}{G_2}\sin(N_{\mathrm{B}}z+\varphi_2)}\mathrm{e}^{\mathrm{i}\omega_{x_3}\frac{c_3}{G_3}}\mathrm{e}^{-\mathrm{i}kz} \\ &= \left(\sum_{n=-\infty}^{\infty}\mathrm{e}^{\mathrm{i}n\varphi_1}J_n\left(\omega_{x_1}\frac{A_1}{G_1}\right)\mathrm{e}^{\mathrm{i}n(N_{\mathrm{B}}-1)z}\right) \\ &\quad \times \left(\sum_{m=-\infty}^{\infty}\mathrm{e}^{\mathrm{i}m\varphi_2}J_m\left(\omega_{x_2}\frac{A_2}{G_2}\right)\mathrm{e}^{\mathrm{i}mN_{\mathrm{B}}z}\right)\cdot\mathrm{e}^{\mathrm{i}\omega_{x_3}\frac{c_3}{G_3}}\mathrm{e}^{-\mathrm{i}kz}. \end{aligned}$$

The series multiplication leads to

$$\mathrm{e}^{\mathrm{i}\boldsymbol{\omega}_{\boldsymbol{x}}^{\mathsf{T}}\boldsymbol{x}_{\mathrm{FFP}}\left(\frac{z}{2\pi f_{\mathrm{D}}}\right)}\mathrm{e}^{-\mathrm{i}kz} = \sum_{n=-\infty}^{\infty}\sum_{m=-\infty}^{\infty}\left[\mathrm{e}^{\mathrm{i}(n\varphi_1+m\varphi_2)}J_n\left(\omega_{x_1}\frac{A_1}{G_1}\right)J_m\left(\omega_{x_2}\frac{A_2}{G_2}\right)\right.$$
$$\left.\times\,\mathrm{e}^{\mathrm{i}[n(N_{\mathrm{B}}-1)+mN_{\mathrm{B}}-k]z}\right]\mathrm{e}^{\mathrm{i}\omega_{x_3}\frac{c_3}{G_3}}.$$

Using this result, (7.16) yields

$$\begin{aligned}P(\boldsymbol{\omega}_{\boldsymbol{x}},k) &= \sum_{n,m\in\mathbb{Z}}\left[\mathrm{e}^{\mathrm{i}(n\varphi_1+m\varphi_2)}J_n\left(\omega_{x_1}\frac{A_1}{G_1}\right)J_m\left(\omega_{x_2}\frac{A_2}{G_2}\right)\right.\\ &\qquad\left.\times\,\frac{1}{2\pi}\int_{-\pi}^{\pi}\mathrm{e}^{\mathrm{i}[n(N_{\mathrm{B}}-1)+mN_{\mathrm{B}}-k]z}\,\mathrm{d}z\right]\mathrm{e}^{\mathrm{i}\omega_{x_3}\frac{c_3}{G_3}}\\ &= \sum_{n,m\in\mathbb{Z}}\left[\mathrm{e}^{\mathrm{i}(n\varphi_1+m\varphi_2)}J_n\left(\omega_{x_1}\frac{A_1}{G_1}\right)J_m\left(\omega_{x_2}\frac{A_2}{G_2}\right)\right.\\ &\qquad\left.\times\,\delta_{(n(N_{\mathrm{B}}-1)+mN_{\mathrm{B}},\,k)}\right]\mathrm{e}^{\mathrm{i}\omega_{x_3}\frac{c_3}{G_3}}.\end{aligned}$$

The comparison of the last result with (7.15) confirms Lemma 7.1. □

The next lemma is provided to remove the double series in the mapping function $P(\boldsymbol{\omega}_{\boldsymbol{x}},k)$.

Lemma 7.2. *The constraint*

$$n(N_{\mathrm{B}}-1)+mN_{\mathrm{B}} = k \tag{7.18}$$

with $n,m,k\in\mathbb{Z}$ is fulfilled for the following line equation

$$\begin{pmatrix}n\\m\end{pmatrix} = \begin{pmatrix}-k\\k\end{pmatrix}+\lambda\begin{pmatrix}N_{\mathrm{B}}\\1-N_{\mathrm{B}}\end{pmatrix}, \tag{7.19}$$

with $\lambda\in\mathbb{Z}$.

Proof of Lemma 7.2. To prove the lemma, (7.19) is inserted into (7.18). This yields

$$\begin{aligned} n(N_\mathrm{B}-1)+mN_\mathrm{B} &= (-k+\lambda N_\mathrm{B})(N_\mathrm{B}-1)+(k-\lambda(N_\mathrm{B}-1))N_\mathrm{B} \\ &= -k(N_\mathrm{B}-1)+kN_\mathrm{B}+\lambda N_\mathrm{B}(N_\mathrm{B}-1)-\lambda(N_\mathrm{B}-1)N_\mathrm{B} \\ &= k. \end{aligned}$$

Assuming $N_\mathrm{B} \geq 2$, $N_\mathrm{B} \in \mathbb{N}$, it remains to show that only $\lambda \in \mathbb{Z}$ guarantees that $n, m \in \mathbb{Z}$. Let us, therefore, consider $\lambda \in \mathbb{R}$ with $\lambda = \hat{\lambda} + \beta$ and $\beta \in [0,1]$ such that $\hat{\lambda}, n, m \in \mathbb{Z}$. Then the following two constraints have to hold:

$$\begin{aligned} n &= -k + \hat{\lambda}N_\mathrm{B} + \beta N_\mathrm{B} \in \mathbb{Z}, \\ m &= k - \hat{\lambda}(N_\mathrm{B}-1) - \beta(N_\mathrm{B}-1) \in \mathbb{Z}. \end{aligned}$$

By adding up both constraints one obtains

$$n + m = \hat{\lambda} + \beta \in \mathbb{Z}.$$

For $n, m, \hat{\lambda} \in \mathbb{Z}$, only $\beta = 0$ and $\beta = 1$ are valid solutions, confirming that $\lambda \in \mathbb{Z}$. □

Based on Lemma 7.2, the expression for $P(\boldsymbol{\omega}_{\boldsymbol{x}}, k)$ in Lemma 7.1 can be simplified, which is given in the following corollary.

Corollary 7.3. *The mapping function $P : \mathbb{R}^3 \times \mathbb{Z} \to \mathbb{C}$ for the two-dimensional Lissajous FFP-trajectory $\boldsymbol{x}_\mathrm{FFP} : \mathbb{R} \to \mathbb{R}^3$ is simplified to*

$$P(\boldsymbol{\omega}_{\boldsymbol{x}}, k) = \left(\sum_{\lambda=-\infty}^{\infty} \mathrm{e}^{\mathrm{i}\theta_k(\lambda)} J_{n_k(\lambda)}\left(\omega_{x_1}\frac{A_1}{G_1}\right) J_{m_k(\lambda)}\left(\omega_{x_2}\frac{A_2}{G_2}\right) \right) \mathrm{e}^{\mathrm{i}\omega_{x_3}\frac{c_3}{G_3}} \tag{7.20}$$

with $n_k(\lambda) = -k + \lambda N_\mathrm{B}$, $m_k(\lambda) = k - \lambda(N_\mathrm{B}-1)$, and $\theta_k(\lambda) = n_k(\lambda)\varphi_1 + m_k(\lambda)\varphi_2$.

Returning to the frequency representation of the three-dimensional MPI system equation with the two-dimensional excitation $\boldsymbol{H}^\mathrm{D}(t)$ and using the same arguments as in the proof of Theorem 7.1 in (7.8), (7.9), (7.10), and using $(-1)^{n_k(\lambda)}(-1)^{m_k(\lambda)} = (-1)^\lambda$, the three-dimensional system function in Fourier domain is given by (7.14).

It remains to show that the components of $\hat{\boldsymbol{s}}_k(\boldsymbol{\omega_x})$, denoted as $\hat{s}_{\nu k}(\boldsymbol{\omega_x})$, are in $L^1(\mathbb{R}^3)$. For this purpose, the Lemma 6.10 is used and it is assumed that $|k| > 0$. The estimate in (6.47) is scale-invariant with respect to ω_k, $\boldsymbol{G}^{-\mathsf{T}}$, β, $\frac{A_1}{G_1}$, $\frac{A_2}{G_2}$, and $\frac{c_3}{G_3}$ up to a constant factor. Additionally, all factors can be combined into constants $C_1 > 0$ and $C_2 > 0$. Using $\|\mathrm{e}^{-\mathrm{i}\omega_{x_3}\alpha_z}\|_{L^\infty} = 1$ and the substitution $\boldsymbol{z} = \frac{\boldsymbol{G}^{-\mathsf{T}}\boldsymbol{\omega_x}}{\beta}$ it can be shown that

$$\begin{aligned}
\|\hat{s}_{\nu k}\|_{L^1} &\leq C_1 \sum_{\lambda\in\mathbb{Z}} \int_{\mathbb{R}^3} \left| \frac{\hat{\mathscr{L}}_\nu\left(\frac{\boldsymbol{G}^{-\mathsf{T}}\boldsymbol{\omega_x}}{\beta}\right)}{|\det(\beta\boldsymbol{G})|} J_{n_k(\lambda)}\left(\omega_{x_1}\frac{A_1}{G_1}\right) J_{m_k(\lambda)}\left(\omega_{x_2}\frac{A_2}{G_2}\right) \right| \mathrm{d}\boldsymbol{\omega_x} \\
&= C_1 \sum_{\lambda\in\mathbb{Z}} \int_{\mathbb{R}^3} \left| \hat{\mathscr{L}}_\nu(\boldsymbol{z}) J_{-k+\lambda N_\mathrm{B}}(A_1 z_1)\, J_{k-\lambda(N_\mathrm{B}-1)}(A_2 z_2) \right| \mathrm{d}\boldsymbol{z} \\
&\leq C_2 \sum_{\lambda\in\mathbb{Z}} \frac{1}{\max(1, |k-\lambda N_\mathrm{B}|^{\frac{4}{3}}) \max(1, |k-\lambda(N_\mathrm{B}-1)|^{\frac{4}{3}})} \\
&< \infty.
\end{aligned}$$

If $|k| > 0$ there is no $\lambda \in \mathbb{Z}$ such that $-k + \lambda N_\mathrm{B} = 0$ and $k - \lambda(N_\mathrm{B} - 1) = 0$. For $k = 0$, the series (7.14) is not valid without further assumptions, because it then formally contains a term for which Lemma 6.10 is no longer applicable. However, by arguing that the measured voltage signal is zero mean, we may set $\boldsymbol{s}_0(\boldsymbol{x}) = \boldsymbol{0}$ and $\hat{\boldsymbol{s}}_0(\boldsymbol{\omega_x}) = \boldsymbol{0}$. This shows that the series is well defined and that the system function $\hat{\boldsymbol{s}}_k(\boldsymbol{\omega_x})$ is in $L^1(\mathbb{R}^3)$, which makes it possible to define the inverse Fourier transform for each $k \in \mathbb{Z}$.

The terms in the series expansion (7.14) are similar to $\hat{a}_\nu^{\mathrm{2D}}(\boldsymbol{\omega_x})$ in Lemma 6.11 up to the factors $(-1)^{\lambda+1}\mathrm{i}\omega_k \mathrm{e}^{\mathrm{i}\theta_k(\lambda)}$ and, using the fact that the Fourier transform is a linear operator, the inverse Fourier transform of $\hat{\boldsymbol{s}}_k(\boldsymbol{\omega_x})$ can be performed and one obtains

$$\begin{aligned}
\boldsymbol{s}_k(\boldsymbol{x}) = \sum_{\lambda\in\mathbb{Z}} \frac{(-\mathrm{i})^{\lambda+1}\omega_k \mathrm{e}^{\mathrm{i}\theta_k(\lambda)}}{\pi^2} \frac{\operatorname{sgn}(A_1 A_2)}{\operatorname{sgn}(G_1 G_2)} \\
\times \int_{\mathbb{R}^2} \left[\frac{\partial^2}{\partial z_1 \partial z_2} \boldsymbol{\mathscr{L}}\left(\beta\boldsymbol{G}\begin{pmatrix} z_1 \\ z_2 \\ x_3 - \frac{c_3}{G_3} \end{pmatrix}\right) \right]_{\substack{z_1 = x_1 - u_1 \\ z_2 = x_2 - u_2}} \\
\times V_{n_k(\lambda)}\left(\frac{G_1}{A_1}u_1\right) V_{m_k(\lambda)}\left(\frac{G_2}{A_2}u_2\right) \mathrm{d}u_1\, \mathrm{d}u_2.
\end{aligned}$$

Finally, (7.13) is confirmed, and the proof of Theorem 7.2 is complete. □

7.2.1 Numerical Evaluation

The numerical results presented here come from [F1]. The two-dimensional excitation model is evaluated for the system function on the x_1-receive path, since the x_2-receive path is simulated numerically in a very similar way and is therefore excluded here for the sake of simplicity. To approximate the infinite series in (7.13), an "optimal" λ^* was estimated by

$$\lambda^* = \arg\min_{\lambda} |k - \lambda N_\mathrm{B}| + |k - \lambda(N_\mathrm{B} - 1)|$$

corresponding to the minimal mixing order [31, 53] and then

$$\begin{aligned} s_{1k}(\boldsymbol{x}) \approx \sum_{\lambda=-60+\lambda^*}^{60+\lambda^*} & \frac{(-\mathrm{i})^{\lambda+1}\omega_k}{\pi^2} \\ & \times \int_{\mathbb{R}^2} \left[\frac{\partial^2}{\partial z_1 \partial z_2} \mathscr{L}_1 \left(\beta \boldsymbol{G} \begin{pmatrix} z_1 \\ z_2 \\ 0 \end{pmatrix} \right) \right]_{\substack{z_1 = x_1 - u_1 \\ z_2 = x_2 - u_2}} \\ & \times V_{-k+\lambda N_\mathrm{B}} \left(\frac{G_1}{A_1} u_1 \right) V_{k-\lambda(N_\mathrm{B}-1)} \left(\frac{G_2}{A_2} u_2 \right) \, \mathrm{d}u_1 \, \mathrm{d}u_2. \end{aligned} \tag{7.21}$$

In [F12, C1] it was shown that in practice only one or two series terms in (7.21) contribute significantly to the series for a given $k \in \mathbb{Z}$, so that the series is approximated quite well by 121 series terms.

Table 7.1 defines all additional simulation parameters. For the simulation of the temporal model in (6.3), the sampling distance Δt for one period of the FFP-trajectory is selected along the temporal dimension so that the sampled signal has 6001 time taps. The frequency components are then approximated using the discrete Fourier transform $s_{1k}^{\mathrm{FFT}}(\boldsymbol{x}_n)$, whereby only frequencies up to $k = 1000$ were used for the numerical evaluation. The spatial sampling distance $\Delta_1 x_i$ for the temporal model results in a grid of size 365×365 in the drive-field FOV.

The frequency model (7.21) ($s_{1k}^{\mathrm{approx}}(\boldsymbol{x}_\ell)$) was simulated up to $k = 1000$ with the spatial sampling distance $\Delta_2 x_i$, which was an 8 times finer grid than for sampling with $\Delta_1 x_i$. The finer sampling with the sampling distance $\Delta_1 x_i$ was used to reduce the errors due to the discretization of the convolution integral in (7.21). In addition, to avoid errors at

Table 7.1: Parameters inside the numerical validation.

Parameter		Value
Vacuum permeability	μ_0	$4\pi \cdot 10^{-7}$ H/m
Boltzmann constant	k_B	$1.380649 \cdot 10^{-23}$ J/K
Particle		
Particle core diameter	D	30 nm
Particle core volume	V_C	$\frac{\pi}{6}D^3$
Temperature	T_P	293 K
Sat. magnetization	M_S	474000 J/m^3/T
	β	$\frac{\mu_0 V_\mathrm{C} M_\mathrm{S}}{k_\mathrm{B} T_\mathrm{P}}$
Scanner Parameter		
Gradient strength	$G_{\{1,2\}}$	1 T/m/μ_0
	G_3	-2 T/m/μ_0
Excitation amplitudes	$A_{\{1,2\}}$	0.0125 T/μ_0
Excitation frequencies	f_1	$2.5/96 \cdot 10^6$ Hz
	f_2	$2.5/93 \cdot 10^6$ Hz
FFP Duration	T_D	$1.1904 \cdot 10^{-3}$ s
Simulation		
Drive-field FOV	Ω_DF	$[-12.5, 12.5]^2$ mm^2
FOV	Ω	$[-32.5, 32.5]^2$ mm^2
Temporal sampling	Δt	$2 \cdot 10^{-7}$ s
Spatial sampling	$\Delta_1 x_i$	$6.36 \cdot 10^{-2}$ mm
	$\Delta_2 x_i$	$7.95 \cdot 10^{-3}$ mm
Max. frequency index	k_max	1000

the boundaries of the drive-field FOV in the simulation, the convolution was simulated in the range of $[-32.5, 32.5]^2$ mm^2. The model $s_{1k}^{\text{approx}}(\boldsymbol{x}_\ell)$ was then downsampled and cropped so that the range of the approximation of the new model $s_{1k}^{\text{approx}}(\boldsymbol{x}_n)$ matches the "old" model $s_{1k}^{\text{FFT}}(\boldsymbol{x}_n)$.

Finally, the spatial frequency model (7.14) was simulated using the two-dimensional Fourier transform of the Langevin function from (6.38). Spatial frequencies were considered in the range of ± 7860.3 cycles/m in each dimension. The model was discretized to 6133×6133 sampling points. The approximation was then transformed back into the spatial domain and matched with the spatial positions against $s_{1k}^{\text{FFT}}(\boldsymbol{x}_n)$.

In order to obtain an objective quality criterion the mean relative error in relation to the temporal model (6.3) was calculated for the other two models:

$$\text{MeRE}(k) = \sqrt{\frac{\sum_n \left| s_{1k}^{\text{FFT}}(\boldsymbol{x}_n) - s_{1k}^{\text{approx}}(\boldsymbol{x}_n) \right|^2}{\sum_n \left| s_{1k}^{\text{FFT}}(\boldsymbol{x}_n) \right|^2}},$$

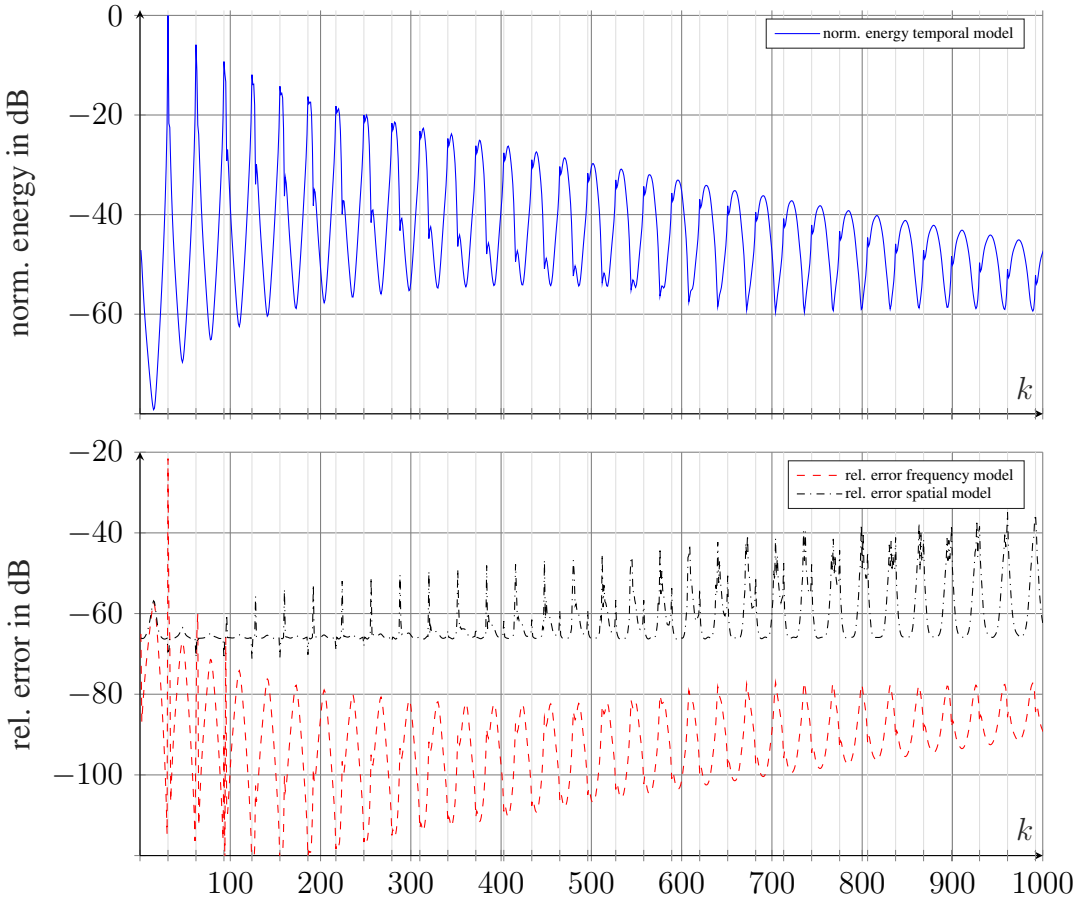

Figure 7.2: Upper plot: The normalized energy (norm. energy) of $s_{1k}^{\mathrm{FFT}}(\boldsymbol{x}_n)$ as a function of k. Lower plot: The mean relative error as a function of k for the system function components of the frequency model (7.14) and the spatial model (7.21) with respect to $s_{1k}^{\mathrm{FFT}}(\boldsymbol{x}_n)$. The function $s_{1k}^{\mathrm{FFT}}(\boldsymbol{x}_n)$ was derived from the temporal model (6.3).

where $s_{1k}^{\mathrm{approx}}(\boldsymbol{x}_n)$ either stems from the model (7.21) or from (7.14). In addition, the normalized energy (norm. energy) of the system functions components was calculated using

$$\mathrm{normEng}_1(k) = \frac{\sum_n \left|s_{1k}^{\mathrm{FFT}}(\boldsymbol{x}_n)\right|^2}{\max_{k\in\{0,1,\ldots,1000\}} \sum_n \left|s_{1k}^{\mathrm{FFT}}(\boldsymbol{x}_n)\right|^2},$$

which means that the energy is normalized so that the largest value in $\mathrm{normEng}(k)$ is one. Figure 7.2 shows in the upper plot the normalized energy of $s_{1k}^{\mathrm{FFT}}(\boldsymbol{x}_n)$ and in the lower plot the relative error (rel. error) for all k up to $k = 1000$ in dB. It can be noticed that the errors for both models are generally quite small. They usually range between -100 and -40 dB. In the longer trend, the relative error increases as the temporal frequency

index k increases. In addition, an oscillating behavior can be observed, which is related to the energy of the system function components, as can be seen in the upper plot in Figure 7.2. Note that the energy itself is again related to the lowest orders for $n_k(\lambda)$ and $m_k(\lambda)$ (see (7.13) and (7.14)), and was investigated in more detail in [F12, C1]. The simulation of the frequency model generally had a much lower relative error than the simulated convolution with the Chebyshev polynomials in the spatial domain. This is due to the strong oscillation of the terms $U_n(x)\sqrt{1-x^2}$ for large n. It can be seen that some system function components of the frequency model have a high relative error, in particular the component $k = 31$. The reason is the singularity at the spatial frequency $\boldsymbol{\omega_x} = \mathbf{0}$ (see Figure 6.6), which is not removed by a multiplication with a tensor product of Bessel functions of the form $J_1(\frac{G_1}{A_1}\omega_{x_1})J_0(\frac{G_2}{A_2}\omega_{x_2})$, which occurs within the series in (7.21). Overall, the simulations confirm the calculations and show that the time, space and frequency models are equivalent.

7.2.2 Mixing Orders, Spatial Frequencies, and Energy

In this part of the work, a connection between the spatial mixing order [31, 51, 81], the spatial frequency representation developed in this chapter and the energy of the system function components is to be established and investigated. The Figures 7.3 and 7.4 show functions from Theorem 7.2 for a sinusoidal drive field, i.e., $\varphi_1 = \varphi_2 = c_3 = 0$. Figure 7.3 shows the magnitude of $\tilde{s}_k(x_1, x_2) = s_{1k}(x_1, x_2, 0)$ (cf. (7.13)) for different system function components $k \in \mathbb{Z}$. The system function components are ordered with respect to the mixing order, i.e., $k = (N_\mathrm{B} - 1)m_x + N_\mathrm{B}m_y$ for $m_x, m_y \in \{1, 3, 5, 7, 9\}$ [51]. A relationship to weighted tensor products of Chebyshev polynomials can be observed and was firstly postulated in [81]. In contrast, the Theorem 7.2 reveals that in reality there are infinitely many tensor products of weighted Chebyshev polynomials of the second kind, which are convolved with a spatial derivative of the Langevin function. Nevertheless, it was shown in [F12] that only one or two series terms contribute significantly to the series. The representation of the mixing orders in Figure 7.3 shows that the number of wave hills and zero crossings increases with increasing mixing orders m_x and m_y. It can also be observed that with increasing mixing orders m_x and m_y the large local contributions in the system function components tend to be in the region of the drive-field FOV. This is highlighted in Figure 7.3 by the central quadratic region using the grids. Therefore, if an SPIO distribution lies outside the drive-field FOV, it can only

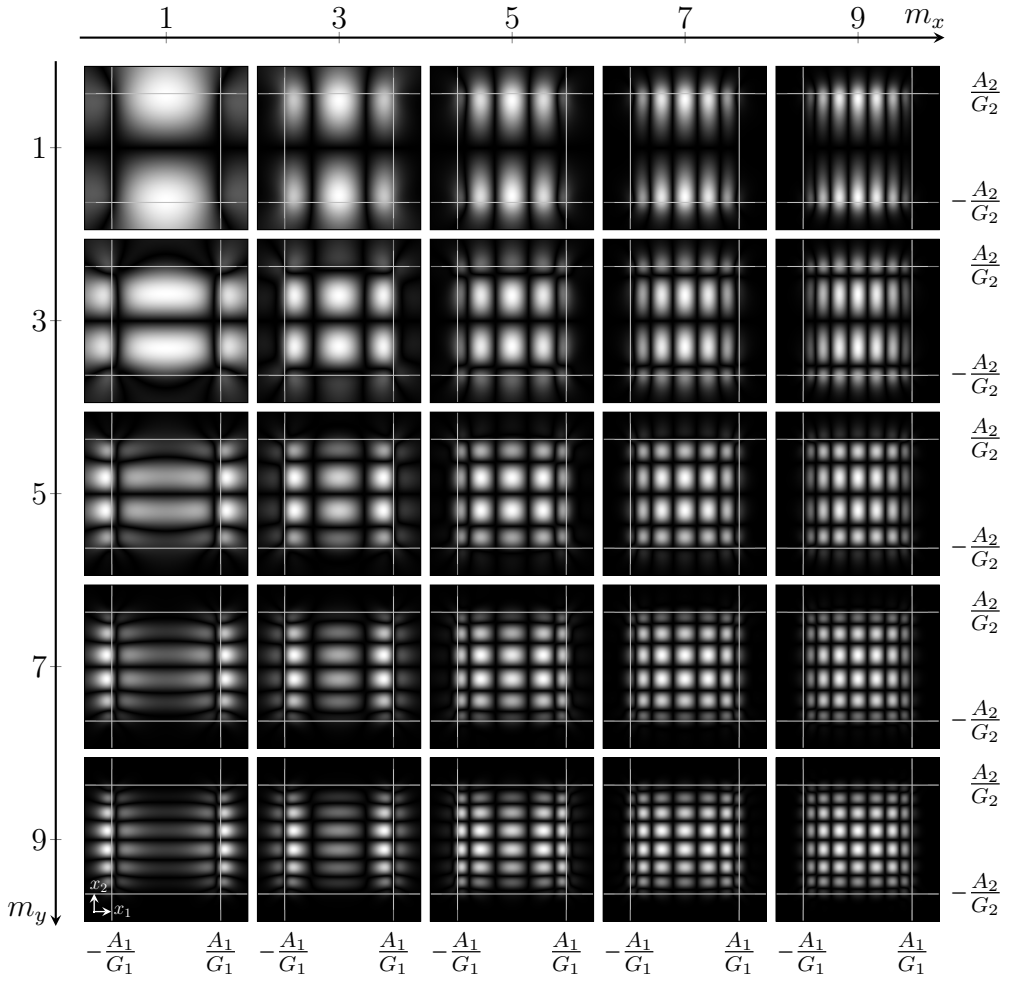

Figure 7.3: The magnitude of the system function components $\tilde{s}_k(x_1, x_2) = s_{1k}(x_1, x_2, 0)$ for a two-dimensional sinusoidal Lissajous FFP-trajectory, i.e., $\varphi_1 = \varphi_2 = c_3 = 0$, and SPIOs with a particle diameter of $D = 30\,\text{nm}$. The system function components are ordered with respect to their mixing orders $m_x, m_y \in \{1, 3, 5, 7, 9\}$ by $k = 31m_x + 32m_y$, as proposed in [51]. For each individual system function component, the largest value corresponds to the white color, while the black color corresponds to zero.

contribute to frequency components in the voltage signal that are related to low mixing orders.

Figure 7.4 shows the corresponding spatial magnitude spectra for the system function components in Figure 7.3, where only the first quadrant is shown, as all other quadrants are only mirrored versions of the first quadrant due to the symmetry of the functions involved. Note that the two-dimensional Fourier transform can be calculated

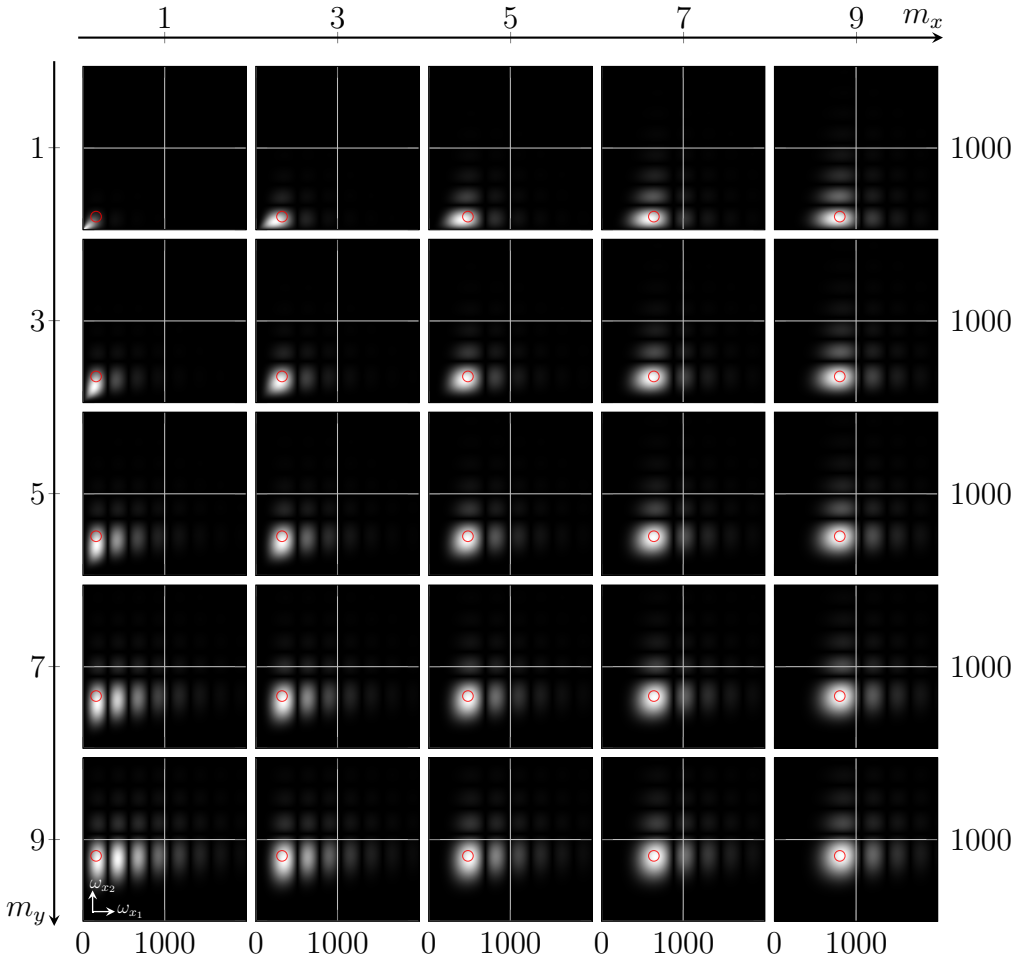

Figure 7.4: The magnitude of the spatial Fourier transforms of system function components $\tilde{s}_k(x_1, x_2)$ from Figure 7.3, i.e., $\hat{\tilde{s}}_k(\omega_{x_1}, \omega_{x_2}) = \mathcal{F}\{\tilde{s}_k(x_1, x_2)\}$, ordered with respect to their mixing orders $m_x, m_y \in \{1, 3, 5, 7, 9\}$ by $k = 31m_x + 32m_y$. In each subplot, the coordinates $(\omega_{x_1}, \omega_{x_2}) = (\frac{G_1}{A_1}(m_x + 1), \frac{G_2}{A_2}(m_y + 1)$ are marked with a red circle.

by replacing the three-dimensional Fourier transform $\hat{\mathscr{L}} : \mathbb{R}^3 \to \mathbb{C}^3$ from (6.39) by the two-dimensional version $\hat{\mathscr{L}} : \mathbb{R}^2 \to \mathbb{C}^2$ from (6.38). It can be observed that the spectra are the result of a multiplication between a series of tensor products of Bessel functions with bandpass characteristics (see Figure 5.4) and the Fourier transform of the Langevin function $\hat{\mathscr{L}}(\frac{\boldsymbol{G}^{-\mathsf{T}}\boldsymbol{\omega}_{\boldsymbol{x}}}{\beta})$ with lowpass characteristic. Note that with increasing mixing orders m_x and m_y the main contribution of $\hat{\tilde{s}}_k(\omega_{x_1}, \omega_{x_2})$ shifts to the higher spatial frequencies ω_{x_1} and ω_{x_2}.

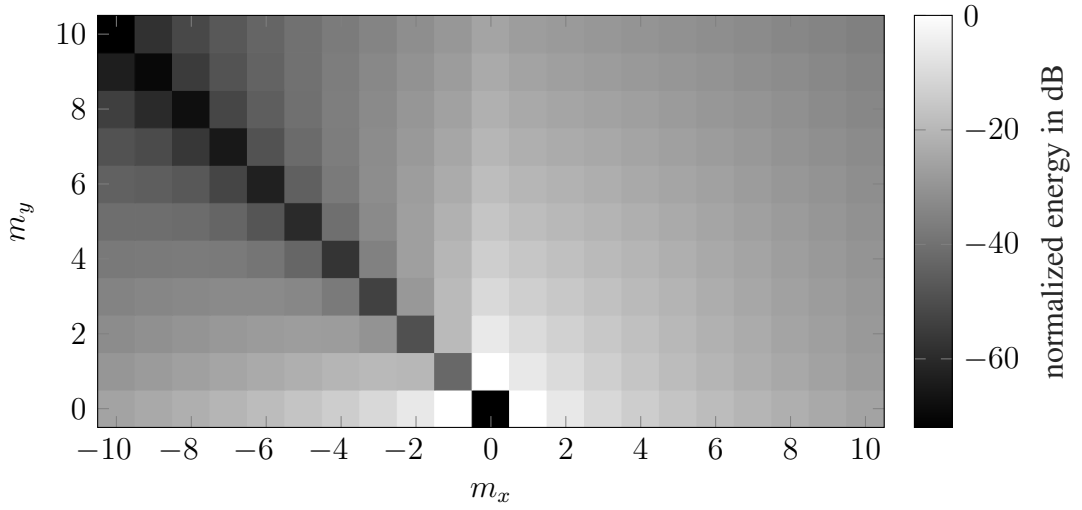

Figure 7.5: The normalized energy (7.22) of the system function components ordered with respect to their mixing orders $m_x \in \{-10, -9, \ldots, 10\}$ and $m_y \in \{0, 1, \ldots, 10\}$ by $k = 31m_x + 32m_y$.

The behavior of the spectrum can be explained by the exponential decay of $\hat{\mathscr{L}}(\frac{\boldsymbol{G}^{\mathsf{T}}\boldsymbol{\omega}_x}{\beta})$ (see Figure 6.6), i.e., only Bessel functions $J_n(\xi)$ with low orders $|n|$ in the series (7.14) can contribute significantly to the energy of the series. Since this behavior is also transferred to the spatial version in (7.13), this explains the observation in [81] and thus represents the starting point for the reduced model from [C1]. It is interesting to note that the Bessel functions have their global function maximum approximately in the vicinity of their order $|n|$, i.e., $|J_n(n)| = |J_n(-n)|$ is a large function value of the Bessel function. Thus, in Figure 6.6 (see the red circles), it can be seen that the maximal magnitude for $\hat{\tilde{s}}_k(\omega_{x_1}, \omega_{x_2})$ is proportional to $\omega_{x_1} = \frac{G_1}{A_1} m_x$ and $\omega_{x_2} = \frac{G_2}{A_2} m_y$. This confirms that the mixing orders are indeed directly related to the spatial frequencies.

The normalized energy of the system function components is given by

$$\text{normEng}(k) = \frac{\int_\Omega |s_{1k}(z_1, z_2, 0)|^2 + |s_{2k}(z_1, z_2, 0)|^2 \, \mathrm{d}\boldsymbol{z}}{\max_{k \in \mathbb{Z}} \int_\Omega |s_{1k}(z_1, z_2, 0)|^2 + |s_{2k}(z_1, z_2, 0)|^2 \, \mathrm{d}\boldsymbol{z}}. \tag{7.22}$$

According to [53], these can also be sorted based on their spatial mixing order, which is shown in Figure 7.5. In contrast to the figure in [53, Fig. 4.6], the negative values for m_x are also included here. The negative values for m_y are not shown here, as they can be derived directly from the positive m_y for reasons of symmetry. For the positive mixing orders $m_x, m_y \in \{0, 1, \ldots 10\}$ it can be seen that the energy decreases monotonically

with increasing m_x and m_y, which was also observed in [53]. However, if the negative m_x are included, there is a break in this relationship. The correlation that can be observed for the purely positive m_x is seemingly not present for the negative ones. This behavior can be fully described by (7.13), but the argumentation is postponed and first a closely related observation shall be discussed to further clarify the relationship between mixing orders and the obtained series expression in (7.13).

In [81] it was observed that in certain cases the same spatial pattern is encoded for two different frequency indices

$$k^{(1)} = (N_\mathrm{B} - 1)m_x^{(1)} + N_\mathrm{B} m_y^{(1)} \quad \text{and} \quad k^{(2)} = (N_\mathrm{B} - 1)m_x^{(2)} + N_\mathrm{B} m_y^{(2)},$$

with $|k^{(1)}| \neq |k^{(2)}|$ and $m_x^{(1)}, m_y^{(1)}, m_x^{(2)}, m_y^{(2)} \in \mathbb{Z}$, if it holds that $|m_x^{(1)}| = |m_x^{(2)}|$ and $|m_y^{(1)}| = |m_y^{(2)}|$. This observation can now also be explained. In [F12] it was shown that only one or two components contribute significantly to the energy, and in [C1] an efficient strategy for finding the series term with the largest energy contribution was derived. For a given frequency index $k \in \mathbb{Z}$, in particular also for the $k^{(i)}$ ($i \in \{1, 2\}$) belonging to the mixing orders, the minimum mixing order can be obtained by

$$m_x^{k^{(i)}} = -k^{(i)} + \lambda^{k^{(i)}} N_\mathrm{B} \quad \text{and} \quad m_y^{k^{(i)}} = k^{(i)} - \lambda^{k^{(i)}}(N_\mathrm{B} - 1),$$

with

$$\lambda^{k^{(i)}} = \underset{\lambda \in \mathbb{Z}}{\arg\min}(-k^{(i)} + \lambda N_\mathrm{B})^2 + (k^{(i)} - \lambda(N_\mathrm{B} - 1))^2.$$

Let us assume, without loss of generality, that $m_x^{(1)} \in \mathbb{N}$ and $m_y^{(1)} \in \mathbb{N}$ already represent minimal mixing orders and are always positive, i.e., $m_x^{(1)} = m_x^{k^{(1)}}$ and $m_y^{(1)} = m_y^{k^{(1)}}$. In order to fulfill the condition for $k^{(2)} \in \mathbb{Z}$ that $|k^{(2)}| \neq |k^{(1)}|$ applies, either $(m_x^{(2)}, m_y^{(2)}) = (-m_x^{(1)}, m_y^{(1)})$ or $(m_x^{(2)}, m_y^{(2)}) = (m_x^{(1)}, -m_y^{(1)})$ can be used. Note that the actual choice of $(m_x^{(2)}, m_y^{(2)})$ does not matter, since either the positive or the negative frequency index is used, both have the same magnitude and for a real-valued function $s_\nu(x, t)$ it holds that $s_{\nu k^{(2)}}(\boldsymbol{x}) = \left(s_{\nu, -k^{(2)}}(\boldsymbol{x})\right)^*$. In contrast to the observation in [81], however, the normalized series in (7.13) will actually be distinct:

$$\left| \frac{s_{\nu k^{(1)}}(\boldsymbol{x})}{\omega_{k^{(1)}}} \right| \neq \left| \frac{s_{\nu k^{(2)}}(\boldsymbol{x})}{\omega_{k^{(2)}}} \right|.$$

The connection between $s_{\nu k^{(1)}}(\boldsymbol{x})$ and $s_{\nu k^{(2)}}(\boldsymbol{x})$ is that they contain the same tensor product structure of the form $V_{m_x^{(1)}}(\xi_1)V_{m_y^{(1)}}(\xi_2) = V_{m_x^{(2)}}(\xi_1)V_{m_y^{(2)}}(\xi_2)$ in the series in (7.13), since $V_{-n}(\xi) = V_n(\xi)$ holds. Although $m_x^{k^{(1)}} = m_x^{(1)}$ and $m_y^{k^{(1)}} = m_y^{(1)}$ have already been constructed as minimal mixing orders, however, it may happen that $m_x^{k^{(2)}} \neq m_x^{(2)}$ and $m_y^{k^{(2)}} \neq m_y^{(2)}$ apply, i.e., one would observe a system function component that refers to the tensor product structure $V_{m_y^{k^{(2)}}}(\xi_1)V_{m_y^{k^{(2)}}}(\xi_2)$ instead of $V_{m_x^{(2)}}(\xi_1)V_{m_y^{(2)}}(\xi_2)$ for $k^{(2)}$ and a comparison of $s_{\nu k^{(1)}}(\boldsymbol{x})$ with $s_{\nu k^{(2)}}(\boldsymbol{x})$ would show a different spatial pattern. However, for the energy of the system function component with small mixing orders, as shown in Figure 7.5, it is the case that only one component in the series in (7.13) contributes significantly [F12] and if $m_x^{k^{(2)}} = m_x^{(2)}$ and $m_y^{k^{(2)}} = m_y^{(2)}$ also applies, the approximation

$$\left| \frac{s_{\nu k^{(1)}}(\boldsymbol{x})}{\omega_{k^{(1)}}} \right| \approx \left| \frac{s_{\nu k^{(2)}}(\boldsymbol{x})}{\omega_{k^{(2)}}} \right| \tag{7.23}$$

can be made. This also explains the observation from [81] that the "same" system function component is observed for different frequency indices $k^{(1)}$ and $k^{(2)}$. So if the approximation in (7.23) can be used, then the following must apply to the energy ratio:

$$\frac{\text{normEng}(k^{(1)})}{\text{normEng}(k^{(2)})} \approx \frac{\left(\omega_{k^{(1)}}\right)^2}{\left(\omega_{k^{(2)}}\right)^2} = \frac{(k^{(1)})^2}{(k^{(2)})^2}.$$

With the energy ratio it is now possible to explain the previous observation for the mixing orders shown in Figure 7.5 that the correlation which can be observed for the positive m_x and m_y is seemingly not present for the negative m_x and positive m_y. At the end of this section, two concrete numerical examples are given with regard to Figure 7.5. As a first example, let the mixing orders be $m_x^{(1)} = 1$ and $m_y^{(1)} = 2$, which results in the frequency index $k^{(1)} = 95$ with $N_{\mathrm{B}} = 32$. However, the mixing orders $m_x^{(2)} = -1$ and $m_y^{(2)} = 2$ also lead to a system function component that encodes the same spatial pattern with the frequency index $k^{(2)} = 33$. Consequently, the energy ratio is

$$\frac{\text{normEng}(k^{(1)})}{\text{normEng}(k^{(2)})} = \frac{95^2}{33^2} \approx 8.2874 \approx 9.1842\,\text{dB}.$$

The values in Figure 7.5 are $\text{normEng}(k^{(1)}) = -19.836\,\text{dB}$ and $\text{normEng}(k^{(2)}) = -10.6518\,\text{dB}$, resulting in the energy ratio

$$\frac{\text{normEng}(k^{(1)})}{\text{normEng}(k^{(2)})} = -10.6518\,\text{dB} - (-19.836\,\text{dB}) = 9.1842\,\text{dB},$$

which agrees with the analytical result. In the second example, let the mixing orders be $m_x^{(1)} = 3$ and $m_y^{(1)} = 3$, which results in $k^{(1)} = 189$. The associated mixing orders are $m_x^{(2)} = -3$ and $m_y^{(2)} = 3$, which now leads to the frequency index $k^{(2)} = 3$. The analytical energy ratio thus results in

$$\frac{\text{normEng}(k^{(1)})}{\text{normEng}(k^{(2)})} = \frac{\left(\omega_{k^{(1)}}\right)^2}{\left(\omega_{k^{(2)}}\right)^2} = \frac{189^2}{3^2} = 3969 \approx 35.9868\,\text{dB}.$$

The values in Figure 7.5 are $\text{normEng}(k^{(2)}) = -17.8701\,\text{dB}$ and $\text{normEng}(k^{(1)}) = -53.8569\,\text{dB}$. Therefore, the energy ratio is

$$\frac{\text{normEng}(k^{(1)})}{\text{normEng}(k^{(2)})} = -17.8701\,\text{dB} - (-53.8569\,\text{dB}) = 35.9868\,\text{dB}.$$

The examples have shown that the different energy that can be observed in Figure 7.5 between positive and negative m_x can actually be explained by the energy ratio $\frac{(k^{(1)})^2}{(k^{(2)})^2}$.

7.3 Fourier Representation for Three-Dimensional Lissajous Trajectories

This section is based on [F1], but with additional phase shifts for the excitation sequence contained in the theorem. The definition of the three-dimensional Lissajous FFP-trajectories is the starting point.

Definition 7.3: Three-dimensional excitation

Let $N_\text{B} \in \mathbb{N}$ be a frequency divider with $N_\text{B} \geq 2$ and let f_B be an arbitrary basis frequency of the MPI scanner. Then the excitation frequencies are chosen in such a way that $f_1 = \frac{f_\text{B}}{N_\text{B}}$, $f_2 = \frac{f_\text{B}}{N_\text{B}-1}$, and $f_3 = \frac{f_\text{B}}{N_\text{B}+1}$. The drive field then has the form

$$\boldsymbol{H}^\text{D}(t) = \begin{pmatrix} -A_1 \sin(\omega_1 t + \varphi_1) \\ -A_2 \sin(\omega_2 t + \varphi_2) \\ -A_3 \sin(\omega_3 t + \varphi_3) \end{pmatrix}, \tag{7.24}$$

where $\omega_i = 2\pi f_i$ with $i \in \{1, 2, 3\}$ denote the angular frequencies, $A_1, A_2, A_3 \in \mathbb{R}$ are the amplitudes, and $\varphi_1, \varphi_2, \varphi_3 \in [0, 2\pi)$ are the phase shifts. The homogeneous selection field $\boldsymbol{H}^\text{S}(\boldsymbol{x}) = \boldsymbol{G}\boldsymbol{x}$ of the MPI scanner has a gradient matrix $\boldsymbol{G} \in \mathbb{R}^{3\times3}$ as in (7.1).

The position of the FFP is given by

$$\boldsymbol{x}_{\mathrm{FFP}}(t) = -\boldsymbol{G}^{-1}\boldsymbol{H}^{\mathrm{D}}(t), \tag{7.25}$$

where the position of the FFP $\boldsymbol{x}_{\mathrm{FFP}}(t)$ has the period length

$$T_{\mathrm{D}} = \begin{cases} \dfrac{(N_{\mathrm{B}}+1)N_{\mathrm{B}}(N_{\mathrm{B}}-1)}{f_{\mathrm{B}}} & \text{for } N_{\mathrm{B}} \text{ even} \\ \dfrac{(N_{\mathrm{B}}+1)N_{\mathrm{B}}(N_{\mathrm{B}}-1)}{2f_{\mathrm{B}}} & \text{for } N_{\mathrm{B}} \text{ odd.} \end{cases}$$

Next, auxiliary parameters should be introduced to help obtaining compact expressions, since the number of parameters increases drastically in the three-dimensional case.

Definition 7.4: Auxiliary functions

Let

$$n_k(\lambda_1,\lambda_2) = \begin{cases} (\lambda_1+2\lambda_2)N_{\mathrm{B}} - k & \text{if } N_{\mathrm{B}} \text{ even}, k \text{ even}, \\ (\lambda_1+2\lambda_2+1)N_{\mathrm{B}} - k & \text{if } N_{\mathrm{B}} \text{ even}, k \text{ odd}, \\ (\lambda_1+\lambda_2)N_{\mathrm{B}} - 2k & \text{if } N_{\mathrm{B}} \text{ odd}, \end{cases}$$

$$m_k(\lambda_1,\lambda_2) = \begin{cases} \frac{k}{2} - (\lambda_1+\lambda_2)(N_{\mathrm{B}}-1) & \text{if } N_{\mathrm{B}} \text{ even}, k \text{ even}, \\ \frac{k}{2} - (\lambda_1+\lambda_2+\frac{1}{2})(N_{\mathrm{B}}-1) & \text{if } N_{\mathrm{B}} \text{ even}, k \text{ odd} \\ k - (\lambda_1+\frac{\lambda_2}{2})(N_{\mathrm{B}}-1) & \text{if } N_{\mathrm{B}} \text{ odd}, \end{cases} \tag{7.26}$$

$$\ell_k(\lambda_2) = \begin{cases} \frac{k}{2} - \lambda_2(N_{\mathrm{B}}+1) & \text{if } N_{\mathrm{B}} \text{ even}, k \text{ even}, \\ \frac{k}{2} - (\lambda_2+\frac{1}{2})(N_{\mathrm{B}}+1) & \text{if } N_{\mathrm{B}} \text{ even}, k \text{ odd}, \\ k - \frac{\lambda_2}{2}(N_{\mathrm{B}}+1) & \text{if } N_{\mathrm{B}} \text{ odd}. \end{cases}$$

The following theorem for three-dimensional Lissajous FFP-trajectory based MPI can be formulated using the above definitions.

Theorem 7.3

The Fourier series coefficients $\boldsymbol{s}_k : \mathbb{R}^3 \to \mathbb{C}^3$ of the MPI system function for a three-dimensional Lissajous FFP-trajectory with the phase shifts $\varphi_1, \varphi_2, \varphi_3 \in [0, 2\pi)$ and $k \in \mathbb{Z}\backslash\{0\}$ can be expressed in terms of tensor products of $V_\ell : \mathbb{R} \to \mathbb{R}$ that are convolved along the spatial dimensions with the spatial derivative of the Langevin function $\mathscr{L} : \mathbb{R}^3 \to \mathbb{R}^3$ by

$$\begin{aligned}\boldsymbol{s}_k(\boldsymbol{x}) = \sum_{\lambda_1,\lambda_2\in\mathbb{Z}} \frac{(-\mathrm{i})^{\lambda_1+1}\omega_k \mathrm{e}^{\mathrm{i}\theta_k(\lambda_1,\lambda_2)}}{\pi^3} \frac{\operatorname{sgn}(A_1A_2A_3)}{\operatorname{sgn}(G_1G_2G_3)} \\ \times \int_{\mathbb{R}^3} \left[\frac{\partial^3}{\partial z_1 \partial z_2 \partial z_3} \mathscr{L}(\beta \boldsymbol{G}\boldsymbol{z})\right]_{\boldsymbol{z}=\boldsymbol{x}-\boldsymbol{u}} V_{n_k(\lambda_1,\lambda_2)}\left(\frac{G_1}{A_1}u_1\right) \\ \times V_{m_k(\lambda_1,\lambda_2)}\left(\frac{G_2}{A_2}u_2\right) V_{\ell_k(\lambda_2)}\left(\frac{G_3}{A_3}u_3\right) \mathrm{d}\boldsymbol{u},\end{aligned} \tag{7.27}$$

where $n_k : \mathbb{Z}\times\mathbb{Z} \to \mathbb{Z}$, $m_k : \mathbb{Z}\times\mathbb{Z} \to \mathbb{Z}$, and $\ell_k : \mathbb{Z} \to \mathbb{Z}$ are defined in (7.26), and $\theta_k(\lambda_1, \lambda_2) = n_k(\lambda_1, \lambda_2)\varphi_1 + m_k(\lambda_1, \lambda_2)\varphi_2 + \ell_k(\lambda_2)\varphi_3$, and

$$V_n(\xi) = \begin{cases} \operatorname{rect}\left(\frac{\xi}{2}\right)\left(-\frac{U_{|n|-1}(\xi)\sqrt{1-\xi^2}}{|n|}\right) & \text{if } |n| > 0 \\ \frac{\pi}{2}\operatorname{sgn}(\xi+1) - \operatorname{rect}\left(\frac{\xi}{2}\right)\arccos(\xi) & \text{if } n = 0, \end{cases}$$

and $U_\ell(\xi)$ denotes the Chebyshev polynomial of the second kind with degree $\ell \in \mathbb{N}_0$.

Equivalently, the spatial Fourier domain representation of $\boldsymbol{s}_k(\boldsymbol{x})$ can be expressed by

$$\begin{aligned}\hat{\boldsymbol{s}}_k(\boldsymbol{\omega}_{\boldsymbol{x}}) = \sum_{\lambda_1,\lambda_2\in\mathbb{Z}} (-1)^{\lambda_1+1}\mathrm{i}\omega_k \mathrm{e}^{\mathrm{i}\theta_k(\lambda_1,\lambda_2)} \frac{\hat{\mathscr{L}}\left(\frac{\boldsymbol{G}^{-\mathsf{T}}\boldsymbol{\omega}_{\boldsymbol{x}}}{\beta}\right)}{|\det(\beta\boldsymbol{G})|} J_{n_k(\lambda_1,\lambda_2)}\left(\omega_{x_1}\frac{A_1}{G_1}\right) \\ \times J_{m_k(\lambda_1,\lambda_2)}\left(\omega_{x_2}\frac{A_2}{G_2}\right) J_{\ell_k(\lambda_2)}\left(\omega_{x_3}\frac{A_3}{G_3}\right),\end{aligned} \tag{7.28}$$

where $J_\ell(\xi)$ denotes the ℓ-th Bessel function of the first kind and $\hat{\mathscr{L}} : \mathbb{R}^3 \to \mathbb{C}^3$ is given by

$$\hat{\mathscr{L}}(\boldsymbol{\omega}_{\boldsymbol{x}}) = -4\pi^2\mathrm{i}\frac{(\pi\|\boldsymbol{\omega}_{\boldsymbol{x}}\| + 1)\,\mathrm{e}^{\pi\|\boldsymbol{\omega}_{\boldsymbol{x}}\|} - 1}{\|\boldsymbol{\omega}_{\boldsymbol{x}}\|^2\left(\mathrm{e}^{\pi\|\boldsymbol{\omega}_{\boldsymbol{x}}\|} - 1\right)^2}\frac{\boldsymbol{\omega}_{\boldsymbol{x}}}{\|\boldsymbol{\omega}_{\boldsymbol{x}}\|}.$$

For $k = 0$ it holds that $\boldsymbol{s}_0(\boldsymbol{x}) = \boldsymbol{0}$ and $\hat{\boldsymbol{s}}_0(\boldsymbol{\omega}_{\boldsymbol{x}}) = \boldsymbol{0}$.

The proof of the theorem is divided into several steps. First, the manifold constraints for the variables $m, n, \ell, k, N_\mathrm{B}, \lambda_1, \lambda_2$ are given, and then the mapping function $P(\boldsymbol{\omega}_x, k)$ is derived.

Lemma 7.4. *If a three-dimensional FFP-trajectory is used in MPI, there are two different manifold constraints, depending on $N_\mathrm{B} \in \mathbb{N}$ and $k \in \mathbb{Z}$ for $n, m, \ell \in \mathbb{Z}$ with $\lambda_1, \lambda_2 \in \mathbb{Z}$.*

1. *If N_B is even, the constraint*

$$k = (N_\mathrm{B}+1)(N_\mathrm{B}-1)n + N_\mathrm{B}(N_\mathrm{B}+1)m + N_\mathrm{B}(N_\mathrm{B}-1)\ell \tag{7.29}$$

is fulfilled for even k by the line equation

$$\begin{pmatrix} n \\ m \\ \ell \end{pmatrix} = \begin{pmatrix} -k \\ \frac{k}{2} \\ \frac{k}{2} \end{pmatrix} + \lambda_1 \begin{pmatrix} N_\mathrm{B} \\ -(N_\mathrm{B}-1) \\ 0 \end{pmatrix} + \lambda_2 \begin{pmatrix} 2N_\mathrm{B} \\ -(N_\mathrm{B}-1) \\ -(N_\mathrm{B}+1) \end{pmatrix}, \tag{7.30}$$

and for odd k by

$$\begin{pmatrix} n \\ m \\ \ell \end{pmatrix} = \begin{pmatrix} -k \\ \frac{k}{2} \\ \frac{k}{2} \end{pmatrix} + \lambda_1 \begin{pmatrix} N_\mathrm{B} \\ -(N_\mathrm{B}-1) \\ 0 \end{pmatrix} + \left(\lambda_2 + \frac{1}{2}\right) \begin{pmatrix} 2N_\mathrm{B} \\ -(N_\mathrm{B}-1) \\ -(N_\mathrm{B}+1) \end{pmatrix}. \tag{7.31}$$

2. *If N_B is odd, the constraint*

$$2k = (N_\mathrm{B}+1)(N_\mathrm{B}-1)n + N_\mathrm{B}(N_\mathrm{B}+1)m + N_\mathrm{B}(N_\mathrm{B}-1)\ell \tag{7.32}$$

is fulfilled by

$$\begin{pmatrix} n \\ m \\ \ell \end{pmatrix} = \begin{pmatrix} -2k \\ k \\ k \end{pmatrix} + \lambda_1 \begin{pmatrix} N_\mathrm{B} \\ -(N_\mathrm{B}-1) \\ 0 \end{pmatrix} + \frac{\lambda_2}{2} \begin{pmatrix} 2N_\mathrm{B} \\ -(N_\mathrm{B}-1) \\ -(N_\mathrm{B}+1) \end{pmatrix}. \tag{7.33}$$

Proof of Lemma 7.4. The aim is to prove the constraints on n, m, ℓ for three-dimensional MPI formulated in Lemma 7.4. For this, different cases need to be distinguished.

Case 1: N_B even The following manifold condition has to hold:

$$k = \Big((N_\mathrm{B}+1)(N_\mathrm{B}-1), \quad N_\mathrm{B}(N_\mathrm{B}+1), \quad N_\mathrm{B}(N_\mathrm{B}-1)\Big) \begin{pmatrix} n \\ m \\ \ell \end{pmatrix}, \tag{7.34}$$

with $k, n, m, \ell \in \mathbb{Z}$. This constraint means that all points (n, m, ℓ) are lying on a plane inside a three-dimensional space. We can verify that

$$\begin{pmatrix} n \\ m \\ \ell \end{pmatrix} = \begin{pmatrix} -k \\ \frac{k}{2} \\ \frac{k}{2} \end{pmatrix} + \lambda_1 \begin{pmatrix} N_\mathrm{B} \\ -(N_\mathrm{B}-1) \\ 0 \end{pmatrix} + (\lambda_2 + \alpha) \begin{pmatrix} 2N_\mathrm{B} \\ -(N_\mathrm{B}-1) \\ -(N_\mathrm{B}+1) \end{pmatrix} \tag{7.35}$$

with $\alpha \in \left\{0, \frac{1}{2}\right\}$ and $\lambda_1, \lambda_2 \in \mathbb{Z}$ is a valid solution that fulfills (7.34) by inserting (7.35) into (7.34):

$$\begin{aligned}
&\Big((N_\mathrm{B}+1)(N_\mathrm{B}-1), \quad N_\mathrm{B}(N_\mathrm{B}+1), \quad N_\mathrm{B}(N_\mathrm{B}-1)\Big) \begin{pmatrix} n \\ m \\ \ell \end{pmatrix} \\
&\quad = -k(N_\mathrm{B}+1)(N_\mathrm{B}-1) + \frac{k}{2}N_\mathrm{B}(N_\mathrm{B}+1) + \frac{k}{2}N_\mathrm{B}(N_\mathrm{B}-1) \\
&\qquad + \lambda_1 \underbrace{\big((N_\mathrm{B}+1)(N_\mathrm{B}-1)N_\mathrm{B} + N_\mathrm{B}(N_\mathrm{B}+1)(-(N_\mathrm{B}-1))\big)}_{=0} \\
&\qquad + (\lambda_2+\alpha)\Big[(N_\mathrm{B}+1)(N_\mathrm{B}-1)2N_\mathrm{B} \\
&\qquad\quad + N_\mathrm{B}(N_\mathrm{B}+1)(-(N_\mathrm{B}-1)) + N_\mathrm{B}(N_\mathrm{B}-1)(-(N_\mathrm{B}+1))\Big] \\
&\quad = \underbrace{-k(N_\mathrm{B}^2-1) + \frac{k}{2}(N_\mathrm{B}^2+N_\mathrm{B}) + \frac{k}{2}(N_\mathrm{B}^2-N_\mathrm{B})}_{=k} \\
&\qquad + (\lambda_2+\alpha)\underbrace{\big[(N_\mathrm{B}^2-1)2N_\mathrm{B} - (N_\mathrm{B}^2-1)N_\mathrm{B} - N_\mathrm{B}(N_\mathrm{B}^2-1)\big]}_{=0} \\
&\quad = k.
\end{aligned} \tag{7.36}$$

This means that the constraint (7.34) is fulfilled for both even and odd k in (7.30) and (7.31), respectively. According to (7.35), for even k and $\alpha = 0$ as well as for odd k and $\alpha = \frac{1}{2}$, we have $\lambda_1, \lambda_2 \in \mathbb{Z}$ and $n, m, \ell \in \mathbb{Z}$. The general case with $\lambda_i \in \mathbb{R}$ can be expressed as $\lambda_i = \tilde{\lambda}_i + \beta_i$ with $\tilde{\lambda}_i \in \mathbb{Z}$ and $\beta_i \in (0, 1)$. Now, we differentiate between $k \in \mathbb{Z}$ even and odd.

1. k even and $\alpha = 0$: It is sufficient to check for which β_i the following constraints are fulfilled:

$$(\beta_1 + 2\beta_2)N_\mathrm{B} \in \mathbb{Z}, \tag{7.37}$$
$$-(\beta_1 + \beta_2)(N_\mathrm{B} - 1) \in \mathbb{Z}, \tag{7.38}$$
$$-\beta_2(N_\mathrm{B} + 1) \in \mathbb{Z}. \tag{7.39}$$

By adding up (7.37) and (7.38) and rearranging the obtained equation we get

$$\beta_1 + \underbrace{\beta_2(N_\mathrm{B} + 1)}_{\in\mathbb{Z} \text{ by } (7.39)} \in \mathbb{Z}. \tag{7.40}$$

Consequently, only $\beta_1 = 0$ or $\beta_1 = 1$ are valid solutions. By subtracting (7.39) from (7.38) and setting $\beta_1 = 0$ we get

$$2\beta_2 \in \mathbb{Z}, \tag{7.41}$$

which only allows a solution with $\beta_2 \in \{0, \frac{1}{2}, 1\}$.

Utilizing that N_B is even, we have $\beta_2 N_\mathrm{B} \in \mathbb{Z}$ and consequently we get from (7.39)

$$-\beta_2(N_\mathrm{B} + 1) = -\beta_2 N_\mathrm{B} - \beta_2 \in \mathbb{Z} \Rightarrow -\beta_2 \in \mathbb{Z}. \tag{7.42}$$

This means that $\beta_2 = 0$ or $\beta_2 = 1$ are the only valid solutions. Therefore, there is no $\beta_1, \beta_2 \in (0, 1)$ such that $n, m, \ell \in \mathbb{Z}$.

2. k odd and $\alpha = \frac{1}{2}$: Here, using that $\frac{N_\mathrm{B}}{2} \in \mathbb{Z}$, (7.35) results in the following constraints:

$$(\beta_1 + 2\beta_2)N_\mathrm{B} \in \mathbb{Z} \tag{7.43}$$
$$-(\beta_1 + \beta_2)(N_\mathrm{B} - 1) \in \mathbb{Z} \tag{7.44}$$
$$-\beta_2(N_\mathrm{B} + 1) \in \mathbb{Z}. \tag{7.45}$$

These are exactly the same constraints as (7.37), (7.38), and (7.39). Consequently, the constraints on β_1 and β_2 are also the same.

Case 2: N_B **odd** To derive the manifold conditions for the case where N_B is odd, we set

$$2k = \Big((N_\mathrm{B}+1)(N_\mathrm{B}-1),\;\; N_\mathrm{B}(N_\mathrm{B}+1),\;\; N_\mathrm{B}(N_\mathrm{B}-1)\Big) \begin{pmatrix} n \\ m \\ \ell \end{pmatrix}. \tag{7.46}$$

It can easily be shown that a possible solution is given for $n = -2k$, $m = k$ and $\ell = k$. The basis vectors are the same as for even N_B, and we can write the possible solutions as

$$\begin{pmatrix} n \\ m \\ \ell \end{pmatrix} = \begin{pmatrix} -2k \\ k \\ k \end{pmatrix} + \lambda_1 \begin{pmatrix} N_\mathrm{B} \\ -(N_\mathrm{B}-1) \\ 0 \end{pmatrix} + \frac{\lambda_2}{2} \begin{pmatrix} 2N_\mathrm{B} \\ -(N_\mathrm{B}-1) \\ -(N_\mathrm{B}+1) \end{pmatrix}. \tag{7.47}$$

The fact that $\lambda_1, \lambda_2 \in \mathbb{Z}$ holds can be concluded from the three constraints

$$(\lambda_1 + \lambda_2) N_\mathrm{B} \in \mathbb{Z}, \tag{7.48}$$

$$-\left(\lambda_1 + \frac{\lambda_2}{2}\right)(N_\mathrm{B}-1) \in \mathbb{Z}, \tag{7.49}$$

$$-\frac{\lambda_2}{2}(N_\mathrm{B}+1) \in \mathbb{Z}. \tag{7.50}$$

By adding up (7.48) and (7.49) and rearranging the obtained equation we get

$$\underbrace{(N_\mathrm{B}+1)\,\frac{\lambda_2}{2}}_{\in\,\mathbb{Z}\text{ due to (7.50)}} + \lambda_1 \in \mathbb{Z}.$$

Consequently, $\lambda_1 \in \mathbb{Z}$. By subtracting (7.50) from (7.49) and setting $\lambda_1 = 0$ we get

$$\lambda_2 \in \mathbb{Z}. \qquad \square$$

Lemma 7.5. *The mapping function $P : \mathbb{R}^3 \times \mathbb{Z} \to \mathbb{C}$ for the three-dimensional Lissajous FFP-trajectory $\boldsymbol{x}_{\mathrm{FFP}} : \mathbb{R} \to \mathbb{R}^3$ is given by*

$$P(\boldsymbol{\omega}_{\boldsymbol{x}}, k) = \sum_{\lambda_1, \lambda_2 \in \mathbb{Z}} \mathrm{e}^{\mathrm{i}\theta_k(\lambda_1,\lambda_2)} J_{n_k(\lambda_1,\lambda_2)}\left(\omega_{x_1}\frac{A_1}{G_1}\right) J_{m_k(\lambda_1,\lambda_2)}\left(\omega_{x_2}\frac{A_2}{G_2}\right) J_{\ell_k(\lambda_2)}\left(\omega_{x_3}\frac{A_3}{G_3}\right) \tag{7.51}$$

with the phase function $\theta_k(\lambda_1, \lambda_2) = n_k(\lambda_1, \lambda_2)\varphi_1 + m_k(\lambda_1, \lambda_2)\varphi_2 + \ell_k(\lambda_2)\varphi_3$ using the mapping functions $n_k : \mathbb{Z} \times \mathbb{Z} \to \mathbb{Z}$, $m_k : \mathbb{Z} \times \mathbb{Z} \to \mathbb{Z}$, and $\ell_k : \mathbb{Z} \to \mathbb{Z}$ as defined in (7.26)*.*

Proof of Lemma 7.5. To confirm (7.51),

$$P(\boldsymbol{\omega}_{\boldsymbol{x}}, k) = \frac{1}{2\pi}\int_{-\pi}^{\pi} \mathrm{e}^{\mathrm{i}\boldsymbol{\omega}_{\boldsymbol{x}}^{\mathsf{T}}\boldsymbol{x}_{\mathrm{FFP}}\left(\frac{z}{2\pi f_{\mathrm{D}}}\right)} \mathrm{e}^{-\mathrm{i}kz}\,\mathrm{d}z \tag{7.52}$$

is considered according to (6.7). Inserting the respective Lissajous trajectory from (7.25) results in the position of the FFP

$$\begin{aligned}
\boldsymbol{x}_{\mathrm{FFP}}\left(\frac{z}{2\pi f_{\mathrm{D}}}\right) &= \begin{pmatrix} \frac{A_1}{G_1}\sin\left(\frac{f_1}{f_{\mathrm{D}}}z + \varphi_1\right) \\ \frac{A_2}{G_2}\sin\left(\frac{f_2}{f_{\mathrm{D}}}z + \varphi_2\right) \\ \frac{A_3}{G_3}\sin\left(\frac{f_3}{f_{\mathrm{D}}}z + \varphi_3\right) \end{pmatrix} \\
&= \begin{cases} \begin{pmatrix} \frac{A_1}{G_1}\sin\big((N_{\mathrm{B}}+1)(N_{\mathrm{B}}-1)z + \varphi_1\big) \\ \frac{A_2}{G_2}\sin\big(N_{\mathrm{B}}(N_{\mathrm{B}}+1)z + \varphi_2\big) \\ \frac{A_3}{G_3}\sin\big(N_{\mathrm{B}}(N_{\mathrm{B}}-1)z + \varphi_3\big) \end{pmatrix} & \text{if } N_{\mathrm{B}} \text{ is even,} \\ \begin{pmatrix} \frac{A_1}{G_1}\sin\left(\frac{(N_{\mathrm{B}}+1)(N_{\mathrm{B}}-1)}{2}z + \varphi_1\right) \\ \frac{A_2}{G_2}\sin\left(\frac{N_{\mathrm{B}}(N_{\mathrm{B}}+1)}{2}z + \varphi_2\right) \\ \frac{A_3}{G_3}\sin\left(\frac{N_{\mathrm{B}}(N_{\mathrm{B}}-1)}{2}z + \varphi_3\right) \end{pmatrix} & \text{if } N_{\mathrm{B}} \text{ is odd.} \end{cases}
\end{aligned} \tag{7.53}$$

With the Jacobi-Anger expansion [8, Ch. 7.2.4, (26)], the term $\mathrm{e}^{\mathrm{i}\boldsymbol{\omega}_{\boldsymbol{x}}^{\mathrm{T}}\boldsymbol{x}_{\mathrm{FFP}}\left(\frac{z}{2\pi f_{\mathrm{D}}}\right)}$ is developed into a series analogous to the two-dimensional FFP and then the integration is carried out in (7.52). Thus, for N_{B}, which is even, one obtains

$$\begin{aligned}
P(\boldsymbol{\omega}_{\boldsymbol{x}}, k) &= \sum_{n,m,\ell\in\mathbb{Z}} \Bigg[\mathrm{e}^{\mathrm{i}(n\varphi_1+m\varphi_2+\ell\varphi_3)} J_n\left(\omega_{x_1}\frac{A_1}{G_1}\right) J_m\left(\omega_{x_2}\frac{A_2}{G_2}\right) J_\ell\left(\omega_{x_3}\frac{A_3}{G_3}\right) \\
&\qquad \times \frac{1}{2\pi}\int_{-\pi}^{\pi} \mathrm{e}^{\mathrm{i}[n(N_{\mathrm{B}}-1)(N_{\mathrm{B}}+1)+mN_{\mathrm{B}}(N_{\mathrm{B}}+1)+\ell N_{\mathrm{B}}(N_{\mathrm{B}}-1)-k]z}\,\mathrm{d}z \Bigg] \\
&= \sum_{n,m,\ell\in\mathbb{Z}} \Bigg[\mathrm{e}^{\mathrm{i}(n\varphi_1+m\varphi_2+\ell\varphi_3)} J_n\left(\omega_{x_1}\frac{A_1}{G_1}\right) J_m\left(\omega_{x_2}\frac{A_2}{G_2}\right) J_\ell\left(\omega_{x_3}\frac{A_3}{G_3}\right) \\
&\qquad \times \delta_{(n(N_{\mathrm{B}}+1)(N_{\mathrm{B}}-1)+mN_{\mathrm{B}}(N_{\mathrm{B}}+1)+\ell N_{\mathrm{B}}(N_{\mathrm{B}}-1),\ k)} \Bigg],
\end{aligned}$$

while for an odd N_{B} it is obtained that

$$\begin{aligned}
P(\boldsymbol{\omega}_{\boldsymbol{x}}, k) &= \sum_{n,m,\ell\in\mathbb{Z}} \Bigg[\mathrm{e}^{\mathrm{i}(n\varphi_1+m\varphi_2+\ell\varphi_3)} J_n\left(\omega_{x_1}\frac{A_1}{G_1}\right) J_m\left(\omega_{x_2}\frac{A_2}{G_2}\right) J_\ell\left(\omega_{x_3}\frac{A_3}{G_3}\right) \\
&\qquad \times \delta_{\left(\frac{1}{2}n(N_{\mathrm{B}}+1)(N_{\mathrm{B}}-1)+\frac{1}{2}mN_{\mathrm{B}}(N_{\mathrm{B}}+1)+\frac{1}{2}\ell N_{\mathrm{B}}(N_{\mathrm{B}}-1),\ k\right)} \Bigg] \\
&= \sum_{n,m,\ell\in\mathbb{Z}} \Bigg[\mathrm{e}^{\mathrm{i}(n\varphi_1+m\varphi_2+\ell\varphi_3)} J_n\left(\omega_{x_1}\frac{A_1}{G_1}\right) J_m\left(\omega_{x_2}\frac{A_2}{G_2}\right) J_\ell\left(\omega_{x_3}\frac{A_3}{G_3}\right) \\
&\qquad \times \delta_{(n(N_{\mathrm{B}}+1)(N_{\mathrm{B}}-1)+mN_{\mathrm{B}}(N_{\mathrm{B}}+1)+\ell N_{\mathrm{B}}(N_{\mathrm{B}}-1),\ 2k)} \Bigg].
\end{aligned}$$

The argument of the Kronecker symbol follows the constraints in Lemma 7.4. □

The frequency-domain representation in (7.28) can be verified using the same arguments as in the proof of the Theorem 7.1 (see (7.8), (7.9), (7.10)), while using the additional relationship $(-1)^{n_k(\lambda_1,\lambda_2)+m_k(\lambda_1,\lambda_2)+\ell_k(\lambda_2)} = (-1)^{\lambda_1}$.

Using Lemma 6.10 and assuming that $|k| > 0$, an upper bound for the L^1-norm of $\hat{s}_{\nu k}(\boldsymbol{\omega}_{\boldsymbol{x}})$ can be calculated. By combining all factors into a constant $C_2 > 0$, similar as for the two-dimensional excitation, it can be shown that

$$\begin{aligned}\|\hat{s}_{\nu k}\|_{L^1} &\leq C_2 \sum_{\lambda_1,\lambda_2\in\mathbb{Z}} \frac{1}{\max(1,|n_k(\lambda_1,\lambda_2)|^{\frac{4}{3}})\max(1,|m_k(\lambda_1,\lambda_2)|^{\frac{4}{3}})\max(1,|\ell_k(\lambda_2)|^{\frac{4}{3}})} \\ &< \infty,\end{aligned} \tag{7.54}$$

where it is used that for $|k| > 0$ there are no $\lambda_1, \lambda_2 \in \mathbb{Z}$ such that $|\ell_k(\lambda_2)| = |m_k(\lambda_1,\lambda_2)| = |n_k(\lambda_1,\lambda_2)| = 0$.

Similar to the two-dimensional case, by assuming a zero-mean voltage signal, one obtains $\boldsymbol{s}_0(\boldsymbol{x}) = \mathbf{0}$ and $\hat{\boldsymbol{s}}_0(\boldsymbol{\omega}_{\boldsymbol{x}}) = \mathbf{0}$. Overall, the series is therefore well-defined and the system function $\hat{\boldsymbol{s}}_k(\boldsymbol{\omega}_{\boldsymbol{x}})$ is in $L^1(\mathbb{R}^3)$, so that an inverse Fourier transform exists.

Analog to Section 7.2, the Lemma 6.11 is used to obtain the inverse Fourier transform of $\hat{\boldsymbol{s}}_k(\boldsymbol{\omega}_{\boldsymbol{x}})$, which is equivalent to the expression in (7.27).

Thus, Theorem 7.3 is finally proven. □

The three-dimensional model is much more difficult to simulate and the representations of its system function components are not so easily accessible and are therefore omitted here. However, it should be mentioned that in [80] a connection of the system function components in (7.27) with tensor products of Chebyshev polynomials of the second kind was also postulated for the three-dimensional excitation case. The exact connection was then the first time shown in [F1]. A numerical investigation of the model was carried out by Droigk et al. in [C1]. There it was shown that the theoretical insight from [F12], that only a few series terms occur in the two-dimensional excitation case, can also be transferred to the three-dimensional excitation case. The reason for that, again, lies in the low-pass characteristic of the three-dimensional Fourier-transformed Langevin function $\hat{\boldsymbol{\mathscr{L}}} : \mathbb{R}^3 \to \mathbb{C}^3$, which can be seen in Figure 6.7. If this function is multiplied by the tensor products of the Bessel function in the double series in (7.28), only combinations with small orders for n_k, m_k and ℓ_k can contribute significantly to the series, which is then also transferred to the series in (7.27).

7.4 A General Concept for Different FFP-Trajectories

The technique for formulating the MPI system function in the spatio-temporal Fourier domain presented before can also be applied to other FFP-trajectories. To illustrate the procedure, it is useful to start with the position-dependent FFP function

$$\boldsymbol{x}_{\mathrm{FFP}}(t) = -\boldsymbol{G}^{-1}\boldsymbol{H}^{\mathrm{D}}(t),$$

which is assumed to be T_{D}-periodic. Note, $\boldsymbol{G} \in \mathbb{R}^{3\times 3}$ is diagonal and defined by

$$\boldsymbol{G} = \begin{pmatrix} G_1 & 0 & 0 \\ 0 & G_2 & 0 \\ 0 & 0 & G_3 \end{pmatrix}.$$

The essential part for the following analysis is the mapping function

$$P(\boldsymbol{\omega}_{\boldsymbol{x}}, k) = \frac{1}{2\pi}\int_{-\pi}^{\pi} \mathrm{e}^{\mathrm{i}\boldsymbol{\omega}_{\boldsymbol{x}}^{\mathrm{T}}\boldsymbol{x}_{\mathrm{FFP}}\left(\frac{z}{2\pi f_{\mathrm{D}}}\right)}\mathrm{e}^{-\mathrm{i}kz}\,\mathrm{d}z, \tag{7.55}$$

as introduced in Theorem 6.1. The mapping function in (7.55) together with the function depending on the magnetization curve, e.g., the Langevin function, plays the central role for the Fourier series expansion of the system function $\boldsymbol{s}_k(\boldsymbol{x})$. Next, the observation that $P(\boldsymbol{\omega}_{\boldsymbol{x}}, k)$ is related to generalized Bessel functions is explained and, subsequently, $P(\boldsymbol{\omega}_{\boldsymbol{x}}, k)$ is presented for different FFP-trajectories. The following contains additional and unpublished findings and, thus, represents an extension of previous works.

7.4.1 Generalized Bessel Functions

With increasing experience of the mathematical structure of the problem, it becomes clear that (7.55) is highly related to the theory of generalized Bessel functions with several variables from [21] and the monograph [22]. For two-dimensional generalized Bessel functions see also [58]. This connection was first briefly mentioned in the conference

paper [F12] without elaborating on it. Therefore, the generalized Bessel functions will be introduced here. For this, they are defined via the generating functions of the form

$$G(\xi_1,\xi_2,\ldots,\xi_M;t)=\exp\left(\sum_{m=1}^{M}\frac{\xi_m}{2}\left(t^m-\frac{1}{t^m}\right)\right)=\sum_{n=-\infty}^{\infty}t^n\,{}^{(M)}J_n(\xi_1,\xi_2,\ldots,\xi_M),$$

where ${}^{(M)}J_n(\xi_1,\xi_2,\ldots,\xi_M)$ defines the M-dimensional Bessel function with the order $n\in\mathbb{Z}$. By setting $t=\mathrm{e}^{\mathrm{i}\theta}$, the corresponding Jacobi-Anger-like expansion is obtained:

$$G(\xi_1,\xi_2,\ldots,\xi_M;\mathrm{e}^{\mathrm{i}\theta})=\exp\left(\mathrm{i}\sum_{m=1}^{M}\xi_m\sin(m\theta)\right)=\sum_{n=-\infty}^{\infty}\mathrm{e}^{\mathrm{i}n\theta}\,{}^{(M)}J_n(\xi_1,\xi_2,\ldots,\xi_M). \tag{7.56}$$

Therefore, the M-dimensional Bessel functions can be defined as the integral expression over the n-th Fourier series coefficient with

$$\begin{aligned}{}^{(M)}J_n(\xi_1,\xi_2,\ldots,\xi_M)&=\frac{1}{2\pi}\int_{-\pi}^{\pi}\exp\left(\mathrm{i}\sum_{m=1}^{M}\xi_m\sin(m\theta)\right)\mathrm{e}^{-\mathrm{i}n\theta}\,\mathrm{d}\theta\\&=\frac{1}{\pi}\int_{0}^{\pi}\cos\left(\sum_{m=1}^{M}\xi_m\sin(m\theta)-n\theta\right)\,\mathrm{d}\theta.\end{aligned} \tag{7.57}$$

According to [22, Ch. 6, (3.4)], the M-dimensional Bessel function can be expressed as a series of $(M-1)$-dimensional Bessel function and classical Bessel functions of the first kind $J_n:\mathbb{R}\to\mathbb{R}$ by

$${}^{(M)}J_n(\xi_1,\xi_2,\ldots,\xi_M)=\sum_{\ell=-\infty}^{\infty}{}^{(M-1)}J_{n-M\ell}(\xi_1,\xi_2,\ldots,\xi_{M-1})J_\ell(\xi_M). \tag{7.58}$$

If the rule in (7.58) is applied to all variables $\xi_1,\xi_2,\ldots,\xi_M$, it becomes clear that the series can be explicitly expressed by M-series with tensor products of Bessel functions of the first kind $J_\ell:\mathbb{R}\to\mathbb{R}$. It should not go unmentioned that under certain conditions the series terms $M\to\infty$ in (7.56) and (7.57) can be used. This then allows for the use of functions $f(\theta)$, which can be developed in Fourier sine series into the expression $\mathrm{e}^{\mathrm{i}f(\theta)}$ in (7.56) [65, 66].

Using the previously defined generalized Bessel functions, it becomes clear that $P(\boldsymbol{\omega}_{\boldsymbol{x}}, k)$ from (7.55) can be represented in the form of generalized Bessel functions in the case of two-dimensional (7.11) and three-dimensional (7.24) excitation for $\boldsymbol{H}^{\mathrm{D}}(t)$ with $\varphi_1 = \varphi_2 = \varphi_3 = c_3 = 0$.

For the two-dimensional Lissajous FFP-trajectory in (7.17) with $\varphi_1 = \varphi_2 = c_3 = 0$, (7.55) is

$$P(\boldsymbol{\omega}_{\boldsymbol{x}}, k) = \frac{1}{2\pi} \int_{-\pi}^{\pi} \exp\left(\mathrm{i} \left(\omega_{x_1} \tfrac{A_1}{G_1} \sin((N_{\mathrm{B}} - 1)z) + \omega_{x_2} \tfrac{A_2}{G_2} \sin(N_{\mathrm{B}} z) \right) \right) \mathrm{e}^{-\mathrm{i}kz} \, \mathrm{d}z. \tag{7.59}$$

By comparing (7.59) with (7.57), the relationship

$$P(\boldsymbol{\omega}_{\boldsymbol{x}}, k) = {}^{(N_{\mathrm{B}})}J_k\big(\underbrace{0, \ldots, 0}_{N_{\mathrm{B}}-2 \text{ times}}, \omega_{x_1} \tfrac{A_1}{G_1}, \omega_{x_2} \tfrac{A_2}{G_2} \big)$$

is obtained. By applying (7.58) twice, one subsequently obtains

$$\begin{aligned} P(\boldsymbol{\omega}_{\boldsymbol{x}}, k) &= \sum_{n,m \in \mathbb{Z}} {}^{(M-2)}J_{k - N_{\mathrm{B}} m - (N_{\mathrm{B}}-1)n}(0, \ldots, 0) J_n\left(\omega_{x_1} \tfrac{A_1}{G_1} \right) J_m\left(\omega_{x_2} \tfrac{A_2}{G_2} \right) \\ &\overset{(7.57)}{=} \sum_{n,m \in \mathbb{Z}} \delta_{(N_{\mathrm{B}} m + (N_{\mathrm{B}}-1)n,\, k)} J_n\left(\omega_{x_1} \tfrac{A_1}{G_1} \right) J_m\left(\omega_{x_2} \tfrac{A_2}{G_2} \right), \end{aligned}$$

which accords with (7.15) in Lemma 7.1.

It is also not difficult to check that the following results for the three-dimensional Lissajous FFP-trajectory in (7.53) with $\varphi_1 = \varphi_2 = \varphi_3 = 0$ and an even N_{B},

$$P(\boldsymbol{\omega}_{\boldsymbol{x}}, k) = {}^{(N_{\mathrm{B}}^2 + N_{\mathrm{B}})}J_k\big(0, \ldots, 0, \underset{\substack{\uparrow \\ \xi_{N_{\mathrm{B}}^2 - N_{\mathrm{B}}}}}{\omega_{x_3} \tfrac{A_3}{G_3}}, 0, \ldots, 0, \underset{\substack{\uparrow \\ \xi_{N_{\mathrm{B}}^2 - 1}}}{\omega_{x_1} \tfrac{A_1}{G_1}}, 0, \ldots, 0, \underset{\substack{\uparrow \\ \xi_{N_{\mathrm{B}}^2 + N_{\mathrm{B}}}}}{\omega_{x_2} \tfrac{A_2}{G_2}} \big),$$

where ξ_m is used to indicate the position of the non-zero variable in the multidimensional Bessel function. The odd case N_{B} follows similarly. Thus, the generalized multidimensional Bessel function seems to be a promising mathematical framework to study various typical FFP-trajectories in MPI. Various extensions of the generalized Bessel functions are also conceivable, so it seems interesting for the purpose of MPI to develop

or use an extended model that also inserts an additional Fourier cosine series in the complex exponent in (7.56) in order to include phase shifts in the model. However, a complete development of the model itself is beyond the scope of this thesis. It should not go unmentioned that the author of this thesis was surprised that the connection through a spatial Fourier transform to series of tensor products of weighted Chebyshev polynomials of the first and second kind under the conditions derived in this thesis does not seem to be discussed in the literature, since the relation is quite right for the classical Bessel functions of the first kind.

An extension of the infinite dimensional theory with $M \to \infty$ in (7.56) and (7.57) can allow one to include tri-like FFP-trajectories as in Theorem 2.2. However, a tri-like excitation leads to a loss of desirable properties due to the convergence properties in the Fourier sine expansion of a tri-like excitation. For details, see [22, 65, 66].

7.4.2 The Pragmatical Approach

In this section, a more pragmatic strategy for FFP-trajectories consisting of sinusoidal periodic functions is presented. In addition, the mapping functions $P(\boldsymbol{\omega}_{\boldsymbol{x}}, k)$ for FFP-trajectories known from the literature (cf. [F3, 2, 34, 50, 52, 76, 99, 100]) are presented here for the first time. The general steps of the algorithm, which could be implemented in a computer algebra system, for example, are as follows:

1. The 2π-periodic function $\boldsymbol{p}_{\mathrm{FFP}}(z) = \boldsymbol{x}_{\mathrm{FFP}}\left(\frac{z}{2\pi f_{\mathrm{D}}}\right)$ with $\boldsymbol{p}_{\mathrm{FFP}} : \mathbb{R} \to \mathbb{R}^3$ is represented by its Fourier series

$$\boldsymbol{p}_{\mathrm{FFP}}(z) = \begin{pmatrix} \sum\limits_{\ell=1}^{N_1} A_\ell^x \sin(\ell z + \varphi_\ell^x) \\ \sum\limits_{\ell=1}^{N_2} A_\ell^y \sin(\ell z + \varphi_\ell^y) \\ \sum\limits_{\ell=1}^{N_3} A_\ell^z \sin(\ell z + \varphi_\ell^z) \end{pmatrix} = \begin{pmatrix} \sum\limits_{\ell=1}^{N_1} (a_\ell^x \sin(\ell z) + b_\ell^x \cos(\ell z)) \\ \sum\limits_{\ell=1}^{N_2} (a_\ell^y \sin(\ell z) + b_\ell^y \cos(\ell z)) \\ \sum\limits_{\ell=1}^{N_3} (a_\ell^z \sin(\ell z) + b_\ell^z \cos(\ell z)) \end{pmatrix}. \tag{7.60}$$

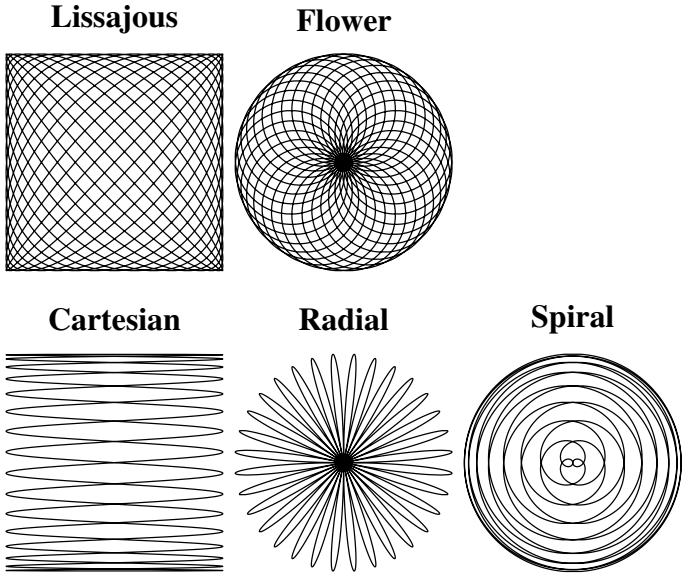

Figure 7.6: Five different two-dimensional FFP-trajectories for $N_\mathrm{B} = 17$. For all trajectories $\varphi_1 = \varphi_2 = 0$ is used.

2. The integral

$$P(\boldsymbol{\omega}_{\boldsymbol{x}}, k) = \frac{1}{2\pi} \int_{-\pi}^{\pi} \mathrm{e}^{\mathrm{i}\boldsymbol{\omega}_{\boldsymbol{x}}^{\mathsf{T}} \boldsymbol{p}_{\mathrm{FFP}}(z)} \mathrm{e}^{-\mathrm{i}kz} \, \mathrm{d}z \tag{7.61}$$

is solved by expanding $\mathrm{e}^{\mathrm{i}\boldsymbol{\omega}_{\boldsymbol{x}}^{\mathsf{T}} \boldsymbol{p}_{\mathrm{FFP}}(z)}$ with help of the Jacobi-Anger expansions

$$\begin{aligned} \mathrm{e}^{\mathrm{i}\xi \sin(u)} &= \sum_{n \in \mathbb{Z}} J_n(\xi) \mathrm{e}^{\mathrm{i}nu}, \\ \mathrm{e}^{\mathrm{i}\xi \cos(u)} &= \sum_{n \in \mathbb{Z}} \mathrm{i}^n J_n(\xi) \mathrm{e}^{\mathrm{i}nu}, \\ \mathrm{e}^{\mathrm{i}\xi \sin(u+\theta)} &= \sum_{n \in \mathbb{Z}} \mathrm{e}^{\mathrm{i}n\theta} J_n(\xi) \mathrm{e}^{\mathrm{i}nu}. \end{aligned} \tag{7.62}$$

Note that it can be helpful to use the following identity $J_n(-\xi) = J_{-n}(\xi) = (-1)^n J_n(\xi)$ for $n \in \mathbb{Z}$.

3. Find the solution to the obtained linear Diophantine equation.
4. Reduce the number of series terms by using the solution of the linear Diophantine equation.

Table 7.2: An overview of different two-dimensional drive fields $\boldsymbol{H}^{\mathrm{D}}(t)$ and the required frequency-ratios, where $\omega_i = 2\pi f_i$ and φ_i denote the phase shifts. The frequency f_1 is chosen in such a way that $f_1 = \frac{f_{\mathrm{B}}}{N_{\mathrm{B}}}$, where $f_{\mathrm{B}} > 0$ is an arbitrary basis frequency of the MPI scanner. The table was modified obtained from [2]. The Lissajous trajectory is only included here for the sake of completeness, for the results see Section 7.2.

Frequency-ratio	**Trajectory**	**Drive field $\boldsymbol{H}^{\mathrm{D}}(t)$**
$\omega_2 = \frac{N_{\mathrm{B}}}{N_{\mathrm{B}}-1}\omega_1$	**Lissajous**	$\begin{pmatrix} -A_1 \sin(\omega_1 t + \varphi_1) \\ -A_2 \sin(\omega_2 t + \varphi_2) \\ 0 \end{pmatrix}$
	Flower	$\begin{pmatrix} -A_1 \sin(\omega_1 t)\cos(\omega_2 t) \\ -A_2 \sin(\omega_2 t)\sin(\omega_1 t) \\ 0 \end{pmatrix}$
$\omega_2 = \frac{\omega_1}{N_{\mathrm{B}}-1}$	**Cartesian**	$\begin{pmatrix} -A_1 \sin(\omega_1 t + \varphi_1) \\ -A_2 \sin(\omega_2 t + \varphi_2) \\ 0 \end{pmatrix}$
	Radial	$\begin{pmatrix} -A_1 \sin(\omega_1 t)\cos(\omega_2 t) \\ -A_2 \sin(\omega_2 t)\sin(\omega_1 t) \\ 0 \end{pmatrix}$
	Spiral	$\begin{pmatrix} -A_1 \sin(\omega_1 t)\sin(\omega_2 t) \\ -A_2 \sin(\omega_2 t)\cos(\omega_1 t) \\ 0 \end{pmatrix}$

In the following, the mapping function $P(\boldsymbol{\omega}_{\boldsymbol{x}}, k)$ is examined for various FFP-trajectories found in the literature [F3, 2, 34, 50, 52, 76, 99, 100]. Among the trajectories examined in the following, the Cartesian-like trajectory is the most commonly used [31–33, 76]. The Cartesian-like trajectory is commonly used in x-space MPI, which refers to the MPI reconstruction in the time domain, while the next result refers to the spatio-temporal frequency domain. In this work, however, a link is thus established between the MPI in x-space and the representation in spatio-temporal frequency domain. The function $P(\boldsymbol{\omega}_{\boldsymbol{x}}, k)$ is now derived using the proposed principle in order to present the corresponding results for MPI for the first time in this thesis. The various two-dimensional FFP-trajectories are shown in Figure 7.6. Table 7.2 shows the corresponding two-dimensional drive fields. Please note that the Lissajous FFP-trajectory is included in Figure 7.6 and Table 7.2 only for the sake of completeness.

7.4.3 Radial Trajectory

The position of the FFP for the two-dimensional radial trajectory (see Table 7.2) is defined by

$$\begin{aligned} \boldsymbol{x}_{\mathrm{FFP}}(t) &= \begin{pmatrix} \frac{A_1}{G_1}\sin(\omega_1 t)\cos(\omega_2 t) \\ \frac{A_2}{G_2}\sin(\omega_2 t)\sin(\omega_1 t) \\ 0 \end{pmatrix} \\ &= \begin{pmatrix} \frac{A_1}{2G_1}\left[\sin\big((\omega_1-\omega_2)t\big)+\sin\big((\omega_1+\omega_2)t\big)\right] \\ \frac{A_2}{2G_2}\left[\cos\big((\omega_1-\omega_2)t\big)-\cos\big((\omega_1+\omega_2)t\big)\right] \\ 0 \end{pmatrix}, \end{aligned} \tag{7.63}$$

where $\omega_1 = 2\pi f_1$ and $\omega_2 = 2\pi f_2$ with $f_1 = \frac{f_\mathrm{B}}{N_\mathrm{B}}$ and $f_2 = \frac{f_\mathrm{B}}{N_\mathrm{B}(N_\mathrm{B}-1)}$. The period length for this trajectory is

$$T_\mathrm{D} = \frac{1}{f_\mathrm{D}} = \begin{cases} \dfrac{N_\mathrm{B}(N_\mathrm{B}-1)}{2f_\mathrm{B}}, & \text{if } N_\mathrm{B} \text{ is even,} \\ \dfrac{N_\mathrm{B}(N_\mathrm{B}-1)}{f_\mathrm{B}}, & \text{if } N_\mathrm{B} \text{ is odd.} \end{cases}$$

1. The function $\boldsymbol{p}_{\mathrm{FFP}}(z)$ is represented as a Fourier series and reformulated as

$$\begin{aligned} \boldsymbol{p}_{\mathrm{FFP}}(z) &= \begin{pmatrix} \frac{A_1}{2G_1}\left[\sin\left(f_\mathrm{B}\frac{N_\mathrm{B}-2}{N_\mathrm{B}(N_\mathrm{B}-1)}\frac{z}{f_\mathrm{D}}\right)+\sin\left(f_\mathrm{B}\frac{N_\mathrm{B}}{N_\mathrm{B}(N_\mathrm{B}-1)}\frac{z}{f_\mathrm{D}}\right)\right] \\ \frac{A_2}{2G_2}\left[\cos\left(f_\mathrm{B}\frac{N_\mathrm{B}-2}{N_\mathrm{B}(N_\mathrm{B}-1)}\frac{z}{f_\mathrm{D}}\right)-\cos\left(f_\mathrm{B}\frac{N_\mathrm{B}}{N_\mathrm{B}(N_\mathrm{B}-1)}\frac{z}{f_\mathrm{D}}\right)\right] \\ 0 \end{pmatrix} \\ &= \begin{cases} \begin{pmatrix} \frac{A_1}{2G_1}\left[\sin\big(\frac{N_\mathrm{B}-2}{2}z\big)+\sin\big(\frac{N_\mathrm{B}}{2}z\big)\right] \\ \frac{A_2}{2G_2}\left[\cos\big(\frac{N_\mathrm{B}-2}{2}z\big)-\cos\big(\frac{N_\mathrm{B}}{2}z\big)\right] \\ 0 \end{pmatrix} & \text{if } N_\mathrm{B} \text{ is even} \\ \begin{pmatrix} \frac{A_1}{2G_1}\left[\sin\big((N_\mathrm{B}-2)z\big)+\sin\big(N_\mathrm{B}z\big)\right] \\ \frac{A_2}{2G_2}\left[\cos\big((N_\mathrm{B}-2)z\big)-\cos\big(N_\mathrm{B}z\big)\right] \\ 0 \end{pmatrix} & \text{if } N_\mathrm{B} \text{ is odd.} \end{cases} \end{aligned} \tag{7.64}$$

2. The integral is solved using the Jacobi-Anger expansions for odd N_B by

$$\begin{aligned}
P(\boldsymbol{\omega}_{\boldsymbol{x}}, k) &= \frac{1}{2\pi}\int_{-\pi}^{\pi} \mathrm{e}^{\mathrm{i}\boldsymbol{\omega}_{\boldsymbol{x}}^{\mathrm{T}}\boldsymbol{p}_{\mathrm{FFP}}(z)}\mathrm{e}^{-\mathrm{i}kz}\,\mathrm{d}z \\
&= \frac{1}{2\pi}\int_{-\pi}^{\pi} \mathrm{e}^{\mathrm{i}\omega_{x_1}\frac{A_1}{2G_1}\sin((N_\mathrm{B}-2)z)}\mathrm{e}^{\mathrm{i}\omega_{x_1}\frac{A_1}{2G_1}\sin(N_\mathrm{B}z)} \\
&\qquad\qquad \times \mathrm{e}^{\mathrm{i}\omega_{x_2}\frac{A_2}{2G_2}\cos((N_\mathrm{B}-2)z)}\mathrm{e}^{-\mathrm{i}\omega_{x_2}\frac{A_2}{2G_2}\cos(N_\mathrm{B}z)}\,\mathrm{d}z \\
&= \sum_{n,m,\ell,o\in\mathbb{Z}} \mathrm{i}^{\ell+o} J_n\left(\frac{A_1}{2G_1}\omega_{x_1}\right) J_m\left(\frac{A_1}{2G_1}\omega_{x_1}\right) J_\ell\left(\frac{A_2}{2G_2}\omega_{x_2}\right) \\
&\qquad\qquad \times J_{-o}\left(\frac{A_2}{2G_2}\omega_{x_2}\right)\delta_{((N_\mathrm{B}-2)n+N_\mathrm{B}m+(N_\mathrm{B}-2)\ell+N_\mathrm{B}o,\ k)}
\end{aligned}$$

   and correspondingly for even N_B by

$$\begin{aligned}
P(\boldsymbol{\omega}_{\boldsymbol{x}}, k) = \sum_{n,m,\ell,o\in\mathbb{Z}} &\mathrm{i}^{\ell+o} J_n\left(\frac{A_1}{2G_1}\omega_{x_1}\right) J_m\left(\frac{A_1}{2G_1}\omega_{x_1}\right) J_\ell\left(\frac{A_2}{2G_2}\omega_{x_2}\right) \\
&\times J_{-o}\left(\frac{A_2}{2G_2}\omega_{x_2}\right)\delta_{((N_\mathrm{B}-2)n+N_\mathrm{B}m+(N_\mathrm{B}-2)\ell+N_\mathrm{B}o,\ 2k)}.
\end{aligned}$$

3. The following linear Diophantine equations must now be solved:

$$\begin{aligned}
k &= (N_\mathrm{B}-2)n + N_\mathrm{B}m + (N_\mathrm{B}-2)\ell + N_\mathrm{B}o, \text{ when } N_\mathrm{B} \text{ is odd} \\
2k &= (N_\mathrm{B}-2)n + N_\mathrm{B}m + (N_\mathrm{B}-2)\ell + N_\mathrm{B}o, \text{ when } N_\mathrm{B} \text{ is even.}
\end{aligned} \tag{7.65}$$

However, before solving the systematic linear Diophantine equation for the case of odd N_B, the solution space for (7.65) should be provided.

Lemma 7.6. *The solution space for the linear Diophantine equations in* (7.65) *with* $n, m, o, k \in \mathbb{Z}$ *and odd* N_B *is spanned by the linear hyperplane equation*

$$\begin{pmatrix} n \\ m \\ \ell \\ o \end{pmatrix} = \begin{pmatrix} -\frac{k}{2} \\ \frac{k}{2} \\ 0 \\ 0 \end{pmatrix} + \lambda_1 \begin{pmatrix} -1 \\ 0 \\ 1 \\ 0 \end{pmatrix} + \lambda_2 \begin{pmatrix} 0 \\ -1 \\ 0 \\ 1 \end{pmatrix} + \left(\lambda_3 - \frac{k \bmod 2}{2} \right) \begin{pmatrix} N_\mathrm{B} \\ -(N_\mathrm{B}-2) \\ 0 \\ 0 \end{pmatrix}$$

with $\lambda_1, \lambda_2, \lambda_3 \in \mathbb{Z}$*. If* N_B *is even, the solution space is spanned by*

$$\begin{pmatrix} n \\ m \\ \ell \\ o \end{pmatrix} = \begin{pmatrix} -k \\ k \\ 0 \\ 0 \end{pmatrix} + \lambda_1 \begin{pmatrix} -1 \\ 0 \\ 1 \\ 0 \end{pmatrix} + \lambda_2 \begin{pmatrix} 0 \\ -1 \\ 0 \\ 1 \end{pmatrix} + \frac{\lambda_3}{2} \begin{pmatrix} N_\mathrm{B} \\ -(N_\mathrm{B}-2) \\ 0 \\ 0 \end{pmatrix}$$

with $\lambda_1, \lambda_2, \lambda_3 \in \mathbb{Z}$*.*

Proof of Lemma 7.6. As an example, the procedure is shown for odd N_B and a fixed $k \in \mathbb{Z}$.

Equation (7.65) for N_B being odd is used. The smallest integer coefficient is $N_\mathrm{B} - 2$, so the equation (7.65) is rearranged with respect to $n \in \mathbb{Z}$ and divided by $N_\mathrm{B} - 2$, which results in

$$\begin{aligned} n &= -\frac{N_\mathrm{B}}{N_\mathrm{B}-2} m - \frac{N_\mathrm{B}-2}{N_\mathrm{B}-2} \ell - \frac{N_\mathrm{B}}{N_\mathrm{B}-2} o + \frac{k}{N_\mathrm{B}-2} \\ &= -\left(1 + \frac{2}{N_\mathrm{B}-2}\right) m - \ell - \left(1 + \frac{2}{N_\mathrm{B}-2}\right) o + \frac{k}{N_\mathrm{B}-2}. \end{aligned} \tag{7.66}$$

The term $\frac{k}{N_\mathrm{B}-1}$ is decomposed into its integer part and its remainder part by

$$\frac{k}{N_\mathrm{B}-1} = \underbrace{\frac{k - (k \bmod (N_\mathrm{B}-2))}{N_\mathrm{B}-2}}_{\text{integer part}} + \underbrace{\frac{(k \bmod (N_\mathrm{B}-2))}{N_\mathrm{B}-2}}_{\text{remainder part}},$$

where $a \bmod b$ denotes a modulo b between two integer values $a, b \in \mathbb{Z}$. Thus, (7.66) can be written as

$$n = \underbrace{-m - \ell - o + \frac{k - (k \bmod (N_\mathrm{B} - 2))}{N_\mathrm{B} - 2}}_{\text{integer part}} + \underbrace{\frac{(k \bmod (N_\mathrm{B} - 2)) - 2m - 2o}{N_\mathrm{B} - 2}}_{\text{remainder part}}.$$

The remainder is independent on the assignment of $\ell \in \mathbb{Z}$, so $\ell = \lambda_1$ is set with $\lambda_1 \in \mathbb{Z}$. Since the remainder must also be in $\mathbb{Z}$, the remainder must fulfill

$$\tilde{\lambda} = \frac{(k \bmod (N_\mathrm{B} - 2)) - 2m - 2o}{N_\mathrm{B} - 2} = \frac{(k \bmod (N_\mathrm{B} - 2))}{N_\mathrm{B} - 2} - \frac{2m}{N_\mathrm{B} - 2} - \frac{2o}{N_\mathrm{B} - 2} \tag{7.67}$$

with $\tilde{\lambda} \in \mathbb{Z}$.

The next step is the reordering in relation to a variable with the smallest absolute coefficient in (7.67), i.e., m and o. Since the variable m is to be used here, the result is

$$m = -o - \frac{(N_\mathrm{B} - 2)\tilde{\lambda}}{2} + \frac{(k \bmod (N_\mathrm{B} - 2))}{2}.$$

Here, too, the equation is decomposed into an integer and a remainder part by

$$m = \underbrace{-o - \frac{\overbrace{(N_\mathrm{B} - 1)}^{\text{is even}}\,\tilde{\lambda}}{2} + \frac{(k \bmod (N_\mathrm{B} - 2)) - ((k \bmod (N_\mathrm{B} - 2)) \bmod 2)}{2}}_{\text{integer part}} + \underbrace{\frac{\tilde{\lambda} + ((k \bmod (N_\mathrm{B} - 2)) \bmod 2)}{2}}_{\text{remainder part}}.$$

The variable o is independent of the assignment and it can therefore be determined that $o = \lambda_2$ with $\lambda_2 \in \mathbb{Z}$. The remainder part must also be an integer, so that the following must apply

$$\lambda_3 = \frac{\tilde{\lambda} + ((k \bmod (N_\mathrm{B} - 2)) \bmod 2)}{2} \qquad \text{with } \lambda_3 \in \mathbb{Z}.$$

Rearranging the equation with respect to $\tilde{\lambda}$ yields

$$\tilde{\lambda} = 2\lambda_3 - ((k \bmod (N_\mathrm{B} - 2)) \bmod 2).$$

Since λ_1, λ_2 and λ_3 can be arbitrary integers, the solution of (7.65) is obtained. The equations for the hyperplane are obtained by substituting the previous equations in the opposite direction, which leads to the following results

$$\begin{aligned} n &= -\lambda_1 + \lambda_3 N_\mathrm{B} - \frac{N_\mathrm{B}}{2}\left(\left(k \bmod (N_\mathrm{B}-2)\right) \bmod 2\right) - \frac{k \bmod (N_\mathrm{B}-2)}{2} \\ &\quad + \frac{k - \left(k \bmod (N_\mathrm{B}-2)\right)}{N_\mathrm{B}-2} \\ m &= -\lambda_2 - (N_\mathrm{B}-2)\lambda_3 + \frac{(N_\mathrm{B}-2)\left(\left(k \bmod (N_\mathrm{B}-2)\right) \bmod 2\right)}{2} \\ &\quad + \frac{k \bmod (N_\mathrm{B}-2)}{2} \\ \ell &= \lambda_1 \\ o &= \lambda_2, \end{aligned}$$

or in vector notation

$$\begin{pmatrix} n \\ m \\ \ell \\ o \end{pmatrix} = \underbrace{\begin{pmatrix} -\frac{N_\mathrm{B}}{2}\left(\left(k \bmod (N_\mathrm{B}-2)\right) \bmod 2\right) - \frac{k \bmod (N_\mathrm{B}-2)}{2} + \frac{k-\left(k \bmod (N_\mathrm{B}-2)\right)}{N_\mathrm{B}-2} \\ \frac{(N_\mathrm{B}-2)\left(\left(k \bmod (N_\mathrm{B}-2)\right) \bmod 2\right)}{2} + \frac{k \bmod (N_\mathrm{B}-2)}{2} \\ 0 \\ 0 \end{pmatrix}}_{=\boldsymbol{v}_0} + \underbrace{\lambda_1 \begin{pmatrix} -1 \\ 0 \\ 1 \\ 0 \end{pmatrix}}_{=\lambda_1 \boldsymbol{v}_1} + \underbrace{\lambda_2 \begin{pmatrix} 0 \\ -1 \\ 0 \\ 1 \end{pmatrix}}_{=\lambda_2 \boldsymbol{v}_2} + \underbrace{\lambda_3 \begin{pmatrix} N_\mathrm{B} \\ -(N_\mathrm{B}-2) \\ 0 \\ 0 \end{pmatrix}}_{=\lambda_3 \boldsymbol{v}_3}. \tag{7.68}$$

Note that $\boldsymbol{v}_0$ can be any vector that is a solution of (7.65). The derived $\boldsymbol{v}_0$ in (7.68) is a particular solution. Another particular solution used in Lemma 7.6 when $\lambda_1 = \lambda_2 = \lambda_3 = 0$ and with even k is

$$\begin{pmatrix} n \\ m \\ \ell \\ o \end{pmatrix} = \begin{pmatrix} -\frac{k}{2} \\ \frac{k}{2} \\ 0 \\ 0 \end{pmatrix}, \tag{7.69}$$

and for an odd k

$$\begin{pmatrix} n \\ m \\ \ell \\ o \end{pmatrix} = \begin{pmatrix} -\frac{k+N_\mathrm{B}}{2} \\ \frac{k+N_\mathrm{B}-2}{2} \\ 0 \\ 0 \end{pmatrix}. \tag{7.70}$$

The three vectors $\boldsymbol{v}_1$, $\boldsymbol{v}_2$, and $\boldsymbol{v}_3$ are linearly independent. Therefore, a hyperplane is spanned with $\lambda_1, \lambda_2, \lambda_3 \in \mathbb{Z}$ and $\boldsymbol{v}_0$. Any other particular solution on the hyperplane defined by (7.65) will span the same hyperplane, therefore $\boldsymbol{v}_0$ can be replaced by any representative on the hyperplane. For an even k, it can be seen that the particular solution in (7.69) is in $\mathbb{Z}^4$. It therefore remains to insert the solution into (7.65), and

$$\begin{aligned} &(N_\mathrm{B}-2)n + N_\mathrm{B}m + (N_\mathrm{B}-2)\ell + N_\mathrm{B}o \\ &\quad = -(N_\mathrm{B}-2)\frac{k}{2} + N_\mathrm{B}\frac{k}{2} + (N_\mathrm{B}-2)0 + N_\mathrm{B}0 \\ &\quad = -\frac{kN_\mathrm{B}}{2} + \frac{2k}{2} + \frac{kN_\mathrm{B}}{2} = k \end{aligned}$$

follows. For odd k the particular solution in (7.70) is in $\mathbb{Z}^4$, and checking the solution gives

$$\begin{aligned} &(N_\mathrm{B}-2)n + N_\mathrm{B}m + (N_\mathrm{B}-2)\ell + N_\mathrm{B}o \\ &\quad = -(N_\mathrm{B}-2)\frac{k+N_\mathrm{B}}{2} + N_\mathrm{B}\frac{k+N_\mathrm{B}-2}{2} + (N_\mathrm{B}-2)0 + N_\mathrm{B}0 \\ &\quad = -(N_\mathrm{B}-2)\frac{k}{2} + N_\mathrm{B}\frac{k}{2} - (N_\mathrm{B}-2)\frac{N_\mathrm{B}}{2} + N_\mathrm{B}\frac{N_\mathrm{B}-2}{2} \\ &\quad = -\frac{kN_\mathrm{B}}{2} + \frac{2k}{2} + \frac{kN_\mathrm{B}}{2} = k. \end{aligned}$$

The formula for an even N_B follows in a similar way and is therefore omitted here. □

Therefore, the generalized Bessel function $P(\boldsymbol{\omega}_{\boldsymbol{x}}, k)$ for the radial trajectory can be formulated in the following corollary.

Corollary 7.7. *The function $P : \mathbb{R}^3 \times \mathbb{Z} \to \mathbb{C}$ for an FFP-trajectory of the radial type* (7.63) *reads*

$$P(\boldsymbol{\omega}_{\boldsymbol{x}}, k) = \sum_{\lambda_1,\lambda_2,\lambda_3 \in \mathbb{Z}} \Bigg[\mathrm{i}^{\lambda_1+\lambda_2} J_{-\frac{k}{2}-\lambda_1+\left(\lambda_3-\frac{k \bmod 2}{2}\right)N_{\mathrm{B}}} \left(\frac{A_1}{2G_1} \omega_{x_1} \right) \times J_{\frac{k}{2}-\lambda_2-\left(\lambda_3-\frac{k \bmod 2}{2}\right)(N_{\mathrm{B}}-2)} \left(\frac{A_1}{2G_1} \omega_{x_1} \right) \times J_{\lambda_1} \left(\frac{A_2}{2G_2} \omega_{x_2} \right) J_{-\lambda_2} \left(\frac{A_2}{2G_2} \omega_{x_2} \right) \Bigg]$$

for N_{B} being odd. For N_{B} being even, the result reads

$$P(\boldsymbol{\omega}_{\boldsymbol{x}}, k) = \sum_{\lambda_1,\lambda_2,\lambda_3 \in \mathbb{Z}} \Bigg[\mathrm{i}^{\lambda_1+\lambda_2} J_{-k-\lambda_1+\lambda_3 N_{\mathrm{B}}} \left(\frac{A_1}{2G_1} \omega_{x_1} \right) \times J_{k-\lambda_2-\lambda_3(N_{\mathrm{B}}-2)} \left(\frac{A_1}{2G_1} \omega_{x_1} \right) \times J_{\lambda_1} \left(\frac{A_2}{2G_2} \omega_{x_2} \right) J_{-\lambda_2} \left(\frac{A_2}{2G_2} \omega_{x_2} \right) \Bigg].$$

It should not go unmentioned that the solution in Corollary 7.7 for the rotated part was solved by another series, so that the individual terms of the series can be represented as tensor products of Bessel functions of the first kind with respect to ω_{x_1} and ω_{x_2}. However, the inverse Fourier transform of the resulting function, which yields the spatial representation, cannot be expressed by simple tensor products of weighted Chebyshev polynomials.

A Radial Solution

In contrast to the solution in Corollary 7.7, the series terms of $P(\boldsymbol{\omega}_{\boldsymbol{x}}, k)$ can also be represented in a radial form. Here the Bessel functions then have the argument $\sqrt{\omega_{x_1}^2 \frac{A_1^2}{4G_1^2} + \omega_{x_2}^2 \frac{A_2^2}{4G_2^2}}$, which results using the trigonometric identity

$$a \sin(\xi) + b \cos(\xi) = c \sin(\xi + \varphi) \tag{7.71}$$

with $a, b, c, \varphi \in \mathbb{R}$,

$$c^2 = a^2 + b^2,$$

and

$$\varphi = \operatorname{atan2}(b, a) = \begin{cases} \arctan\left(\frac{b}{a}\right) & \text{if } a > 0, \\ \arctan\left(\frac{b}{a}\right) + \pi & \text{if } a < 0 \text{ and } b \geq 0, \\ \arctan\left(\frac{b}{a}\right) - \pi & \text{if } a < 0 \text{ and } b < 0, \\ \frac{\pi}{2} & \text{if } a = 0 \text{ and } b > 0, \\ -\frac{\pi}{2} & \text{if } a = 0 \text{ and } b < 0, \\ 0 & \text{if } a = 0 \text{ and } b = 0. \end{cases}$$

Note that the case $a = 0$ and $b = 0$ is generally undefined, but because of the occurrence in the complex exponential term $\mathrm{e}^{\mathrm{i}\varphi}$ it is useful to define $\mathrm{e}^{\mathrm{i}0} = 1$.

It should therefore be noted that using (7.64) for odd N_B, the term $\boldsymbol{\omega}_x^\mathsf{T} \boldsymbol{p}_\mathrm{FFP}(z)$ can be rewritten using the following formula

$$\begin{aligned} \boldsymbol{\omega}_x^\mathsf{T} \boldsymbol{p}_\mathrm{FFP}(z) &= \omega_{x_1} \frac{A_1}{2G_1} \sin\big((N_\mathrm{B} - 2)z\big) + \omega_{x_1} \frac{A_1}{2G_1} \sin(N_\mathrm{B} z) \\ &\quad + \omega_{x_2} \frac{A_2}{2G_2} \cos\big((N_\mathrm{B} - 2)z\big) - \omega_{x_2} \frac{A_2}{2G_2} \cos(N_\mathrm{B} z) \\ &= \omega_{x_1} \frac{A_1}{2G_1} \sin\big((N_\mathrm{B} - 2)z\big) + \omega_{x_2} \frac{A_2}{2G_2} \cos\big((N_\mathrm{B} - 2)z\big) \\ &\quad + \omega_{x_1} \frac{A_1}{2G_1} \sin(N_\mathrm{B} z) - \omega_{x_2} \frac{A_2}{2G_2} \cos(N_\mathrm{B} z) \\ &= \sqrt{\omega_{x_1}^2 \frac{A_1^2}{4G_1^2} + \omega_{x_2}^2 \frac{A_2^2}{4G_2^2}} \sin\big((N_\mathrm{B} - 2)z + \theta(\omega_{x_1}, \omega_{x_2})\big) \\ &\quad + \underbrace{\sqrt{\omega_{x_1}^2 \frac{A_1^2}{4G_1^2} + \omega_{x_2}^2 \frac{A_2^2}{4G_2^2}}}_{=A(\omega_{x_1},\, \omega_{x_2})} \sin\big(N_\mathrm{B} z + \underbrace{\theta(\omega_{x_1}, -\omega_{x_2})}_{=-\theta(\omega_{x_1},\, \omega_{x_2})}\big) \end{aligned}$$

with

$$\theta(\omega_{x_1}, \omega_{x_2}) = \operatorname{atan2}\left(\omega_{x_2} \frac{A_2}{2G_2}, \omega_{x_1} \frac{A_1}{2G_1}\right).$$

In the case that N_B is even, one obtains in a similar way

$$\begin{aligned}\boldsymbol{\omega}_{\boldsymbol{x}}^{\mathsf{T}}\boldsymbol{p}_{\mathrm{FFP}}(z) = A(\omega_{x_1},\,\omega_{x_2})\sin\!\left(\frac{N_\mathrm{B}-2}{2}z+\theta(\omega_{x_1},\omega_{x_2})\right)\\ + A(\omega_{x_1},\,\omega_{x_2})\sin\!\left(\frac{N_\mathrm{B}}{2}z-\theta(\omega_{x_1},\omega_{x_2})\right).\end{aligned}$$

The solution of the integral in (7.61) using the Jacobi-Anger expansion (7.62) for odd N_B gives

$$\begin{aligned}P(\boldsymbol{\omega}_{\boldsymbol{x}},k) &= \frac{1}{2\pi}\int_{-\pi}^{\pi}\mathrm{e}^{\mathrm{i}\boldsymbol{\omega}_{\boldsymbol{x}}^{T}\boldsymbol{p}_{\mathrm{FFP}}(z)}\mathrm{e}^{-\mathrm{i}kz}\,\mathrm{d}z\\ &= \sum_{n,m\in\mathbb{Z}}\mathrm{e}^{\mathrm{i}(n-m)\theta(\omega_{x_1},\,\omega_{x_2})}J_n\big(A(\omega_{x_1},\omega_{x_2})\big)J_m\big(A(\omega_{x_1},\omega_{x_2})\big)\\ &\qquad\times\delta_{((N_\mathrm{B}-2)n+N_\mathrm{B}m,\,k)},\end{aligned}$$

and for even N_B

$$\begin{aligned}P(\boldsymbol{\omega}_{\boldsymbol{x}},k) = \sum_{n,m\in\mathbb{Z}}\mathrm{e}^{\mathrm{i}(n-m)\theta(\omega_{x_1},\,\omega_{x_2})}J_n\big(A(\omega_{x_1},\omega_{x_2})\big)J_m\big(A(\omega_{x_1},\omega_{x_2})\big)\\ \times\delta_{((N_\mathrm{B}-2)n+N_\mathrm{B}m,\,2k)}.\end{aligned}$$

The constraint

$$k=(N_\mathrm{B}-2)n+N_\mathrm{B}m$$

for an odd N_B is solved by

$$\begin{pmatrix}n\\m\end{pmatrix}=\begin{pmatrix}-\frac{k}{2}\\ \frac{k}{2}\end{pmatrix}+\left(\lambda-\frac{k\bmod 2}{2}\right)\begin{pmatrix}N_\mathrm{B}\\-(N_\mathrm{B}-2)\end{pmatrix},\qquad\lambda\in\mathbb{Z},$$

with $k,n,m\in\mathbb{Z}$ and for an even N_B the constraint

$$2k=(N_\mathrm{B}-2)n+N_\mathrm{B}m$$

is solved by

$$\begin{pmatrix}n\\m\end{pmatrix}=\begin{pmatrix}-k\\k\end{pmatrix}+\frac{\lambda}{2}\begin{pmatrix}N_\mathrm{B}\\-(N_\mathrm{B}-2)\end{pmatrix},\qquad\lambda\in\mathbb{Z},$$

with $k, n, m \in \mathbb{Z}$. Both solutions can be deduced from Lemma 7.6. Finally, the following corollary can be formulated similarly to Corollary 7.7.

Corollary 7.8. *The function $P : \mathbb{R}^3 \times \mathbb{Z} \to \mathbb{C}$ for an FFP-trajectory of the radial type* (7.63) *is*

$$P(\boldsymbol{\omega}_{\boldsymbol{x}}, k) = \sum_{\lambda \in \mathbb{Z}} \mathrm{e}^{\mathrm{i}[n_k(\lambda) - m_k(\lambda)]\theta(\omega_{x_1},\, \omega_{x_2})} J_{n_k(\lambda)}\big(A(\omega_{x_1}, \omega_{x_2})\big) J_{m_k(\lambda)}\big(A(\omega_{x_1}, \omega_{x_2})\big),$$

where

$$A(\omega_{x_1}, \omega_{x_2}) = \sqrt{\omega_{x_1}^2 \frac{A_1^2}{4G_1^2} + \omega_{x_2}^2 \frac{A_2^2}{4G_2^2}},$$

$$\theta(\omega_{x_1}, \omega_{x_2}) = \operatorname{atan2}\left(\omega_{x_2} \frac{A_2}{2G_2}, \omega_{x_1} \frac{A_1}{2G_1}\right),$$

$$n_k(\lambda) = \begin{cases} -\frac{k}{2} + \left(\lambda - \frac{k \bmod 2}{2}\right) N_{\mathrm{B}}, & \text{if } N_{\mathrm{B}} \text{ is odd,} \\ -k + \frac{\lambda}{2} N_{\mathrm{B}}, & \text{if } N_{\mathrm{B}} \text{ is even,} \end{cases}$$

and

$$m_k(\lambda) = \begin{cases} \frac{k}{2} - \left(\lambda - \frac{k \bmod 2}{2}\right)(N_{\mathrm{B}} - 2), & \text{if } N_{\mathrm{B}} \text{ is odd,} \\ k - \frac{\lambda}{2}(N_{\mathrm{B}} - 2), & \text{if } N_{\mathrm{B}} \text{ is even.} \end{cases}$$

It should be noted that the complex exponential term in Corollary 7.8 could also be rewritten as

$$\mathrm{e}^{\mathrm{i}\theta(\omega_{x_1},\, \omega_{x_2})} = \frac{\omega_{x_1} \frac{A_1}{2G_1} + \mathrm{i}\omega_{x_2} \frac{A_2}{2G_2}}{A(\omega_{x_1}, \omega_{x_2})},$$

which allows for an alternative expression of $P(\boldsymbol{\omega}_{\boldsymbol{x}}, k)$.

The inverse spatial Fourier transform of $P(\boldsymbol{\omega}_{\boldsymbol{x}}, k)$ in Corollary 7.8 is not easy to specify because there is no Chebyshev polynomial correspondence as in the case of the fully separated solution in Corollary 7.7.

7.4.4 Spiral Trajectory

The spiral trajectory (see Table 7.2) is

$$\begin{aligned}\boldsymbol{x}_{\mathrm{FFP}}(t) &= \begin{pmatrix} \frac{A_1}{G_1}\sin(\omega_1 t)\sin(\omega_2 t) \\ \frac{A_2}{G_2}\sin(\omega_2 t)\cos(\omega_1 t) \\ 0 \end{pmatrix} \\ &= \begin{pmatrix} \frac{A_1}{2G_1}\left[\cos\big((\omega_2-\omega_1)t\big) - \cos\big((\omega_2+\omega_1)t\big)\right] \\ \frac{A_2}{2G_2}\left[\sin\big((\omega_2-\omega_1)t\big) + \sin\big((\omega_2+\omega_1)t\big)\right] \\ 0 \end{pmatrix}, \end{aligned} \tag{7.72}$$

where $\omega_1 = 2\pi f_1$, $\omega_2 = 2\pi f_2$, $f_1 = \frac{f_B}{N_B}$, and $f_2 = \frac{f_{\mathrm{B}}}{N_{\mathrm{B}}(N_{\mathrm{B}}-1)}$. The period length for this trajectory is

$$T_{\mathrm{D}} = \frac{1}{f_{\mathrm{D}}} = \begin{cases} \dfrac{N_{\mathrm{B}}(N_{\mathrm{B}}-1)}{2f_{\mathrm{B}}}, & \text{if } N_{\mathrm{B}} \text{ is even,} \\ \dfrac{N_{\mathrm{B}}(N_{\mathrm{B}}-1)}{f_{\mathrm{B}}}, & \text{if } N_{\mathrm{B}} \text{ is odd.} \end{cases}$$

For the spiral FFP in (7.72), the function $\boldsymbol{p}_{\mathrm{FFP}}(z)$ is given by

$$\begin{aligned}\boldsymbol{p}_{\mathrm{FFP}}(z) &= \begin{pmatrix} \frac{A_1}{2G_1}\left[\cos\left(f_{\mathrm{B}}\frac{2-N_{\mathrm{B}}}{N_{\mathrm{B}}(N_{\mathrm{B}}-1)}\frac{z}{f_{\mathrm{D}}}\right) - \cos\left(f_{\mathrm{B}}\frac{N_{\mathrm{B}}}{N_{\mathrm{B}}(N_{\mathrm{B}}-1)}\frac{z}{f_{\mathrm{D}}}\right)\right] \\ \frac{A_2}{2G_2}\left[\sin\left(f_{\mathrm{B}}\frac{2-N_{\mathrm{B}}}{N_{\mathrm{B}}(N_{\mathrm{B}}-1)}\frac{z}{f_{\mathrm{D}}}\right) + \sin\left(f_{\mathrm{B}}\frac{N_{\mathrm{B}}}{N_{\mathrm{B}}(N_{\mathrm{B}}-1)}\frac{z}{f_{\mathrm{D}}}\right)\right] \\ 0 \end{pmatrix} \\ &= \begin{cases} \begin{pmatrix} \frac{A_1}{2G_1}\left[\cos\big(\frac{N_{\mathrm{B}}-2}{2}z\big) - \cos\big(\frac{N_{\mathrm{B}}}{2}z\big)\right] \\ \frac{A_2}{2G_2}\left[\sin\big(\frac{N_{\mathrm{B}}}{2}z\big) - \sin\big(\frac{N_{\mathrm{B}}-2}{2}z\big)\right] \\ 0 \end{pmatrix}, & \text{if } N_{\mathrm{B}} \text{ is even,} \\ \begin{pmatrix} \frac{A_1}{2G_1}\left[\cos\big((N_{\mathrm{B}}-2)z\big) - \cos\big(N_{\mathrm{B}}z\big)\right] \\ \frac{A_2}{2G_2}\left[\sin\big(N_{\mathrm{B}}z\big) - \sin\big((N_{\mathrm{B}}-2)z\big)\right] \\ 0 \end{pmatrix}, & \text{if } N_{\mathrm{B}} \text{ is odd,} \end{cases} \end{aligned} \tag{7.73}$$

where $\sin(-\xi) = -\sin(\xi)$ and $\cos(-\xi) = \cos(\xi)$ were used in the second equation.

Therefore, the integral can be solved using the Jacobi-Anger expansions in (7.62) for an odd N_B as follows,

$$P(\boldsymbol{\omega}_{\boldsymbol{x}}, k) = \sum_{n,m,\ell,o\in\mathbb{Z}} \mathrm{i}^{\ell+o} J_\ell\left(\frac{A_1}{2G_1}\omega_{x_1}\right) J_{-o}\left(\frac{A_1}{2G_1}\omega_{x_1}\right) J_{-n}\left(\frac{A_2}{2G_2}\omega_{x_2}\right) J_m\left(\frac{A_2}{2G_2}\omega_{x_2}\right) \times \delta_{((N_\mathrm{B}-2)n+N_\mathrm{B}m+(N_\mathrm{B}-2)\ell+N_\mathrm{B}o,\ k)},$$

and for an even N_B by

$$P(\boldsymbol{\omega}_{\boldsymbol{x}}, k) = \sum_{n,m,\ell,o\in\mathbb{Z}} \mathrm{i}^{\ell+o} J_\ell\left(\frac{A_1}{2G_1}\omega_{x_1}\right) J_{-o}\left(\frac{A_1}{2G_1}\omega_{x_1}\right) J_{-n}\left(\frac{A_2}{2G_2}\omega_{x_2}\right) J_m\left(\frac{A_2}{2G_2}\omega_{x_2}\right) \times \delta_{((N_\mathrm{B}-2)n+N_\mathrm{B}m+(N_\mathrm{B}-2)\ell+N_\mathrm{B}o,\ 2k)}.$$

This results in the same condition as for the radial FFP-trajectory in (7.65), which means that the result from Lemma 7.6 can be used. Note that the indices $n, m, \ell, o \in \mathbb{Z}$ are deliberately chosen so that the complex phase term $\mathrm{i}^{\ell+o}$ behaves in a similar way to step 2 in the radial FFP-trajectory case. Consequently, the corollary is formulated equivalently to Corollary 7.7.

Corollary 7.9. *The function $P : \mathbb{R}^3 \times \mathbb{Z} \to \mathbb{C}$ for an FFP-trajectory of the spiral type* (7.72) *with odd N_B reads*

$$P(\boldsymbol{\omega}_{\boldsymbol{x}}, k) = \sum_{\lambda_1,\lambda_2,\lambda_3\in\mathbb{Z}} \Bigg[\mathrm{i}^{\lambda_1+\lambda_2} J_{\lambda_1}\left(\frac{A_1}{2G_1}\omega_{x_1}\right) J_{-\lambda_2}\left(\frac{A_1}{2G_1}\omega_{x_1}\right) \times J_{\frac{k}{2}+\lambda_1-\left(\lambda_3-\frac{k \bmod 2}{2}\right)N_\mathrm{B}}\left(\frac{A_2}{2G_2}\omega_{x_2}\right) \times J_{\frac{k}{2}-\lambda_2-\left(\lambda_3-\frac{k \bmod 2}{2}\right)(N_\mathrm{B}-2)}\left(\frac{A_2}{2G_2}\omega_{x_2}\right) \Bigg].$$

If N_B is even, the result is

$$P(\boldsymbol{\omega}_{\boldsymbol{x}}, k) = \sum_{\lambda_1,\lambda_2,\lambda_3\in\mathbb{Z}} \Bigg[\mathrm{i}^{\lambda_1+\lambda_2} J_{\lambda_1}\left(\frac{A_1}{2G_1}\omega_{x_1}\right) J_{-\lambda_2}\left(\frac{A_1}{2G_1}\omega_{x_1}\right) \times J_{k+\lambda_1-\lambda_3 N_\mathrm{B}}\left(\frac{A_2}{2G_2}\omega_{x_2}\right) \times J_{k-\lambda_2-\lambda_3(N_\mathrm{B}-2)}\left(\frac{A_2}{2G_2}\omega_{x_2}\right) \Bigg].$$

A Radial Solution

The radial solution can be derived in a similar way as for Corollary 7.8, therefore it is formulated below without derivation.

Corollary 7.10. *The function $P : \mathbb{R}^3 \times \mathbb{Z} \to \mathbb{C}$ for an FFP-trajectory of the spiral type* (7.72) *is*

$$\begin{aligned} P(\boldsymbol{\omega}_{\boldsymbol{x}}, k) &= \sum_{\lambda\in\mathbb{Z}} \Bigg[\mathrm{e}^{\mathrm{i}[n_k(\lambda)\tilde{\theta}(\omega_{x_1},\, -\omega_{x_2}) + m_k(\lambda)\tilde{\theta}(-\omega_{x_1},\, \omega_{x_2})]} J_{n_k(\lambda)}\big(A(\omega_{x_1},\omega_{x_2})\big) \\ &\qquad \times J_{m_k(\lambda)}\big(A(\omega_{x_1},\omega_{x_2})\big) \Bigg] \\ &= \sum_{\lambda\in\mathbb{Z}} \Bigg[(-1)^{n_k(\lambda)} \mathrm{e}^{-\mathrm{i}[n_k(\lambda)+m_k(\lambda)]\tilde{\theta}(\omega_{x_1},\, \omega_{x_2})} J_{n_k(\lambda)}\big(A(\omega_{x_1},\omega_{x_2})\big) \\ &\qquad \times J_{m_k(\lambda)}\big(A(\omega_{x_1},\omega_{x_2})\big) \Bigg], \end{aligned}$$

where

$$A(\omega_{x_1},\omega_{x_2}) = \sqrt{\omega_{x_1}^2 \frac{A_1^2}{4G_1^2} + \omega_{x_2}^2 \frac{A_2^2}{4G_2^2}},$$

$$\tilde{\theta}(\omega_{x_1},\omega_{x_2}) = \operatorname{atan2}\left(\omega_{x_1}\frac{A_1}{2G_1}, \omega_{x_2}\frac{A_2}{2G_2}\right),$$

$$n_k(\lambda) = \begin{cases} -\frac{k}{2} + \left(\lambda - \frac{k \bmod 2}{2}\right) N_{\mathrm{B}}, & \textit{if } N_{\mathrm{B}} \textit{ is odd,} \\ -k + \frac{\lambda}{2} N_{\mathrm{B}}, & \textit{if } N_{\mathrm{B}} \textit{ is even,} \end{cases}$$

and

$$m_k(\lambda) = \begin{cases} \frac{k}{2} - \left(\lambda - \frac{k \bmod 2}{2}\right)(N_{\mathrm{B}} - 2), & \textit{if } N_{\mathrm{B}} \textit{ is odd,} \\ k - \frac{\lambda}{2}(N_{\mathrm{B}} - 2), & \textit{if } N_{\mathrm{B}} \textit{ is even.} \end{cases}$$

The exponential term $\mathrm{e}^{\mathrm{i}\tilde{\theta}(\omega_{x_1},\omega_{x_2})}$ can be rewritten equivalently to the radial FFP case as

$$\mathrm{e}^{\mathrm{i}\tilde{\theta}(\omega_{x_1},\omega_{x_2})} = \frac{\omega_{x_2}\frac{A_2}{2G_2} + \mathrm{i}\omega_{x_1}\frac{A_1}{2G_1}}{A(\omega_{x_1},\omega_{x_2})},$$

so that the exponential term in Corollary 7.10 can also be expressed by

$$\begin{aligned}
\mathrm{e}^{\mathrm{i}[n_k\tilde{\theta}(\omega_{x_1},\,-\omega_{x_2})+m_k\tilde{\theta}(-\omega_{x_1},\,\omega_{x_2})]} &= \left(\frac{-\omega_{x_2}\frac{A_2}{2G_2}+\mathrm{i}\omega_{x_1}\frac{A_1}{2G_1}}{A(\omega_{x_1},\omega_{x_2})}\right)^{n_k}\left(\frac{\omega_{x_2}\frac{A_2}{2G_2}-\mathrm{i}\omega_{x_1}\frac{A_1}{2G_1}}{A(\omega_{x_1},\omega_{x_2})}\right)^{m_k}\\
&= (-1)^{n_k}\left(\frac{\omega_{x_2}\frac{A_2}{2G_2}-\mathrm{i}\omega_{x_1}\frac{A_1}{2G_1}}{A(\omega_{x_1},\omega_{x_2})}\right)^{n_k+m_k}\\
&= (-1)^{n_k}\,\mathrm{e}^{-\mathrm{i}(n_k+m_k)\tilde{\theta}(\omega_{x_1},\,\omega_{x_2})},
\end{aligned}$$

where λ has been omitted for the sake of simplicity.

7.4.5 Cartesian-like Trajectory

In two-dimensional MPI the position of the Cartesian-like FFP-trajectory (see Table 7.2) reads

$$\boldsymbol{x}_{\mathrm{FFP}}(t) = \begin{pmatrix} \frac{A_1}{G_1}\sin(\omega_1 t+\varphi_1) \\ \frac{A_2}{G_2}\sin(\omega_2 t+\varphi_1) \\ 0 \end{pmatrix}, \tag{7.74}$$

where $\omega_1 = 2\pi f_1$, $\omega_2 = 2\pi f_2$, $f_1 = \frac{f_B}{N_\mathrm{B}}$, $f_2 = \frac{f_\mathrm{B}}{N_\mathrm{B}(N_\mathrm{B}-1)}$, and $\varphi_1, \varphi_2 \in [0, 2\pi)$. The period length for this trajectory is

$$T_\mathrm{D} = \frac{1}{f_\mathrm{D}} = \frac{N_\mathrm{B}(N_\mathrm{B}-1)}{f_\mathrm{B}}.$$

For the two-dimensional Cartesian drive field in (7.74), the position of the FFP $\boldsymbol{p}_{\mathrm{FFP}}(z)$ is

$$\boldsymbol{p}_{\mathrm{FFP}}(z) = \begin{pmatrix} \frac{A_1}{G_1}\sin\big((N_\mathrm{B}-1)\,z+\varphi_1\big) \\ \frac{A_2}{G_2}\sin(z+\varphi_2) \\ 0 \end{pmatrix}.$$

To obtain the mapping function $P(\boldsymbol{\omega}_{\boldsymbol{x}}, k)$, the integral in (7.61) is evaluated and results in

$$P(\boldsymbol{\omega}_{\boldsymbol{x}}, k) = \sum_{n,m\in\mathbb{Z}} \mathrm{e}^{\mathrm{i}(n\varphi_1+m\varphi_2)} J_n\left(\frac{A_1}{G_1}\omega_{x_1}\right) J_m\left(\frac{A_2}{G_2}\omega_{x_2}\right) \delta_{((N_\mathrm{B}-1)n+m,\,k)} \tag{7.75}$$

with the help of (7.62). The following corollary holds.

Corollary 7.11. *The function $P : \mathbb{R}^3 \times \mathbb{Z} \to \mathbb{C}$ for an FFP-trajectory of the two-dimensional Cartesian-like type* (7.74) *with $N_\mathrm{B} \in \mathbb{N}$ is*

$$P(\boldsymbol{\omega}_{\boldsymbol{x}}, k) = \sum_{\lambda \in \mathbb{Z}} \mathrm{e}^{\mathrm{i}(\lambda\varphi_1 + (k - \lambda(N_\mathrm{B}-1))\varphi_2)} J_\lambda\left(\frac{A_1}{G_1}\omega_{x_1}\right) J_{k-\lambda(N_\mathrm{B}-1)}\left(\frac{A_2}{G_2}\omega_{x_2}\right).$$

Proof of Corollary 7.11. The constraint that have to be fulfilled is

$$k = (N_\mathrm{B} - 1)n + m$$

with $k, n, m \in \mathbb{Z}$. By rearranging this equation with respect to m one obtains

$$m = k - (N_\mathrm{B} - 1)n,$$

which is the solution to the constraint. Inserting this solution in (7.62) completes the proof of Corollary 7.11. □

For three-dimensional MPI, the Cartesian FFP-trajectory position reads [53]

$$\boldsymbol{x}_\mathrm{FFP}(t) = \begin{pmatrix} \frac{A_1}{G_1}\sin(\omega_1 t + \varphi_1) \\ \frac{A_2}{G_2}\sin(\omega_2 t + \varphi_2) \\ \frac{A_3}{G_3}\sin(\omega_3 t + \varphi_3) \end{pmatrix} \tag{7.76}$$

with $\omega_i = 2\pi f_i$, $i \in \{1, 2, 3\}$ and $f_\mathrm{B} = f_1 = N_\mathrm{B} f_2 = N_\mathrm{B}^2 f_3$. With such a choice of the frequency dividers, the period length results in

$$T_\mathrm{D} = \frac{N_\mathrm{B}^2}{f_\mathrm{B}}.$$

Consequently, the three-dimensional Cartesian FFP in (7.76) results in the function

$$\boldsymbol{p}_\mathrm{FFP}(z) = \begin{pmatrix} \frac{A_1}{G_1}\sin(N_\mathrm{B}^2 z + \varphi_1) \\ \frac{A_2}{G_2}\sin(N_\mathrm{B} z + \varphi_2) \\ \frac{A_3}{G_3}\sin(z + \varphi_3) \end{pmatrix}. \tag{7.77}$$

The integral in (7.61) is evaluated with the help of (7.62) according to

$$P(\boldsymbol{\omega}_{\boldsymbol{x}}, k) = \sum_{n,m,\ell\in\mathbb{Z}} \mathrm{e}^{\mathrm{i}(n\varphi_1+m\varphi_2+\ell\varphi_3)} J_n\left(\frac{A_1}{G_1}\omega_{x_1}\right) J_m\left(\frac{A_2}{G_2}\omega_{x_2}\right) J_\ell\left(\frac{A_3}{G_3}\omega_{x_3}\right) \times \delta_{\left(N_\mathrm{B}^2 n+N_\mathrm{B} m+\ell,\, k\right)}.$$

The related constraint is

$$k = N_\mathrm{B}^2 n + N_\mathrm{B} m + \ell$$

with $k, n, m, \ell \in \mathbb{Z}$. The subsequent rearrangement of the constraint with respect to ℓ results in

$$\ell = k - N_\mathrm{B}^2 n - N_\mathrm{B} m$$

and, thus, the following corollary can be formulated.

Corollary 7.12. *The function* $P : \mathbb{R}^3 \times \mathbb{Z} \to \mathbb{C}$ *for an FFP-trajectory of the three-dimensional Cartesian-like type* (7.76) *with* $N_\mathrm{B} \in \mathbb{N}$ *reads*

$$P(\boldsymbol{\omega}_{\boldsymbol{x}}, k) = \sum_{\lambda_1,\lambda_2\in\mathbb{Z}} \mathrm{e}^{\mathrm{i}[n_k(\lambda_1)\varphi_1+m_k(\lambda_2)\varphi_2+\ell_k(\lambda_1,\lambda_2)\varphi_3]} J_{n_k(\lambda_1)}\left(\frac{A_1}{G_1}\omega_{x_1}\right) J_{m_k(\lambda_2)}\left(\frac{A_2}{G_2}\omega_{x_2}\right) \times J_{\ell_k(\lambda_1,\lambda_2)}\left(\frac{A_3}{G_3}\omega_{x_3}\right),$$

where $n_k(\lambda_1) = \lambda_1$, $m_k(\lambda_2) = \lambda_2$, *and* $\ell_k(\lambda_1, \lambda_2) = k - \lambda_1 N_\mathrm{B}^2 - \lambda_2 N_\mathrm{B}$.

7.4.6 Flower Trajectory

The position of the two-dimensional flower trajectory (see Table 7.2) is defined by

$$\boldsymbol{x}_{\mathrm{FFP}}(t) = \begin{pmatrix} \frac{A_1}{G_1}\sin(\omega_1 t)\cos(\omega_2 t) \\ \frac{A_2}{G_2}\sin(\omega_2 t)\sin(\omega_1 t) \\ 0 \end{pmatrix} = \begin{pmatrix} \frac{A_1}{2G_1}\left[\sin\big((\omega_1-\omega_2)t\big)+\sin\big((\omega_1+\omega_2)t\big)\right] \\ \frac{A_2}{2G_2}\left[\cos\big((\omega_2-\omega_1)t\big)-\cos\big((\omega_2+\omega_1)t\big)\right] \\ 0 \end{pmatrix}, \tag{7.78}$$

where $\omega_1 = 2\pi f_1$, $\omega_2 = 2\pi f_2$, $f_1 = \frac{f_B}{N_\mathrm{B}}$, and $f_2 = \frac{f_\mathrm{B}}{N_\mathrm{B}-1}$. The period length for this trajectory is

$$T_\mathrm{D} = \frac{1}{f_\mathrm{D}} = \frac{N_\mathrm{B}(N_\mathrm{B}-1)}{f_\mathrm{B}}.$$

The rescaled FFP position function is

$$\boldsymbol{p}_{\mathrm{FFP}}(z) = \begin{pmatrix} \frac{A_1}{2G_1}\left[\sin\big((2N_\mathrm{B}-1)z\big)-\sin(z)\right] \\ \frac{A_2}{2G_2}\left[\cos(z)-\cos\big((2N_\mathrm{B}-1)z\big)\right] \\ 0 \end{pmatrix}. \tag{7.79}$$

The mapping function $P(\boldsymbol{\omega}_{\boldsymbol{x}}, k)$ in (7.61) is evaluated with the help of (7.62) according to

$$P(\boldsymbol{\omega}_{\boldsymbol{x}}, k) = \sum_{n,m,\ell,o\in\mathbb{Z}} \mathrm{i}^{\ell+o} J_n\left(\frac{A_1}{2G_1}\omega_{x1}\right) J_{-m}\left(\frac{A_1}{2G_1}\omega_{x1}\right) J_{-\ell}\left(\frac{A_2}{2G_2}\omega_{x2}\right) J_o\left(\frac{A_2}{2G_2}\omega_{x2}\right) \times \delta_{((2N_\mathrm{B}-1)n+m+(2N_\mathrm{B}-1)\ell+o,\ k)}.$$

The solution of the linear Diophantine equation finally leads to the following corollary.

Corollary 7.13. *The function $P : \mathbb{R}^3 \times \mathbb{Z} \to \mathbb{C}$ for an FFP-trajectory of the two-dimensional flower type* (7.78) *with $N_\mathrm{B} \in \mathbb{N}$ reads*

$$P(\boldsymbol{\omega}_{\boldsymbol{x}}, k) = \sum_{\lambda_1,\lambda_2,\lambda_3\in\mathbb{Z}} \mathrm{i}^{\lambda_2+\lambda_3} J_{\lambda_1}\left(\frac{A_1}{2G_1}\omega_{x1}\right) J_{-k+(2N_\mathrm{B}-1)(\lambda_1+\lambda_2)+\lambda_3}\left(\frac{A_1}{2G_1}\omega_{x1}\right) \times J_{-\lambda_2}\left(\frac{A_2}{2G_2}\omega_{x2}\right) J_{\lambda_3}\left(\frac{A_2}{2G_2}\omega_{x2}\right).$$

A Radial Solution

Like the radial FFP in Corollary 7.8 and the spiral FFP in Corollary 7.10, the flower FFP mapping function $P(\boldsymbol{\omega}_{\boldsymbol{x}}, k)$ can also be formulated in a radial form. Therefore, the scalar product between $\boldsymbol{\omega}_{\boldsymbol{x}}$ and $\boldsymbol{p}_{\mathrm{FFP}}(z)$ is calculated first, resulting in

$$\begin{aligned}
\boldsymbol{\omega}_{\boldsymbol{x}}^{\mathsf{T}}\boldsymbol{p}_{\mathrm{FFP}}(z) &= \omega_{x_1}\frac{A_1}{2G_1}\sin\big((2N_{\mathrm{B}}-1)z\big) - \omega_{x_1}\frac{A_1}{2G_1}\sin(z) \\
&\quad + \omega_{x_2}\frac{A_2}{2G_2}\cos(z) - \omega_{x_2}\frac{A_2}{2G_2}\cos\big((2N_{\mathrm{B}}-1)z\big) \\
&= \omega_{x_1}\frac{A_1}{2G_1}\sin\big((2N_{\mathrm{B}}-1)z\big) - \omega_{x_2}\frac{A_2}{2G_2}\cos\big((2N_{\mathrm{B}}-1)z\big) \\
&\quad - \omega_{x_1}\frac{A_1}{2G_1}\sin(z) + \omega_{x_2}\frac{A_2}{2G_2}\cos(z) \\
&= A(\omega_{x_1},\omega_{x_2})\sin\big((2N_{\mathrm{B}}-1)z + \theta(\omega_{x_1},-\omega_{x_2})\big) \\
&\quad + A(\omega_{x_1},\omega_{x_2})\sin\big(z + \theta(-\omega_{x_1},\omega_{x_2})\big)
\end{aligned}$$

with

$$A(\omega_{x_1},\omega_{x_2}) = \sqrt{\omega_{x_1}^2\frac{A_1^2}{4G_1^2} + \omega_{x_2}^2\frac{A_2^2}{4G_2^2}}$$

and

$$\theta(\omega_{x_1},\omega_{x_2}) = \operatorname{atan2}\left(\omega_{x_2}\frac{A_2}{2G_2}, \omega_{x_1}\frac{A_1}{2G_1}\right).$$

The evaluation of (7.61) results in

$$\begin{aligned}
P(\boldsymbol{\omega}_{\boldsymbol{x}}, k) = \sum_{n,m\in\mathbb{Z}} &\mathrm{e}^{\mathrm{i}[n\theta(\omega_{x_1},\,-\omega_{x_2})+m\theta(-\omega_{x_1},\,\omega_{x_2})]} J_n\big(A(\omega_{x_1},\omega_{x_2})\big) J_m\big(A(\omega_{x_1},\omega_{x_2})\big) \\
&\times \delta_{((2N_{\mathrm{B}}-1)n+m,\,k)}.
\end{aligned}$$

The reformulation of the complex exponential, as carried out for the radial FFP and the spiral FFP, finally results in

$$\begin{aligned}
\mathrm{e}^{\mathrm{i}[n\theta(\omega_{x_1},\,-\omega_{x_2})+m\theta(-\omega_{x_1},\,\omega_{x_2})]} &= \left(\frac{\omega_{x_1}\frac{A_1}{2G_1} - \mathrm{i}\omega_{x_2}\frac{A_2}{2G_2}}{A(\omega_{x_1},\omega_{x_2})}\right)^n \left(\frac{-\omega_{x_1}\frac{A_1}{2G_1} + \mathrm{i}\omega_{x_2}\frac{A_2}{2G_2}}{A(\omega_{x_1},\omega_{x_2})}\right)^m \\
&= (-1)^m \left(\frac{\omega_{x_1}\frac{A_1}{2G_1} - \mathrm{i}\omega_{x_2}\frac{A_2}{2G_2}}{A(\omega_{x_1},\omega_{x_2})}\right)^{n+m} \\
&= (-1)^m \mathrm{e}^{-\mathrm{i}(n+m)\theta(\omega_{x_1},\,\omega_{x_2})}.
\end{aligned}$$

Thus, the corollary that summarizes the previous result can now be formulated.

Corollary 7.14. *The function* $P : \mathbb{R}^3 \times \mathbb{Z} \to \mathbb{C}$ *for an FFP-trajectory of the flower type* (7.78) *is*

$$P(\boldsymbol{\omega}_{\boldsymbol{x}}, k) = \sum_{\lambda \in \mathbb{Z}} \Bigg[(-1)^{m_k(\lambda)} \mathrm{e}^{-\mathrm{i}[\lambda + m_k(\lambda)]\theta(\omega_{x_1},\, \omega_{x_2})} J_\lambda\big(A(\omega_{x_1}, \omega_{x_2})\big) \times J_{m_k(\lambda)}\big(A(\omega_{x_1}, \omega_{x_2})\big) \Bigg],$$

where

$$A(\omega_{x_1}, \omega_{x_2}) = \sqrt{\omega_{x_1}^2 \frac{A_1^2}{4G_1^2} + \omega_{x_2}^2 \frac{A_2^2}{4G_2^2}},$$

$$\theta(\omega_{x_1}, \omega_{x_2}) = \operatorname{atan2}\left(\omega_{x_2} \frac{A_2}{2G_2}, \omega_{x_1} \frac{A_1}{2G_1} \right),$$

and

$$m_k(\lambda) = k - (2N_\mathrm{B} - 1)\lambda.$$

8 Conclusions & Outlook

In this thesis, a general mathematical framework based on the Langevin model of paramagnetism was introduced to describe the mapping of magnetic particles in the spatio-temporal Fourier domain for arbitrary periodic FFP-trajectories. For this purpose, the multidimensional Fourier transform of the Langevin function (see Theorem 6.5) was derived and combined with a concept of the FFP-trajectory-dependent mapping function of (6.7). It was also pointed out that the Langevin function can be replaced by other magnetization curves given by the anisotropic equilibrium model and its series representation in (3.39).

To illustrate and verify the obtained expressions, simulations were performed that enrich the results presented in [F1]. In addition, expressions for the corresponding mapping function (6.7) for the flower, Cartesian, radial and spiral FFP-trajectories were derived for the first time in this thesis (see Figure 7.6).

The results presented are of great importance for a deeper theoretical and mathematical understanding of MPI. Many observed phenomena in MPI can be explained or proven using this model. For instance, the formulation helps to validate reconstruction strategies based on Chebyshev polynomials and matrix compression strategies [F2, 57, 60, 91] and explains the frequency mixing between spatial and temporal frequencies.

A major problem, as mentioned in this thesis, is the lack of a good model for the system function in MPI, i.e., the system function is usually measured in a time-consuming procedure that, for example, takes up to three days for a three-dimensional system function of size $64 \times 64 \times 64$ [40]. During this time, the MPI scanner is blocked and cannot be used for clinical measurements, which would not be acceptable in clinical routine. The situation is even worse, as small changes in the measurement procedure, such as using a different SPIO tracer or changing scanner parameters, mean that a

completely new calibration scan is required. A suitable mathematical model that can be simulated in an acceptable time is therefore of utmost importance and can help to reduce the calibration effort. The spatio-temporal Fourier representation of the MPI system function is a suitable candidate for such a model as it allows for the decoupling of the SPIO magnetization behavior from the excitation sequence, i.e., it enables the separation of particle and scanner parameters, which is desirable as it allows for the independent optimization and calibration of the two.

Nevertheless, many physically relevant aspects are not captured by the Langevin model of paramagnetism, such as relaxation effects and particle anisotropies. However, the use of the anisotropic equilibrium model presented in Section 3.1.2 and Section 3.1.3 seems to be a good candidate for the introduction of particle anisotropies. The use of the extended model was proposed in [F5, F7, 3] and recently experimentally validated in [F6]. Compared to the stronger differential equation-based approaches [48, 49, 86, 111, 112], which can also model SPIO distributions with relaxation effects, it is much faster to simulate [F6].

One point that has not yet been fully discussed in this thesis is the transfer function in (2.5) and (2.38). It is usually estimated using a least squares method, in which some calibration scans of SPIOs in an MPI scanner are used and compared with the simulated results of the system function model [51]. Alternatively, the use of a measured transfer function was also recently demonstrated [6]. Here, only the receive path of the scanner is measured without using SPIOs. In [6], however, a model based on partial differential equations was used to simulate the polydisperse SPIO distribution, which is computationally demanding. A combination of [6] with the extended model in [F5–F7] seems to be the next step towards a fully-fledged mathematical MPI model that can be evaluated quickly.

At the moment, the lack of relaxation effects seems to be the main drawback of the model (cf. Theorem 6.1) presented in this thesis, although it was shown in [F5–F7] that the relaxation behavior due to Néel rotation is negligible for the Lissajous FFP-trajectories and typical MPI tracers. To consider one kind of relaxation effects in a first approximation, the model could be combined with the Debye model, which is often used to model relaxation effects in MPI systems with one-dimensional excitation and is described by temporal convolution with an exponentially decaying kernel [10, 20].

Note that when fitting the transfer function, as proposed in [51], the Debye model is basically included, since the Debye model is only described by a convolution in time. In order to increase the modeling power of the mathematical model presented in this thesis, a relaxation model should therefore be developed in the future that exhibits spatio-temporal relaxation effects but is not as complex to simulate as differential-equation based approaches.

Another aspect that is not taken into account in the spatio-temporal frequency model are magnetic field inhomogeneities. It is to be expected that a field inhomogeneity in the drive field $\boldsymbol{H}^{\mathrm{D}}(t)$ leads to a different FFP-trajectory. However, such inhomogeneities can be explained within the mapping function by a probably more complicated FFP-trajectory. The assumption of a linear gradient field for the selection field $\boldsymbol{H}^{\mathrm{S}}(\boldsymbol{x})$ is more delicate, but despite the incorrect assumption, with the proposed theory the field inhomogeneity could be interpreted as a spatially dependent change in the magnetization curve (cf. (2.18) and (2.27)). Therefore, the problem of field inhomogeneities can be solved by a spatially dependent magnetization model, which was basically done for the anisotropic equilibrium model with varying kernel in [F5, C3].

It should also be mentioned that the developed mathematical descriptions have provided new insights into the MPI imaging process and that a direct Chebyshev reconstruction could be obtained for multidimensional MPI based on the Lissajous FFP-trajectories [C1, C3]. This reconstruction method works system-matrix free based on series expansion and only one deconvolution step has to be performed with respect to the assumed SPIO magnetization curve. Furthermore, the close relationship between the weighted Chebyshev polynomials and the Bessel functions may allow for the development of a direct reconstruction approach based on the Bessel functions in the spatio-temporal frequency domain in the future. A first step in this direction was made for the one-dimensional excitation in [F4]. Such a multidimensional method directly reconstructs the Fourier-transformed SPIO distribution. Since the deconvolution usually takes place in the frequency domain, a reconstruction method in the frequency domain would be well suited.

Also worth mentioning is the convolution structure in (6.57), which was formulated more explicitly in this thesis than in previous publications. For example, with its help, it can be justified that a combination of Chebyshev polynomials of the first and second

kind is better suited to compress a system matrix than only with Chebyshev polynomials of the second kind [C2]. The clou of (6.57) is that the derivative between the Chebyshev polynomials and the magnetization curve can be exchanged arbitrarily, which could possibly be used in the future to further optimize the direct reconstruction algorithm in [C1] and also offers advantages regarding the numerical simulation of the system function.

Besides, it was shown in [59] that using sinusoidal excitation with variable DC offsets and the techniques developed in [F1], i.e., using Bessel functions and Chebyshev polynomials, a static nonlinearity in a Wiener-Hammerstein cascade can be identified, suggesting that some of the results developed in this thesis may have a much wider range of applications beyond MPI. An investigation of the relationship between the FFP mapping function and the generalized Bessel function, as shown in this thesis in Section 7.4.1, seems interesting for future research.

For a more general theoretical description of MPI, the inclusion of an FFL in the mathematical framework presented is also of interest, but this is not simple to realize, since the FFL is generally described by a gradient matrix for $\boldsymbol{H}^{\mathrm{D}}(t)$, which is not invertible. The invertibility of the gradient matrix is used in (2.25) to define the function $\boldsymbol{x}_{\mathrm{FFP}}(t)$, which is then used to define the mapping function. Whether this is possible with the concept of generalized functions is an open question, as this point has not yet been investigated.

Contributed Work

First Author

[F1] M. Maass and A. Mertins. “On the representation of magnetic particle imaging in Fourier space”. In: *International Journal on Magnetic Particle Imaging* 6.1 (2020), pp. 1–21, Art. no. 1912001.

[F2] M. Maass, K. Bente, M. Ahlborg, H. Medimagh, H. Phan, T. M. Buzug, and A. Mertins. “Optimized compression of MPI system matrices using a symmetry-preserving secondary orthogonal transform”. In: *International Journal on Magnetic Particle Imaging* 2.1 (2016), pp. 1–5, Art. no. 1607002.

[F3] M. Maass, M. Ahlborg, A. Bakenecker, F. Katzberg, H. Phan, T. M. Buzug, and A. Mertins. “A trajectory study for obtaining MPI system matrices in a compressed-sensing framework”. In: *International Journal on Magnetic Particle Imaging* 3.2 (2017), pp. 1–14, Art. no. 1706005.

[F4] M. Maass, C. Droigk, and A. Mertins. “MPI reconstruction using Bessel functions”. In: *International Journal on Magnetic Particle Imaging* 6.2 Suppl. 1 (2020), pp. 1–3, Art. no. 2009017.

[F5] M. Maass, C. Droigk, M. Eulers, and A. Mertins. “A system function component model for magnetic particle imaging with anisotropic particles”. In: *International Journal on Magnetic Particle Imaging* 9.1 Suppl. 1 (2023), pp. 1–4, Art. no. 2303076.

[F6] M. Maass, T. Kluth, C. Droigk, H. Albers, K. Scheffler, A. Mertins, and T. Knopp. “Equilibrium model with anisotropy for model-based reconstruction in magnetic particle imaging”. In: *IEEE Transactions on Computational Imaging* 10 (2024), pp. 1588–1601.

[F7] M. Maass, C. Droigk, M. Eulers, and A. Mertins. “An analytical equilibrium solution to the Néel relaxation Fokker-Planck equation”. In: *International Journal on Magnetic Particle Imaging* 8.1 Suppl. 1 (2022), pp. 1–4, Art. no. 2203008.

[F8] M. Maass and A. Mertins. “On the formulation of the magentic particle imaging system function in Fourier space”. In: *Proc. International Workshop on Magnetic Particle Imaging*. 2018, pp. 39–40.

[F9] M. Maass, C. Mink, and A. Mertins. “Joint multiresolution magnetic particle imaging and system matrix compression”. In: *International Journal on Magnetic Particle Imaging* 4.2 (2018), pp. 1–8, Art. no. 1811002.

[F10] M. Maass, C. Droigk, F. Katzberg, P. Koch, and A. Mertins. “A recovery algorithm based on the Kaczmarz algorithm and ADMM splitting with application to convex optimization in magnetic particle imaging”. In: *Proc. European Signal Processing Conference*. 2021, pp. 2135–2139.

[F11] M. Maass, C. Droigk, H. Albers, K. Scheffler, A. Mertins, T. Kluth, and T. Knopp. “Magnetic particle imaging with non-oriented immobilized particles: Why the Langevin model of paramagnetism is sufficient”. In: *International Journal on Magnetic Particle Imaging* 10.1 Suppl. 1 (2024), pp. 1–4, Art. no. 2403007.

[F12] M. Maass, C. Droigk, and A. Mertins. “A novel representation of the MPI system function”. In: *International Journal on Magnetic Particle Imaging* 6.2 Suppl. 1 (2020), pp. 1–3, Art. no. 2009050.

Co-Author

[C1] C. Droigk, M. Maass, and A. Mertins. “Direct multi-dimensional Chebyshev polynomial based reconstruction for magnetic particle imaging”. In: *Physics in Medicine and Biology* 67.4 (2022), pp. 1–18, Art. no. 045014.

[C2] C. Droigk, M. Maass, and A. Mertins. “System matrix compression using Chebyshev polynomials of first and second kind”. In: *International Journal on Magnetic Particle Imaging* 8.2 (2022), pp. 1–7, Art. no. 2212003.

[C3] C. Droigk, M. Maass, M. Eulers, and A. Mertins. “Adaption of direct Chebyshev reconstruction to an anisotropic particle model”. In: *International Journal on Magnetic Particle Imaging* 9.1 Suppl. 1 (2023), pp. 1–4, Art. no. 2303027.

[C4] C. Droigk, M. Maass, and A. Mertins. “Multiresolution vessel detection in magnetic particle imaging using wavelets and a Gaussian mixture model”. In: *International Journal of Computer Assisted Radiology and Surgery* 14.11 (2019), pp. 1913–1921.

Bibliography

[1] M. Abramowitz and I. A. Stegun. *Handbook of Mathematical Functions with Formulas, Graphs, and Mathematical Tables*. Vol. 55. Applied Mathematics Series. Washington, D.C.: National Bureau of Standards, 1964.

[2] M. Ahlborg. *Bildgebungskonzepte für Magnetic Particle Imaging: Bildgebungskonzepte und Rekonstruktionsansätze für große Bildgebungsvolumen bei Magnetic Particle Imaging*. Lübeck, Germany: Infinite Science Publishing, 2016.

[3] H. Albers and T. Kluth. "Immobilized nanoparticles with uniaxial anisotropy in multi-dimensional Lissajous-type excitation: An equilibrium model approach". In: *International Journal on Magnetic Particle Imaging* 8.1 Suppl. 1 (2022), pp. 1–4, Art. no. 2203048.

[4] H. Albers, T. Kluth, and T. Knopp. "Simulating magnetization dynamics of large ensembles of single domain nanoparticles: Numerical study of Brown/Néel dynamics and parameter identification problems in magnetic particle imaging". In: *Journal of Magnetism and Magnetic Materials* 541 (2022), pp. 1–15, Art. no. 168508.

[5] H. Albers, T. Knopp, M. Möddel, M. Boberg, and T. Kluth. "Modeling the magnetization dynamics for large ensembles of immobilized magnetic nanoparticles in multi-dimensional magnetic particle imaging". In: *Journal of Magnetism and Magnetic Materials* 543 (2022), pp. 1–11, Art. no. 168534.

[6] H. Albers, F. Thieben, M. Boberg, K. Scheffler, T. Knopp, and T. Kluth. "Model-based calibration and image reconstruction with immobilized nanoparticles". In: *International Journal on Magnetic Particle Imaging* 9.1 Suppl. 1 (2023), pp. 1–5, Art. no. 2303002.

[7] R. Askey and S. Wainger. "Mean convergence of expansions in Laguerre and Hermite series". In: *American Journal of Mathematics* 87.3 (1965), pp. 695–708.

[8] H. Bateman and A. Erdelyi. *Higher Transcendental Functions*. Vol. 2. New York, NY: McGraw-Hill Book Company, 1953.

[9] H. O. Bećа. "An orthogonal set based on Bessel functions of the first kind". In: *Publikacije Elektrotehničkog fakulteta. Serija Matematika i fizika* 678/715 (1980), pp. 85–90.

[10] K. Bente, M. Weber, M. Graeser, T. F. Sattel, M. Erbe, and T. M. Buzug. "Electronic field free line rotation and relaxation deconvolution in magnetic particle imaging". In: *IEEE Transactions on Medical Imaging* 34.2 (2015), pp. 644–651.

[11] C. Brandt and C. Schmidt. "Motion compensation for non-periodic dynamic tracer distributions in multi-patch magnetic particle imaging". In: *Physics in Medicine and Biology* 67.8 (2022), pp. 1–18, Art. no. 085005.

[12] C. Brandt and C. Schmidt. "Modeling magnetic particle imaging for dynamic tracer distributions". In: *Sensing and Imaging* 22 (2021), pp. 1–24, Art. no. 45.

[13] S. Bregner, T. Möller, D. Weiskopf, and D. J. Muraki. "A spectral analysis of function composition and its implications for sampling in direct volume visualization". In: *IEEE Transactions on Visualization and Computer Graphics* 12.5 (2006), pp. 1353–1360.

[14] W. F. Brown. "Thermal fluctuations of a single-domain particle". In: *Physical Review* 130.5 (1963), pp. 1677–1686.

[15] D. C. Champeney. *A Handbook of Fourier Theorems*. Cambridge, UK: Cambridge University Press, 1987.

[16] W. T. Coffey, P. J. Cregg, and Y. U. P. Kalmykov. "On the theory of Debye and Néel relaxation of single domain ferromagnetic particles". In: *Advances in Chemical Physics*. Ed. by I. Prigogine and S. A. Rice. Vol. 83. New York, NY: John Wiley & Sons, 1992. Chap. 5, pp. 263–464.

[17] A. Cordes and T. M. Buzug. "Deconvolution kernel for 1D x-space MPI". In: *Proc. International Workshop on Magnetic Particle Imaging*. 2018, pp. 49–50.

[18] P. J. Cregg and L. Bessais. "A single integral expression for the magnetisation of a textured superparamagnetic system". In: *Journal of Magnetism and Magnetic Materials* 203.1–3 (1999), pp. 265–267.

[19] P. J. Cregg and L. Bessais. "Series expansions for the magnetisation of a solid superparamagnetic system of non-interacting particles with anisotropy". In: *Journal of Magnetism and Magnetic Materials* 202.2–3 (1999), pp. 554–564.

[20] L. R. Croft, P. W. Goodwill, and S. M. Conolly. "Relaxation in x-space magnetic particle imaging". In: *IEEE Transactions on Medical Imaging* 31.12 (2012), pp. 2335–2342.

[21] G. Dattoli, C. Chiccoli, S. Lorenzutta, G. Maino, M. Richetta, and A. Torre. "A note on the theory of n-variable generalized Bessel functions". In: *Il Nuovo Cimento B* 106.10 (1991), pp. 1159–1166.

[22] G. Dattoli and A. Torre. *Theory and applications of generalized Bessel functions*. Rome, Italy: Aracne, 1996.

[23] R. J. Deissler, Y. Wu, and M. A. Martens. "Dependence of Brownian and Néel relaxation times on magnetic field strength". In: *Medical Physics* 41.1 (2013), pp. 1–12, Art. no. 012301.

[24] W. Erb, A. Weinmann, M. Ahlborg, C. Brandt, G. Bringout, T. M. Buzug, J. Frikel, C. Kaethner, T. Knopp, T. März, M. Möddel, M. Storath, and A. Weber. “Mathematical analysis of the 1D model and reconstruction schemes for magnetic particle imaging”. In: *Inverse Problems* 34.5 (2018), pp. 1–21, Art. no. 055012.

[25] G. B. Folland. *Fourier Analysis and its Applications*. The Wadsworth & Brooks/Cole Mathematics Series. Pacific Grove, CA: Wadsworth & Brooks/Cole, 1992.

[26] G. B. Folland. *Real Analysis: Modern Techniques and Their Applications*. 2nd ed. Pure and Applied Mathematics. New York, NY: John Wiley & Sons, 1999.

[27] J. Franke, U. Heinen, H. Lehr, A. Weber, F. Jaspard, W. Ruhm, M. Heidenreich, and V. Schulz. “System characterization of a highly integrated preclinical hybrid MPI-MRI scanner”. In: *IEEE Transactions on Medical Imaging* 35.9 (2016), pp. 1993–2004.

[28] N. Gdaniec, M. Schlüter, M. Möddel, M. G. Kaul, K. M. Krishnan, A. Schlaefer, and T. Knopp. “Detection and compensation of periodic motion in magnetic particle imaging”. In: *IEEE Transactions on Medical Imaging* 36.7 (2017), pp. 1511–1521.

[29] N. Gdaniec, M. Boberg, M. Möddel, P. Szwargulski, and T. Knopp. “Suppression of motion artifacts caused by temporally recurring tracer distributions in multi-patch magnetic particle imaging”. In: *IEEE Transactions on Medical Imaging* 39.11 (2020), pp. 3548–3558.

[30] B. Gleich and J. Weizenecker. “Tomographic imaging using the nonlinear response of magnetic particles”. In: *Nature* 435 (2005), pp. 1214–1217.

[31] P. W. Goodwill, G. C. Scott, P. P. Stang, and S. M. Conolly. “Narrowband magnetic particle imaging”. In: *IEEE Transactions on Medical Imaging* 28.8 (2009), pp. 1231–1237.

[32] P. W. Goodwill and S. M. Conolly. “The x-space formulation of the magnetic particle imaging process: 1-D signal, resolution, bandwidth, SNR, SAR, and magnetostimulation”. In: *IEEE Transactions on Medical Imaging* 29.11 (2010), pp. 1851–1859.

[33] P. W. Goodwill and S. M. Conolly. “Multidimensional x-space magnetic particle imaging”. In: *IEEE Transactions on Medical Imaging* 30.9 (2011), pp. 1581–1590.

[34] M. Graeser, K. Bente, A. Neumann, and T. M. Buzug. “Trajectory dependent particle response for anisotropic mono domain particles in magnetic particle imaging”. In: *Journal of Physics D: Applied Physics* 49.4 (2015), pp. 1–8, Art. no. 045007.

[35] M. Graeser, F. Thieben, P. Szwargulski, F. Werner, N. Gdaniec, M. Boberg, F. Griese, M. Möddel, P. Ludewig, D. van de Ven, O. M. Weber, O. Woywode, B. Gleich, and T. Knopp. "Human-sized magnetic particle imaging for brain applications". In: *Nature Communications* 10.1 (2019), pp. 1–9, Art. no. 1936.

[36] M. Graeser, T. Knopp, M. Grüttner, T. F. Sattel, and T. M. Buzug. "Analog receive signal processing for magnetic particle imaging". In: *Medical Physics* 40.4 (2013), pp. 1–9, Art. no. 042303.

[37] L. Grafakos. *Classical Fourier Analysis*. 3rd ed. Graduate Texts in Mathematics. New York, NY: Springer, 2014.

[38] L. Grafakos and G. Teschl. "On Fourier transforms of radial functions and distributions". In: *Journal of Fourier Analysis and Applications* 19.1 (2013), pp. 167–179.

[39] K. Gräfe, A. von Gladiss, G. Bringout, M. Ahlborg, and T. M. Buzug. "2D images recorded with a single-sided magnetic particle imaging scanner". In: *IEEE Transactions on Medical Imaging* 35.4 (2016), pp. 1056–1065.

[40] M. Grüttner, T. Knopp, J. Franke, M. Heidenreich, J. Rahmer, A. Halkola, C. Kaethner, J. Borgert, and T. M. Buzug. "On the formulation of the image reconstruction problem in magnetic particle imaging". In: *Biomedizinische Technik/Biomedical Engineering* 58.6 (2013), pp. 583–591.

[41] S. Herz, P. Vogel, T. Kampf, P. Dietrich, S. Veldhoen, M. A. Rückert, R. Kickuth, V. C. Behr, and T. A. Bley. "Magnetic particle imaging–guided stenting". In: *Journal of Endovascular Therapy* 26.4 (2019), pp. 512–519.

[42] S. Herz, P. Vogel, T. Kampf, M. A. Rückert, S. Veldhoen, V. C. Behr, and T. A. Bley. "Magnetic particle imaging for quantification of vascular stenoses: A phantom study". In: *IEEE Transactions on Medical Imaging* 37.1 (2018), pp. 61–67.

[43] D. I. Hoult and R. E. Richards. "The signal-to-noise ratio of the nuclear magnetic resonance experiment". In: *Journal of Magnetic Resonance* 24.1 (1976), pp. 71–85.

[44] X. Huang, H. Hui, W. Shang, P. Gao, Y. Zhou, W. Pang, C. M. Woo, J. Tian, and P. Lai. "Deep penetrating and sensitive targeted magnetic particle imaging and photothermal therapy of early-stage glioblastoma based on a biomimetic nanoplatform". In: *Advanced Science* 10.19 (2023), pp. 1–11, Art. no. 2300854.

[45] C. Kaethner, W. Erb, M. Ahlborg, P. Szwargulski, T. Knopp, and T. M. Buzug. "Non-equispaced system matrix acquisition for magnetic particle imaging based on Lissajous node points". In: *IEEE Transactions on Medical Imaging* 35.11 (2016), pp. 2476–2485.

[46] M. G. Kaul, J. Salamon, T. Knopp, H. Ittrich, G. Adam, H. Weller, and C. Jung. "Magnetic particle imaging for in vivo blood flow velocity measurements in mice". In: *Physics in Medicine and Biology* 63.6 (2018), pp. 1–10, Art. no. 064001.

[47] T. Klemme, T. M. Buzug, and A. Neumann. "Exploring parameters of magnetic particles in 1D field excitation". In: *International Journal on Magnetic Particle Imaging* 6.2 (2020), pp. 1–4, Art. no. 2004001.

[48] T. Kluth. "Mathematical models for magnetic particle imaging". In: *Inverse Problems* 34.8 (2018), pp. 1–27, Art. no. 083001.

[49] T. Kluth, P. Szwargulski, and T. Knopp. "Towards accurate modeling of the multidimensional magnetic particle imaging physics". In: *New Journal of Physics* 21.10 (2019), pp. 1–10, Art. no. 103032.

[50] T. Knopp, N. Gdaniec, and M. Möddel. "Magnetic particle imaging: From proof of principle to preclinical applications". In: *Physics in Medicine and Biology* 62.14 (2017), R124–R178.

[51] T. Knopp, S. Biederer, T. F. Sattel, J. Rahmer, J. Weizenecker, B. Gleich, J. Borgert, and T. M. Buzug. "2D model-based reconstruction for magnetic particle imaging". In: *Medical Physics* 37.2 (2010), pp. 485–491.

[52] T. Knopp, S. Biederer, T. F. Sattel, J. Weizenecker, B. Gleich, J. Borgert, and T. M. Buzug. "Trajectory analysis for magnetic particle imaging". In: *Physics in Medicine and Biology* 54.2 (2009), pp. 385–397.

[53] T. Knopp and T. M. Buzug. *Magnetic Particle Imaging: An Introduction to Imaging Principles and Scanner Instrumentation*. Berlin/Heidelberg, Germany: Springer, 2012.

[54] T. Knopp, J. Rahmer, T. F. Sattel, S. Biederer, J. Weizenecker, B. Gleich, J. Borgert, and T. M. Buzug. "Weighted iterative reconstruction for magnetic particle imaging". In: *Physics in Medicine and Biology* 55.6 (2010), pp. 1577–1589.

[55] T. Knopp, T. F. Sattel, S. Biederer, J. Rahmer, J. Weizenecker, B. Gleich, J. Borgert, and T. M. Buzug. "Model-based reconstruction for magnetic particle imaging". In: *IEEE Transactions on Medical Imaging* 29.1 (2010), pp. 12–18.

[56] T. Knopp and A. Weber. "Sparse reconstruction of the magnetic particle imaging system matrix". In: *IEEE Transactions on Medical Imaging* 32.8 (2013), pp. 1473–1480.

[57] T. Knopp and A. Weber. "Local system matrix compression for efficient reconstruction in magnetic particle imaging". In: *Advances in Mathematical Physics* 2015 (2015), pp. 1–7, Art. no. 472818.

[58] H. J. Korsch, A. Klumpp, and D. Witthaut. "On two-dimensional Bessel functions". In: *Journal of Physics A: Mathematical and General* 39.48 (2006), pp. 14947–14964.

[59] T. C. Kranemann and G. Schmitz. “Identification of static nonlinearities by sinusoidal excitation with variable DC offsets”. In: *Review of Scientific Instruments* 92.3 (2021), pp. 1–6, Art. no. 035103.

[60] J. Lampe, C. Bassoy, J. Rahmer, J. Weizenecker, H. Voss, B. Gleich, and J. Borgert. “Fast reconstruction in magnetic particle imaging”. In: *Physics in Medicine and Biology* 57.4 (2012), pp. 1113–1134.

[61] L. J. Landau. “Bessel functions: Monotonicity and bounds”. In: *Journal of the London Mathematical Society* 61.1 (2000), pp. 197–215.

[62] F. Lieb and T. Knopp. “A wavelet-based sparse row-action method for image reconstruction in magnetic particle imaging”. In: *Medical Physics* 48.7 (2021), pp. 3893–3903.

[63] F. Lieb and H.-G. Stark. “Background removal by mixing factor based filtering of the system matrix”. In: *Proc. International Workshop on Magnetic Particle Imaging*. 2019, pp. 33–34.

[64] M. J. Lighthill. *An Introduction to Fourier Analysis and Generalised Functions*. Cambridge Monographs on Mechanics and Applied Mathematics. Cambridge, UK: Cambridge University Press, 1958.

[65] S. Lorenzutta, G. Maino, G. Dattoli, A. Torre, and C. Chiccoli. “On infinite-variable Bessel functions”. In: *Rendiconti di Matematica e delle sue Applicazioni. Serie VII* 15.3 (1995), pp. 405–420.

[66] S. Lorenzutta, G. Maino, G. Dattoli, A. Torre, and C. Chiccoli. “Infinite-variable Bessel functions of the Anger type and the Fourier expansions”. In: *Reports on Mathematical Physics* 39.2 (1997), pp. 163–176.

[67] F. Ludwig, D. Eberbeck, N. Löwa, U. Steinhoff, T. Wawrzik, M. Schilling, and L. Trahms. “Characterization of magnetic nanoparticle systems with respect to their magnetic particle imaging performance”. In: *Biomedizinische Technik/Biomedical Engineering* 58.6 (2013), pp. 535–545.

[68] M. A. Martens, R. J. Deissler, Y. Wu, L. Bauer, Z. Yao, R. Brown, and M. Griswold. “Modeling the Brownian relaxation of nanoparticle ferrofluids: Comparison with experiment”. In: *Medical Physics* 40.2 (2013), pp. 1–8, Art. no. 022303.

[69] T. März and C. B. Macdonald. “Calculus on surfaces with general closest point functions”. In: *SIAM Journal on Numerical Analysis* 50.6 (2012), pp. 3303–3328.

[70] T. März and A. Weinmann. “Model-based reconstruction for magnetic particle imaging in 2D and 3D”. In: *Inverse Problems and Imaging* 10.4 (2016), pp. 1087–1110.

[71] E. E. Mason, C. Z. Cooley, S. F. Cauley, M. A. Griswold, S. M. Conolly, and L. L. Wald. “Design analysis of an MPI human functional brain scanner”. In: *International Journal on Magnetic Particle Imaging* 3.1 (2017), pp. 1–12, Art. no. 1703008.

[72] E. E. Mason, E. Mattingly, K. Herb, M. Śliwiak, S. Franconi, C. Z. Cooley, P. J. Slanetz, and L. L. Wald. “Concept for using magnetic particle imaging for intraoperative margin analysis in breast-conserving surgery”. In: *Scientific Reports* 11.1 (2021), pp. 1–8, Art. no. 13456.

[73] M. Möddel, F. Griese, T. Kluth, and T. Knopp. “Estimating the spatial orientation of immobilized magnetic nanoparticles with parallel-aligned easy axes”. In: *Physical Review Applied* 16.4 (2021), pp. 1–6, Art. no. L041003.

[74] L. Néel. “Thermoremanent magnetization of fine powders”. In: *Reviews of Modern Physics* 25.1 (1953), pp. 293–295.

[75] A. Neumann and T. M. Buzug. “Simulations of magnetic particles with arbitrary anisotropies”. In: *International Journal on Magnetic Particle Imaging* 6.2 Suppl. 1 (2020), pp. 1–3, Art. no. 2009032.

[76] A. A. Ozaslan, A. Alacaoglu, O. B. Demirel, T. Çukur, and E. U. Saritas. “Fully automated gridding reconstruction for non-Cartesian x-space magnetic particle imaging”. In: *Physics in Medicine and Biology* 64.16 (2019), pp. 1–18, Art. no. 165018.

[77] R. Piessens. “Hankel transform”. In: *Transforms and Applications Handbook*. Ed. by A. D. Poularikas. 3rd ed. CRC Press, 2010. Chap. 9.

[78] H. Pollard. “The mean convergence of orthogonal series. I”. In: *Transactions of the American Mathematical Society* 62.3 (1947), pp. 387–403.

[79] H. Pollard. “The mean convergence of orthogonal series. II”. In: *Transactions of the American Mathematical Society* 63.2 (1948), pp. 355–367.

[80] J. Rahmer, J. Weizenecker, B. Gleich, and J. Borgert. “Analysis of a 3-D system function measured for magnetic particle imaging”. In: *IEEE Transactions on Medical Imaging* 31.6 (2012), pp. 1289–1299.

[81] J. Rahmer, J. Weizenecker, B. Gleich, and J. Borgert. “Signal encoding in magnetic particle imaging: Properties of the system function”. In: *BMC Medical Imaging* 9 (2009), pp. 1–21, Art. no. 4.

[82] J. Rahmer, D. Wirtz, C. Bontus, J. Borgert, and B. Gleich. “Interactive magnetic catheter steering with 3-D real-time feedback using multi-color magnetic particle imaging”. In: *IEEE Transactions on Medical Imaging* 36.7 (2017), pp. 1449–1456.

[83] D. B. Reeves. “Nonlinear nonequilibrium simulations of magnetic nanoparticles”. In: *Magnetic Characterization Techniques for Nanomaterials*. Ed. by C. S. S. R. Kumar. Berlin/Heidelberg, Germany: Springer, 2017. Chap. 4, pp. 121–156.

[84] H. Risken. *The Fokker-Planck Equation: Methods of Solution and Applications*. 2nd ed. Springer Series in Synergetics. Berlin/Heidelberg, Germany: Springer, 1996.

[85] H. Robbins. “A remark on stirling’s formula”. In: *The American Mathematical Monthly* 62.1 (1955), pp. 26–29.

[86] H. Rogge, M. Erbe, T. M. Buzug, and K. Lüdtke-Buzug. “Simulation of the magnetization dynamics of diluted ferrofluids in medical applications”. In: *Biomedizinische Technik/Biomedical Engineering* 58.6 (2013), pp. 601–609.

[87] J. Salamon, M. Hofmann, C. Jung, M. G. Kaul, F. Werner, K. Them, R. Reimer, P. Nielsen, A. vom Scheidt, G. Adam, T. Knopp, and H. Ittrich. “Magnetic particle / magnetic resonance imaging: In-vitro MPI-guided real time catheter tracking and 4D angioplasty using a road map and blood pool tracer approach”. In: *PloS one* 11.6 (2016). Ed. by M. Yamamoto, pp. 1–14, Art. no. e0156899.

[88] T. F. Sattel, T. Knopp, S. Biederer, B. Gleich, J. Weizenecker, J. Borgert, and T. M. Buzug. “Single-sided device for magnetic particle imaging”. In: *Journal of Physics D: Applied Physics* 42.2 (2009), pp. 1–5, Art. no. 022001.

[89] K. Scheffler, M. Boberg, and T. Knopp. “Extrapolation of system matrices in magnetic particle imaging”. In: *IEEE Transactions on Medical Imaging* 42.4 (2023), pp. 1121–1132.

[90] C. Schmidt. “Magnetic Particle Imaging – Modeling and Solving a Dynamic Inverse Problem”. PhD thesis. University of Hamburg, 2022.

[91] L. Schmiester, M. Möddel, W. Erb, and T. Knopp. “Direct image reconstruction of Lissajous-type magnetic particle imaging data using Chebyshev-based matrix compression”. In: *IEEE Transactions on Computational Imaging* 3.4 (2017), pp. 671–681.

[92] H. Schomberg. “Magnetic particle imaging: Model and reconstruction”. In: *Proc. IEEE International Symposium on Biomedical Imaging: From Nano to Macro*. 2010, pp. 992–995.

[93] M. I. Shliomis and V. I. Stepanov. *Theory of the Dynamic Susceptibility of Magnetic Fluids. Relaxation Phenomena in Condensed Matter*. Ed. by W. Coffey. Vol. 87. Advances in Chemical Physics. New York, NY: John Wiley & Sons, 1994, pp. 1–30.

[94] N. Smith. “Reciprocity principles for magnetic recording theory”. In: *IEEE Transactions on Magnetics* 23.4 (1987), pp. 1995–2002.

[95] K. Stempak. “A weighted uniform L^p-estimate of Bessel functions: A note on a paper of Guo”. In: *Proceedings of the American Mathematical Society* 128.10 (2000), pp. 2943–2945.

[96] E. C. Stoner and E. P. Wohlfarth. “A mechanism of magnetic hysteresis in heterogeneous alloys”. In: *Philosophical Transactions of the Royal Society of London. Series A, Mathematical and Physical Sciences* 240.826 (1948), pp. 599–642.

[97] M. Storath, C. Brandt, M. Hofmann, T. Knopp, J. Salamon, A. Weber, and A. Weinmann. “Edge preserving and noise reducing reconstruction for magnetic particle imaging”. In: *IEEE Transactions on Medical Imaging* 36.1 (2017), pp. 74–85.

[98] K. R. Stromberg. *An Introduction to Classical Real Analysis*. AMS Chelsea Publishing. Providence, RI: American Mathematical Society, 2015.

[99] P. Szwargulski, C. Kaethner, M. Ahlborg, and T. M. Buzug. “A radial Lissajous trajectory for magnetic particle imaging”. In: *Proc. International Workshop on Magnetic Particle Imaging*. 2015, p. 1.

[100] P. Szwargulski, M. Ahlborg, C. Kaethner, and T. M. Buzug. “Trajectory analysis using static patches for magnetic particle imaging”. In: *IEEE Transactions on Magnetics* 51.2 (2015), pp. 1–4.

[101] W. Tong, Y. Zhang, H. Hui, X. Feng, B. Ning, T. Yu, W. Wang, Y. Shang, G. Zhang, S. Zhang, F. Tian, W. He, Y. Chen, and J. Tian. “Sensitive magnetic particle imaging of haemoglobin degradation for the detection and monitoring of intraplaque haemorrhage in atherosclerosis”. In: *eBioMedicine* 90 (2023), pp. 1–16, Art. no. 104509.

[102] C. B. Top and A. Gungor. “Tomographic field free line magnetic particle imaging with an open-sided scanner configuration”. In: *IEEE Transactions on Medical Imaging* 39.12 (2020), pp. 4164–4173.

[103] P. Vogel, M. A. Rückert, C. Greiner, J. Günther, T. Reichl, T. Kampf, T. A. Bley, V. C. Behr, and S. Herz. “iMPI: Portable human-sized magnetic particle imaging scanner for real-time endovascular interventions”. In: *Scientific Reports* 13.1 (2023), pp. 1–14, Art. no. 10472.

[104] P. Vogel, S. Lother, M. A. Rückert, W. H. Kullmann, P. M. Jakob, F. Fidler, and V. C. Behr. “MRI meets MPI: A bimodal MPI-MRI tomograph”. In: *IEEE Transactions on Medical Imaging* 33.10 (2014), pp. 1954–1959.

[105] P. Vogel, J. Markert, M. A. Rückert, S. Herz, B. Keßler, K. Dremel, D. Althoff, M. Weber, T. M. Buzug, T. A. Bley, W. H. Kullmann, R. Hanke, S. Zabler, and V. C. Behr. “Magnetic particle imaging meets computed tomography: First simultaneous imaging”. In: *Scientific Reports* 9.1 (2019), pp. 1–9, Art. no. 12627.

[106] P. Vogel, M. A. Rückert, T. Kampf, S. Herz, A. Stang, L. Wöckel, T. A. Bley, S. Dutz, and V. C. Behr. “Superspeed bolus visualization for vascular magnetic particle imaging”. In: *IEEE Transactions on Medical Imaging* 39.6 (2020), pp. 2133–2139.

[107] P. Vogel, M. A. Rückert, P. Klauer, W. H. Kullmann, P. M. Jakob, and V. C. Behr. "Traveling wave magnetic particle imaging". In: *IEEE Transactions on Medical Imaging* 33.2 (2014), pp. 400–407.

[108] G. N. Watson. *A Treatise on the Theory of Bessel Functions*. 2nd ed. Cambridge Mathematical Library. Cambridge, UK: Cambridge University Press, 1944, Art. no. Previous ed.: 1922, Reprinted in 1995.

[109] A. Weber and T. Knopp. "Symmetries of the 2D magnetic particle imaging system matrix". In: *Physics in Medicine and Biology* 60.10 (2015), pp. 4033–4044.

[110] F. Wegner, T. Friedrich, A. von Gladiss, U. Grzyska, M. M. Sieren, K. Lüdtke-Buzug, A. Frydrychowicz, T. M. Buzug, J. Barkhausen, and J. Haegele. "Magnetic particle imaging: Artifact-free metallic stent lumen imaging in a phantom study". In: *CardioVascular and Interventional Radiology* 43.2 (2019), pp. 331–338.

[111] J. Weizenecker. "The Fokker–Planck equation for coupled Brown–Néel-rotation". In: *Physics in Medicine and Biology* 63.3 (2018), pp. 1–21, Art. no. 035004.

[112] J. Weizenecker, B. Gleich, J. Rahmer, and J. Borgert. "Particle dynamics of mono-domain particles in magnetic particle imaging". In: *Magnetic Nanoparticles: Particle Science, Imaging Technology and Clinical Applications*. World Scientific, 2010, pp. 3–15.

[113] J. Weizenecker, B. Gleich, J. Rahmer, H. Dahnke, and J. Borgert. "Three-dimensional real-time in vivo magnetic particle imaging". In: *Physics in Medicine and Biology* 54.5 (2009), pp. L1–L10.

[114] G. M. Wing. "The mean convergence of orthogonal series". In: *American Journal of Mathematics* 72.4 (1950), pp. 792–808.

[115] T. Yoshida and K. Enpuku. "Simulation and quantitative clarification of AC susceptibility of magnetic fluid in nonlinear Brownian relaxation region". In: *Japanese Journal of Applied Physics* 48.12 (2009), pp. 1–7, Art. no. 127002.

[116] T. Yoshida, Y. Matsugi, N. Tsujimura, T. Sasayama, K. Enpuku, T. Viereck, M. Schilling, and F. Ludwig. "Effect of alignment of easy axes on dynamic magnetization of immobilized magnetic nanoparticles". In: *Journal of Magnetism and Magnetic Materials* 427 (2017), pp. 162–167.

[117] X. Zhu, J. Li, P. Peng, N. Hosseini Nassab, and B. R. Smith. "Quantitative drug release monitoring in tumors of living subjects by magnetic particle imaging nanocomposite". In: *Nano Letters* 19.10 (2019), pp. 6725–6733.

Acronyms and Notations

A/D Analog-to-digital

FFL Field-free line

FFP Field-free point

FOV Field of view

MPI Magnetic particle imaging

FFL Field-free line

PDF Probability density function

SPIO Superparamagnetic iron oxide nanoparticles

Notations	
Symbol	Description
$\mathbb{N}$	Set of natural numbers without zero
$\mathbb{N}_0$	Set of natural numbers including zero
$\mathbb{Z}$	Set of integer numbers
$\mathbb{R}$	Set of real numbers
$\mathbb{R}_+ = [0, \infty)$	Set of non-negative real numbers
$\mathbb{C}$	Set of complex number
$N, M \in \mathbb{N}$	Sizes of the dimensions
$C_0(\mathbb{R}^N)$	Space of functions which are continuous and vanish at infinity
$L^p(\Omega)$	Set of functions on $\Omega \subseteq \mathbb{R}^N$ with finite L^p-norm
L^p	Shorthand for $L^p(\Omega)$
$\mathbb{S}^2 \subset \mathbb{R}^3$	Surface area of the unit sphere
$\|\boldsymbol{x}\|_p$	Vector-valued p-norm with $1 \leq p \leq \infty$ and $\boldsymbol{x} \in \mathbb{C}^N$
$\|\boldsymbol{x}\| = \|\boldsymbol{x}\|_2$	Euclidean vector norm
$\|f\|_{L^p}$	L^p-norm of function $f : \Omega \to \mathbb{C}$ with $1 \leq p \leq \infty$
$\boldsymbol{x}^\mathsf{T}$, $\boldsymbol{A}^\mathsf{T}$	Transpose of the vector $\boldsymbol{x} \in \mathbb{C}^N$ and matrix $\boldsymbol{A} \in \mathbb{C}^{M \times N}$
$\boldsymbol{f}^\mathsf{T}(\boldsymbol{x}) = (\boldsymbol{f}(\boldsymbol{x}))^\mathsf{T}$	Transpose of vector-valued function $\boldsymbol{f} : \Omega \to \mathbb{C}^N$
$\boldsymbol{A}^{-\mathsf{T}} = (\boldsymbol{A}^{-1})^\mathsf{T}$	Shorthand for inverse and transpose of a matrix $\boldsymbol{A} \in \mathbb{R}^{N \times N}$